The Transition to Asymmetry in Pipe Flow of Shear-thinning Fluids

by

Chaofan Wen

A thesis submitted in partial
fulfillment of the requirements for
the degree of Doctor of Philosophy
University of Liverpool
School of Engineering

Declaration

I hereby declare that this dissertation is a record of work carried out in the School of Engineering at the University of Liverpool during the period from October 2013 to September 2016. The dissertation is original in content except where otherwise indicated. September 2016

.....
(Chaofan Wen)

Abstract

This thesis focuses on a particularly confusing aspect of the pipe flow of shear-thinning polymer solutions, which remains unexplained despite its ubiquity in all experimental results since its discovery around 2 decades ago. This is the observation that, time-averaged velocity profiles are axisymmetric when the flow is purely laminar or fully turbulent, contrary to expectations it is asymmetric when flow is in the vicinity of the transitional flow regime. This phenomenon is repeatable and many potential causes have been ruled out, such as the rotation of the earth, curvature of the pipe axis, major imperfection of flow geometry, upstream and downstream disturbances or temperature gradients. Therefore, this asymmetry is thought to be attributed to some, as yet unknown, fluid mechanism. In this work we provide new experimental results using stereoscopic particle image velocimetry that simultaneously capture the three-component velocity field across the entire pipe cross-section, which provides a much clearer picture of the behaviour of the asymmetric velocity profile and reveals that the asymmetry is produced by a pathway that has not previously been proposed.

We first investigated the characteristics of flow asymmetry using an aqueous solution of 0.15% xanthan gum, which is essentially shear-thinning without large elastic effects. We experimentally observed that the asymmetry is not stationary but is actually time-varying, although it does have a preferred orientation in the cross-sectional plane. The asymmetry occurs when the Reynolds number (Re) exceeds a critical value Re_c and the degree of asymmetry increases steadily with Re until the onset of turbulent puffs. In fact, the asymmetry approximately grows with the square root of Reynolds numbers, i.e. $(Re - Re_c)^{0.5}$, suggesting a supercritical instability of the laminar base state leading to the flow asymmetry. The asymmetry is also non-hysteretic, reversible, and contrary to what was previously believed, the classical laminar-turbulent transition is actually responsible for returning symmetry to the flow.

Different concentrations of xanthan gum solutions, namely 0.07%, 0.08%, 0.1%, 0.125%, 0.15%, 0.2% were investigated to study the effect of shear-thinning characteristics on the asymmetry. The asymmetry is prevalent throughout all xanthan gum solutions with different shear-thinning characteristics and, the greater the shear-thinning characteristics, the stronger the fluid asymmetry will appear. However, the critical Reynolds number for transition from axisymmetry to asymmetry remains unchanged ($\approx$2000) when the shear-thinning characteristics of the fluid varied. The shear-thinning characteristics also delay the onset of laminar turbulent transition compared with Newtonian fluids.

We also investigated the effect of viscoelastic characteristics on asymmetry using polyacrylamide (PAA) aqueous solution. The asymmetry was absent in pure PAA solutions with concentration of 0.09%, 0.125% and 0.2%. However, once shear-induced degradation was deliberately imposed on the 0.125% PAA solution to destruct the viscoelasticity while preserving the shear-thinning characteristics, the asymmetry reappears. The asymmetry in degraded PAA solution was also observed to evolve in a supercritical form which is similar to that of the xanthan gum solutions. Also 100, 200 and 500ppm PAA was added to a 0.15% xanthan gum solution, the maximum degree of asymmetry was decreased with higher addition concentration of PAA, also suggesting that the viscoelasticity may inhibit asymmetry.

Publications

- C. Wen, R. Poole, D. Dennis, New insights into the nature of the asymmetrical flow of shear-thinning polymer solutions in transitional pipe flow. Proceedings of the 67th Annual Meeting of the Division of Fluid Dynamics of the American Physical Society, San Francisco, California, November 2014.

- C. Wen, R. Poole, D. Dennis, The time-varying nature of the asymmetrical flow of a shear-thinning polymer solution in transitional pipe flow. 15th European turbulence conference, Delft, Netherlands, August 2015.

- D. Dennis, C. Wen, R. Poole, Transition to asymmetry in pipe flow of shear-thinning fluids: a linear instability? Proceedings of the 68th Annual Meeting of the Division of Fluid Dynamics of the American Physical Society, Boston, Massachusetts, November 2015.

- C. Wen, R. Poole, D. Dennis, Investigation of transition to asymmetry in pipe flow of shear-thinning fluids. 8th European Postgradute Fluid Dynamics Conference, Warsaw, July 2016

- C. Wen, R. Poole, D. Dennis, Transition to asymmetry in pipe flow of shear-thinning fluids. The XVIIth International Congress on Rheology, Kyoto, Japan, August 2016

- C. Wen, R. Poole, A.P. Willis, D. Dennis, Symmetry-breaking supercritical transition in pipe flow of shear-thinning fluids . Physical Review Letter (under review)

Acknowledgements

It is really my happy time to express my gratitude to all those people who have supported me and had their contributions in making this thesis possible. Writing this note of thanks represents not only the work on the keyboard, it is my pleasurable and valuable memories of sharing my times with these nice people during my pursuit of PhD.

Firstly, I would like to express my sincere thanks to my supervisor Dr David Dennis. I appreciate all his contributions of time, ideas, constructive suggests and criticisms to improve my research. I have benefited immensely from his knowledge on SPIV experiments and fluid dynamics. He is more than professional on the research, he is also soooo (not typo) friendly to students, people around him, like bringing us to his home to have a nice BBQ in weekend, sharing some of his PhD experience in Cambridge or giving some suggestions on my holiday trips, etc.. I am also grateful to my supervisor Prof. Robert Poole. The enthusiasm, Prof. Robert Poole natively has for the research, has been always contagious and motivational for the students. His rich experience and knowledge on this project and non-Newtonian fluids mechanics benefit me a lot and I am appreciated for his insightful suggestions which always improved my research work. Personally, I am jealous of his cute puppy and also grateful for the Costa coffee and biscuit he provided in group meeting.

Secondly, the financial support by the China Scholarship Council and my domestic university, National University of Defense Technology are gratefully acknowledged. They generously provide me the tuition fee, living expenses, air tickets and hotel fee for conferences in San Francisco, Delft and Warsaw as well as the air tickets between China and U.K. Thanks for them to think about everything from my position and give me their thoughtful concerns to make sure my life in U.K. is well and carefree.

The fruitful discussions with Prof. Rich Kerswell, Prof. Michael Graham, Prof. X. Wu, Dr Alexander Morozov and Dr Ashley Willis on this phenomenon and DNS simulations are also gratefully acknowledged.

I want to express my thanks and give a big hug to my colleagues in office and laboratory. Thanks for their time with me in school, restaurants, gym, pubs and make my time in Liverpool more enjoyable. Mr Mahdi Davoodi discussed with me a lot on the project, some papers and he is also my free fitness instructor in gym. I am also thankful to Mr Waleed M. Abed for his kind help on rheological measurements in my first year and his hospitality to me. Mr Bayode Owolabi, who spend most of time with me in the laboratory also deserves a big thank you. He is a nice person and always provides me assists on LDV settings and measurements. Mr Allysson Domingues also shared his CFD knowledge to me and organized so many good events for us. Mr Haonan Xu and Simeng Chen are not only my colleagues but also my housemates, with whom I shared the high and low of my research, together with numerous 'game nights' in weekends. I also feel privileged to thank all other faculty members in School of Engineering, To Mr Jack Carter-Hallam, who provides excellent administrative help. To Mr Christopher Hinchliffe and Mr Derek Neary, who give their technical skills and knowledge for numerous occasions in using the experimental rig. I also appreciate the help from Mr Robert Jaryczewski in Dantec Dynamic, who helps me a lot on SPIV system.

I thank my friends here, Vladimir Leble, Antonio Jimenez-Garcia, Junjie Wang, Simone Colonia, Savio Badu. I enjoy the super time with them in football pitch, pubs, parks, homes and multicultural experience they bring to me. This friendship is my unforgettable memory.

Lastly, I would like to thank my mum, dad and girlfriend Gao Ya. They always give me unconditional support and encouragement. Their love transcends distance, which makes me feel peaceful and settled in the heart.

Contents

List of Figures

List of Tables

Nomenclature

α	asymmetry factor
f_D	Darcy friction facter
f_F	Fanning friction facter
Re	Reynolds number for Newtonian fluid
Re_c	critical Reynolds number
Re_w	Reynolds number based on wall shear stress viscosity
Re_{MR}	Metzner-Reed Reynolds number
λ_{ci}	swirl strength
u	axial velocity(m/s)
u'	axial velocity fluctuation (m/s)
U_b	bulk velocity (m/s)
$\dot{Q}$	volumetric flow rate (m^3/s)
D	pipe inner diameter (m)
R	pipe radius (m)
r	radius (m)
p	pressure (Pa)
h	head loss (m)
r_p/D	dimensionless radius of peak velocity
t	time (s)
c	concentration w/w (%)
ρ	fluid density (kg$\cdot$ m^{-3})
μ	fluid viscosity (kg$\cdot$ m^{-1}s^{-1})
μ_0	zero fluid viscosity (kg$\cdot$ m^{-1}s^{-1})
μ_∞	infinite fluid viscosity (kg$\cdot$ m^{-1}s^{-1})
μ_w	viscosity based on wall shear stress (kg$\cdot$ m^{-1}s^{-1})
Ω	angular velocity of the earth (rad/s)
τ	shear stress (Pa)
τ_Y	yield stress (Pa)
τ_w	wall shear stress (Pa)
$f\#$	f-number or relative aperture
$\dot{\gamma}$	shear rate (s^{-1})
u_{rms}/U_b	streamwise velocity fluctuations
$v_{r\theta,rms}/U_b$	cross-stream velocity fluctuations
λ_M	relaxation time based on small amplitude oscillatory shear measurement (s)
λ_c	relaxation time based on capillary breakup extensional rheometer (s)
n	flow behaviour index
k	flow consistency index (Pa$\cdot$s^n)

Acronyms

CCD	Charge Coupled Device
CMOS	Complementary Metal-Oxide-Semiconductor
CMC	CarboxyMethyl Cellulose
CARB	Carbopol
DNS	Direct Numerical Simulation
FOV	Field of View
IA	Interrogation Area
IF	Intermittency factor
LAP	Laponite
LDV	Laser Doppler Velocimetry
PIV	Particle Image Velocimetry
SPIV	Stereoscopic Particle Image Velocimetry
PAA	Polyacrylamide
rms	root mean square
MDR	Maximum Drag Reduction
RSS	Residual Sum of Squares
XG	Xanthan Gum
SAOS	Small Amplitude Oscillatory Shear
fps	frame per second

Chapter 1

Introduction

1.1 Background

Rheology is defined as the science of the deformation and flow of matter. The term rheology originates from Greek words rheos and the Greek philosopher Heraclitus described rheology as "panta rei" i.e. everything flows. The matter studied in rheology is primarily in a liquid state, but also as soft matter or solids, therefore rheology is applicable to all substances, from gases to solids and herein, the rheology of liquid-like materials were specifically studied. The fluids surrounding us can be generally categorized into two types. The first category of fluids is *Newtonian fluid*, e.g. air, water. For Newtonian fluids, the viscosity, μ, depends only on temperature and pressure and is independent of the shear rate. The diagram relating shear stress and shear rate for Newtonian fluids, i.e. *flow curve*, is therefore a straight line of slope μ, the viscosity is uniform in the fluid and completely characterizes the fluid. The other category of fluids is *non-Newtonian fluids*. Non-Newtonian fluid is a fluid whose flow properties differ in any way from those of a Newtonian fluid. Non-Newtonian fluids are those for which the flow curve is not linear. It means the viscosity of non-Newtonian fluids is not constant at a given temperature and pressure but depends on other factors such as the shear rate, external stress or the shear rate history in the fluid. The rheological characterization of non-Newtonian fluids is

more complicated than that of Newtonian fluids. The different non-Newtonian fluids could display shear-thinning, shear-thickening, time-dependent and viscoelastic flow behaviours under proper circumstances, which is essentially different from Newtonian fluids [9, 24, 35]. Many commonly found substances, such as shampoo, ketchup, paint, toothpaste, syrup, blood, foams, suspensions, polymer solutions etc. can be classified into non-Newtonian fluids (see Table 1.1).

•Adhesives (wall paper paste, carpet adhesive, for instance)	•Food stuffs (Fruit/vegetable purees and concentrates, sauces, salad dressings, mayonnaise, jams and marmalades, ice-cream, soups, cake mixes and cake toppings, egg white, bread mixes, snacks)
•Ales (beer, liqueurs, etc.)	•Greases and lubricating oils
•Animal waste slurries from cattle farms	•Mine tailings and mineral suspensions
•Biological fluids (blood, synovial fluid, saliva, etc.)	•Molten lava and magmas
•Bitumen	•Paints, polishes and varnishes
•Cement paste and slurries	•Paper pulp suspensions
•Chalk slurries	•Peat and lignite slurries
•Chocolates	•Polymer melts and solutions, reinforced plastics, rubber
•Coal slurries	•Printing colors and inks
•Cosmetics and personal care products (nail polish, lotions and creams, lipsticks, shampoos, shaving foams and creams, toothpaste, etc)	•Pharmaceutical products (creams, foams, suspensions, for instance)
•Dairy products and dairy waste streams (cheese, butter, yogurt, fresh cream, whey, for instance)	•Sewage sludge
•Drilling muds	•Wet beach sand
•Fire fighting foams	•Waxy crude oils

Table 1.1: Examples of substances exhibiting non-Newtonian fluid behaviour, data from Chhabra [24].

Table 1.1 clearly shows the non-Newtonian fluids are ubiquitous in a very wide range of engineering systems and industrial applications [26]. Herein, we particularly restrict our attention to polymer solutions, which are one type of non-Newtonian fluids. Polymer molecules are long chain molecules composed of many repeating units. These polymers also have different physical properties because of the different structure and bonding of their molecules but generally the polymer solution has a pseudo-plastic behaviour i.e., its viscosity decreases with increasing

shear rate. Most of the polymer are water soluble and used in industries as a rheology control additive, i.e. rheology modifiers [117].

In the manufacturing and transportation process of these man-made non-Newtonian fluids, pipe flows are invariably involved. The study of pipe flows can be traced back to the work of Gotthilf Heinrich Ludwig Hagen (Hagen 1839, 1854), Jean Louis Marie Poiseuille (Poiseuille 1840) and most famously, Osborne Reynolds (Reynolds 1883) [47, 114] and now it still remains a scientific challenge. Experimentally, Reynolds observed that at low flow rates, a filament of dyed fluid was convected to the end of the pipe without mixing and this flow state is defined as *laminar flow*. In laminar flow, the motion of fluids is orderly without disruption between parallel layers in the mean flow direction. At high flow rates, the dyed fluid blended quickly and the entire pipe was coloured. This flow state is termed as *turbulent flow*. Turbulent flow was characterized by chaotic changes in pressure and velocity. In turbulent flow, eddies of various sizes are superimposed onto the mean flow as depicted in Figure 1.1. When dye enters the turbulent region, it traces a path dominated by both the mean flow (streamlines) and the eddies. Larger eddies carry the dye laterally across streamlines. Smaller eddies create smaller scale stirring that causes the dye filament to spread (diffuse).

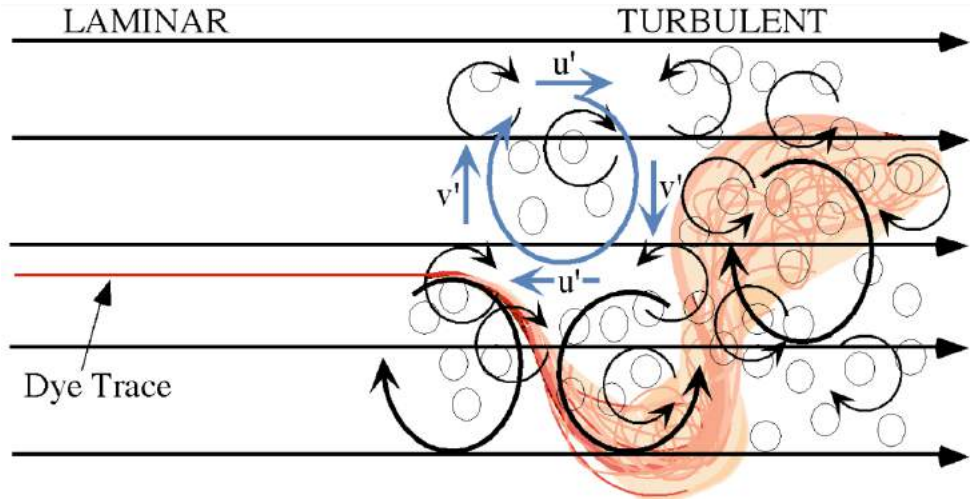

Figure 1.1: Flow streamlines in laminar and turbulent flow. The straight, parallel black lines are streamlines of mean flow while the chaotic streamlines are turbulent flow. Figure from McDonough [100].

The process of laminar flow becoming turbulent is described as laminar-turbulent transi-

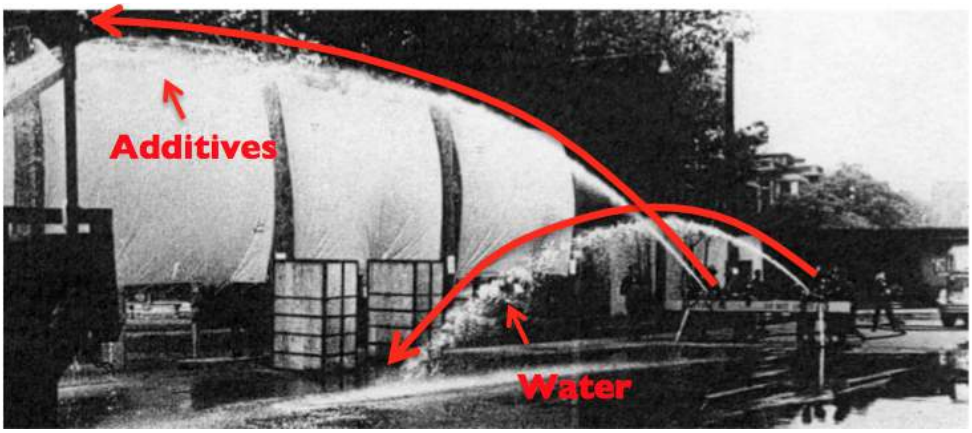

Figure 1.2: Demonstration of the benefit of polymers in May 1969, New York. The two jets are of equal size and fed from pumps at the same pressure. The jet barely reaching the holding tank is the standard water, the other contains water-soluble polyethylene oxide polymer additives. Cited from the *The New York Times*, May 13, 1969.

tion. The transition from laminar to turbulent flow is linked with a large change in flow-related processes, for instance, a significant change of mass diffusion, heat transfer and friction when transition occurs. Reynolds discovered a laminar flow becomes unstable and chaotic (turbulent) if the dimensionless number exceeds a certain critical value and this dimensionless number now is known as Reynolds number, defined as $Re = UD/\nu$, where U is the bulk velocity, D is the pipe diameter and ν is the kinematic viscosity of the fluid. The laminar-turbulent transition is a very complex process, even in Newtonian fluids, the transition from stable flow state to chaotic flow state is still the most intriguing, puzzling and important aspects of fluid dynamics [46]. The problem of turbulence and flow instability which will result in the development of turbulence, have been studied by many greatest physicists and engineers from the 19^{th} century to date, starting with the recognition of this unique and distinct phenomenon from da Vinci and followed by the works of Boussinesq and Reynolds in the 19^{th} century, continuing with outstanding work of Prandtl, Taylor, Kolmogorov and many others in the 20^{th} century [99].

One interesting flow behaviour is observed in pipe flow when a small amount of long-chain polymer is added into a Newtonian solvent, which produces a non-Newtonian fluid solution. The frictional drag of polymer solution is significantly reduced in turbulent pipe flow and such phenomenon was first discovered by Toms [155] in the 1940s. Virk [161] reported the existence

of a maximum level or achievable drag reduction by empirical observation now known as the *Virk asymptote*. Virk's asymptote indicates the maximum drag reduction in pipe flow and the turbulent friction losses after adding some polymers could reach up to 80% in comparison with the Newtonian solvent. The drag-reducing ability of the polymer solution has attracted extensive research interest [14, 33, 93, 161, 166] as its practical and economical applications, such as flow driving power supply reduction in oil pipe lines, public sewer, district cooling/heating system, food product transportation and fire control (depicted in Figure 1.2).

Figure 1.3: Schematic of polymer stretch-coil transition in shear flow. The end-to-end vector of the molecule is denoted as q. Figure from the MTFC research group.

The complexity of drag reduction using polymer solution lies in the coupling of near-wall turbulence dynamics and the dynamics of the polymer solution. The degree of drag reduction relies on the molecular weight, mobility of polymer chain as well as the various conformations of molecule. The flow-induced stress in turbulent flow can strongly modify the configuration of molecule, particularly, stretch them, which is namely as coil-stretch transition [61] of polymers, shown in Figure 1.3. The polymer molecules can be modeled as bead-spring chains and in the bead-spring chain model, the bead locations are tracked, and they are the points where the hydrodynamic forces are applied. Springs between the beads indicate the variation of free energy of the chain as regions of the polymer are stretched. Because the hydrodynamic interactions are decreased by stretching, a polymer coil can unwind abruptly when a certain critical value of the velocity gradient is obtained. The conformation of flexible long-chain polymers can affect the fluid property and therefore result in some different flow behaviours compared with Newtonian fluids. White and Mungal [166] reviews recent (until 2008) progress in understanding the interaction between the turbulent flow and high-molecular weight polymers. It reveals the polymer interacts with flow and alters the nature and strength of the vortices formed, leading to

a significant modification of the near-wall turbulence structure and thus changes to the flow.

1.2 Motivation

The aforementioned considerations, both in fundamental research interests and industrial applications, provide us a motivation to further investigate the pipe flow of non-Newtonian fluids. In contrast with the substantial progress made in understanding the flow mechanism of instability and turbulence for Newtonian fluids in pipes, given the inherent additional complexity introduced by the polymer molecular chains, for non-Newtonian fluids much less is known. Aside from comparatively broad study of turbulent flow in adding some polymers as drag reducing agent, far fewer studies about flow transition mechanism of non-Newtonian fluids have been done theoretically, numerically or experimentally. The existing handful of papers regarding transitional pipe flow of non-Newtonian fluids reveals an intriguing, and as yet unexplained effect: above a critical Reynolds number, the flow develops an asymmetric distribution of mean axial velocity profile. This asymmetry has been found experimentally in independent research programmes in U.K., France and Australia [51], and subsequently in Canada [64]. This phenomenon can be often observed repeatedly and remains for the whole duration of the experiments (a few weeks) and is thought to be due to some, as yet unknown, fluid mechanism. This observation of asymmetry in transitional pipe flow of shear-thinning fluids motivates us to re-examine this distinct phenomenon and further study the fundamental nature of flow instability and laminar-turbulent transition in pipe flow using non-Newtonian fluids.

1.3 Aim and objectives

- The primary aim of this work endeavours to address this unusual asymmetry phenomenon in shear-thinning fluids. We attempt to experimentally explain the mechanism leading to the asymmetry of shear-thinning fluids in pipe flow, together with investigating the effect of shear-thinning/viscoelastic characteristics on flow asymmetry using different types and

concentrations of fluids.

- Another objective of the study is to perform novel experiments to reveal the flow characteristics of shear-thinning fluids covering the laminar, transitional and fully-turbulent regimes. The majority of previous experimental works utilized the Laser Doppler velocimetry (LDV) technique to investigate the flow, which is a single-point measurement. The LDV investigation can provide a very quick dynamic response measurement, but the probe volume of LDV is typically dozens to hundreds microns long and therefore incapable of investigating the features of the whole field, particularly the three-dimensional flow structure of turbulence in transitional flow. In this work, we present stereoscopic particle image velocity (SPIV) data to characterize the pipe flow of shear-thinning and viscoelastic fluids, which can provide complete flow-field information in a cross-sectional plane of the pipe instantaneously.

- This work also aims to shed more light on understanding of fundamental nature of pipe flow using shear-thinning and viscoelastic fluids, which is an essential requirement for potentially controlling the flow.

1.4 Outlines of thesis

The thesis consists of eight chapters in total. The fundamental theories of non-Newtonian fluids and pipe flows are introduced in chapter 2. Chapter 3 reviews previous works and literature about pipe flow of Newtonian/non-Newtonian fluids. Chapter 4 presents the experimental setup and experimental techniques, together with the data-processing methodologies. Chapter 5 investigates the flow characteristics of the asymmetry using an aqueous solution of 0.15% xanthan gum and elaborates the mechanism underneath the flow asymmetry. In chapter 6, the effect of shear-thinning characteristics on asymmetry is studied using various concentrations of

xanthan gum solutions. Chapter 7 endeavours to clarify the effect of viscoelastic characteristics on asymmetry using pure polyacrylamide and xanthan gum/polyacrylamide blends. The thesis ends with chapter 8 with the conclusions of the current work and some suggestions for future work.

Chapter 2

Theoretical background of rheology and pipe flow

This chapter discusses the fundamental theory of rheology and flow in pipes. Generally, non-Newtonian fluids may be classified into three broad types:

- fluids which have a time-independent viscosity, the rate of shear at any point is some function of the shearing stress at that point and depends on nothing else;
- systems for which exhibit both viscous and elastic characteristics when undergoing deformation, the so-called viscoelastic fluids. Viscoelastic materials have elements of both of viscous and elastic properties;
- more complex systems which have a time-dependent viscosity, the relation between shear stress and shear rate depends on the time the fluid has been sheared or on its previous history;

We confine ourselves here to the first two fluid types. This is because the fluids (polymer solutions) we or previous works utilized essentially belong to the first two types of non-Newtonian fluids, which have a time-independent viscosity or viscoelasticity.

2.1 Governing equations for non-Newtonian fluids

The flow of fluids, both Newtonian or non-Newtonian, are invariably governed by the laws of conservation of mass and momentum [125]. The conservation of mass equation or the continuity equation is displayed below:

$$\frac{\partial \rho}{\partial t} + \frac{\partial (\rho v_i)}{\partial x_i} = 0 \tag{2.1}$$

where x_i is the displacement component in i^{th} direction, i.e. x, y, z in three-dimensional Cartesian coordinate system, v_i is the velocity component in i^{th} direction and ρ is the density of fluids. The momentum equation is derived in a control volume using Newton's second law to balance the force in fluids. The momentum equation is given:

$$\frac{\partial \rho v_i}{\partial t} + \frac{\partial (\rho v_j v_i)}{\partial x_j} = f_i + \frac{\partial \tau_{ij}}{\partial x_j} - \frac{\partial p}{\partial x_i} \tag{2.2}$$

where f_i is the body force in i^{th} direction, for example gravity, inertial acceleration, Coriolis acceleration etc. p is the pressure, τ_{ij} is the ij component of the viscous stress tensor acting on fluid element. To note, the viscous stress τ_{ij} depends on the deformation of the material. For different materials, the constitutive equation or constitutive relation is introduced to describe the material properties in order to close the momentum equation described by Equation 2.2. The constitutive equation gives the relation between stress and deformation of fluids empirically and therefore Newtonian and non-Newtonian fluids are distinguished based on the constitutive equation. To note, there is no universal constitutive equation for non-Newtonian fluids, e.g. polymer solutions used in this project [131]. This is due to the intrinsic complexity of polymer solution and there are some inadequacies in understanding the flow characteristics of this fluid.

2.2 Rheological characterization of non-Newtonian fluids

One objective of rheology is to study the deformations and flows of matter. For the Newtonian incompressible fluid, the constitutive equation regresses to the simplest case (also the most

familiar scenario, e.g. in water): the viscous stress is proportional to shear rate, i.e. Newton's law of viscosity:

$$\tau_{ij} = \mu \cdot \dot{\gamma}_{ij} \tag{2.3}$$

where μ is the viscosity of fluids, which is independent of shear rate $\dot{\gamma}_{ij}$ at given temperature and pressure. The shear rate $\dot{\gamma}_{ij}$ is written as:

$$\dot{\gamma}_{ij} = \left(\frac{\partial v_i}{\partial x_j} + \frac{\partial v_j}{\partial x_i} \right) \tag{2.4}$$

which represents the velocity variation in the direction perpendicular to main flow. If the fluids do not satisfy the relationship given in Equation 2.3, e.g. the viscosity is not constant for different shear rate, the fluid is termed as non-Newtonian fluids. Newtonian behaviour is exhibited by fluids in which the dissipation of viscous energy is due to the collision of comparatively small molecular species. All gases and liquids and solutions of low molecular weight come into this category. However, the non-Newtonian fluids, for example, some colloidal solution and polymeric solutions, the molecular weight is quite large. This long-chain materials will generate *non-Newtonian stress*, therefore giving the fluid different dynamic behaviours. Broadly, the physical properties of non-Newtonian fluids can be manifested as shear-thinning, viscoelastic, presence of yield-stress, etc. . In consideration of the polymer solutions used in our experiments, the following content will emphasize the shear-thinning and viscoelastic property of such fluids.

2.2.1 Shear viscosity in shear flow

In this subsection, a more complicated constitutive equation for non-Newtonian fluids will be discussed first. Regarding the non-Newtonian fluids, the shear stress τ_{ij} and shear rate $\dot{\gamma}_{ij}$ do not possess the linear relationship, which is essentially different from that of Newtonian fluids as shown in Equation 2.3. To generate analogous definition of viscosity comparing with Newtonian fluids, the apparent non-Newtonian shear viscosity $\mu(\dot{\gamma}_{ij})$ is introduced below:

$$\tau_{ij} = \mu(\dot{\gamma}_{ij}) \cdot \dot{\gamma}_{ij} \tag{2.5}$$

for non-Newtonian fluids, the shear viscosity $\mu(\dot{\gamma}_{yx})$ is the function of shear rate $\dot{\gamma}_{ij}$. For simplicity, shear stress τ_{ij} and stress rate $\dot{\gamma}_{ij}$ are also written as τ and $\dot{\gamma}$ hereinafter. Based on the different relationship (function) between shear viscosity and shear rate, the fluids can be further classified into 3 types:

- *shear-thinning*: the apparent viscosity decreases with increasing shear rate
- *shear-thickening*: the apparent viscosity increases with increasing shear rate
- *Bingham fluids*: material behaves like a rigid body when the stress is below a certain stress called the *yield stress*. Material will begin to flow when the stress exceeds the yield stress.

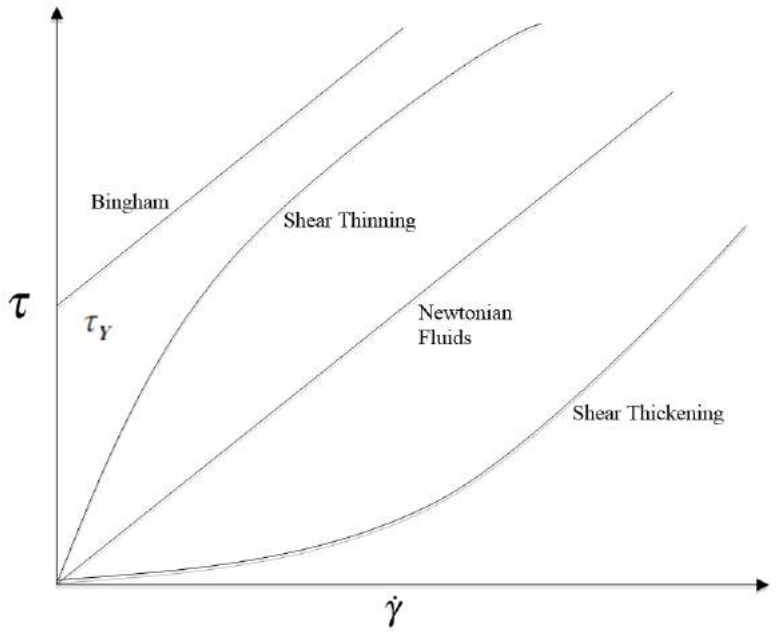

Figure 2.1: Qualitative flow curves of different types of non-Newtonian fluids. Shear stress is denoted as τ and the shear rate is denoted as $\dot{\gamma}$, the yield stress is denoted as τ_Y. The Newtonian fluid possesses a constant slope, indicating the viscosity is independent of shear rate.

The classification of fluids with shear stress (τ) as a function of shear rate ($\dot{\gamma}$) is depicted in Figure 2.1. To note, the fluids used in this project are the aqueous solutions of xanthan gum (shear-thinning), polyacrylamide (also shear-thinning) or the mixture of these two. Different phenomenological and empirical models [16] have been reported to characterize the non-Newtonian behaviour of these fluids under equilibrium, steady shear flow conditions. A brief

description of each relationship is given in the following content with examples of the types of materials to which they typically are applied.

Power Law Model

The power law model is a two parameter model for describing shear-thinning or shear-thickening behaviour in materials that shows a negligible yield response and a varying differential viscosity. A log-log plot of shear stress versus shear rate gives a slope n (the power-law exponent or flow behaviour index), where $n < 1$ indicates pseudoplastic behaviour (shear-thinning fluids) and $n > 1$ indicates dilatant behavior (shear-thickening fluids). The power law model is given by Equation 2.6

$$\tau = K\dot{\gamma}^n \quad \text{or} \quad \mu = K\dot{\gamma}^{n-1} \tag{2.6}$$

where τ is the shear stress, μ is the viscosity and $\dot{\gamma}$ is the shear rate. K is the flow consistency index in the power law model, n is power-law exponent, which shows the flow behaviour.

Cross Model

The Cross model describes pseudoplastic flow with asymptotic viscosities at zero and infinite shear rate without yield stress. Cross model is shown in Equation 2.7.

$$\mu_C = \mu_\infty + \frac{\mu_0 - \mu_\infty}{1 + (\lambda_C \cdot \dot{\gamma})^m} \tag{2.7}$$

Where μ_C is the apparent viscosity based on the Cross model. There are four variables in Cross model: μ_∞ is the viscosity at infinite shear rate, μ_0 is the viscosity at zero shear rate, λ_C is a constant with unit of time and m is a parameter introduced in Cross model [49, 132].

Carreau-Yasuda Model

Carreau-Yasuda model describes shear-thinning (pseudoplastic) flow with asymptotic viscosities at zero shear rate and infinite shear rate, and without yield stress. Carreau-Yasuda model is shown in Equation 2.8

$$\mu_{CY} = \mu_\infty + \frac{\mu_0 - \mu_\infty}{(1 + (\lambda_{CY} \cdot \dot{\gamma})^a)^{n/a}} \tag{2.8}$$

On the left hand of Equation 2.8, μ_{CY} is the apparent viscosity according to the Carreau-Yasuda model, μ_∞ is the viscosity at infinite shear rate, μ_0 is the viscosity at zero shear rate, λ_{CY} is

a constant with unit of time, where λ_{CY}^{-1} is the critical shear rate at which viscosity begins to decrease and a is a parameter introduced by Yasuda *et al.* [9].

These different models give the different curve fittings of viscometric viscosity data, as shown in Figure 2.2, using the Cross, Carreau-Yasuda, power law models. The power law model fails both at low and high shear rates, where the viscosity ultimately approaches a constant value. This failure of the power law model can be rectified by the use of Cross and Carreau-Yasuda model. However, in the intermediate range of the viscosity data i.e. in the shear-thinning region, all of these models have a similar trend and can well describe the viscometric characterization of fluids.

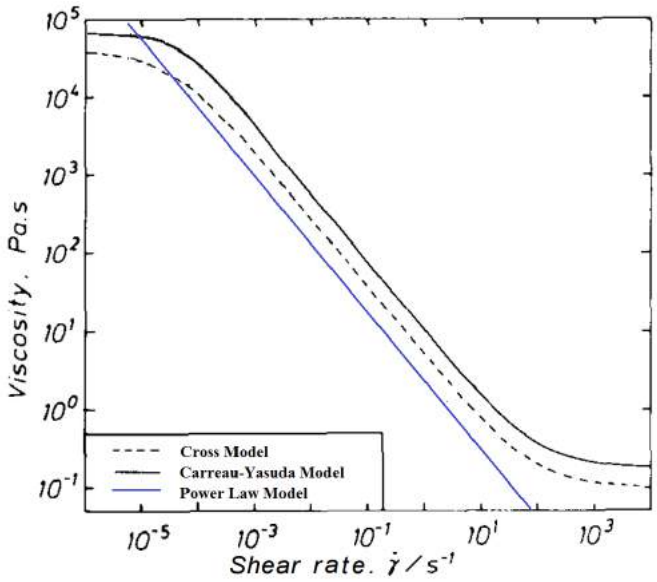

Figure 2.2: Typical viscometric viscosity versus shear rate schematic obtained using the Cross, Carreau-Yasuda, power law models. The viscosity data is the same and the curves have been shifted for clarity, cited from Barnes *et al.* (1989) [9].

2.2.2 Viscoelasticity in shear flow

For some flexible long-chain polymer solution, some elastic recovery is exhibited when undergoing deformation [34]. The elasticity indicates when the stress is removed, the material has the tendency to restore to the initial shape and size. It is essentially different from viscous effects as viscosity is a measure of resistance to flow. The viscoelasticity of materials can

be modelled as a linear combination of springs and dashpots (see [9]), which indicates the relaxation process of viscoelastic materials. The measurement of viscoelasticity can be obtained by the *oscillatory shear* experiments. Purely viscous materials are the materials that resist shear flow and strain linearly with time when a stress is applied. Purely elastic materials are materials that strain when stretched and quickly return to their original state once the stress is released. When the small amplitude oscillatory shear is imposed on a viscoelastic fluid, a phase shift between the shear rate and shear stress appears. This is due to the fact that for purely elastic material, the shear stress and shear rate have an immediate response, thus no phase lag exists, while in purely viscous fluids, shear strain lags shear stress by 90 degree phase lag. For viscoelastic fluids, suppose the phase lag is δ and if a sinusoidal oscillation with frequency ω and a small amplitude γ_0 is imposed on viscoelastic fluids [68], which gives:

$$\gamma(t) = \gamma_0 \cdot sin(\omega t) \tag{2.9}$$

$$\dot{\gamma}(t) = \gamma_0 \omega \cdot cos(\omega t) \tag{2.10}$$

$$\tau = \tau_0 \cdot sin(\omega t + \delta) = \tau_0 \cdot (sin(\omega t) cos\delta + cos(\omega t) sin\delta) = \tau_0' \cdot sin(\omega t) + \tau_0'' \cdot cos(\omega t) \tag{2.11}$$

where δ represents the phase angle of the strain wave, $\gamma(t)$ is the shear displacement, $\dot{\gamma}(t)$ is the shear rate, τ is the shear stress, γ_0 is the amplitude of the oscillation. Suppose the shear stress is *linear* in strain (in reality to ensure the linearity, the γ_0 must be kept small), the Equation 2.11 can be rewritten as:

$$\tau = G'\gamma_0 \cdot sin(\omega t) + G''\gamma_0 \cdot cos(\omega t) \tag{2.12}$$

In Equation 2.12, the G' is the storage modulus which measures the elastic energy stored in the viscoelastic fluids and G'' is the loss modulus indicating the dissipation of energy due to the viscosity of fluids [59]. The loss tangent is defined in Equation 2.13, which is an indicator bearing information on which contribution prevails in the viscoelastic fluids, if elastic effect prevails, $tan\delta < 1$ or $\delta < 45^o$, if effect viscous prevails, $tan\delta > 1$ or $\delta > 45^o$.

$$tan\delta = \frac{G''}{G'} \tag{2.13}$$

A relaxation process is exhibited when the fluids are viscoelastic. Relaxation means the fluid eventually relaxes to its undeformed condition when the stress is released. The relaxation process can be broadly described as a function of exponential decay and the relaxation time indicates the degree of viscoelasticity of the fluids [8]. The relaxation time can be estimated by taking the value of the critical frequency f^* at which the G' and G'' curves cross and apply τ_M=$1/f^*$ as the approximation of the relaxation time. This approximation is based on the Maxwell model where the viscoelasticity is modelled as a spring and dashpot in series [9] and the subscript $_M$ in τ_M stands for the Maxwell model. The relaxation time τ_M in Maxwell model is essentially obtained from a response of imposed small amplitude oscillatory shear on fluid.

The capillary breakup extensional rheometer (CaBER) is also used to determine the relaxation time, which is a transient extensional flow measurement in nature [29, 102, 135]. The schematic diagram of capillary breakup extensional rheometry (CaBER) is displayed in Figure 2.3. The nearly cylindrical fluid sample is put into the gap between two plates of extensional rheometer. The top plate of rheometer moves upwards and stretches the fluid in an exponential form. Instead of immediate breakup, a cylindrical filament is produced due to the high viscoelastic stresses. The transient midpoint diameter of shrinking filament is recorded by the rheometer and an exponential decay of the filament diameter can be used to determine the relaxation time. Therefore, the viscoelasticity of fluids can be measured in this extensional flow.

2.3 Pipe flow of Newtonian fluids

The pipe flow of Newtonian fluids, e.g. water, is a classical and fundamental issue in fluid mechanics. After a brief discussion of pipe flow in chapter 1, this section provides some theoretical background of pipe flow for both Newtonian and non-Newtonian fluids.

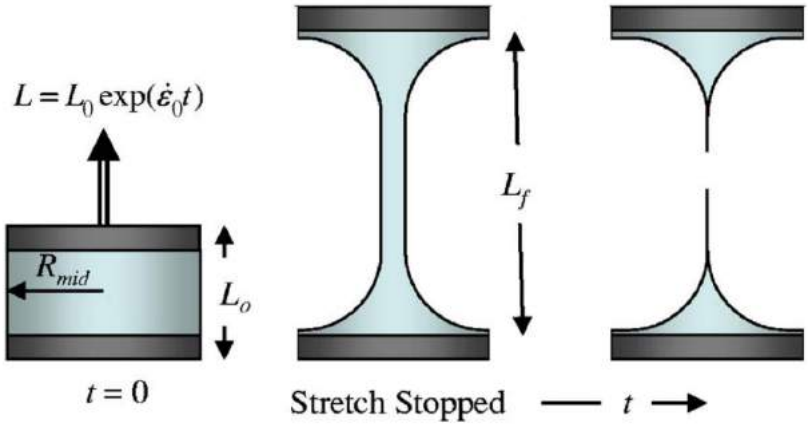

Figure 2.3: Schematic diagram of capillary breakup extensional rheometry (CaBER). The radius of fluid filament was recorded, which is stretched in the exponential form. The $\dot{\varepsilon}_0$ indicates the relaxation time. Figure cited from Miller *et al.* (2009) [108].

2.3.1 Instability and bifurcation

The transition from laminar to turbulent in pipe is one of the most intriguing issues of classical hydrodynamics [17, 70, 145]. Experiments [31, 84, 89] have revealed that a critical Reynolds number Re_c (which is defined as the Reynolds number at which the laminar flow in a circular pipe becomes naturally turbulent [11]) exists so that a sustained transition to turbulence is impossible below this Re_c, as all perturbations of arbitrary magnitude with respect to the laminar base flow will decay in this case [104, 143]. Theoretically, the pipe flow of Newtonian fluids is *linearly stable*, i.e. the linear stability analyses lead to no transition in pipe flow, even at infinite Reynolds number [42, 143]. However, in a practical experiment, if no special attentions are taken to control the initial disturbance, transition can be easily observed at Re approximately 2000$\sim$3000 in a pipe. To bridge the gap between linear stability theory and experimental observation, some theories have been proposed, for example, the self-sustaining process theory proposed by Waleffe [162, 163] and the transient growth theory proposed by Trefethen *et al.* [42, 146, 156]. These theories shed more light on the onset of transition and self-sustenance of turbulence in shear flow.

In this part, the theoretical background of bifurcation and stability will be discussed briefly. In practical applications, for example, a dynamic system which includes some differential equa-

tions, like the Navier-Stokes equations, it usually happens that when a small smooth change conducted to the parameter values (the bifurcation parameters) of a system leads to a sudden 'qualitative' or topological change in its behaviour and bifurcation of a dynamical system is defined as a qualitative change in its dynamics produced by varying parameters [81]. From a mathematical perspective, transition from laminar to turbulent is reached by the superposition of successive oscillatory bifurcations and the Reynolds number *Re* is usually defined as the control parameter in this bifurcation process [82]. Some other theories, such as the self-sustaining process proposed by Waleffe *et al.* [65] also elaborates the mechanism to maintain the turbulence by self-excited oscillation process which is deemed to the periodic solution of Navier-Stokes equation. The bifurcation broadly has two different types: *supercritical* and *subcritical* bifurcation [81]. From the general viewpoint, the difference between these two different bifurcation scenarios is briefly shown below:

- The *subcritical* bifurcation scenario is featured by a discontinuity and coexistence of a number of possible stable phases at a given value of control parameter i.e. *Re* for the laminar turbulent transition in pipe flow. The self-sustaining mechanism involves the streamwise vortical perturbation producing alternatively slow and fast streaks and the longitudinal vortices lift-up the slow-moving near-wall fluid and exchange the momentum with the fast-moving fluid off the wall. The lift-up loop mechanism is closed by a non-linear feedback which regenerates the vortices [162, 163]. The similar loop is expected to exist on the *turbulent spot* and the transition to turbulence generally follows the subcritical scenario in a wide a range of *Re* between the laminar flow to turbulence as the turbulent spots emerges abruptly and is characterized with discontinuity.
- In contrast, in the *supercritical* bifurcation, a continuous evolution of states is observed when the control parameter, i.e. *Re* is changed. The supercritical bifurcation manifests continuous and steady change between two regimes, often as the *square root* relationship to the bifurcation threshold (forkpitch bifurcation) [97]. When the perturbation grows and approaches into the non-linear problem, the base state is replaced by the primary

bifurcated state and then the bifurcation cascades then grows to a secondary bifurcation, then proceeds to a higher bifurcation etc., until chaos. In supercritical bifurcation, the bifurcated state remains next to the bifurcating state and *no hysteresis* is observed as *Re* is varied.

From a physical viewpoint, instabilities and the transition to turbulence occur in systems driven far from *equilibrium*. In fluid mechanics, the distance to equilibrium is measured by the Reynolds number *Re* which compares the effects of applied shear disturbing the fluid to those of viscous dissipation ironing out velocity inhomogeneities. The state directly stemming from equilibrium is referred to as the *base flow*.

2.3.2 Friction in pipe flow

To study friction in a pipe, *Hagen-Poiseuille* equation for laminar fully-developed pipe flow is introduced first [101], see Equation 2.14. Hagen-Poiseuille equation is derived from *Navier-Stokes* equation written in cylindrical coordinates. Hagen-Poiseuille equation 2.14 describes the velocity distribution of fully developed pipe flow which is driven by pressure, gravity or both,

$$u = \frac{1}{4\mu}\left[-\frac{d}{dx}\left(P+\rho g h\right)\right]\left(R^2 - r^2\right) \tag{2.14}$$

where P is the pressure, μ is the density of fluids, x is the distance in streamwise direction, g is the gravity acceleration, h is the head loss, R is the radius of the pipe.

To study the frictional force in the pipe, the dimensionless parameter f is introduced by John Thomas Fanning, which is now named the *Fanning friction factor* [86]. By dimensional analysis, *Fanning friction factor* could be written as:

$$f_F = \frac{2\tau_w}{\rho U_b^2} \tag{2.15}$$

where τ_w is the wall shear stress, f_F is the *Fanning friction factor* of the pipe, U_b is the fluid bulk velocity in the pipe and ρ is the density of the fluid. When the pipe and channel flows are

fully developed the skin-friction is balanced by a favourable pressure gradient:

$$\tau_w = -\frac{R}{2} \cdot \frac{\Delta P}{L} \tag{2.16}$$

where ΔP is the pressure drop for the distance of L in flow direction and R is the radius of the pipe. The bulk velocity can be approximated by the equation below,

$$U_b = \frac{\dot{Q}}{\pi R^2} \tag{2.17}$$

where $\dot{Q}$ is the volumetric flow rate and R is the radius of the pipe. Substitute Equation 2.16 and Equation 2.17 into Equation 2.15, it gives:

$$f_F = \frac{-\pi^2 R^5 \Delta P}{\rho \dot{Q}^2 L} \tag{2.18}$$

Based on Equation 2.14, the following part will derive the relationship between the Fanning friction factor and Reynolds number. For the pipe flow, the volume flow rate can be calculated by the velocity integration along the radial direction, the velocity distribution is given by Hagen-Poiseuille equation, see Equation 2.14, that is,

$$\dot{Q} = \int_0^R u dA = \int_0^R u_{max} \left(1 - \frac{r^2}{R^2}\right) 2\pi r \cdot dr = \frac{1}{2} u_{max} \pi \cdot R^2 \tag{2.19}$$

where u_{max} is the maximum velocity at pipe axis. The wall shear stress τ_w is computed from the wall velocity gradient, the velocity gradient could also be obtained by Hagen-Poiseuille equation, which gives:

$$\tau_w = \left| \mu \frac{du}{dr} \right|_{r=R} = \frac{2\mu u_{max}}{R} \tag{2.20}$$

Substituting Equation 2.19, 2.20 and 2.17 into Equation 2.15, it gives an exact theory for laminar Fanning friction factor

$$f_D = \frac{2\tau_w}{\rho U^2} = \frac{2\,(8\mu U_b/D)}{\rho {U_b}^2} = \frac{16\mu}{\rho U_b D} = \frac{16}{Re} \tag{2.21}$$

Equation 2.21 gives the relationship between Fanning friction factor and Reynolds number for laminar flow, typically when the $Re < 2300$. When flow occurs between the laminar and turbulent flow conditions, the flow condition is known as transition and the flow dynamics is

difficult to predict. The flow features a combination of laminar and turbulent flow. No equation is available to predict friction factor for the critical flow condition. For fully turbulent flow, *Blasius* [78] presented an explicit approximation:

$$f_F = 0.079 \cdot Re^{-1/4} \tag{2.22}$$

Considering the laminar flow, the friction factor and Reynolds number are linked by given equations below,

$$f_F = \begin{cases} 16/Re & \text{laminar} \\ 0.079 \cdot Re^{-1/4} & \text{turbulent} \end{cases} \tag{2.23}$$

where f_F represents the Fanning friction factor. The characteristic length of the Reynolds number is the inner diameter of the pipe. To be noted, the relationship between Re and friction factor f_F shown in Equation 2.23 is confined to Newtonian fluids. With regards to some shear-thinning fluids, significant drag reduction characteristics are manifested, which yields a lower friction factor.

2.3.3 Ekman number

The Coriolis acceleration arises due to the rotation of earth. The Coriolis acceleration could change the direction of flow and thus produces flow asymmetry [41]. A dimensionless number named *Ekman number* is introduced to describe the ratio of the viscous force to the Coriolis force due to the rotation of earth. The Ekman number is defined as below:

$$Ek = \frac{\mu}{2\Omega\rho D^2 sin\beta} \tag{2.24}$$

where Ω is angular velocity of the Earth, which is $7.3 \times 10^{-5} rad/s$, β indicates the angle between the pipe axis and the rotation axis of the earth (in our rig $\beta \approx 52^{o}$), μ is the viscosity of the fluid, for the non-Newtonian fluids, the viscosity based on the wall shear stress i.e. μ_w is employed, ρ is the density of fluid and D is the inner diameter of pipe. For fully-developed laminar flow of low viscous fluid in a large diameter pipe and significant β, the Ekman number is small, ($Ek \sim \mathcal{O}(1)$ if the fluid is water in our rig, which the pipe diameter is 100 mm), indicating the

Coriolis force is in the same order of magnitude as viscous force. The non-ignorable asymmetry will thus emerge, resulted from the secondary flows driven by the Coriolis force. However, for some highly viscous fluids, the Ekman number is generally very large (Ek approximately varies from 17 to 46 for 0.15% xanthan gum solutions for different Reynolds numbers from 230 to 3150) [137] indicating the asymmetry triggered by Coriolis force is not pronounced.

2.4 Pipe flow of Non-Newtonian fluids

In this section, the fundamental background regarding the non-Newtonian fluids in pipe flow will be discussed. Specifically, the flow characteristics of polymer solutions in pipe flow is introduced among a broad class of non-Newtonian fluids.

2.4.1 Reynolds number for non-Newtonian fluids

For non-Newtonian fluids, the Reynolds number can not be definitively defined as the viscosity μ of non-Newtonian fluids usually varies with shear rate. As a consequence, there are different definitions [96, 124] of Reynolds number for non-Newtonian fluids due to the intrinsic difficulties to define the viscosity. Metzner and Reed [105] derived their generalized Reynolds number Re_{MR} from its relation to the Fanning friction factor such that the data under investigation collapsed. Their approach is to correlate the pressure-drop data in pipe flow into the definition of Reynolds number to enable $f = 16/Re_{MR}$ in laminar flow. The definition of Re_{MR} is:

$$Re_{MR} = \frac{\rho U_b^{2-n} D^n}{k} \left(\frac{n}{2+6n} \right)^{n-1} \tag{2.25}$$

where k and n are the parameters in the power law fitting: $\mu = k \cdot \dot{\gamma}^{n-1}$.

Another approach is to obtain the Reynolds number of non-Newtonian flow by measuring the shear stress on the wall. For non-Newtonian fluids, the viscosity is shear rate dependent and the shear stress varies over the location of the pipe, theoretically becoming zero in the centre of the pipe and maximum at the wall. The Reynolds number based on the wall viscosity, i.e. Re_w

provides a better indication of transitional and turbulent flow as the viscous stress dominates in the wall region. Another advantage of this Re_w definition lies in the simplicity and robustness, it can be applied to any rheological model and only the viscosity at the wall is required and also this definition is consistent with preceding research [51, 54, 64]. The definition of Reynolds number based on wall shear stress is given by:

$$Re_w = \frac{\rho U_b D}{\mu_w} \tag{2.26}$$

where the U_b is the bulk velocity, ρ is the density of the fluid and μ_w is the dynamic viscosity of the fluid at the wall which can be derived from the pressure-drop data. These definitions of Reynolds number are inter-related, in laminar flow, for example, there is: $Re_{MR}/Re_w = 8n/6n+2$, where n is the power-law exponent in power law fitting. In terms of the shear-thinning fluids, where $n \leq 1$, the Re_{MR} should be systemically lower than Re_w.

2.4.2 Velocity profile for power law fluids in fully-developed laminar flow

For smooth pipes, if the flow is fully developed, in purely laminar regime, assuming the Coriolis force is negligible, the velocity profile of Newtonian fluids is axisymmetric and parabolic, and can be described by Equation 2.27:

$$u(r) = 2U_b(1 - \frac{r^2}{R^2}) \tag{2.27}$$

where U_b is bulk velocity, R is the radius of pipe, $u(r)$ is local velocity at radius r. At the center of the pipe, the peak axis velocity is supposed to be twice as much as the bulk velocity U_b [57]. However, for the power-law fluid, Equation 2.27 can be modified to [9]:

$$u(r) = \frac{\dot{Q}(3n+1)}{\pi R^2(n+1)} \left(1 - (\frac{r}{R})^{(n+1)/n}\right) \tag{2.28}$$

where $\dot{Q}$ is volumetric flow rate, n is power law index and R is the radius of pipe. When n=1, the velocity profile described in Equation 2.28 regresses to Equation 2.27, which is essentially a Newtonian fluid. In terms of the shear-thinning fluids where $n < 1$, progressively decreasing the power-law index, i.e. increasing the degree of shear thinning results in an increasingly plug-like

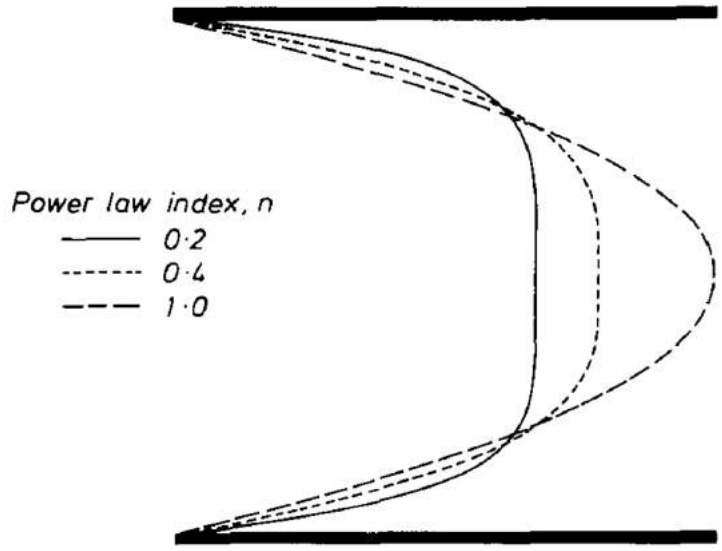

Figure 2.4: The velocity profiles for the laminar flow of power-law liquids in a straight circular pipe, calculated for the same volumetric flow rate. Note the increasingly plug-like nature of the flow as power law index *n* decreases. Data from Barnes *et al.* (1989) [9].

nature of the velocity profile, as shown in Figure 2.4. This theoretical estimation of velocity profile in purely laminar regime for shear-thinning fluids can help us to assess the uncertainty of experimental measurements.

Chapter 3

Literature Review

In this chapter, the previous works on pipe flow using Newtonian and non-Newtonian fluids will be reviewed. Although the mechanism of the transition from laminar to turbulent flow of Newtonian fluids is not completely understood yet, substantial progresses have been made in understanding the flow transition and flow instabilities using Newtonian fluids. Regarding non-Newtonian fluids, besides a few limited papers which will be discussed afterwards, little is known about the flow asymmetry and instability of non-Newtonian fluids. The following will provide a literature review about previous works on pipe flow using different types of fluids.

3.1 Pipe flow of Newtonian fluids

3.1.1 Linear stability and transient growth

The understanding of Hagen-Poiseuille flow (pressure driven pipe flow) transition is much less progressed than that of plane Poiseuille flow [147]. For the plane Poiseuille flow, from the Orr-Sommerfeld equation [42] it was deduced that linear instabilities should be present in a boundary layer, know as the Tollmien-Schilichting waves [63]. When these linear instabilities grow large enough, nonlinear effects become important. Secondary instabilities emerge in the form of lambda-vortex patterns and they are known as Klebanov-modes and Herbert-modes

[72]. However, the scenario of linear and secondary instabilities observed in the plane flow is not appropriate for pipe flow. The fully-developed laminar profile in a pipe is theoretically *linearly stable* for all Reynolds number indicating all infinitesimal perturbations will decay in pipe flow for Newtonian fluids [85, 91, 143]. Actually, experiments show that by suppressing disturbances, pipe flow could remain laminar up to $Re \approx 100000$. But if no special measures are taken to control the initial disturbance, laminar turbulent transition is usually observed at $Re \approx 2300$ in a pipe, which is inconsistent with the theoretical stability analysis of pipe flow.

Recently, the nonlinear stability theory analysis has been proposed to bridge the gap between theoretical value $Re = \infty$ and the experimentally observed value $Re \approx 2300$ of laminar turbulent transition in pipe flow. One is the transient growth mechanism reported by Trefethen *et al.* 1993 [156]. Before the energy decay occurs, the initial kinetic energy of small perturbations are first amplified at an early stage of disturbance evolution as the flow experiences a transient growth from the linear dynamics to a level that non-linear interactions become active and take over the future transition to turbulence. From a view of fluid mechanics, the physical interpretation of the transient growth is that a small perturbation of the wall normal velocity will transfer fluid from a region of lower to higher streamwise velocity, or vice versa, where it results in a large perturbation of the streamwise velocity. This normal-wall velocity disturbance will generate streamwise vortices by shearing effect and the low-amplitude vortex or counter-rotating pair of vortices approximately aligned with the streamwise flow entrains fluid from regions of high to low axial velocity and vice versa. This mechanism is also referred to as the lift-up mechanism, because fluid with little momentum is lifted from the wall region. The entrained fluid appears as a streak of locally high or low streamwise velocity. In the linear regime, the streaks will also be dissipated after the decay of the vortices. However, when the streaks reach a sufficiently large amplitude, they become unstable and will breakdown to turbulence [157].

3.1.2 Puffs and slugs

Experiments show that transitional pipe flows are characterized by different flow structures usually referred to as "puffs" and "slugs" [28, 44, 45, 76, 103]. Early experimental investigation of turbulent slugs and streaks in transitional pipe flow could be found in Lindgren (1969) [88]. Due to restrictions with technology at the time, pressure drop measurements were adopted to investigate the flow. For the pressure measurements, the initial disturbance may lead to the signal flash, also referred to as a spike. The spike may or may not trigger a burst of turbulence forming a 'turbulent spot', characterized by intensive small scale flow fluctuation, travelling with the flow along the wall. As the turbulent spots are transported along the walls by the flow, they may decay, increase or maintain in size according to the Reynolds number. When $Re < 2000$, the flash will travel some distance down the pipe and then decay. With the increasing Reynolds number, the frequency of spikes and flashes increase. When $2000 < Re < 2400$, the turbulent flashes appear unchanged in length and they do not appear to decay. Some apparent flow structures at the wall continuously regenerate eddies that diffuse into the more central part of the pipe. The downstream velocity of the flashes decrease with increasing Reynolds number and when $Re \approx 2400$, the flash velocity downstream is about $0.9U_b$ [172, 173]. It indicates laminar flow must therefore enter the rear of the slug and become turbulent, while at the front end, turbulent flow must leave the flash and become laminar again. Lindgren states that it seems logical that the higher kinetic energy dissipation of the turbulent flow within the flash should be supplied by the kinetic energy of the laminar flow entering the flash at its rear. When $2400 < Re < 2800$, a flash may split in two or more flashes within this Re range. As the Reynolds number increases, the turbulent flashes elongate and follow each other more closely. The front velocity on the streak is larger than the rear velocity and increases as Reynolds number is increased. For $Re > 2800$, the flow disturbances at the entrance of the pipe is comparatively large and the disturbance leads to the formation of turbulent flashes which never return to the laminar state (a flash never splits in two). When the Re increases further, the turbulence regions become more and more frequent until the flow goes into the fully turbulent regime.

Wygnanski *et al.* (1973,1975) [172, 173] investigated transition from conditionally sampled hot-wire measurements. Based on the Reynolds number, flow perturbations evolve into two different turbulent states depending on the Reynolds number, i.e. puff ($Re \approx 2700$, caused by the instability of the boundary layer to small disturbances) and slug ($Re \approx 3000$, generated by large disturbances at the inlet). The distinction between the two structures is given by the behaviours of the velocity near the leading edge, with a puff showing a gradual change of the velocity in the leading edge while a slug has a more abrupt velocity gradient. The velocity measurement from a puff or a slug at a fixed point in the centreline of the pipe can be seen in Figure 3.1.

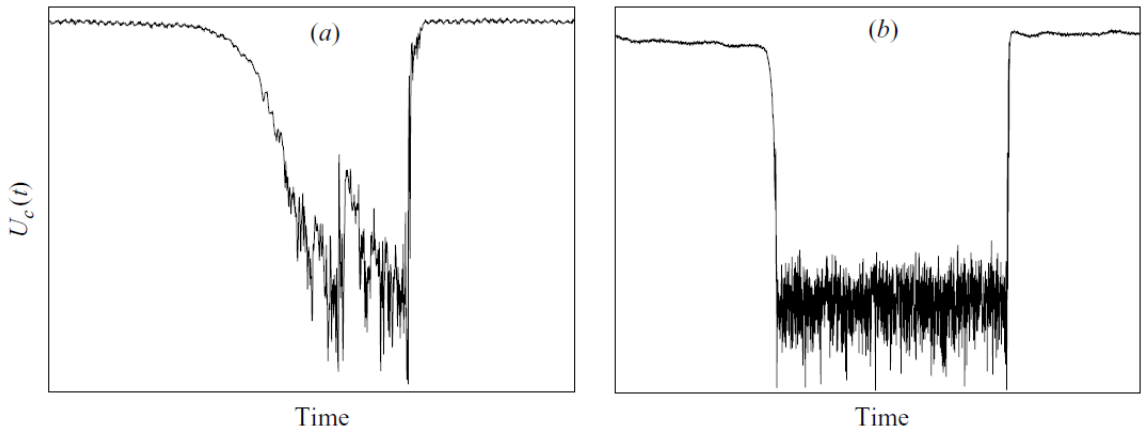

Figure 3.1: Schematic trace of the velocity of a puff (a) and slug (b) as a function of time during their passage past a fixed probe point on the centreline of pipe by hot-wire velocity measurement. The velocity fluctuation indicates inside the puff or slug, the flow state is essentially turbulent while out of them, the flow state is laminar. Taken from Durst *et al.* (2006) [45].

A puff is furthermore approximately of constant length and is convected downstream at a velocity slightly smaller than the bulk velocity. Slugs are characterized by a sharp laminar-turbulent interface at both the downstream end (leading edge) and the upstream end (trailing edge) of the turbulent region. Puffs were observed in the range of $2000 < Re < 2700$, and they were generated by a very strong disturbance at the inlet of the pipe. At the downstream end of a puff the centreline velocity is found to decrease gradually, and therefore it is often said that the leading edge is not so well defined. In contrast, the trailing edge is well defined, but only in the central region of the pipe [7, 149].

The velocity of the trailing edge is smaller than the bulk velocity, while the leading edge travels faster than the bulk velocity. This means that the length of a slug increases as it moves downstream [31, 88, 138]. Farther downstream different slugs will merge to form one large region of continuous turbulence [160]. Wygnanski *et al.* (1973) also studied the mean flow field, the turbulent statistics of 3 velocity components, the Reynolds stress, the dissipation and kinetic energy inside a slug and on the interface. The result shows that the flow inside the slug, about $20D$ from the leading edge to the trailing edge, is identical to fully developed turbulence. Wygnanski *et al.* (1975) further investigated the puff and showed that the flow structure of a puff does not depend on the form of disturbance by which it is created but depends on the Reynolds number only. The development of the puff was also studied. The puff remains unchanged over a some range of Reynolds number, which was named equilibrium puff and increasing the Reynolds number will lead to the puff splitting and merging. An explanation which not strictly proved, is that the sharp trailing edge could be explained by the quick transition from the laminar flow, whereas at the leading edge the flow relaminarizes and is governed by the relatively slow dissipation of the turbulent fluctuations that results in a more gradual change of the velocity at the leading edge. Nishi *et al.* (2008) [115] investigated the behaviours of puffs/slugs in transition. The information was obtained by measuring the time variation of the streamwise velocity at the centreline of the pipe by hot-wire measurements. The results show

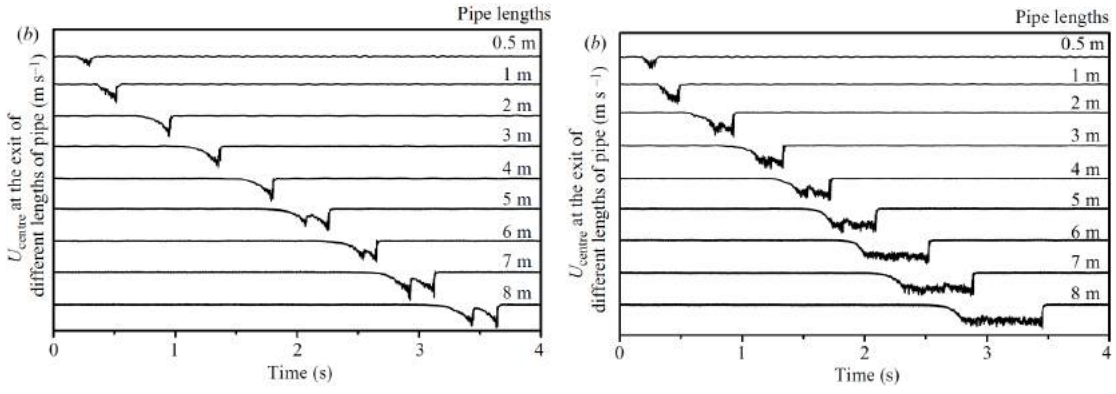

(a) puff splits. $Re = 2495$ (b) puffs merge. $Re = 2865$

Figure 3.2: Puff development with increasing Reynolds number of different pipe length for (a) puff splits. (b) puffs merge. Taken from Nishi *et al.* (2008) [115]

how slugs and puffs develop, i.e. merge or split, along the pipe. The Reynolds number plays an important role on the flow structure of puffs and slugs. At a lower Reynolds number, puffs generate and remain unchanged along the pipe. However, when the Reynolds number increases, the puff will split into two or more puffs and for sufficiently high Reynolds number, the puffs merge into slugs and begin to expand as slugs in the pipe, see Figure 3.2. When Reynolds number continues to increase, the sequences of slugs will merge and finally form the state of fully turbulent flow.

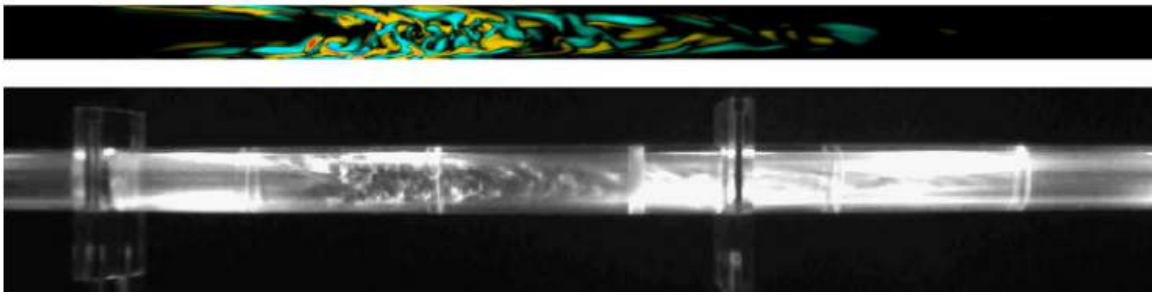

Figure 3.3: Experimental flow visualization of puff (bottom) compared with axial vorticity for a numerically calculated puff (top) at the same Re=1800. The working fluid is water and the computational domain is 50 pipe diameter. Taken from Willis [170].

The flow structure visualized in Figure 3.3 (bottom) is an experimentally observed puff. These structures greatly determine the random appearance of the flow, and they could be visualized by the iso-contours of the axial vorticity, see Figure 3.3 (top), which is taken from simulations performed by Willis *et al.* [168, 170] in the domain of 50 pipe diameters. The puff characterized by spatio-temporal intermittency appears stochastically in pipe, indicating the onset of laminar turbulent transition. Some recent studies also focused on the threshold to trigger a transition. These studies investigated two questions, i.e. what amplitude of perturbation is required to trigger turbulence, and what magnitude of Re is required to sustain turbulence. In the experiment, the transition to turbulence could be observed when a threshold have been crossed, i.e. the bulk velocity (Reynolds number) should be large enough or the perturbation has to be sufficiently strong [47]. Hof *et al.* (2004) [67] reported an experimental investigation to uncover the scaling of the turbulence transition threshold in a pipe, which indicated the amplitude of disturbances (defined by the injection volume flux) required to trigger transition scales as O

(Re^{-1}). Peixinho and Mullin (2007) [120] changed the disturbance pattern where just one jet as a perturbation is kept. By varying the angle of the jet the threshold changes from the scaling O ($Re^{-1.3}$) to O ($Re^{-1.5}$). Perturbations with amplitudes below the threshold decay as they propagate downstream and no transition occurs. On the other hand, disturbances with the amplitude above this amplitudes will lead to a sustained chaotic flow downstream which had the shape of a localized puff or slug.

3.1.3 Coherent structures and travelling waves

The approaches to study turbulence include the theoretical investigations (e.g. , the stochastic model for turbulence [112], the topology of turbulence [110], the proper orthogonal decomposition in the analysis of turbulent flows[13, 19]), experimental observations and numerical simulations [1, 27, 37, 38, 60, 133]. More recently, the dynamical systems theory has been in-

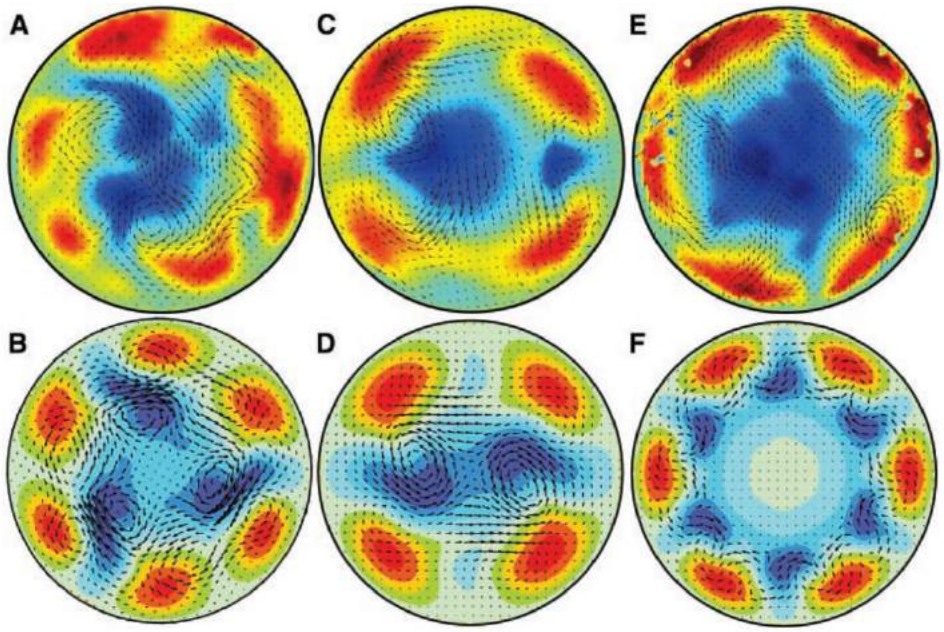

Figure 3.4: Comparison of experimentally (top) and numerically (bottom) observed streak patterns for travelling wave solutions. The velocity components in the plane are indicated by arrows. For the axial component the difference to a parabolic profile with the same mean speed is colour-coded. Regions where the fluid flows faster are shown in red and correspond to high-speed streaks. Similarly, regions where the speed is lower are shown in blue and correspond to low-speed streaks

troduced to investigate turbulence, concentrating on recently discovered invariant solutions and their significance for dynamical and statistical features of turbulence at low Reynolds number [23, 32, 47, 67, 74] and newly extended to higher Reynolds number (Re=35000) [39]. The turbulent dynamics can be interpreted as the cumulation of a family of invariant solutions, e.g. a combination of many different periodic solutions. These invariant solutions have been proposed as the building blocks of the fully-turbulent state and responsible for the evolution of turbulent dynamics.

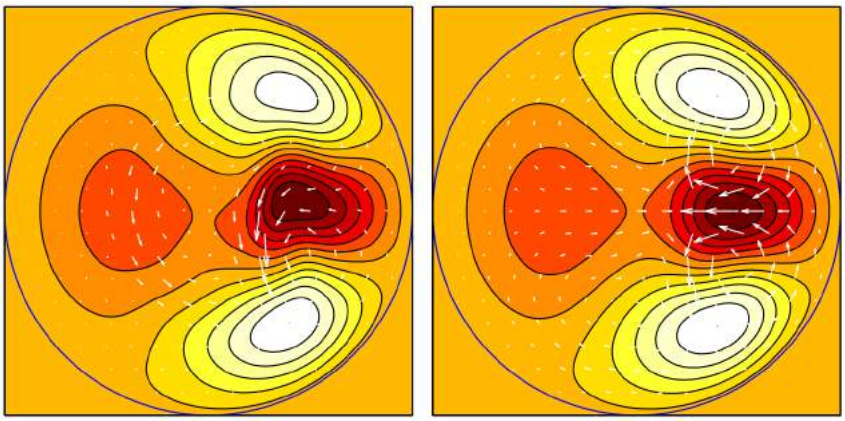

Figure 3.5: Velocity fields for the asymmetric mode of travelling wave solution at Re=2900. An instantaneous state is shown on the left and a streamwise-averaged state on the right. The coloring indicates the downstream velocity relative to the parabolic laminar profile: red (dark) through white (light) represents slow through fast (with zero corresponding to the shading outside the pipe).

In terms of pipe flow, the first unstable invariant solutions have been discovered by Faisst & Eckhardt (2003) [58] , Wedin & Kerswell (2004) [164] and Hof *et al.* (2004) [67] as coherent states comprising of different vortex pairs with m-fold rotational symmetry C_m (m=2,3,4...). High/low streaks were also observed in the vicinity of wall [169]. These different pairs of vortices yield symmetric coherent travelling wave states (TWs), see Figure 3.4. The travelling wave of C_m (m=2,3,4...) symmetric state was observed at different Reynolds number. The C_3 travelling wave occurred at Re=1250 and the C_2, C_4 travelling waves were discovered at Re=1350 and Re=1590 respectively. Pringle & Kerswell (2007) [128] observed the new families of three-dimensional non-linear travelling waves solution which possess no discrete rotational symmetry but asymmetric modes arising through a symmetry-breaking bifurcation. The coherent structure

in the asymmetric travelling wave consisting of one slow streak sandwiched between two fast streaks located preferentially to one side of the pipe causing the flow asymmetry, see Figure 3.5.

The analytical and experimental viewpoints of pipe flow as a function of Reynolds number are displayed in the bifurcation diagram as depicted in Figure 3.6. The simplest solution is the parabolic velocity profile, which is referred to as the *laminar base flow*. At low Reynolds numbers, the laminar base flow is the unique solution and, as already discussed, the linear theory suggests all small disturbances in circular pipe will decay for all Reynolds numbers using Newtonian fluids. Some exact solutions of Navier-Stokes equation are also provided by the recently reported dynamical system approaches, showing the different families of travelling wave solutions. The experimental observations of laminar turbulent transition process illustrate the characteristic of puffs changes along with the Reynolds number and slugs are formed at relatively high Reynolds number.

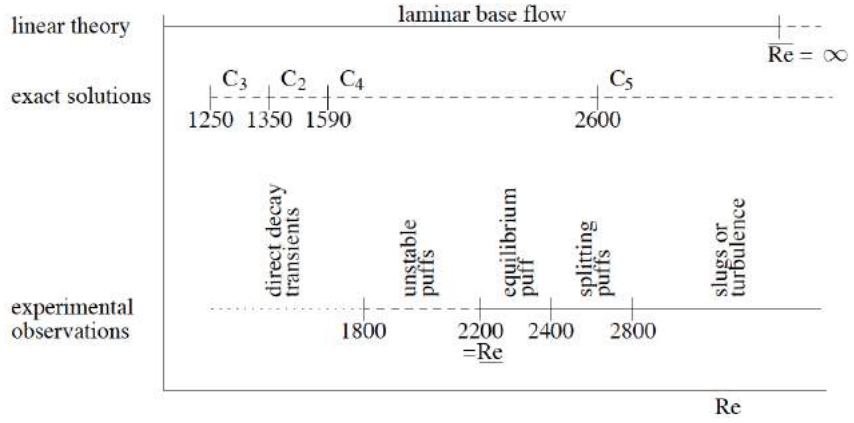

Figure 3.6: The bifurcation diagram of transition scenarios for linear theory, exact solutions of Navier-Stokes equation, experimental observations of Newtonian fluids, C_m specifies an m-fold rotational symmetry. Data is from C.W.H. van Doorne [157].

3.2 Pipe flow of non-Newtonian fluids

Concerning the stability of flow and laminar-turbulent transition process of non-Newtonian fluids, very little literature is available either experimental or numerical [122, 167]. Particularly for this flow asymmetry phenomenon in shear-thinning fluids, a handful of paper is avail-

able and the understanding of flow asymmetry is lacking. In this section, we primarily review the literature of pipe flow of non-Newtonian fluids in transition regime, stressing the observed asymmetric feature.

3.2.1 Observation of flow asymmetry

An early experimental observation of asymmetry in transitional pipe flow could be traced back to the work by Escudier *et al.* (1996) [52]. In this paper, the velocity profile of thixotropic

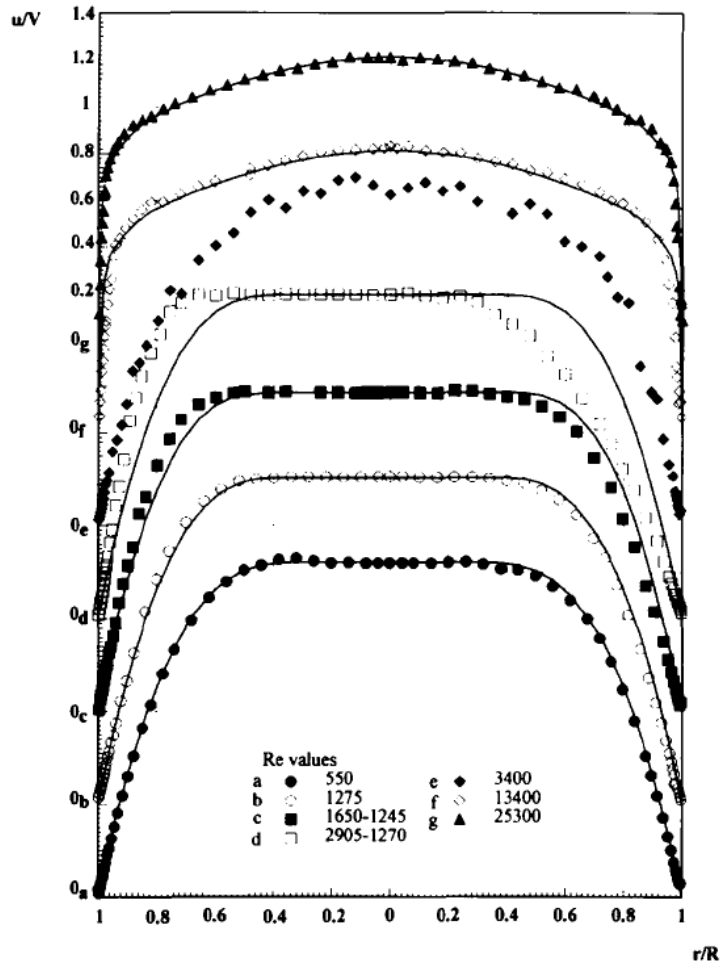

Figure 3.7: Mean velocity profiles for different Reynolds numbers, obvious asymmetry was found when *Re* was 1650 and 2905. the *x*-axis is the normalized radius, the *y*-axis is the streamwise velocity normalized by bulk velocity. The original point shifts upwards for clarity. The solid line indicates the mean velocity of two points which are have some radius but on the opposite sides of centerline of pipe. The dots means the averaged LDV results, data cited from Escudier (1996) [52].

liquid (1.5% Laponite, a name for synthetic clay, shear-thinning with yield-stress and slightly viscoelasic) was measured by Laser Doppler Velocimetry (LDV). An unexplained, but *repeatable* asymmetry of velocity profile was found in the measurement when Reynolds numbers Re_w ($Re_w = \rho UD/\mu_w$, where μ_w is wall shear stress viscosity, U is bulk velocity and D is pipe inner diameter, which is 100 *mm*.) was in the approximate range 1300-3000, as shown in Figure 3.7. The measured mean velocity profiles show a clear progression with increasing Reynolds number from laminar flow (a-d) through transition (e) into turbulent flow (f,g). For laminar and fully turbulent flows, the profiles are symmetrical. However, the asymmetry appears once transitional conditions is established, which suggests the asymmetry may be linked with the stability characteristics of the flow of a non-Newtonian fluid. The friction factor and turbulence intensity, indicated by velocity fluctuations at $r/R \approx 0.8$, were also obtained, shown in Figure 3.8. In the region where the velocity profiles are asymmetric, i.e. , transitional regime, the u' levels are generally higher than other domain and the drag-reducing characteristics is manifested. For thixotropic liquid, the turbulence intensity distributions are also consistent with the characteristics exhibited by drag-reducing polymers, i.e. , u'/U_b is unchanged whereas v'/U_b and w'/U_b are reduced in comparison with the levels of Newtonian fluids.

Rudman *et al.* (2004) [139] implemented a direct numerical simulation of transitional and turbulent pipe flow using shear-thinning fluids, showing permanent asymmetry might be sustained in the transitional flow of shear-thinning fluids. When the flow behaviour index n of power-law fluid equals to 0.5, the author found the active region (asymmetry) continually moves along the pipe and preferentially appears at certain azimuthal location thus triggering the flow asymmetry for long-time averaging results. The significance of this work lies in that it not only numerically validates the existence of asymmetry in pipe flow of shear-thinning fluids but also reveals the time-varying nature of the asymmetry in transitional regime whereas the experimental work of Escudier *et al.* (1996) [52] suggests the asymmetry is stationary. The observation of flow asymmetry in numerical simulation also implies the asymmetry is not triggered by the major imperfection of rig or some undesired pipe inlet condition, e.g. bend orientation of in-

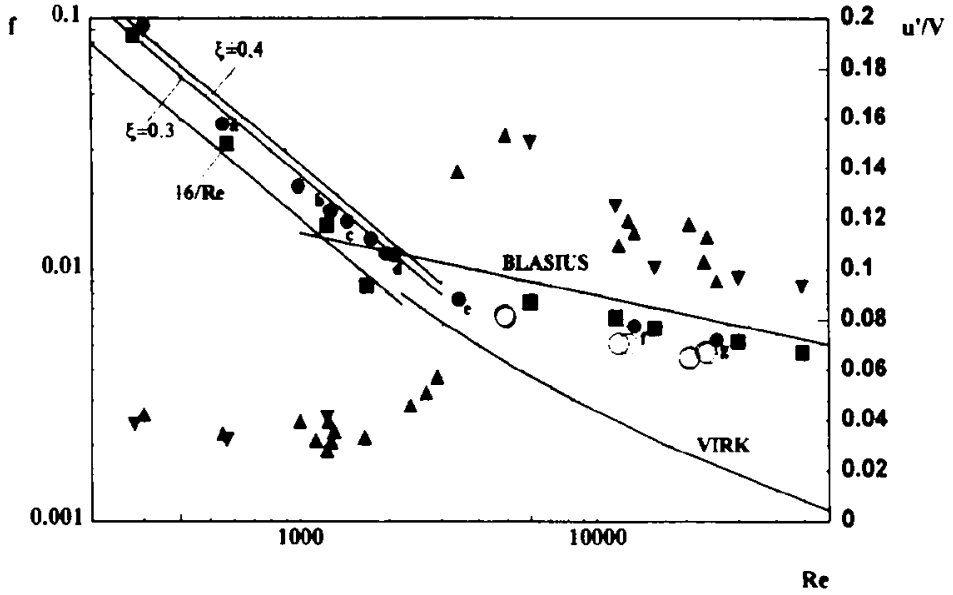

Figure 3.8: Friction factor and near-wall turbulence intensity vs. Reynolds number, black circle, square and white circle represent friction factor and black triangles represent turbulence intensities, cited from Escudier (1996) [52].

let pipe. Rudman *et al.* (2004) also investigated the distribution of wall streaks for fluids with different flow behaviour index n, i.e. n=0.5, 0.69, 0.75 and 1 (Newtonian) at same Reynolds number. They observed that the Newtonian fluid has a more random turbulent structure and shorter streaks, indicative of more developed turbulence in contrast with the shear-thinning fluids [91].

Peixinho *et al.* (2005) [121] presented another experimental investigation of laminar, transitional and turbulent flows in a circular pipe rig, using 0.2% carbopol (shear-thinning with yield stress), 2% carboxymethy cellulose, i.e. CMC (shear-thinning without yield stress) and glucose syrup (Newtonian) as a reference fluid. The pipe is 5.5m long with 30mm inner diameter and velocity profiles were measured in the horizontal plane at 4.5m from the inlet. The authors adopted the definition of generalized Reynolds number Re_{MR} proposed by Metzner and Reed [105] and the flow asymmetry appeared significantly in transitional regime while in laminar and fully turbulent regimes, no significant asymmetry was observed. Compared to Newtonian fluid, the yield stress and shear-thinning characterizations were found to increase the stability of the flow and delay the transition [50]. The power spectra of axial velocity fluctuation of 0.2%

carbopol was calculated at Re_{MR}=2600,2700,3200. The authors proposed that the transition for the yield stress fluid takes place in a different manner than that of Newtonian fluids, occurring in two stages: in the first stage (prior to the laminar turbulent transition), the experimental profiles manifest a slight departure from the laminar profile meanwhile the velocity fluctuation remained at a low level. With the increasing Reynolds number, turbulent spots occurred and large velocity fluctuation was observed which is referred to as the second stage of transition.

A jointly published paper, reported by Escudier *et al.* (2005) [51] was produced to highlight this asymmetry effect utilizing a wide range of polymer solutions. This paper provides rich experimental data of flow asymmetry and summarizes the independent investigations of this counter-intuitive phenomenon at independent laboratories in U.K. [51, 52], France [121] and Australia [139] all using LDV as the measurement technique. It suggests the flow asymmetry is ubiquitous in polymer solutions and the asymmetry, to varying degrees, is significant at all stages of transition from laminar to turbulent regime. The testing fluids contain the water&glycerine (Newtonian fluids) and a variety of non-Newtonian fluids, i.e., carboxymethyl cellulose (CMC), xanthan gum (XG), polyacrylamide (PAA), carbopol (CARB), Laponite (LAP) with different concentrations. These testing fluids possess different rheological characterization, e.g. some are shear-thinning with slight viscoelasticity, some are viscoelastic, some are with yield stress, however, the common ground of the fluids when asymmetry observed is shear-thinning which implies this asymmetry is induced by the shear-thinning characterization of fluids, which will be further investigated in the SPIV investigation.

Esmael *et al.* (2008) [55] offered a possible explanation for these asymmetries: a robust nonlinear coherent structure characterized by two weakly modulated counter-rotating longitudinal vortices existed in the pipe flow of shear-thinning fluids, as shown in Figure 3.9, leading to the flow asymmetry. The working fluid is a 0.2 wt.% aqueous solution of carbopol 940 (shear-thinning with yield stress) and the experimental facility is the same as that in the work of Peixinho *et al.* (2005) [121]. The authors measured the axial velocity profiles at three axial positions when $Re_w = 2420$: $x = 20\ D$ (near the pipe inlet and D is pipe diameter), $x = 54\ D$

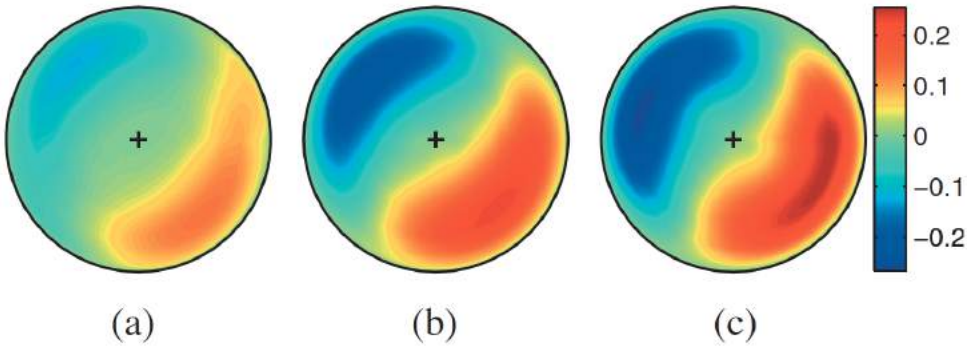

Figure 3.9: Velocity contours at a cross section of the pipe at each axial position. (a) $x = 54D$, $Re_w = 2420$ (b) $x = 122D$, $Re_w = 2420$ (c) $x = 122D$, $Re_w = 3650$. The red indicates flow is faster than averaged mean velocity and slower flow in blue zone. These streaks suggest the existence of a coherent structure characterized by two counter-rotating longitudinal vortices [55].

(middle of pipe), $x = 122\ D$ (flow is fully developed), and four different azimuthal locations θ=0 (horizontal plane), $\pm\pi/4$ and $\pi/2$ (vertical plane).

Figure 3.10 shows the azimuthal variation of the streak velocity at different streamwise locations. It reveals the asymmetry actually develops along the pipe axis as the amplitude of streak velocity at $x = 20\ D$ is much smaller than that at $x = 122\ D$. To be noted, the azimuthal orientation of fast/slow streaks or asymmetry remains invariant along the pipe implying the

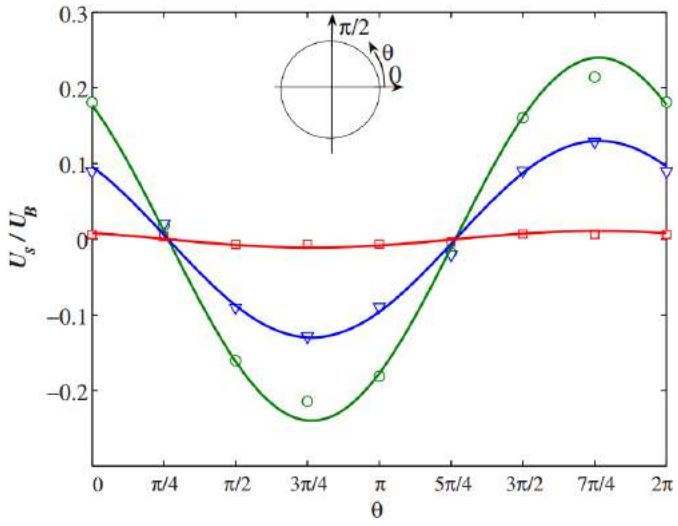

Figure 3.10: Azimuthal variation of the streak velocity at Re_w=2420, r/R=0.72 and at the axial locations: $x = 20\ D$ (square), $x = 54\ D$ (triangle), $x = 122\ D$ (circle). The anticlockwise orientation is adopted to define the azimuthal angle [55].

asymmetry does not possess a helical structure in the axial direction.

Esmael *et al.* (2010) [56] and Bahrani & Nouar (2014) [6] analysed the flow region in which the asymmetry is observed, from a perspective of statistical analysis of velocity fluctuations. By statistical analysis, the authors demonstrate this flow regime when asymmetry occurs exhibits features of a weak turbulence: chaotic in time and regular in space, which indicates the existence of coherent structure. This conclusion is obtained by analysing the power spectra of streamwise velocity fluctuations decay, showing that the energy decays with the power law behaviour f^{-3}. Figure 3.11 depicts the time history of axial velocity in the asymmetric state and corresponding frequency power spectra of the axial velocity fluctuations in the vicinity of the centre of the high speed streak. The velocity fluctuations were measured at different Reynolds numbers and with increasing Re_w, the spectra have a broad region of frequencies and the power law decay region spans about an order of magnitude in f: $2< f <10$ Hz. The large value of the exponent (f^{-3}) indicates that the power of fluctuations decays very rapidly as the scale of eddies reduce. Therefore, the fluctuations of the velocity and the velocity gradient are both determined by the integral scale thus the flow is supposed to be smooth in space and random in time.

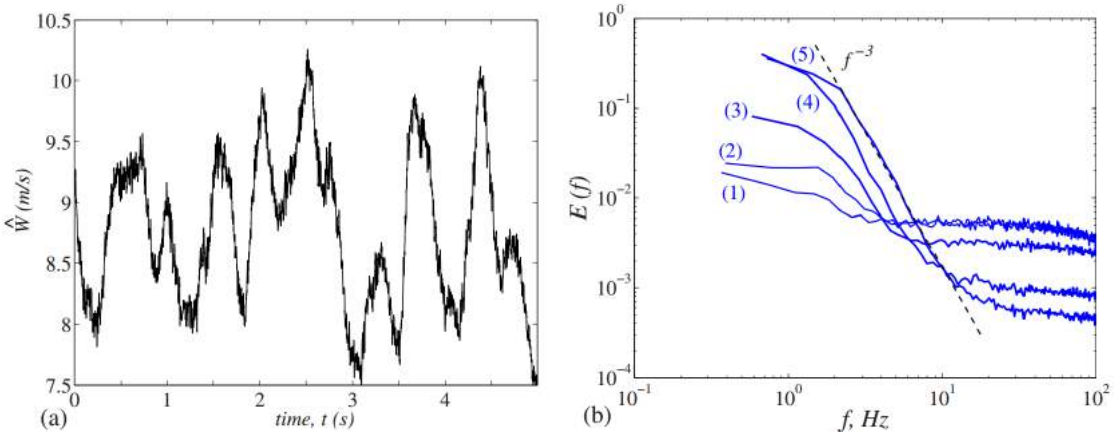

(a) puff (b) slug

Figure 3.11: (a) Time series of axial velocity for Re_w=3650 at $x = 122\ D$, r=0.7 and θ=-$\pi/4$. (b) Energy spectra of axial velocity fluctuations at $x = 122\ D$, r=0.7 and θ=-$\pi/4$: (1) $Re_w = 2010$, (2) $Re_w = 2161$, (3) $Re_w = 2327$, (4) $Re_w = 2680$, (5) $Re_w = 3650$. The dashed line indicates the power law decay f^{-3}.

Güzel *et al.* (2009) [64] revealed a systematic description of flow regimes from laminar

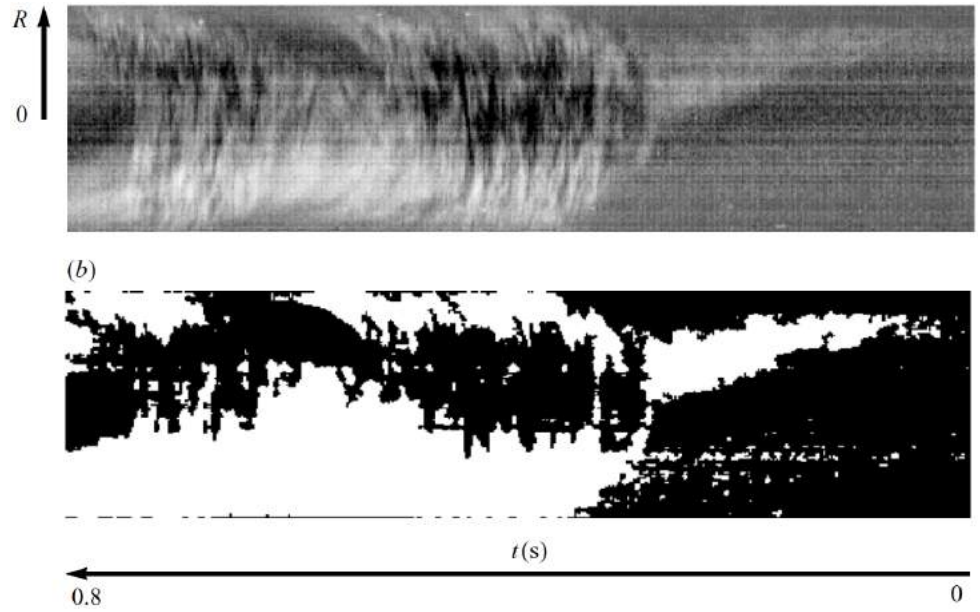

Figure 3.12: Space-time plot for 0.075% carbopol at Re=1850, flow is visualized via seeding particles and a two-coloured art dye: (a) obtained from raw high-speed flow images and (b) obtained from filtered, background subtracted images. The puff shows asymmetry. Cited from Güzel 2009 [64].

to fully turbulent using glycerin (Newtonian), xanthan gum (shear-thinning without large viscoelasticity) and carbopol (shear-thinning with yield stress) at different concentrations. The experiments were conducted in a $10m$ long flow loop with an inner diameter of $50.8m$. The LDV test section was placed at about $5.5m$ downstream of inlet. As previous experimental works revealed the asymmetry was uniquely observed in transitional regime of non-Newtonian fluids, thus the asymmetry was considered to be linked with observed puffs and slugs. Güzel *et al.* (2009) focused on the flow scenario in presence of puffs and slugs and particular attention was put on analysis of turbulence statistics, e.g. autocorrelation of velocity, the probability distribution and the structure functions in an attempt to further characterize transition. Güzel *et al.* (2009) examined the reproducibility of the directional bias of asymmetry. The authors concluded that the asymmetry systematically has a preferred biased orientation and the asymmetry is consistently in the same part of pipe for identical fluids. The authors observed that the carbopol and xanthan gum solutions persistently have a favourite but different asymmetry orientation in the same rig and the asymmetry was found both in time-averaged result and lo-

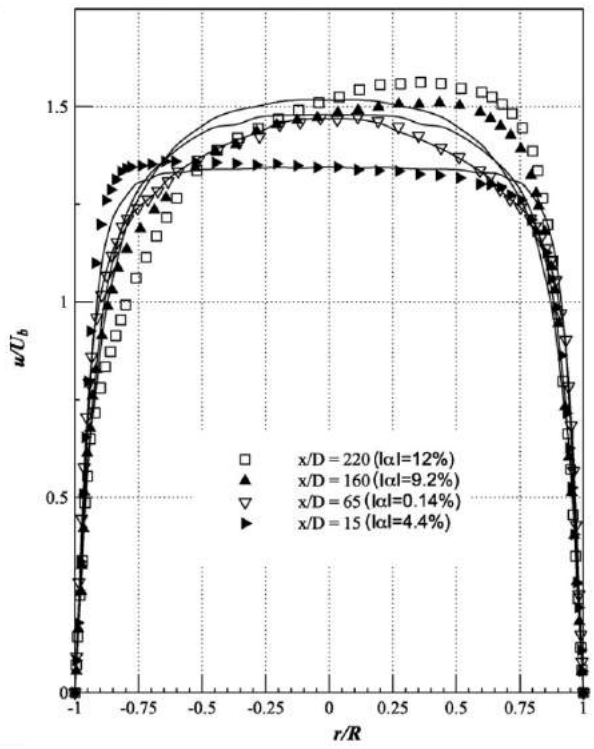

Figure 3.13: Development with axial location of measured velocity distributions in horizontal plane using 0.15% xanthan gum solution at Re_w=7120. The LDV was measured at different axial locations. To note, the plenum disc upstream the inlet was partially blocked [54].

cal *rms* of axial velocity fluctuation. The autocorrelation function indicates weakly coherent unsteady structures existed and located away from the axis in the non-Newtonian fluids and asymmetrical structures were observed using high-speed video imaging when puffs appeared, as shown in Figure 3.12. Compared with Newtonian fluids, the flow structure in carpobol solution manifested asymmetry, therefore, suggesting some asymmetrical structure in puff leads to the asymmetry.

Escudier *et al.* (2009) [54] provided a detailed investigation on a number of possible causes, which may trigger the flow transition, e.g. the rotation of the earth (inherent Coriolis acceleration), curvature of pipe axis, temperature influence, upstream and downstream disturbances. In addition to the xanthan gum and carbopol in previous work, i.e. the polyacylamide (PAA, which is shear-thinning with pronounced viscoelasticity) was also investigated. The authors took all precautions possible to eliminate systematic bias in the rig and the asymmetry was still present. The authors calculated the Ekman number of the testing fluids and, as the se-

lected shear-thinning fluids are all highly viscous, the Ekman number is generally in the range of 20-50, indicating the Coriolis acceleration is not strong enough to produce a very significant asymmetry. Likewise, the temperature gradients as well as the longitudinal curvature of the pipe are probably too weak to modify the velocity profile. Upstream of the pipe inlet, a plenum chamber with a symmetrically perforated disc was introduced specifically to minimise any asymmetry entering the pipe. A interesting observation was described in Figure 3.13. The authors intentionally block a section of the plenum disc, therefore an initial asymmetry was introduced, see the measurement data at $x/D = 15$ with the asymmetry factor equals to 4.4%. With the flow evolution in steamwise direction, the orientation of 'final' asymmetry turned into the other side of pipe, see the measurement data at $x/D = 220$ with the asymmetry factor equals to 12%. It clearly indicates the asymmetry is not due to the minor geometric imperfection far upstream and the asymmetry prefers to stay in the certain orientation in cross-sectional plane.

Pipe flow of purely viscous shear-thinning fluids was studied by López-Carranza *et al.* (2012) [91] and López-Carranza *et al.* (2013) [90] using numerical methods. The shear-thinning behaviour was indicated by Carreau model. The flow was decomposed as the base flow and perturbation. The numerical methods reveal that pipe flow of shear-thinning fluids is linearly stable and some vortices are optimally amplified. The authors also find the shear-thinning characteristics stabilize the flow due to the reduction of the exchange energy between the laminar mean flow and the perturbation.

The flow asymmetry was also observed in transitional regime of pipe flow using bio-fluids, i.e. blood (which is shear-thinning), see the work of Biswas *et al.* (2016) [18] and bentonite suspensions (shear thinning and yield stress), see Benslimane *et al.* (2016) [12]. The flow behaviour in blood and suspensions is similar to that of polymer solutions: in purely laminar and fully-turbulent regime, the velocity profile is axisymmetric and near the transitional regime, the asymmetrical experimental velocity profiles are manifested. Above a critical Reynolds number, the axial velocity profiles were observed to have a stable and increasing asymmetry with Re_{MR} using Laser Doppler velocimetry technique. The persistent observations of flow asymmetry in

various categories of shear-thinning fluids indicate the ubiquity of this asymmetry and deserves more credit to further investigate this counter-intuitive and unexplained phenomenon. The Table 4.1 summarizes the recent discoveries about the flow asymmetry:

Authors	Re definition	Re range	Fluids	Comments
Escudier *et al.* (1996) [52]	Re_w	from 550 to 25300	LAP*	first paper noticed this flow asymmetry
Escudier *et al.* (2005) [51]	Re_w	from 2000 to 8000	0.1% CARB*, 0.08% ULTREZ* 1.5% LAP*, 0.2% XG$^{\bullet}$/PAA$^{\square}$ 0.25% CMC* 0.09% CMC/XG$^{\bullet}$	summarize observations of asymmetry from UK France and Australia
Rudman *et al.* (2004) [139]	Re_w	5500	Power-law Herschel-Bulkley model	reveal the time-varying nature of asymmetry numerically
Peixinho *et al.* (2005) [121]	Re_{MR}	2100 2500 2700	Glucose syrup$^{\diamond}$ 2% CMC* 0.2% CARB*	yield stress and shear thinning stabilize the flow
Esmael *et al.* (2008) [55]	Re_w	1805-4867	0.2% CARB 940*	suggest the transition is dominated by co-rotating coherent structures
Güzel *et al.* (2009) [64]	Re_w	2573 1218 937	65% Glycerin$^{\diamond}$ 0.2% Xanthan$^{\bullet}$ CARB 940*	same fluid has same orientation of asymmetry
Escudier *et al.* (2009) [54]	Re_w	from 2000 to 8000	60% glycerol$^{\diamond}$, 0.03% PAA$^{\square}$ 0.125% PAA$^{\square}$, 0.15% XG$^{\bullet}$ 0.03% PAA$^{\square}$, 0.15% XG$^{\bullet}$	rule out some factors that could lead to flow asymmetry
Esmael *et al.* (2010) [56]	$Re_{GJ} = \frac{\rho u(r) D}{\mu(r)}$	1805-4867	0.2% CARB 940*	a feature of week turbulence was exhibited
Bahrani *et al.* (2014) [6]	Re_w	1080-9811	0.2% CARB 940*	define two stages during transition to turbulence
Biswas *et al.* (2016) [18]	Re_w	2300 2450 2600	blood$^{\bullet}$	find asymmetry in bio-fluid in transitional regime
Benslimane *et al.* (2016) [12]	Re_w	360-2920	Bentonite$^{\bullet}$	find asymmetry in suspension in transitional regime

Table 3.1: Literature review of experimental and numerical investigation of flow asymmetry in the pipe for Newtonian and non-Newtonian fluids. Superscript symbols represent different fluid properties. $\bullet$: Shear-thinning fluid without yield stress. $\star$: Shear-thinning fluid with yield stress. $\diamond$: Newtonian fluid. $\square$: shear-thinning with large viscoelasticity. CARB stands for carbopol; CMC stands for carboxymethyl cellulose; XG stands for xanthan gum; LAP stands for Laponite; PAA stands for polyacrylamide. Re_w indicates the Reynolds number based on wall shear viscosity and Re_{MR} is generalized Reynolds number by proposed by Metzner and Reed [105].

Generally, the previous studies regarding the flow asymmetry in the last 2 decades enable us to see the tip of the 'iceberg'. However, the limitation of previous investigations is also quite clear: the time-averaged point-wise measurements of asymmetrical velocity profiles do not provide a complete picture of this unusual flow behaviour. This limitation is a motivation to review this phenomenon but using more recent experimental technique i.e. stereoscopic particle image velocity to characterize the nature of this asymmetry in a three-dimensional and time-resolved manner.

3.2.2 Drag reduction

From a fundamental research perspective, the deep understanding of polymer turbulence interaction in drag reduction can provide more insight into the mechanism of wall turbulence and potentially provides a method of reducing drag. The drag reduction generally appears when the flow is fully turbulent and in comparison to the Newtonian solvent, the drag can be reduced by up to 80 percent by addition of a polymer [80, 94, 118, 129, 150]. Although the mechanism underlying the onset of drag reduction is not fully understood, a number of theories [14, 33, 79, 92, 93, 166] have been proposed since its discovery. Generally the current theories regarding the drag reduction of polymer solution can be classified into two categories. One, based on the viscous effects [94, 141, 142], states that time scale of coil-stretch transition in polymer is larger than the characteristic time scale of turbulence and the polymer close to the wall was stretched by the turbulent stress. Because of the stretching (akin to the flow scenario in capillary breakup extensional rheometer), the elongational viscosity increases dramatically and thus suppress the turbulent fluctuation and reduce the drag of pipe wall. The other theory [71, 152] believes the drag reduction is linked with elasticity of fluid as this theory claims the fluctuated strain rate is not enough to fully stretch the polymer. The drag reduction appears when stored elastic energy of moderately stretching polymer is comparable with turbulent kinetic energy. The usual Kolmogorov energy cascade is then terminated prematurely, and scales below this cut-off scale are believed to behave elastically [166]. These elastic effects are believed to

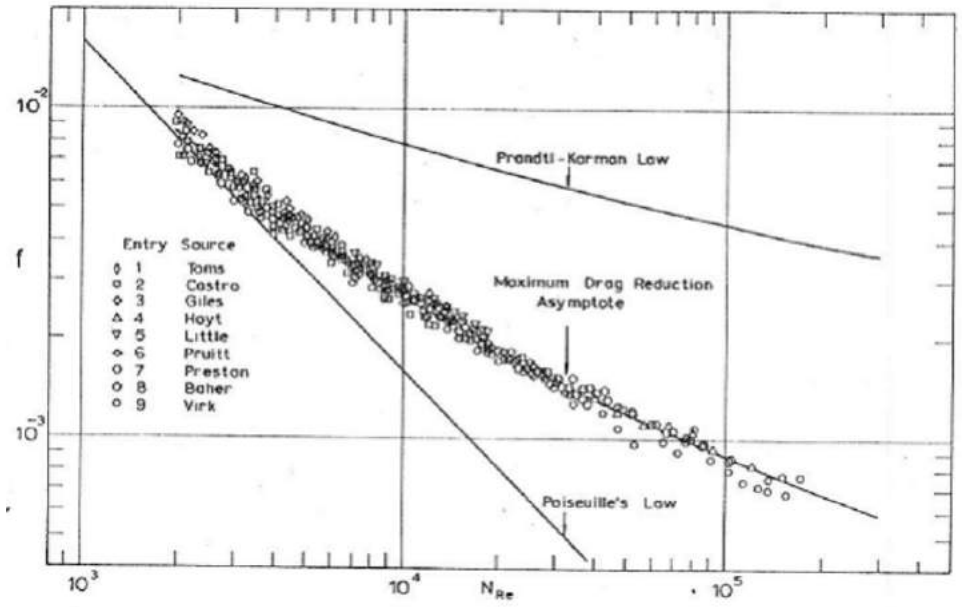

Figure 3.14: Friction factor at maximum drag reduction, Virk *et al.* (1975) [161]. The Prandtl-Karman law corresponds to the turbulent flow of Newtonian fluids and Poiseuille's law indicates the friction of laminar flow.

yield a thickened buffer layer and subsequent drag reduction.

The drag reduction ability is observed to enhance with increasing flow velocity, polymer concentration, molecular weight of polymer and decreasing pipe diameter. Virk *et al.* [161] proposed the maximum drag reduction asymptote (see Figure 3.14) to indicate the upper limit of drag reduction. This Virk's maximum drag reduction asymptote was obtained by empirical observation of the limit on the polymer drag reduction. In the fully-turbulent regime, the drag in polymer solution was enormously reduced, in comparison with that of Newtonian fluids (represented by the Prandtl-Karman law). In laminar regime, the friction factor of the polymer solutions is close to that of Newtonian fluids, indicating the drag reducing ability of polymer solutions is not prominent in the laminar regime. This can be explained that the polymer molecular structure is still coiled in laminar regime as the stress is lower than that in turbulent regime in the pipe, thus the polymer does not interact with flow.

Chapter 4

Experimental Techniques

This chapter describes the experimental facilities, measuring technique and data processing methods employed in this study. The experimental rig utilized is the Very Large Scale Pipe Flow Facility, which gives the opportunity to implement the measurements ranging from purely laminar ($Re_w \approx 800$) to fully turbulent ($Re_w \approx 23000$) conditions. The measuring techniques include pressure measurement, rheological measurement and primarily the stereoscopic particle image velocimetry (SPIV). Laser Doppler Velocimetry (LDV) is also utilized to detect the transition onset and provide localized axial velocity information to supplement the SPIV data. A number of data-processing methods are introduced to describe the techniques of extracting flow information from the raw three-component velocity SPIV data.

4.1 Very Large Scale Pipe Flow Facility

Figure 4.1 shows the schematic description of the flow loop used for the experiments. The flow loop rig consists of a pipe flow arrangement with associated instrumentation, mixing and pumping facilities. Flow is driven by a progressive cavity pump, fed directly from a circa $500L$ capacity stainless steel tank. The volume of the whole system including the pipe and the flexible tubing is approximately $750L$. The tank is supported at a height of $0.55m$ above the test section

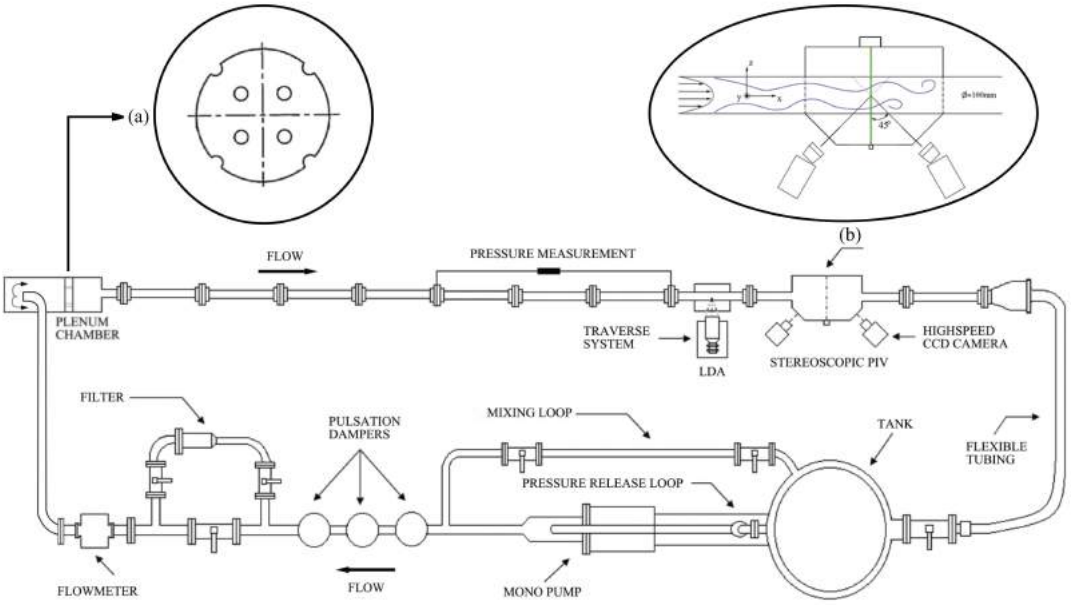

Figure 4.1: Schematic of Very Large Scale Pipe Flow facility (top view). (a): axisymmetric design in the plenum chamber; (b): Scheimpflug configuration in the SPIV system.

Figure 4.2: Photograph illustrating the sections of pipe, SPIV system and mixing tank.

to provide enough head to fill the system. Three dampers positioned closely after the pump outlet remove pulsations in the flow before entry into the test section. The plenum chamber is introduced immediately upstream of the pipe inlet to minimize swirl and ensure the incoming flow is uniform. The special design of the plenum chamber is that: when the flow enters the plenum chamber from the upstream, the flow is redirected and turned through 90^o so that the flow is initially directed to the back wall of the chamber. An axisymmetric disc with four peripheral cutouts (see Figure 4.1a) is intended to uniformly distribute the flow prior to the outlet contraction of chamber and flow straightener to minimize the asymmetry. The pipe system is made up of 23 modules each $1.027m(\pm 3mm)$ long and $100.4 \pm 0.1mm$ internal diameter. Each module consists of a precision-bore borosilicate glass tube with a matched male/female stainless steel flange at either end fixed onto a rigid table. The glass tube is separated from the stainless steel by a thin PTFE ring and each end of the module (assembled in a vertical jig to ensure concentricity between the bore of the glass tube and that of the fringe) is fixed using Devcon urethane rubber. The purpose of the Devcon urethane rubber is to compensate for any expansion or contraction of the stainless steel and glass due to temperature variations. To avoid geometric imperfections and the possibility of longitudinal-curvature effects leading to secondary flow, the pipe system was assembled guided by a laser and target alignment process, which ensured the overall end-to-end straightness well within $1mm$. Figure 4.2 shows a photograph of Very Large Scale Pipe Flow Facility.

Mixing of the additives to the solvent is accomplished by circulating the fluid through a return loop before the fluid enters into the pipe. Generally, the fluid circulates in the loop with minimum pump speed until homogeneity is achieved with minimum polymer degradation. The pressure release valve, positioned near the tank, is incorporated as a mean of providing a larger range of flowrates within the test section by regulating the ball-valve installed on the loop. The mass flowrate can be obtained by a Coriolis flowmeter ($25kg/s$ full scale, resolution of $0.025kg/s$), and the flowmeter can also provide the fluid temperature in order to obtain the accurate viscosity which is associated with Reynolds number.

Pressure tappings of 1*mm* diameter are provided on each mating flange pair. The pressure tappings are connected to a Validyne® differential pressure transducer by a hose filled with the working fluid. The stereoscopic PIV system sits around 220*D* downstream from the pipe inlet and *D* is the inner diameter of the pipe. The LDV instrumentation is located close to the SPIV system, which is roughly 20*D* upstream of the SPIV location. The purpose of LDV measurement is to detect the instantaneous flow state before the SPIV data acquisition. The LDV measurement can provide an accurate and almost instantaneous streamwise velocity value. The observed axial velocity drop in LDV can be regard as a 'transition indicator' to determine whether the flow state is in the transition regime. Further descriptions of the SPIV and LDV instrumentation are provided in Section 4.3 and Section 4.4, respectively.

4.2 Pressure drop measurement

Pressure drop measurements were made by employing a Validyne differential pressure transducer (DP15-20) in conjunction with a Validyne CD223 digital transducer indicator. The pressure transducer was periodically calibrated before usage and the voltage output for the pressure transducer was sampled by an analogue-to-digital converter (LabJack) at sampling rate of 100 Hz. The full-scale pressure range is 8.6 *mbar* with a quoted accuracy of $\pm 0.25\%$ full scale, i.e. ± 2.15 *Pa* accuracy. The pressure transducer gives a more precise reading in the range of approximately $20\% \sim 80\%$ of full scale, in order to enable the pressure transducer to work in an intermediate range, the measurement length of the pressure drop was selected to be 8.2 *m*. Zero readings, i.e. measurements under static conditions were conducted at the beginning and end of each flow experiment to account for drift of the pressure drop. Special care was taken at the pressure tapping to make sure the edge of each pressure tapping is not rounded and remained flush with the inner wall of the test-section to minimize any potential error triggered by burrs or rounded edges of the pressure hole. However, for high concentration viscoelastic fluids, errors could be introduced into the instantaneous pressure-drop measurement due to viscoelastic

effects. The time scale of polymer relaxation may be much larger than that of the pressure fluctuation, which may lead to a damping of the instantaneous pressure fluctuation measurements. Therefore, only the long time-averaged pressure measurement value is used in the calculation of wall shear stress and Reynolds number of fluids.

4.3 SPIV measurement

4.3.1 SPIV overview

Particle image velocimetry (PIV) is a planar flow diagnostic technique that depends on seeding tracer particles into fluids and observing the motions of the particles to derive fluid velocities [3, 130, 158, 159, 165]. For PIV measurements, a planar laser sheet is usually employed to illuminate the region of interest. The particles scatter the laser light when they move through it and the location of these particles can be recorded by photographic film or digital cameras at two different times separated by a prescribed time interval. The displacements of individual tracer particle, more accurately, groups of tracer particles, are determined by the PIV image post-processing algorithm. The particle velocity vectors can be straightforwardly obtained by displacements over a known time interval. Supposing the particles to have an excellent flow-following ability, the velocity of particles could be approximated to the velocity of the working fluid.

A classical PIV technique is a two-dimensional (2D) measuring technique. It only enables two components of velocity in the plane of laser sheet to be obtained. The out-of-plane motion is lost as the displacement component perpendicular to the laser sheet is projected as an identical point on the image plane. In order to acquire complete instantaneous three components of fluid velocity vectors, stereoscopic PIV (SPIV) technique is employed to study complex spatial flow structures over the complete circular cross-section of the pipe. A planar laser beam, i.e. the measurement plane is positioned perpendicular to the streamwise flow direction, thus flow structures are advected through the laser beam and recorded by two high-speed CMOS (complementary

metal-oxide semiconductor) cameras aligned in an angular displacement of $\pm 45^{o}$ to the light sheet, satisfying the Scheimpflug configuration [3]. Both cameras must be focused on the same location and properly calibrated to have the same point in focus. The velocity vector can then be obtained by using a correlation algorithm to the raw PIV image to calculate the mean velocity of each interrogation area. Applying *Taylor's hypothesis* [36, 66, 153], the quasi-instantaneous three components velocity field can be reconstructed from a set of time-resolved measurements, which offers an opportunity to study the asymmetric feature of shear-shinning fluids in a full field way.

4.3.2 SPIV setup

Figure 4.3 shows the configuration of the stereoscopic PIV system and the laboratory co-ordinate reference.

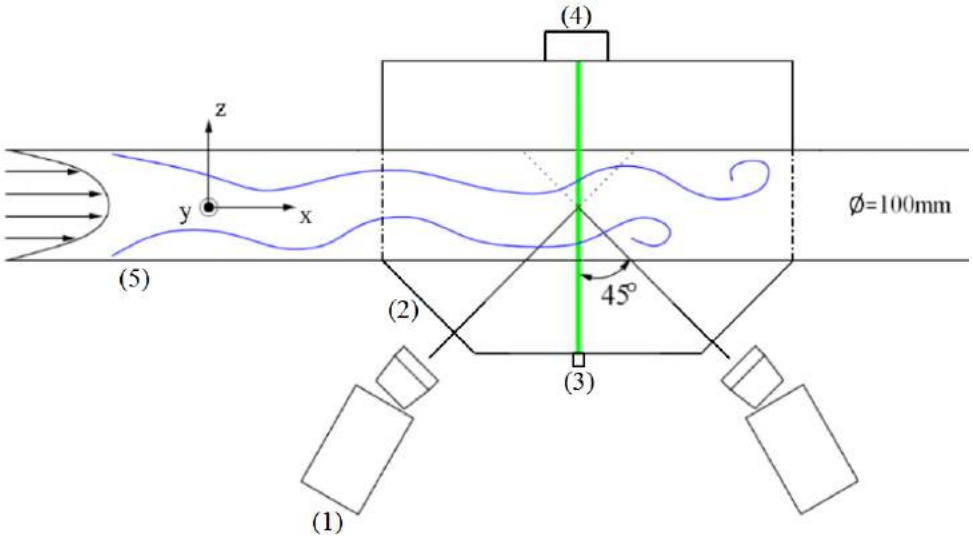

Figure 4.3: Schematic (top view) of stereoscopic PIV configuration. (1). high-speed CMOS cameras on Scheimpflug mount. (2). water prism. (3). Nd:YAG-laser. (4). laser damper. (5). laser-aligned borosilicate glass pipe.

A detailed description of the overall pipe rig has already been provided in Section 4.1 and this subsection highlights the experimental setup of the SPIV system. Image recording devices are key components of the system. The measurements use two Dantec SpeedSense

M110 CMOS cameras which could operate from few fps (frame per second) to maximum 1630 fps in full resolution of 1280×800 pixels. The size of the pixel pitch is $10 \times 10\ \mu m$ with the pixel depth of 12 bits/pixel. The camera lens used is a Sigma 105mm lens with the minimum f-number of 2.8 so that the camera FOV (field of view) fully covers the circular cross-section of pipe. The two cameras are fixed on Scheimpflug mounts located on opposite sides of the laser sheet and observe the beam in the perspective of $\pm 45^{o}$. The oblique view of the measurement plane results in blurred particles due to the fixed focus length of the lens. To have a sharp focus of all particles in the entire field of view, the Scheimpflug criterion [126, 127] has to be fulfilled, i.e. image plane, lens plane and object plane for each of the cameras need to intersect in a common line. This is practically achieved by means of camera-lens tilt mechanisms with the rotation axis freely adjustable, therefore tilt-adapters are used in our experiments. However, the Scheimpflug condition is not sufficient to ensure that particle images are in focus over the entire depth of the measurement volume. This requirement is satisfied with an appropriate depth of focus by selecting an appropriate lens aperture. The focus length and the angular offset of the tilt-adaptor requires a precise fine-tuning to achieve the optimal particle focus, which is achievable in a trial-and-error procedure [116].

The particles are illuminated by a dual cavity frequency-doubled Q-switch (pulsed) Nd:YAG laser from Dantec Dynamic (Lee Laser LDP-100MQG). The laser is capable of operation at nominal speed 15 kHz with a maximum pulse energy about 200 $mJ/pulse$. The wavelength of the laser is 532 nm and is transported by a light-guiding arm in conjunction with light sheet optics to the flow rig. The optics produce a light sheet with an adjustable thickness and in our measurements the thickness of the laser sheet is about 1.5 mm. A convex polygon shaped test section filled with water encloses the pipe and two water-prisms are installed to minimise the optical deformation due to the curvature of the round pipe wall. A laser dump sits at the opposite side of the pipe, aligned with the laser beam to reduce the laser reflection inside the test section. The calibration target is inserted into the pipe overlapping with the laser in the calibration stage. The detailed description of the calibration procedure is provided in subsection 4.3.3.

The working fluid is homogeneously mixed and tracking particles are seeded in the fluid mixing process. The tracking particles used for flow investigations in this study are silver coated hollow glass spheres with a mean particle diameter of 10 μm (Dantec Dynamics® S-HGS, silver coated hollow glass spheres). The silver coated hollow glass spheres are borosilicate glass particles with a spherical shape and a smooth surface, preferable for liquid flow applications. The thin silver coating further increases the reflectivity to generate sufficient light scattering and high visibility signals. The density of particles is roughly 10 particles per interrogation area in order to get a good correlation of PIV image pairs. A complete overview of the experimental parameters is shown in Table 4.1.

Pipe	Diameter	100 mm
	Length	23 m
	Material	borosilicate glass
	Wall thickness	5 mm
Seedings	Type	silver coated hollow glass spheres
	Specific weight	1 g/cm^3
	Diameter	10 μm
	Concentration	5 g/cm^3
Laser sheet	laser type	Nd:YAG
	Maximum energy	200 $mJ/pulse$
	Wave length	532 nm
	Pulse duration	6 ns
	Thickness	1.5 mm
Camera	Type	high-speed CMOS
	Resolution	1280 $px \times 800$ px
	Pixel depths	12 $bits/px$
	Pixel size	10 μm
Imaging	$f-$number	4
	Viewing angles	$\pm 45^o$
	Tilted angles	7^o
	Image mode	single/double frame mode
	Frame rate	5 to 200 fps at full resolution
PIV analysis	Reconstruction method	three-dimensional target calibration
	Interrogation Area(IA)	$32px \times 32px$
	Overlap IA	50%

Table 4.1: Experimental parameters for flow measurements

4.3.3 Velocity reconstruction

To reconstruct the velocity component of the out-of-plane direction, correct calibration is an essential prerequisite for stereoscopic PIV [20]. Most often, a multi-level calibration target, consisting of precisely spaced grid markers (white dots on black background) is employed. The image processing techniques can detect the position of grid dots and a reference system built on grid markers. A single level of planar calibration in one plane is sufficient to calculate the mapping between image space and object space but it does not provide information on the camera viewing angles that are essential to extract the third velocity component (i.e. as in stereo PIV). This viewing perspective information can be determined from a set of non-coplanar target markers that are slightly displaced at known positions in the orientation normal to the laser sheet plane. This is achieved by using a multi-level double sided target plane. The markers are located on three different parallel planes, which are 3 *mm* apart respectively. The middle-plane of the calibration target is placed coincident with the laser sheet plane and the middle-plane (also the laser plane) position is set as the zero position in the streamwise direction. The application of the multi-level calibration target averts the offset in the direction normal to the laser plane for the single level calibration target and cameras can be mounted on opposite sides of the laser sheet. Although small angles between the two cameras can be employed, the out-of-plane velocity component is acquired more accurately with larger angles between the two cameras. The most accurate calibration is obtained when the perspective between the two cameras is 90^{o} . The calibration target has a larger centre dot as a reference marker, which corresponds to the level at which the big dot in the centre of calibration target is placed. The geometric reconstruction is possible only when the calibration target configuration is accurately known and could be mathematically modelled, the detailed distribution of calibration dots and dimensions are shown in Figure 4.4.

The mathematical model obtained in the calibration procedure gives a mapping function between the image plane and real physical space providing a direct relationship between the particle location in the physical plane and its corresponding position on the image plane. The

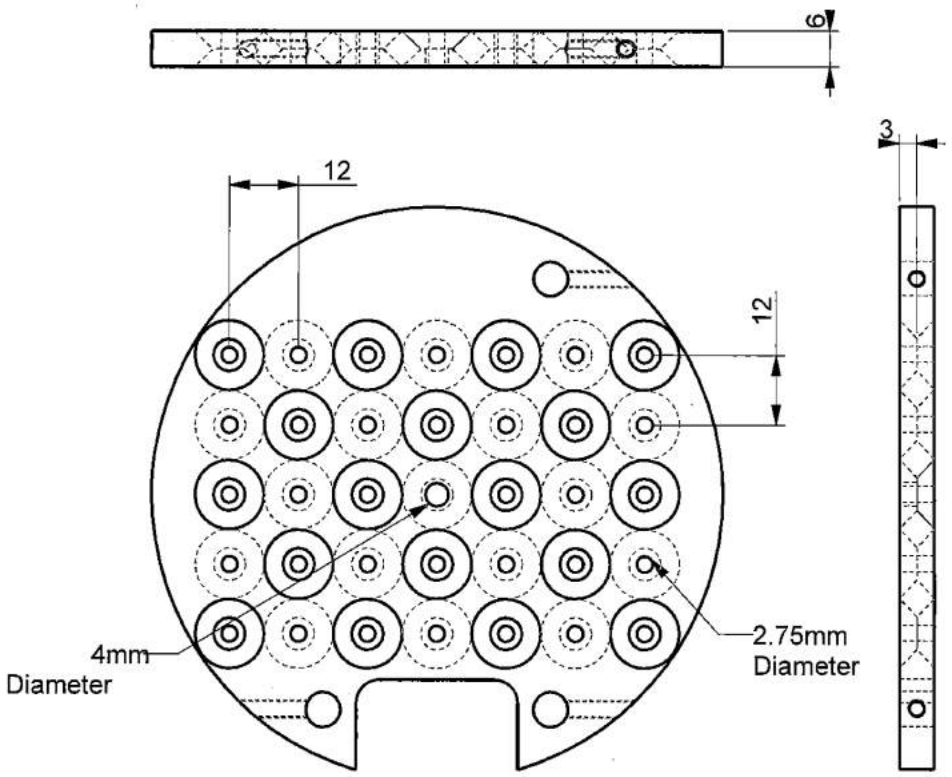

Figure 4.4: Geometry of the multi-level calibration target with the white dots locating on the black background. All dimensions are in *mm*.

mapping function can then be inverted to reconstruct the three-dimensional displacement of particles. The estimation of the particle displacement is achieved by spatial cross-correlation PIV technique [3, 10, 75]. The displacement correlation peak gives the ensemble averaging velocity of all particles dwelling in the interrogation volume. The 3D velocity field is then obtained based on the given calibration geometry information and the 2D vector map on each camera. The procedure of calibration and velocity reconstruction in the laboratory is described below:

1. Ensure that the calibration target is perpendicular to the axial direction of pipe.

2. Place calibration coincident with laser sheet. The thickness of the laser beam should be set to $1 \sim 2$ mm and overlapped with the marker line on the calibration target.

3. Focus the particles on the entire measurement plane. Care needs to be taken to achieve a good focus of observation via: (a) Adjust to correct aperture to have a good depth-of-

field. The large depth-of-field by increasing the $f^{\#}$ could give a sharp image but reduced the amount of light. (b) Adjust the degree of the tilt angle between the lens and optical axis of camera to reduce blurring. The *focal assist* function in *Dynamic Studio 4.10* is helpful to achieve a corner-to-corner sharpness of particles.

4. Record image of two-sided target on each camera at multiple x-locations, i.e. pipe axis direction. Over 10 images should be taken and the camera can be overexposed to increase the contrast between white target dots and black background.

5. Determine mapping function between the image plane and three-dimensional physical space using direct linear transformation or pinhole model (comparative assessments of different calibration methods are given in [144]). The pixel error should be approximately half a pixel and at least 31 in 35 calibration dots should be recognized in calibration.

6. Perform a calibration refinement to correct for the residual misalignment between calibration target and laser light sheet.

7. Remove the calibration target and record PIV images on each camera. To determine the proper time interval between image pair, the particle displacement should be about $20\% \sim 50\%$ of the length of the interrogation area.

8. Process the image: (a) Average the PIV images and use the mean image subtraction to reduce the background noise. (b) Add the mask to filter out the redundant part out of the flow section. (c) Use the image arithmetic to process the brightness of pixels. (d) Use correlative PIV or adaptive PIV [154] to estimate velocity vectors. The adaptive PIV has a better performance to process the velocity gradient of the flow near the wall. The correlative PIV is less time-consuming and more robust to raw image quality.

9. Reconstruction of 3D velocity field by inverting mapping function obtained in calibration step.

4.4 LDV measurement

The measurements of mean streamwise velocity and turbulence intensity at different axial positions were made using a laser Doppler velocimetry (LDV). The LDV technique is an optical non-intrusive measurement for fluid velocity by means of a Doppler frequency shift caused in a monochromatic coherent light beam by scattering particles in a fluid [4]. The reflected light fluctuates in intensity, the frequency of which is equivalent to the Doppler shift between the incident and scattered light, and is thus proportional to the component of particle velocity which lies in the plane of two laser beams. The laser Doppler anemometer system utilized in the project was a Dantec FibreFlow system. The laser used was an Argon-Ion supplied by Laser Physics. The laser light was transmitted from the laser generator to transmitting optics through optical fibres. The laser can work in three different wavelengths of light, in here, green light (wavelength=514.5nm) was utilized to achieve a higher signal-noise ratio. The probe head, housing both the transmitting and receiving optics, was mounted on a traverse system perpendicular to the streamwise flow direction. The measurement plane, i.e. the plane generated by two crossed laser beams, horizontally passed through the centreline of the pipe to minimise the effect of light refraction due to the curvature of round pipe. The backscatter mode is applied as its transmitting and receiving optics are essentially aligned and this mode is also easy to use with an acceptable measurement accuracy. The signal is processed by Dantec Burst Spectrum Analyser F30. The green laser beam separation was 51.5 mm and the focal length was 160 mm. The measured half angle between the laser beams is 9.1^{o} which generated a measurement volume $36\mu m$ and a length of 220 μm.

The conveniences the LDV technique brings to the project lies in: first, the probing point in the LDV measurement system can be easily changed along the axial position so that it can be checked whether this asymmetry has a helical structure along the axial direction. This is a supplemental data for SPIV system, as for the SPIV system, the measurement plane is fixed at 220 pipe diameter downstream of the inlet and no measurement data is available at other axial locations. Second, the LDV can perform a high-resolution measurement at the near-wall

region and enable us to obtain the axial velocity fluctuation (indicators of transition) instantaneously at a specified point. The detection of transition is of importance at the early stage of the project, as previously the general consensus is that the significant asymmetry appears near or in the regime of laminar-turbulent transition thus the asymmetry is deemed to be linked with the turbulent puffs. Therefore, the LDV measurement is applied initially to detect transition before the SPIV system. The LDV probing point is set at 80% of the pipe radius R, i.e. r/R=0.8, in the horizontal plane crossing the pipe axis to measure the *rms* of axial velocity fluctuation u' at 20 pipe diameter upstream of the SPIV system. The LDV data acquisition rate is roughly 20$\sim$100Hz since the backscattering is applied and the time duration of the LDV measurement is set to 300 seconds when flow is steady, therefore roughly 6000$\sim$30000 points are acquired during the LDV measurement.

4.5 Rheological measurement

For the non-Newtonian fluids, since the viscosity is not constant with shear rate, rheological measurement are necessary to obtain the viscometric characterization [40, 107, 148]. All rheological measurements for shear-thinning and viscoelastic solutions were conducted using a TA Instruments RheolystAR 1000N controlled-stress rheometer. The TA instruments offer a range of geometries for each applications. The geometries of rheometer are divided into the three groups: cone and plate, parallel plate and double concentric cylinders, each with a range of sizes available. The geometries are shown in Figure 4.5.

The measuring system consists of two parts: one is the fixed part, which is either the Peltier plate, or a system attached to the Peltier plate. The second part (i.e. the geometry) is attached to the driving motor spindle, which is the moving member of the system (the rotor). Temperature control of the TA rheometer is achieved via the fixed Peltier plate that uses the Peltier effect to control the temperature of the sample within ± 0.1 °C. In the measurements, the temperature is set to 20 °C, which is close to the temperature of the working fluid in pipe. Geometries

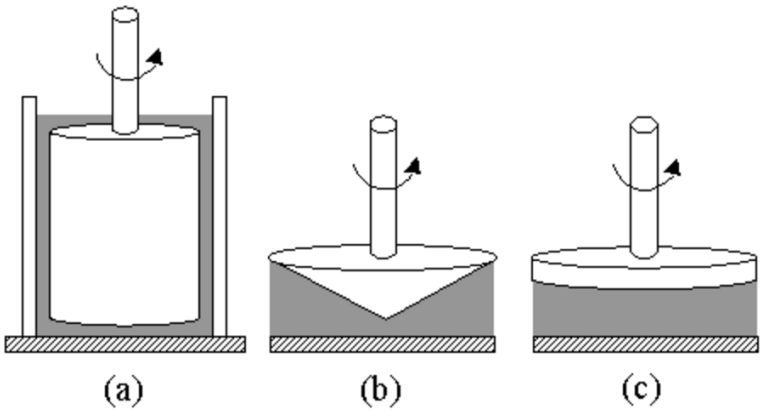

Figure 4.5: Schematic diagram of basic geometries for the rotational rheometer: (a) concentric cylinder, (b) cone and plate, (c) parallel plate.

are usually constructed from stainless steel, aluminum, or acrylic. In this project, the acrylic geometry was used due to the lower inertia of the geometry and it is transparent so the visual behavior of the sample can be observed.

The rheometer applies a given torque or stress to fluid then measures the resulting deformation of the fluid, e.g. shear rate. Different geometries are applied in different shear rate range. A parallel plate was used to achieve the highest possible shear rate ($10^{-3} - 2 \times 10^4\ s^{-1}$). For a wide range of intermediate shear rates ($10^{-2} - 2 \times 10^3\ s^{-1}$), a cone and plate geometry was used. The lowest shear rates were achieved using a double concentric cylinder arrangement, in steady shear rates down to $10^{-3}\ s^{-1}$. The shear-thinning characteristics of the fluids utilized in the project are approximately manifested in the shear rate range from $5 \times 10^{-2} s^{-1}$ to $2 \times 10^3\ s^{-1}$, therefore the acrylic cone-and-plate geometry (60 *mm* diameter, 2^o cone angle) was used, which has an uncertainty in viscosity of $\pm 2\%$ [49]. The sample was carefully loaded ensuring correct filling between the geometry and fixed bottom plate. The sample fluids rest minutes on the bottom plate before the flow tests were performed in order to get an equilibrium state of fluid.

The polymeric solution can be characterized by means of different types of rheometrical experiments. In this project, the rheometrical experiments comprise the steady-shear measurements and small-amplitude oscillatory shear measurements (SAOS). These different rheo-

metrical test modes can be selected in the TA instrument rheometer software using the same measurement geometry.

The steady-shear measurement gives the relationship between shear rate and shear viscosity i.e. the flow curve. From the flow curve, we can extract the information of fluids properties, e.g. the shear-thinning characteristics of fluids. In our experiments, the shear rate range of steady-shear measurement is from $2 \times 10^{-2} s^{-1}$ to $2 \times 10^{3}\ s^{-1}$, which is determined by trial-and-error procedure. For the identical sample, the steady-shear measurements were repeatedly implemented 2 or 3 times until the viscosity curves overlapped.

In small-amplitude oscillatory shear measurements (SAOS), the storage modulus G' and loss modulus G'' of fluids are measured. The oscillatory shear is used widely in characterization of viscoelastic materials. In this method, both stress and strain vary cyclically with time, with sinusoidal variation being the most commonly used. This method is used to characterize viscoelasticity, since relative contributions of viscous and elastic response of materials are measured. The SAOS test assumes that the material response is in the linear regime and therefore the material functions, e.g. G' and G'' can fully describe the material response. In order to determine the linear regime, the amplitude of the oscillatory test is selected with care in our experiment. If the strain is too large, the fluid sample will be deformed beyond its linear viscoelastic regime, where the measured component becomes dependent on the extent of the deformation. For this reason, in the experiment, a strain sweep was conducted prior to a frequency sweep to determine the strain where the material function becomes dependent only on the strain. Then the frequency sweep was implemented by imposing the small-amplitude oscillatory shear to fluid sample to get the G' and G'' in the linear regime, which can characterizes the viscoelasticity of fluids.

Chapter 5

Flow Characteristics of Asymmetry

This chapter examines the experimental data in detail using an aqueous solution of nominal 0.15wt % xanthan gum. Since xanthan gum solution is an essentially inelastic shear-thinning polymer solution [9], it is an ideal fluid to characterize the asymmetry where shear-thinning characteristics manifest without large elastic effects. Initially, our investigation concentrates on the laminar-turbulent transition regime in order to be consistent with the previous studies and as previously reported, a clear asymmetry was repeatedly observed in a long time-averaged result (dimensionless time: t^*=1800, where $t^* = t \cdot U_b/D$, U_b is the bulk velocity and D is the pipe diameter). The author first experimentally reveal that the asymmetry is not stationary in time but is actually time-varying although it does have a preferred orientation in the cross-stream plane i.e. $r-\theta$ plane. Then the investigation of the asymmetry was extended from a fixed Reynolds number to a broad range of Reynolds numbers covering purely laminar to fully turbulent flow, in order to obtain a complete picture of the phenomenon and shed light on the mechanism leading to the asymmetry.

5.1 Fluid characterization

The fluid characterization section includes rheological and pressure-drop measurement of 0.15 % xanthan gum solution. The rheological measurements highlighted the shear-thinning nature of the working fluid and the drag-reducing characteristic was illustrated in pressure-drop measurements. Since mechanical and biological degradation may occur to change the fluid properties, the rheology and pressure drop of fluids before and after each experiment is concluded to examine the degradation of the fluid.

5.1.1 Rheological measurement

Xanthan gum is a high-molecular-weight, semi-rigid polymer and does not possess a very flexible molecular structure [9]. Xanthan gum could be found as a stabiliser, thickener or gelling agent in cosmetics and food products like shampoos, sauces, tomato ketchup and is also used in the pharmaceutical care industry [73]. The molecular configuration of xanthan gum is rod-like and lacks flexibility which indicates the xanthan gum does not possess a large viscoelasticity [134]. This xanthan gum is often assumed inelastic and this could help to isolate the effects of shear-thinning and elasticity. The xanthan gum utilized in this project is in powder form with the molecular weight of an individual xanthan gum chain to be in excess of 10^6 g/mol from the CP Kelco company. The density of 0.15% xanthan gum aqueous solution is $998 g/l$ when uniformly mixed. Based on the previous experimental data in our lab [50], the critical overlap concentration of identical xanthan gum solution c^* is approximately 0.067%. In this project, the high concentrations of xanthan gum solution were utilized, ranging from 0.07% to 0.2%, therefore, they are all in semi-dilute regime (i.e. $c > c^*$). If the concentration of polymer solution $c < c^*$, the molecules are sufficiently far apart and minimal interactions between molecules exist, the fluid is therefore in dilute regime.

Figure 5.1 shows flow curve of aqueous solution of nominal 0.15wt % xanthan gum. In the limit of very high shear rate the viscosity is constant, whist in the limit of the low shear rate

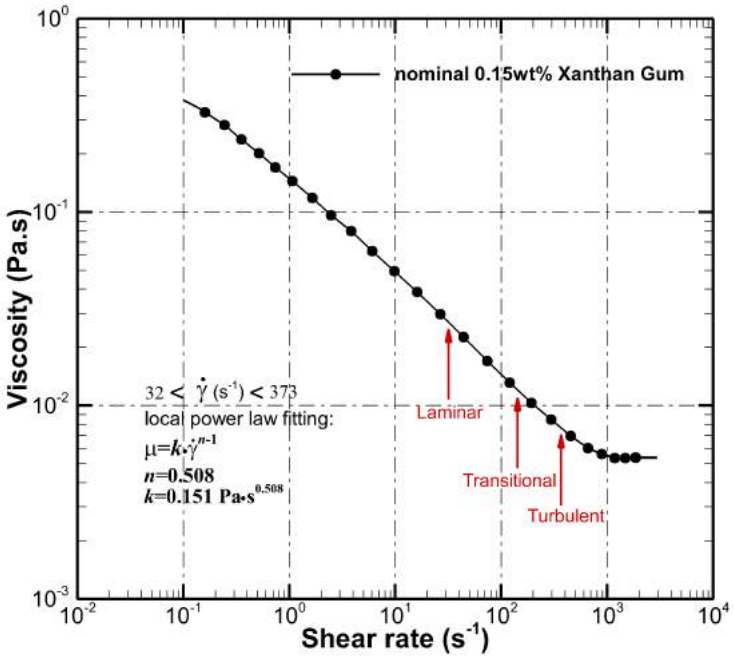

Figure 5.1: Flow curve of aqueous solution of nominal 0.15wt % xanthan gum. The data is fitted by the Carreau-Yasuda model, see Equation 2.8. Red arrows indicates the range of wall shear rate where the experiment was conducted. Local power law fitting was implemented in this shear rate range.

the viscosity asymptotically approaches a constant viscosity too, but at a higher level. There two extremes are known as the lower and upper Newtonian regions, which is usually called infinite-shear rate viscosity and zero-shear rate viscosity, respectively. In intermediate shear strain region, the viscosity decreases with increasing shear rate. This region shows linearity with a constant gradient on a log-log plot of viscosity against shear rate, i.e. exhibits power law dependence. It is worth mentioning that all flow regimes from purely laminar to fully turbulent are in the power law region which indicates the shear-thinning effect exists during the full *Re* range. Wall shear stress was derived based on pressure-drop measurement in the pipe (see Equation 2.16) thus allowing the range of wall shear rates to be determined. The local power law fitting was conducted in the shear rate range which the fluid was working in to get local power law index. This power law index can be applied to predict the velocity profile of power-law fluids (see Equation 2.28), e.g. xanthan gum solution in laminar regime of pipe flow.

When power law index is 1, the fluid is Newtonian and the velocity profile of laminar flow is parabolic. When power law index is less than 1, the fluid is shear-thinning and the profile of the flow is flatter in the middle and decays faster towards the wall [9]. The overall viscosity data were fitted by Carreau-Yasuda model and the Carreau-Yasuda parameters of the fluid are listed in Table 5.1:

Zero-shear viscosity $\mu_0(Pa.s)$	Infinite-shear viscosity $\mu_\infty(Pa.s)$	Constant representing onset of shear thinning $\lambda_{CY}(s)$	Power-law exponent n	Carreau-Yasuda parameter a
0.8108	0.0033	4.75	0.5379	1.041

Table 5.1: The Carreau-Yasuda parameters for nominal 0.15% xanthan gum solution.

where μ_∞ is the infinity-shear viscosity, μ_0 is the zero-shear viscosity, λ_{CY} is a constant with unit of time, where λ^{-1} is the critical shear rate at which viscosity begins to decrease and a is a parameter introduced by Yasuda *et al.* [174]. As the consequence of the inhomogeneity of shear viscosity in non-Newtonian fluids, the viscosity based on the wall shear stress τ_w is selected to characterize the fluids. The Reynolds number is defined as:

$$Re_w = \frac{\rho U_b D}{\mu_w} \tag{5.1}$$

where ρ is density of the working fluid, U_b is the bulk velocity, D is the diameter of pipe, μ_w represents the viscosity calculated from wall shear stress τ_w in conjunction with Carreau-Yasuda fit.

5.1.2 Pressure-drop measurement

One distinct feature of shear-thinning fluid often observed is the prominent drag reduction in the turbulent flow regime. As a consequence of decreased wall friction, the shear layer near the wall is redistributed and further causes the modification of mean velocity profile [166]. Therefore it is important to investigate the wall fiction when flow asymmetry occurs. For the Newtonian fluids in the Hagen-Poiseuille flow, the relationship between the Fanning friction factor f_F and Re in laminar flow is derived analytically from the Navier-Stokes equation written

in cylindrical coordinates, giving $f_F \cdot Re = 16$. For the fully turbulent flow, the friction is also estimated by Blasius approximation based on Re, assuming that the logarithmic law correlates the local mean velocity across the pipe. When flow is in transitional regime, the dynamics are difficult to predict thus no theoretical solution exists for this Re region for Newtonian fluids. In terms of non-Newtonian fluids, Virk [161] reported the existence of a maximum level of achievable drag reduction of viscoelastic fluids by empirical observation now known as the *Virk asymptote*. Virk's asymptote was obtained for dilute solutions of flexible polymers, since the xanthan gum has a rigid-rod-like molecular structure (largely inelastic), the xanthan gum solution has a less drag-reducing ability compared with that of viscoelastic polymer (very flexible molecular structure) [53]. Virk describes the different regimes for fully-developed turbulent flows. The first regime, named Newtonian regime, experiences no drag reduction and the flow obeys Prandtl-Karman law for Newtonian fluids in turbulent flow. The second regime, named the polymeric regime, relying on the nature of the polymer solution, it starts at a specific onset and is insensitive to concentration of polymer and pipe inner diameter. For comparison purposes, the Zakin-Myska-Chara asymptote [175] is also introduced, which ideally describes the drag-reducing effect of surfactant additives [15].

In the purely laminar regime, the friction data does not rigorously collapse on the $f_F \cdot Re_w = 16$ curve due to the intrinsic difficulties of non-Newtonian fluids. A generalization of the Reynolds number Re_{MR} was proposed by Metzner and Reed [105]. Using the definition of Re_{MR}, a more robust $f_F - Re$ correction is gained for different types and concentration of non-Newtonian fluids in order to reconcile the friction factor regardless of the rheological characteristics of fluids in laminar regime. Therefore a unique $f_F \cdot Re_{MR}$=16 is acquired in laminar flow for various shear-thinning and viscoelastic fluids. The definition of Re_w, Re_{MR} are interrelated by Equation 5.2 in the purely laminar regime [124]:

$$Re_{MR}/Re_w = 8n/(6n+2) \tag{5.2}$$

where n is flow behaviour index of power-law fluids. To be consistent with previous data, Re_w definition is still applied and in conjunction with Equation 5.2, the $f_F - Re_w$ correlation

is modified to $f_F \cdot Re_w$ =19.9 when n=0.508 for 0.15% xanthan gum solution. Figure 5.2 il-

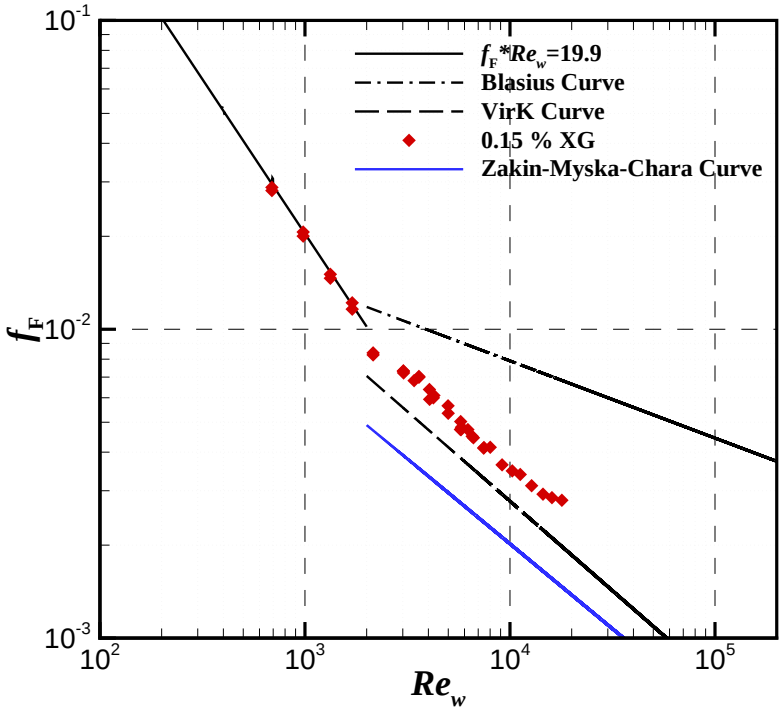

Figure 5.2: The Fanning friction factor f_F against Reynolds number Re_w for 0.15wt% xanthan gum. The red diamond symbols indicate the measured friction factor, the solid black curve represents theoretical prediction $f_F \cdot Re_w = 19.9$ for laminar region, the dot dashed line is the Blasius relationship for friction factor in turbulent pipe flow, the long dashed line shows the Virk asymptote for the maximum drag reduction of shear-thinning fluids.

lustrates the Fanning friction factor f_F against a wide range of Re_w for 0.15% xanthan gum solution. It is generally found a steep increase in f_F occurs at $Re_w \approx 2300$, growing from laminar prediction (on $f_F \cdot Re_w$ =19.9 i.e. $f_F \cdot Re_{MR}$=16 curve) about 0.008 to a turbulent value (on Blasius curve) of 0.011 and this region of increase could be identified as the start of laminar turbulent transition for a practical purpose. For the shear-thinning fluids, in the laminar region ($Re_w < 2300$), the polymer solution didn't manifest significant drag-reducing ability as the long-chain molecular structure of polymer was not stretched at weak shear stress, therefore good agreement is obtained with the analytical friction prediction of Newtonian fluids in the laminar-flow regime using 0.15%wt xanthan gum. However, in the laminar-turbulent transition region, the friction factor of shear-thinning fluids changed smoothly in contrast to the abrupt

change in data observed for Newtonian fluids. Therefore it is difficult to detect the onset of transition in $f_F - Re_w$ plot. When the flow is in turbulent flow regimes, the friction is reduced substantially in comparison with the Blasius prediction of Newtonian fluids due to the dynamical interactions between turbulence and polymers [166], therefore a great drag-reducing ability emerges when Re_w>3000.

5.1.3 Degradation of fluid

Fluid degradation of aqueous solution of xanthan gum is also discussed in following content. This deterioration of fluid primarily results from the mechanical scission and bacteriological influences. The mechanical scission during the mixing or experimental process leads to irreversible changes of rheological properties as the molecular breakage of the polymer [21]. To minimize this undesirable effect, the mixing process was implemented at a very low flow rate and the turbulent flow data was acquired at the final stage of the experiments to minimize the degradation effect on the fluid. Biological degradation may also arise as xanthan gum is a biopolymer. The experiment was conducted shortly after the fluid was uniformly mixed and a suitable amount (at a concentration of 75 ppm) of formaldehyde solution (35% w/w solution) was added to inhibit bacteriological growth. Measurement of the fluid rheology was conducted from various positions in the pipe to check whether the fluid was uniformly mixed.

Continual rheological tests of working fluid were implemented before, during and after the experiments to check the degree of degradation. During the experiment, the working fluid was subjected to a shear stress in flow, which was dependent on the Reynolds number. One of merits of the SPIV experimental technique is to be able to acquire whole-flow-field data in a much shorter time scale than that of single-point, single velocity component LDV technique (approximately one order of magnitude lower), thus the fluid is less affected by mechanical degradation. The whole SPIV experimental duration was approximately 6 hours and the flow was pumped for a few minutes only in the fully turbulent regime at the end of the SPIV measurements. By comparing viscometric flow curves in Figure 5.3, no significant decrease of viscosity was observed

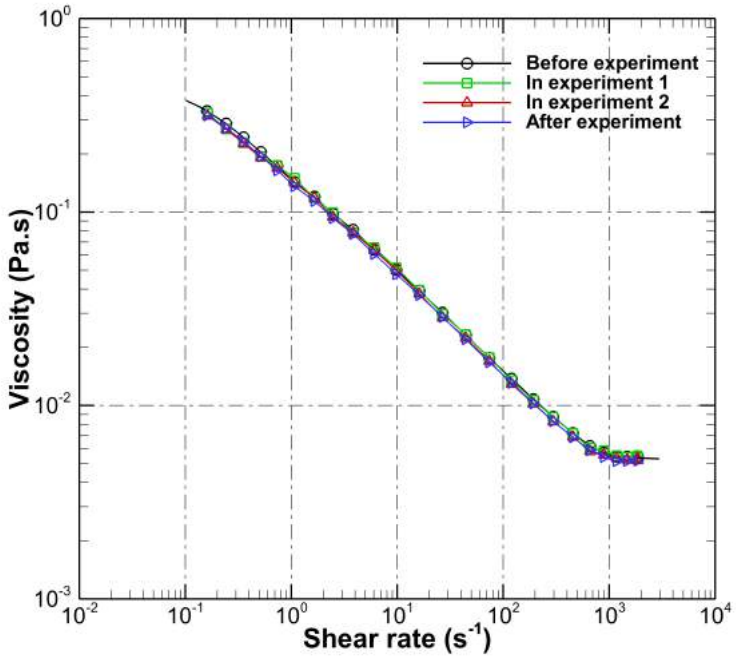

Figure 5.3: Flow curves of aqueous solution of nominal 0.15wt % xanthan gum before, during and after the experiment. The data is fitted by the Carreau-Yasuda model.

before, during and after the experiment for 0.15% xanthan gum solution. This is because the rigid molecular structure of xanthan gum has a good resistance to mechanical degradation and also the fluid was primarily working at the laminar or low Reynolds number transitional regimes thus the stress was unable to break the long molecular chain. Although, no notable decrease of viscosity was discovered, however this mild shear can still degrade the deform the xanthan gum and bring about a decease of its drag-reducing ability. The comparative pressure measurements were conducted before and after the experiment to evaluate the variation of pressure drop over the identical measurement length when the mass flow rate is constant. A slight increase of the pressure drop was observed in the comparative measurements. These comparative measurements were repeated for different independent experiments, the penalty of drag-reducing ability due to shear were generally 3% to 5% of the mean pressure drop which indicates the degree of degradation is not too pronounced.

5.2 Assessments of SPIV accuracy

Since the objects of study in this project are shear-thinning fluids in the vicinity of the transitional flow regime, therefore limited benchmark data, e.g. the DNS data, analytical or empirical data is available to assess the experimental accuracy of the SPIV measurement. The approaches applied in the following are to assess the uncertainty of SPIV data by comparing the data with the analytical velocity profile of power-law fluid in purely laminar flow and previous LDV data at higher Reynolds numbers.

5.2.1 Analytical solution for purely laminar flow

Purely laminar pipe flow is a critical test case to assess the measurement accuracy of the SPIV system, as the flow is stationary and hence all variations in the experiment data are theoretically triggered by the measurement noise. Furthermore, the purely laminar flow only has the streamwise component thus all measured velocities in cross-sectional plane, i.e. $r-\theta$ plane are also attributed to experimental noise. The experimental data were acquired at Re_w=1210, for which the bulk velocity is 0.25 m/s. The mean flow and the *rms* of the velocity fluctuation were obtained from ensemble averaging 1000 successive independent realisations, corresponding to t^*=500. The experimental fluid is nominal 0.15% xanthan gum aqueous solution working approximately at a temperature of 20 degrees.

The asymmetry is primarily manifested in the streamwise velocity profile, thus the accuracy in the axial velocity component is particularly important. The velocity profile in pipe is parabolic for Newtonian liquids. For the power-law fluids, this is modified to [9]:

$$u(r) = \frac{\dot{Q}(3n+1)}{\pi R^2(n+1)}\left(1-(\frac{r}{R})^{(n+1)/n}\right) \tag{5.3}$$

where $\dot{Q}$ is volumetric flow rate, n is power law index and R is the radius of pipe. When n=1, the velocity profile described in Equation 5.3 regresses to the parabolic. In terms of the shear-thinning fluids where $n<1$, progressively decreasing the power law index, i.e. increasing the degree of shear thinning results in the increasing plug-like nature of the velocity profile. Fig-

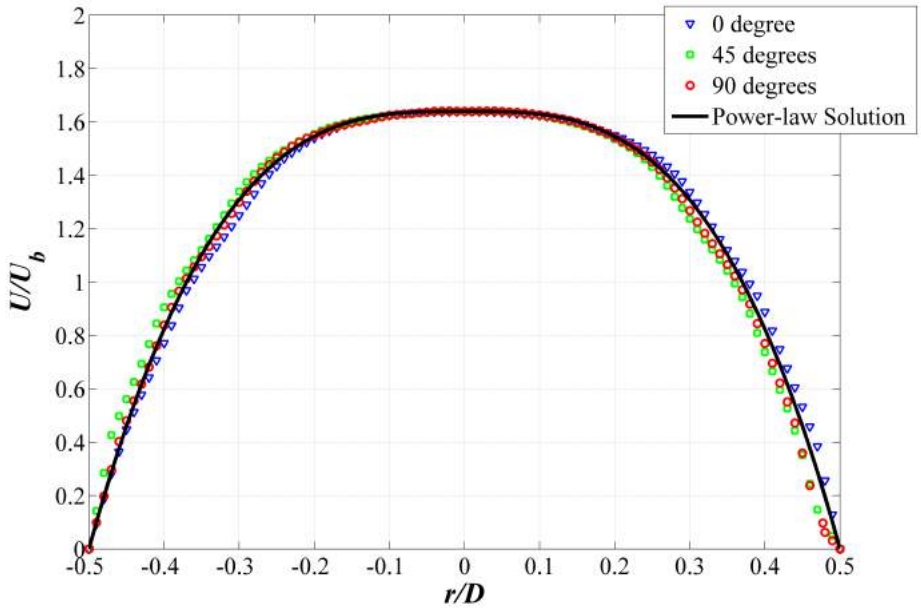

Figure 5.4: Time-averaged velocity profiles at different azimuth angles in cross-sectional plane at Re_w=1210 for 0.15% xanthan gum solution. The solid curve represents the analytical prediction of power-law fluids in pipe flow, see Equation 5.3, 0 degree indicates the horizontal plane which crosses pipe centre, 90 degrees is the vertical plane which crosses pipe centre. The azimuthal angle is defined in counter-clockwise direction.

ure 5.4 demonstrates the mean axial velocity profiles selected at horizontal (0 degree), vertical (90 degrees) and 45^o inclined plane in the purely laminar regime of shear-thinning fluids. The velocity profiles all exhibit axisymmetry and the normalized peak velocity at the pipe centre is lower than that of Newtonian fluids as described in Equation 5.3. The experimental data is compared with analytical velocity profile of power law fluids in laminar flow. The measured velocity profile agrees well with theoretical solution of laminar flow especially in the pipe central region, where r/D <0.4. A discrepancy is noticeable near the wall, this is due to the observation of asymmetry demands a large field of view and thus sacrifices good resolution near the wall. However, the spatial resolution near the pipe wall is not crucial in this project as the interest of the current study is flow asymmetry, and the peak velocity of asymmetry primarily occurs in the region of r/D <0.25, in which a good accuracy is achieved in the SPIV measurement. Therefore, the resolution near the pipe wall is acceptable for experimental purpose of observing the asymmetry.

5.2.2 Comparison with previous LDV data

Besides the analytical solution for purely laminar flow, previous LDV data also provides the benchmark in order to access the experimental accuracy across extended flow regimes. Since LDV only gives pointwise flow information, many individual measurement points are required to generate a full velocity profile in LDV and thus the acquisition time to take a mean velocity profile is generally an order of magnitude higher than that of SPIV. Figure 5.5 gives the compar-

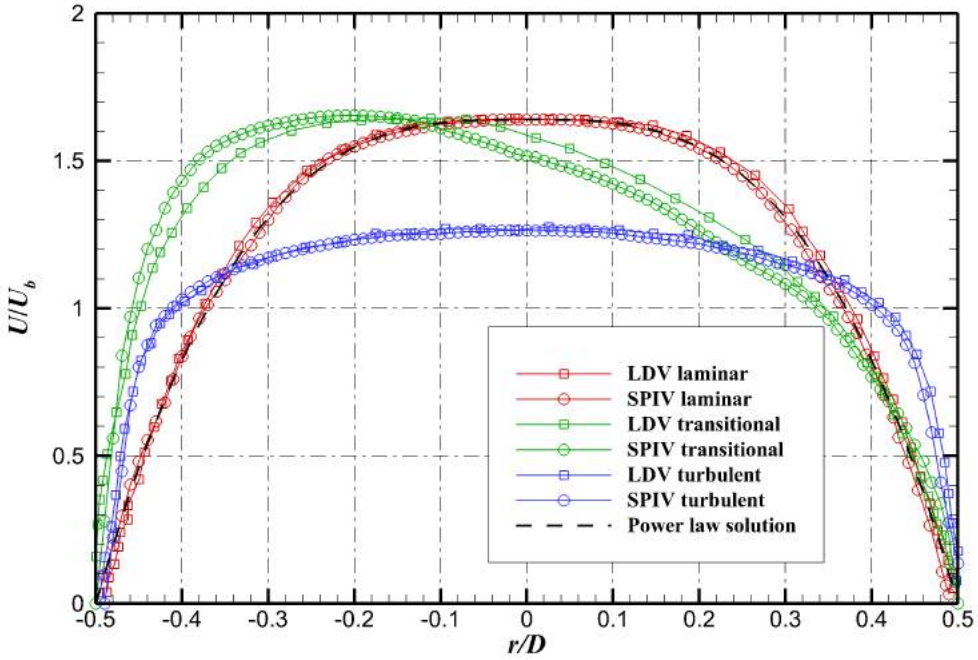

Figure 5.5: Comparison between existing LDV measurements [54] and current SPIV measured velocity distributions for 0.15% xanthan gum solution. The red symbols indicate the velocity profile in laminar regime for SPIV (Re_w ≈1210) and LDV (Re_w ≈1330), the blue symbols represent the velocity profile in fully turbulent regime for SPIV (Re_w ≈15780) and LDV (Re_w ≈16020), the green symbols show the velocity profile in transitional regime for SPIV (Re_w ≈ 7939) and LDV (Re_w ≈10260), the black dashed line indicates the analytical prediction of laminar velocity profile, the power law index is 0.50 for SPIV data and 0.48 for LDV data, n=0.50 is adopted to generate the analytical velocity profile.

ison between horizontal velocity profiles using LDV and SPIV for purely laminar ($Re_w \approx 1210$), transitional ($Re_w \approx 8330$) and fully turbulent ($Re_w \approx 16020$) flow, respectively. The LDV data was extracted from the experimental work of Escudier *et al.* (2009) [54]. Due to the opposite

definition of x positive axis (x represents the streamwise direction), i.e. x_{LDV} = - x_{SPIV} in coordinate system, the x axis in LDV data is flipped to agree with the SPIV reference frame. The detailed definition of coordinate system in the LDV data is provided in [137].

For laminar regime, the analytical velocity profile of power law fluids is presented in dashed black curve to assess the experimental data. In purely laminar and turbulent regime, the time-averaged LDV and SPIV velocity profiles both show axisymmetry thus the selection of the azimuthal angle of sectional plane does not affect the velocity profile significantly. The LDV and SPIV data are in good agreement and further validated by theoretical prediction for laminar velocity profile. However, a difference is perceptible in the transitional regime. The causes of discrepancy could lie in the time-varying nature of the asymmetry (see subsection 5.3.3) when flow is in the vicinity of the transitional regime. Although the asymmetry prefers to stay in the favoured azimuthal position, a slight alternation of the preferential orientation of asymmetry between the LDV and SPIV measurements will result in a noticeable discrepancy of the velocity profile in the horizontal sectional plane. Another possible cause of the discrepancy particularly in the transition is the Re_w effect. In comparison with the LDV result ($Re_w \approx 10260$), current SPIV dataset were primarily conducted at a lower transitional Reynolds number, which is $Re_w \approx 7939$. Therefore, direct comparison between the LDV and SPIV in certain azimuthal angle is not strictly possible, but still provides a general assessment of the SPIV data accuracy.

Figure 5.6 shows the effect of the selection of velocity profile in different azimuthal angles when flow is in the transitional regime. Figure 5.6 (b) illustrates the contour of normalized streamwise velocity at $Re_w \approx 7939$. It was obtained by taking the ensemble average of 21 datasets thus a total of 21000 realizations of the instantaneous velocity field were acquired (the overall experimental time is accordingly approximately 60 minutes) to minimize the effect of different test duration between LDV and SPIV. The velocity contour gives a complete two-dimensional velocity distribution in the cross-sectional plane illustrating the asymmetry appears in the preferred azimuthal position with a normalized peak velocity approximately $U/U_b \approx 1.6$. The blue, green and red lines indicate the selected one-dimensional velocity profile in compar-

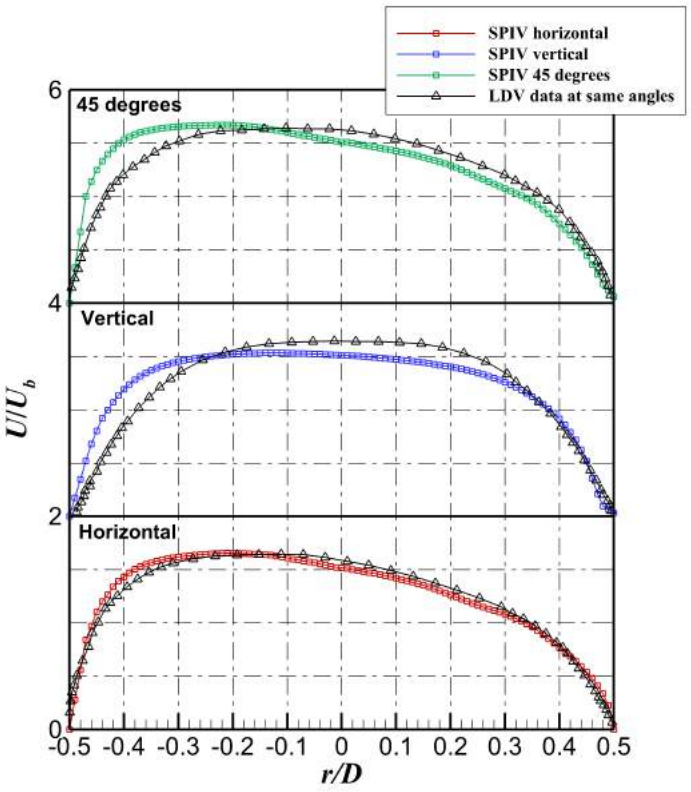

(a) Velocity profiles at different azimuthal angles

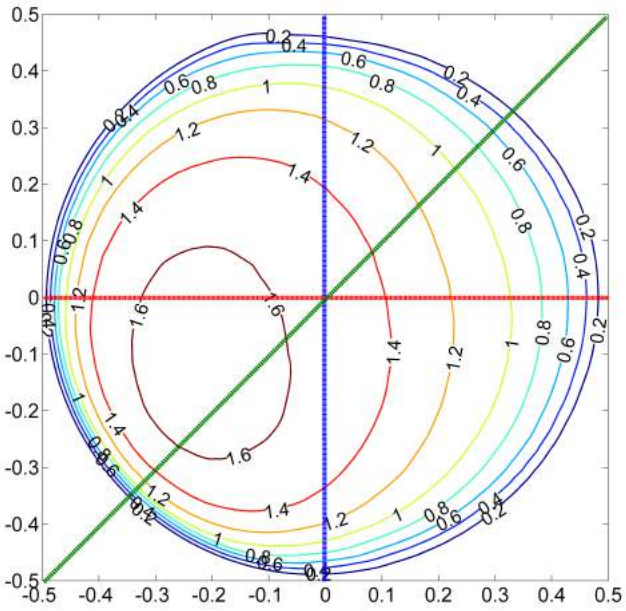

(b) Contour of axial velocity component in cross-sectional plane of pipe

Figure 5.6: Comparison between existing LDV measurements [54] (Re_w≈10260) and current SPIV measured velocity distributions (Re_w≈7939) for 0.15% xanthan gum solution in transtional regime.

ison with existing LDV data [54] shown in Figure 5.6 (a). The SPIV data has a good agreement with the LDV data at certain azimuthal angle i.e. in horizontal plane, however, the apparent discrepancy is observed at vertical and 45^{o} inclined slice. This could be explained by the preferential azimuthal position of asymmetry in SPIV data alters in contrast with that in LDV, resulting in the difference in one dimensional comparison. However, the biased velocity profile in Figure 5.6 (a) shows the similar distortion trend i.e. skewing to similar position in cross-sectional plane ($r-\theta$ plane), demonstrating the asymmetry shows analogous azimuthal location in LDV and SPIV experiments. This discrepancy actually reveals the non-stationary characteristics of flow asymmetry, i.e. the slight change of the favoured asymmetry position rather than the experimental accuracy as this discrepancy could be reconciled by slightly shifting the azimuthal angle of the velocity profile.

5.2.3 Comparison with mass flowmeter

Since the SPIV is capable of obtaining the whole-flow-field velocity vectors in the cross-sectional plane, it provides another approach to assess the experimental data accuracy by comparing the calculated mass flow rate from SPIV with the readings from the mass flow meter. The calculated mass flow rate is acquired by integrating the velocity vector over the entire cross-sectional plane in the pipe, indicated by the Equation 5.4

$$\dot{m} = \oint \rho \cdot U \cdot dA \tag{5.4}$$

where U represents the local streamwise velocity, ρ is the fluid density and dA represents the integral area in cross-sectional plane. The advantage of this approach is to enable us to assess the overall experimental accuracy over the whole flow field rather than a certain slice and the estimation of accuracy for the streamwise velocity component is of much importance as the streamwise velocity is most pertinent to the flow asymmetry. Figure 5.7 shows a time series of mass flow rate between the reading given by mass flow meter and calculated mass flow rate using integral of the SPIV axial velocity. In the transitional regime, as the flow is characterized by a remarkable time-varying nature resulting in the discrepancy in velocity profile when

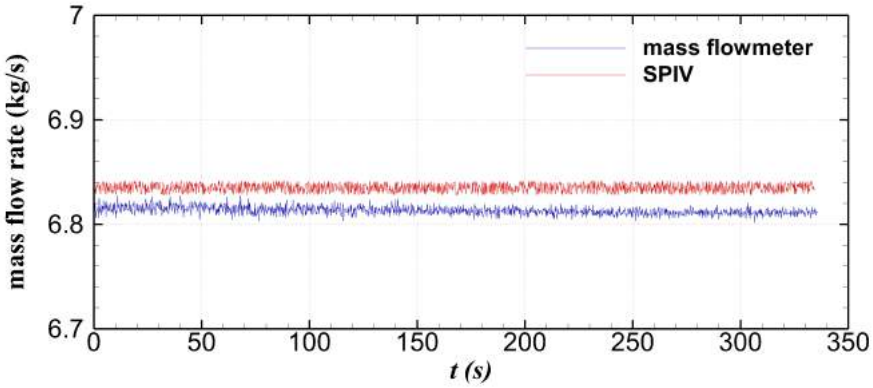

Figure 5.7: Comparison of mass flow rate obtained from mass flowmeter and SPIV velocity intergral when the flow is in the transitional regime at $Re_w \approx 7939$.

comparing to that with LDV data at certain cross-sectional plane, therefore, this flow regime is selected in to further examine the validation of experimental data. The mass flow rate is calculated due to the convenience that it is an invariant despite of instantaneous flow pattern and this conservativeness contributes to validating the data in the scale of the whole cross-sectional plane globally. The calculated mass flow rate reasonably agrees with readings from mass flow meter (with the resolution of $0.025 kg/s$) but is systematically lower (approximately 1.4% below) than the readings from mass flow meter. The systematic deviation arises from the fact that SPIV cannot provide a refined spatial resolution near the pipe wall when the field of camera's view is the entire circular cross-section, thus a linear interpolation is used to process the velocity data in the near wall region (5% of the pipe radius close to the wall) which can account for this error. Well-resolved measurement near the pipe wall is less pertinent to this project as the asymmetry primarily features the flow in central region of the pipe and the reasonably matched mass flow rate data indicates a good experimental accuracy in the overall cross-sectional plane of pipe. Furthermore, when the flow pattern changes, e.g. the location of asymmetry alters, the SPIV measured mass flow rate still approximately keep a constant, verifying the reliability of the SPIV measurement.

5.3 Symmetric and asymmetric flow patterns

This section presents the time-averaged velocity profiles for purely laminar, transitional and fully turbulent regimes, respectively. Particular attention is given to the transitional regime to characterize asymmetry in time.

5.3.1 Asymmetry parameter

An asymmetry parameter α is introduced to quantify the degree of azimuthal flow asymmetry and reveal how the asymmetry develops with streamwise distance along the pipe. The parameter is defined as:

$$\alpha = \frac{\int_0^R \int_0^{2\pi} |u(r,\theta) - u_M(r)| \cdot r \cdot d\theta \cdot dr}{\int_0^R u_M(r) \cdot 2\pi r \cdot dr} \tag{5.5}$$

where u_M is the arithmetic mean of the streamwise velocity u at the same specified radial location r along the circumference direction defined as below:

$$u_M(r) = \frac{\int_0^{2\pi} u(r,\theta) \cdot d\theta \cdot r}{2\pi r} \tag{5.6}$$

The velocity integral is weighted by $2\pi r$ such that the flow rate can be considered from the physical perspective. The u_M in Equation 5.6 is actually linked with volumetric flow rate if the axial velocity profile is perfectly axisymmetric.

5.3.2 Time-averaged velocity profiles

Previous studies regarding the asymmetry mainly focussed on the description of the time-averaged streamwise velocity profile by means of LDV. The LDV data was generally collected in hours to produce the time-averaged velocity profile (it took 3 to 4 hours to generate a velocity profile consisting of 50 probing points at a certain Reynolds number using LDV in experimental work of Escudier *et al.* [54]). In the current SPIV study, a frame rate of 5Hz is used to compare with LDV, and the corresponding dimensionless acquisition time $t^* \approx 1720$ (dimensional time

is 200s) when the flow is in the laminar-turbulent transition regime at $Re_w \approx 7939$. Figure 5.8 shows the time-averaged axial velocity profiles at different Reynolds numbers. The flow patterns from the SPIV data present axisymmetric velocity profiles for both laminar ($\alpha \approx 0.021$, the definition of asymmetry indicator α is in Equation 5.5, $Re_w \approx 990$) and turbulent flow ($\alpha \approx 0.047$, $Re_w \approx 14720$) and a significant departure from axisymmetry is observed when flow is in the transitional regime ($\alpha \approx 0.157$, $Re_w \approx 7939$). This is consistent with observations from previous LDV data but the novel SPIV data here provides a three-dimensional view of the asymmetrical flow pattern. In a single run of camera recording, 1000 successive pairs of PIV images can be obtained. For a good statistical convergence purpose, 21 repeated runs were implemented at the same flow condition thus a total of 21000 realizations of the instantaneous velocity field were acquired (the according overall experimental duration is approximately 60 minutes). Intriguingly, the asymmetry prefers to stay in a certain azimuthal location in $r-\theta$ plane in all of the datasets tested. The ensemble average of all the SPIV experimental datasets validates the existing LDV results and confirms the asymmetry in the transitional regime.

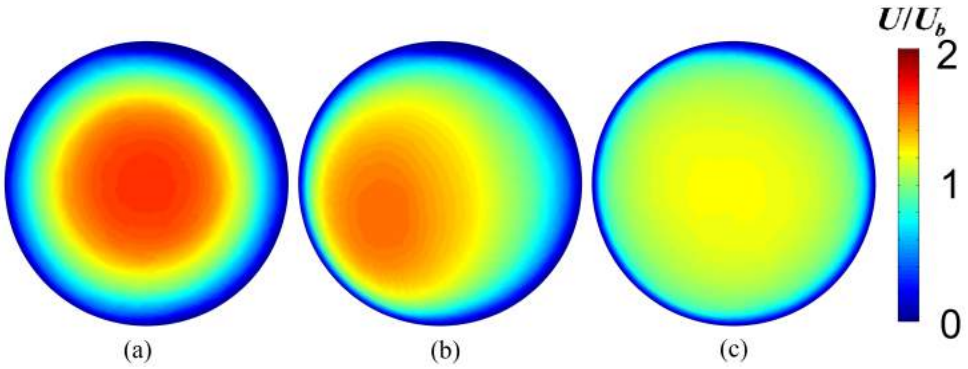

Figure 5.8: Time-averaged streamwise velocity profile normalized by bulk velocity for laminar (a), transitional (b) and turbulent (c) flow regime, respectively.

5.3.3 Time-varying nature of asymmetry

One of the major insights provided by our SPIV measurements in comparison to all other previous work is the time-varying behaviour of the asymmetric flow pattern, which was hitherto considered stationary. The general consensus of previous LDV experiments was that, for the

asymmetric flow pattern, the location of the peak velocity remained at a fixed point in space. This agrees with our new experimental data to some degree since the time-averaged SPIV velocity profile also reveals the asymmetry pattern prefers to stay a certain location in $r-\theta$ plane after a long time averaging, however we found this asymmetry is indeed not stationary. This conclusion is supported by a direct numerical simulation of pipe flow using power-law model suggested by Rudman *et al.* [139]. The authors wrote "*active region of the flow continually moves along the pipe and appears to preferentially occur at one azimuthal location for extended times, so that the average velocity profile shows some asymmetry*". However, in their work, due to the limitation of computational effort, the mean asymmetric velocity profile was estimated approximately in the domain of 100 pipe diameters (i.e. t^*=100) and the authors observed the asymmetry by extracting the contours of instantaneous axial velocity but did not give a comprehensive description of the asymmetry.

The following will provide experimental evidence of the time-varying nature of the asymmetry and attempt to give a more clear scenario about the asymmetry in contrast with the DNS conclusion. The experiments were repeatedly concluded in the transitional regime ($Re_w \approx 7939$). The dimensionless time t^* for one single run was roughly 1720 and 1000 successive velocity vector maps were obtained. The time history of the asymmetry factor and selected instantaneous velocity profiles are presented in Figure 5.9. The variation of asymmetry factor clearly indicates the flow pattern is not stationary, although the asymmetry preferentially appears in certain azimuthal position. When the asymmetry is very pronounced (indicated by a higher asymmetry factor $\alpha \approx 0.22$), the instantaneous flow pattern (Figure 5.9a) is similar to the time-averaged flow pattern (Figure 5.8b). This flow pattern dominates the flow in the vast majority of observation instances and therefore has a significant influence on the asymmetric time-averaged velocity profile. Some small amplitude fluctuation of the asymmetry factor α can be observed, for example, that in time domain $t^* = 100 \sim 300$. Physically, the asymmetric flow pattern slightly fluctuates around the favoured asymmetry position in the circumferential direction. The small amplitude fluctuation is essentially different from the flow event which is shown in Figure 5.9

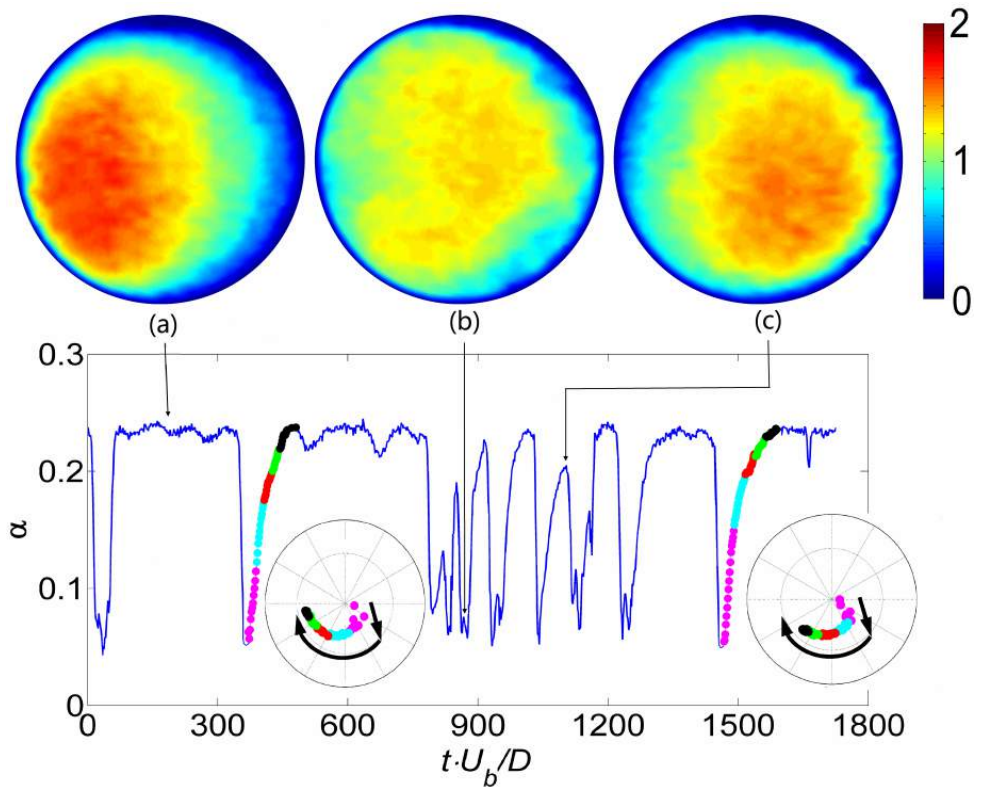

Figure 5.9: The time-varying nature of the asymmetric flow pattern at $Re_w \approx 8000$ is shown by the time history of asymmetry factor, α (bottom) and instantaneous cross-stream snapshots of the streamwise velocity (U/U_b). (a) asymmetric flow with preferred orientation, (b) temporarily axisymmetric flow induced by a turbulent puff, and (c) a brief visit to asymmetric flow with an alternative orientation. The experimental duration is approximately 200s and the SPIV acquisition rate is 5Hz. The two insets show the location of the peak velocity in the radial-azimuthal plane as the asymmetry returns following the passing of a puff.

(b), where the asymmetry factor abruptly drops to a low value, indicating that the flow is briefly returning to a quasi-axisymmetric state. In Figure 5.9 (b), the instantaneous velocity presents the "breakdown" of this asymmetry and clearly flow is restored to more axisymmetric pattern instantaneously. The time scale of asymmetry to axisymmetry transition is comparatively short with a dimensionless time scale $t^* \approx 10$. Applying Taylor hypothesis [36, 111] to transfer the flow event from time domain to space domain, it implies the asymmetry disappears in a spatial scale of $\approx$10 pipe diameters and in this domain, the flow is characterized by a strong random turbulent velocity fluctuation.

Although the asymmetric flow pattern is most commonly observed in this orientation, there are numerous brief instances when the orientation is different. One example is indicated in

Figure 5.9 (c). This is from an instance when the flow is returning to asymmetry after the passing of a turbulent puff. This flow pattern is commonly seen that immediately following a puff, the asymmetry reappears in a different orientation and then slowly rotates to its preferred location as shown in the insets in Figure 5.9. The color-coded inset plot and time history of the asymmetry factor α show the path in the $r-\theta$ plane that the asymmetry takes to reach its favoured orientation at $Re_w \approx 8000$. Each dot corresponds to an instant in time and colour-coded by the even time interval in this process. Interestingly, a favoured symmetry to asymmetry transition path is observed. The asymmetry moves outward from the centre of the pipe and then rotates to its preferred azimuthal location along an approximately constant radius. These results clearly reveal the time-varying nature of asymmetry and provide new insight in this poorly understood phenomenon.

The above-mentioned experimental conclusion is drawn from the data computed at a low sampling rate at 5Hz (dimensionless time t^* spacing is 1.7, i.e. the space interval between two laser frames is 1.7 pipe diameter). This low sampling rate result gives a general perspective of flow characteristics of asymmetry over a long time scale. In the following section, we will extract some distinct flow events from this long time scale result and implemented some SPIV experiments at a high sampling rate at 100 and 200 Hz, therefore we can investigate these flow events in a time-resolved manner.

5.4 Observation of turbulent structures

5.4.1 Elimination of asymmetry

A distinguishing flow feature in the laminar-turbulent transition regime in Newtonian fluids is the existence of turbulent puffs and slugs [172]. With regard to the flow asymmetry, the given LDV experimental evidence [54, 64, 69] suggest the asymmetry is absent in the purely laminar and fully turbulent flow regimes while it uniquely exists in the laminar-turbulent transition, therefore, it is natural to speculate that turbulent puffs may be relevant to the asymmetry,

although how the turbulent puffs affect the asymmetry is unknown. The general speculation based on the previous experiments was that the asymmetric mean velocity profiles are produced by some particular asymmetric flow structure in the transitional regime or due to the turbulent puffs [64]. Esmael *et al.* (2008, 2010) [55, 56] suggest this asymmetric velocity profile is the consequence of the fast and low speed streaks and these streaks imply the existence of a coherent structure characterized by two counter-rotating longitudinal vortices. In the work of Esmael *et al.* (2010) [56] and Bahran *et al.* (2014) [6], frequency power spectra of the axial velocity fluctuations were also calculated at r/D=0.7 for a flow rate where asymmetry appears. Multiple spatial and temporal scales were observed in the spectra analysis and this multiplicity is a typical feature of turbulence but the authors conclude it is a weak turbulence which is chaotic in time and regular in space.

In the following, we show a SPIV investigation of the asymmetric to axisymmetric transition process to give a new insight into this phenomenon. The preceding SPIV studies in subsection 5.3 were conducted at a low frame rate. In these long time scale studies, the asymmetry to axisymmetry transition process were already observed but the experimental data was acquired in low time resolution (t^* spacing is 1.7). To extract transitional events and further investigate them, the time-resolved SPIV experiments were implemented in the temporal interval of 0.01s and 0.005s (t^*=0.085 and 0.0425). Since the velocity fluctuation is generally one order of magnitude lower than the streamwise convection speed and, also the time interval is very small, the three-dimensional flow structure could be well reconstructed in this refined time resolution using Taylor's hypothesis [36]. We attempt to characterize the turbulent puff in three dimensionality based on our SPIV velocity vector field. Physically, the turbulent puff can be interpreted as an isolated patch of turbulent flow embedded into the laminar flow. With increasing Reynolds number, the turbulent puffs will grow in size and eventually these separate turbulent puffs merge into an extensive region of turbulence, i.e. a slug. When the flow is saturated with these turbulent puffs, the flow becomes fully turbulent. Since puffs emerge irregularly in time and at arbitrary positions, to study the impact of turbulent puffs to flow asymmetry, we need to

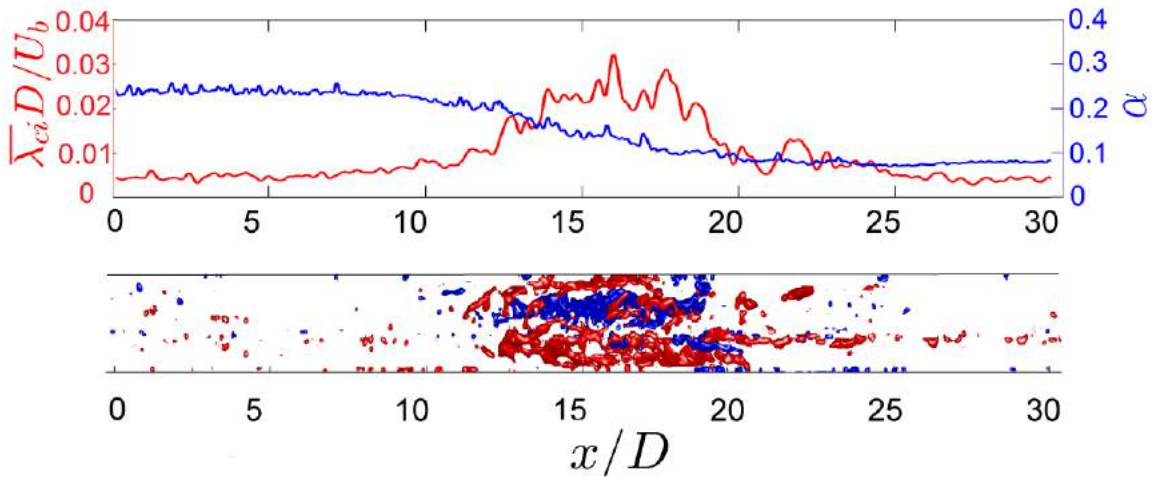

Figure 5.10: The temporary elimination of the asymmetry by a turbulent puff at $Re_w \approx 8000$. The top panel shows simultaneous time histories of the non-dimensional swirling strength and the asymmetry factor (α). The bottom panel shows a visualization of puff using iso-surfaces of swirling strength ($\overline{\lambda_{ci}}D/U_b$=0.012); red and blue indicate regions on the iso-surface where the local axial vorticity is positive and negative respectively. The SPIV acquisition rate is 200Hz.

identify these puffs so that we can distinguish whether the flow is laminar or turbulent and how the corresponding degree of flow asymmetry varies when the flow is intermittent. The turbulent puff is characterized by the unsteady vortices on many scales, therefore the vortex identification method is applied in the work to capture the turbulent puffs.

The vortex identification criteria employed here is swirling strength criterion proposed by Zhou *et al.* [177]. The vortex identification criteria is based on the kinematics indicated by the velocity gradient tensor, $\nabla \cdot \boldsymbol{v}$. In three dimensions, the local $\nabla \cdot \boldsymbol{v}$ has one real eigenvalue (λ_r) and a pair of complex conjugate eigenvalues ($\lambda_{cr} \pm i\lambda_{ci}$) if the discriminant of the characteristic equation is positive (see [2, 22, 43]). The swirling strength of the vortex is identified by the imaginary part of the complex conjugate eigenvalue of $\nabla \boldsymbol{v}$, i.e. λ_{ci}, and λ_r exhibits a swirling, spiral motion of the vortex. The swirling direction of the vortex can be determined with the help of the vorticity $\boldsymbol{w}$, where $\boldsymbol{w}=\nabla \times \boldsymbol{v}$. To visualize the turbulent puffs, the three-dimensional iso-surface of swirl strength λ_{ci} is used and the opposite rotation direction of the vortex is indicated by the sign of axial $\boldsymbol{w}$. Therefore, using this vortex identification, we achieve an extraction of the three-dimensional vortex structure of a turbulent puff from 3D velocity vector fields.

Figure 5.10 reveals the asymmetric to axisymmetric transition process and how the turbulent puff affects the flow. The turbulent puff is characterized by vortical structures therefore is visualized by the iso-value of the swirling strength in a three-dimensional plot using the λ_{ci} vortex identification criterion, see subsection 5.4.1. The time history of the asymmetry factor α and swirling strength $\overline{\lambda_{ci}}D/U_b$ are plotted simultaneously. The bottom plot in Figure 5.10 shows the scenario that a turbulent puff is propagating in the laminar base flow. The turbulent puff is essentially an isolated turbulent region characterized by a strong velocity fluctuation [62], therefore, a peak value of swirling strength is observed in the turbulent puff region.

The asymmetry factor clearly decreases in the turbulent puff region. The higher asymmetry factor ($\alpha \approx 0.23$) before the turbulent puff indicates the flow is already substantially asymmetric. This asymmetric state characterizes the flow in a long time scale until the appearance of turbulent puff as seen in subsection 5.3.3. In the turbulent puff region, the asymmetry factor is reduced, indicating the flow is restored into a more axisymmetric state. It can be interpreted as the turbulent dynamics dominate the flow in the puff and the substantial fluctuations break the asymmetric flow pattern and restore it to axisymmetry. The spatial scale of the puff is of the order of 10 pipe diameters, which agrees reasonably with the dimensionless time scale t^* of asymmetry to axisymmetry transition process shown in Figure 5.9. It further demonstrates the turbulent puff is responsible for restoring the flow into axisymmetry rather than the previous common speculation that the asymmetry is caused by asymmetric structures in the laminar-turbulent transition regime. Although the turbulent puff intermittently appears at arbitrary locations in the pipe, it should be noted that with increasing Reynolds number, the turbulent puff grows in size and merges with neighbouring puffs into larger turbulent region and eventually the flow reaches the fully turbulent state. Therefore, the turbulent puffs could be interpreted as the building block to form the fully turbulent flow, i.e. the flow becomes fully turbulent once it is saturated with turbulent puffs. This explains the reason why in the fully turbulent flow no asymmetry was observed, since the fully turbulent flow can be interpreted as the flow which is saturated with turbulent puffs and the flow recovers to axisymmetry due to the

turbulence.

Figure 5.11 presents streamwise velocity and velocity vectors in the $r-\theta$ plane when the turbulent puff appears ($Re_w \approx 7939$). The velocity components in the $r-\theta$ plane are an order of magnitude smaller than the axial velocity component, therefore a refined spatial resolution is vital to capture this secondary flow. These three-dimensional velocity vector fields provide another perspective to interpret the effect of the turbulent puff on the asymmetry-axisymmetry transition process. Figure 5.11 (a) shows contour plots of the streamwise velocity component and corresponding velocity in-plane vectors upstream of the puff. The position of the peak axial velocity manifests a clear departure from centre of pipe and the instantaneous velocity distribution is similar to that in the long time average as shown in Figure 5.8 (b). The in-plane velocity vectors do not exhibit a distinct secondary flow pattern and the magnitude of the velocity vector is relatively small compared with that in Figure 5.11 (b) when instantaneous velocity field was selected inside the turbulent puff. The presence of swirling motion and strong streamwise velocity fluctuation characterizes the flow in the turbulent puff. The strong turbulent motion breaks the asymmetry and yields a more axisymmetric axial velocity distribution, which intuitively illustrates the turbulent puff is in fact responsible for asymmetry to axisymmetry transition process. The velocity vector fields after the turbulent puff are displayed in Figure

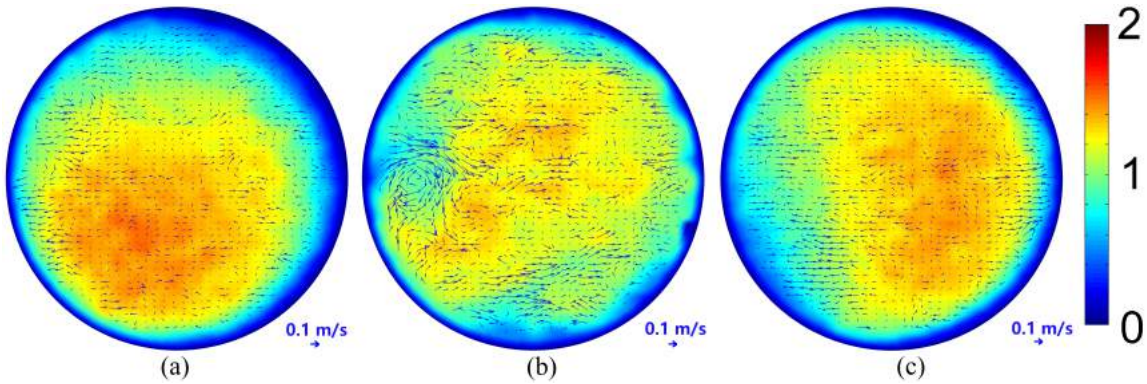

Figure 5.11: Cross sections of instantaneous velocity field in transitional regime ($Re_w \approx 7939$). (a) upstream of turbulent puff, (b) in turbulent puff, (c) downstream of turbulent puff. The normalized axial component is colour coded, the velocity components in $r-\theta$ plane are indicated by arrows. The reference length of velocity arrows, physically equivalent to 0.1 m/s, is plotted when the bulk velocity U_b is 0.86 m/s.

5.11 (c). The axial location was selected at 100 pipe diameter downstream of the puff and obvious asymmetric streamwise velocity distribution reappears without existence of distinct in-plane vortex. The asymmetric flow pattern was observed to become re-formed in an alternative azimuthal position and then eventually moves back to the favoured asymmetry location along a preferential path as in Figure 5.9 (c).

It is notable that the aforementioned experimental observations were captured in the laminar-turbulent transition regime ($Re_w \approx 8000$) where a remarkable asymmetry already excited. To study the mechanism leading to the onset of asymmetry, it is requisite to extend the experimental investigations to a broad *Re* range, which covers from purely laminar state to fully turbulent state thus showing how the asymmetry arises and develops.

5.4.2 Puff frequency in transitional regime

In this subsection, we will examine the puff frequency for different Reynolds numbers. One significant characteristic of transitional flow is the occurrence of intermittent laminar and turbulent puffs. Wygnanski & Champagne [172, 173] reported the characteristics of turbulent puffs: the *rms* of axial velocity fluctuation and swirling strength within a puff is much stronger than that of the laminar base flow and in the interior of the puff the flow physics are characterized as a fully turbulent flow. The axial extent of a individual puff is approximately $10-40D$. For larger *Re*, the puffs begin merging/splitting and the fully turbulent flow will form with increasing *Re*. These flow features of puffs and slugs are independent of how the transition is triggered and boundary condition (e.g. the diameter of the pipe), it is only determined by the Reynolds number. The puff frequency can be indicated by intermittency factor (denoted as IF) of the flow. The intermittency factor is defined by the ratio of the time of turbulent puff in the observation to the total time of the observation, see Equation 5.7.

$$\mathrm{IF} = \frac{\text{time of turbulent puff}}{\text{time of experiment}} \tag{5.7}$$

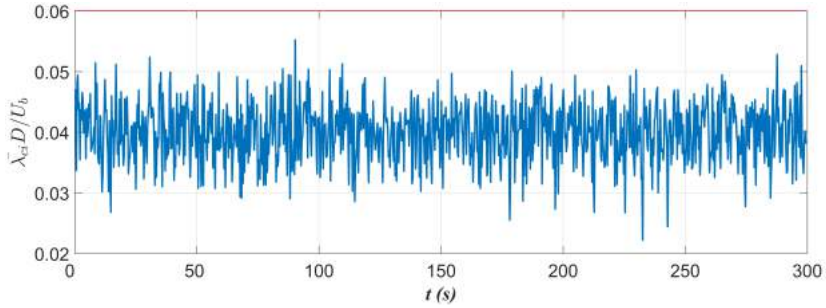

(a) Re_w≈6539, laminar

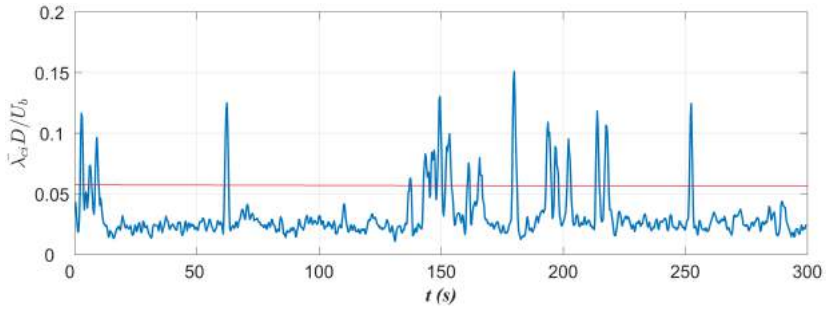

(b) Re_w≈7450, transitional

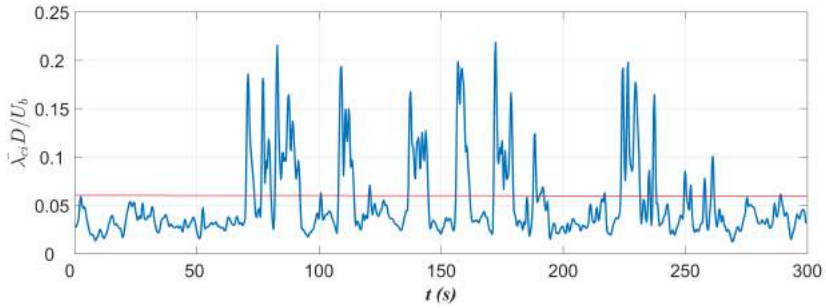

(c) Re_w≈7939, transitional

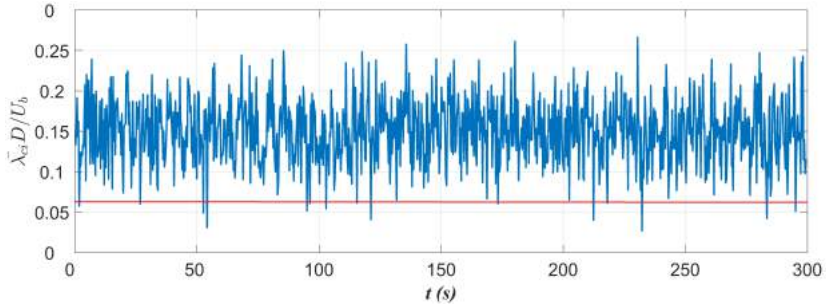

(d) Re_w≈14720, turbulent

Figure 5.12: The simultaneous time histories of the non-dimensional swirling strength for high laminar Reynolds number (Re_w≈6539), transitional regime (Re_w≈7450 and 7939) and turbulent regime (Re_w≈14720). The red solid line indicates the threshold ($\overline{\lambda_{ci}}D/U_b$=0.06) to identify the turbulent puffs.

therefore the intermittency factor (IF) can indicate the degree of intermittency for different Reynolds numbers.

Figure 5.12 shows the time series of the swirling strength $\overline{\lambda_{ci}}D/U_b$ when flow is in laminar, transitional and turbulent regimes. When the flow is in the laminar regime (Re_w≈6539), the time series of swirling strength is random but with a low time-averaged swirling strength $\overline{\lambda_{ci}}D/U_b$ (mean $\overline{\lambda_{ci}}D/U_b \approx 0.04$), indicating there is no pronounced turbulent vortical structures i.e. no turbulent puffs observed. In the transitional regime (Re_w≈7450, 7939), when the turbulent puffs passed through the measurement plane, the swirling strength $\overline{\lambda_{ci}}D/U_b$ increased dramatically as shown in Figure 5.12 (b). The puff frequency increased with the increasing Reynolds number in transitional regime as displayed in Figure 5.12 (c). When the flow is in the fully turbulent regime, the swirling strength returns to a random state, however, compared with the case in laminar regime, the averaged value of swirling strength is much higher, approximately $\overline{\lambda_{ci}}D/U_b \approx 0.15$, implying the turbulence can be interpreted to be composed of numerous turbulent puffs.

The puff frequency or the intermittency factor is plotted in Figure 5.13. To identify the turbulent puff, we set the threshold of swirling strength to be 0.06 in the time series of swirling strength (see the red line in Figure 5.12), i.e. the time portion when swirling strength is greater than 0.06 is detected as turbulent puff. When the Reynolds number is 7450, the flow is in the transitional regime and with higher Reynolds number 7939, more turbulent events were identified and the puff frequency increased as shown in Figure 5.13.

5.4.3 Transition detection using LDV

This subsection provides some supplementary data, which attempts to detect transition using LDV system. It was implemented in the beginning of project, as the Reynolds number for laminar-turbulent transition using shear-thinning fluid (0.15% xanthan gum solution) is initially unknown and needs to be estimated. To detect the transition, the characteristics of high velocity/pressure fluctuation at the interface of puffs and slugs could be utilized. Based on this feature, two measurement techniques are available: the quick response pressure transducer or

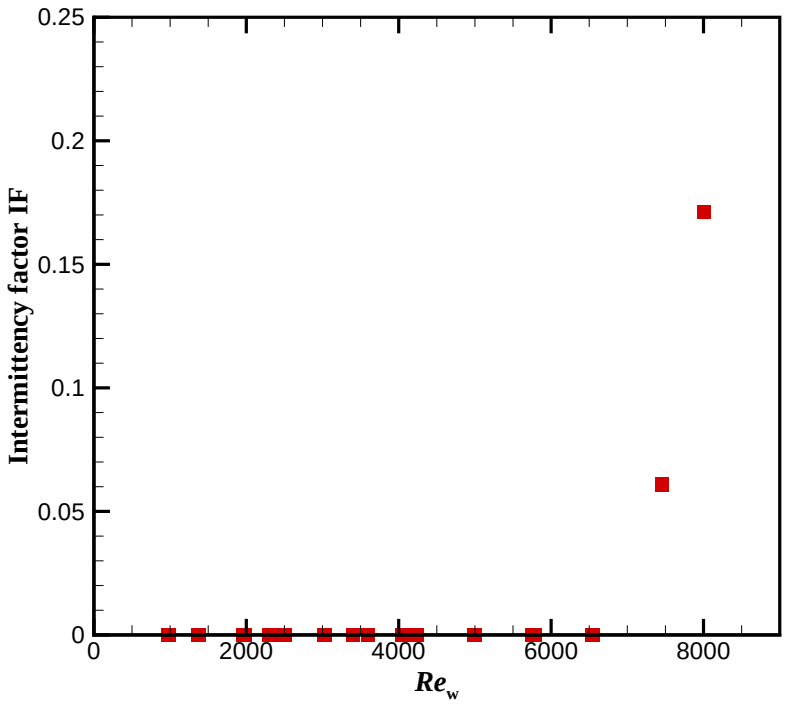

Figure 5.13: The intermittency factors for a range of Reynolds numbers, showing the puff frequency increase with increasing Reynolds number.

LDV measurement. For both techniques, they are sufficient to capture the evident fluctuations, no matter velocity or pressure fluctuation, to detect the transition. However, since the quick response pressure transducer is used in conjunction with a long tube connected to the pressure tappings on the pipe, the time lag between the pressure tapping and transducer could probably overwhelm or in the same order of the puff/slug lifetime as the working fluid in the curved, small diameter hose (1mm) has a slow dynamic response, therefore, only the smooth pressure signals are obtained. To have sufficient resolution of the fluctuation in puff/slug, the LDV is applied as this laser measurement could directly measure the axial velocity thus avoid the smooth effect of connection hose in pressure measurement.

For the LDV measurement, it has been suggested that the axial velocity fluctuation (turbulent intensity) near the wall is the best transition indicator of non-Newtonian fluids, originally proposed by Zakin (1977) [176], following by Escudier and Presti (1996) [52], Escudier

et al. (2005) [51], Esmael and Nouar (2008) [55] amongst others. Figure 5.14 shows the instantaneous axial velocity in the vicinity of $r/R = 0.8$ in the horizontal plane crossing the pipe axis at Re_w=7200. The velocity fluctuation level distinctly demonstrate the flow is in a transitional state. When an individual or a train of puffs are passing the measuring point, the signal feature i.e. the high amplitude velocity fluctuation (spike) is identical to that in a fully developed turbulent pipe flow, indicating the flow structure in the interior of the puff/slug is intrinsically turbulent. When the flow state becomes laminar, axial velocity is almost a constant although

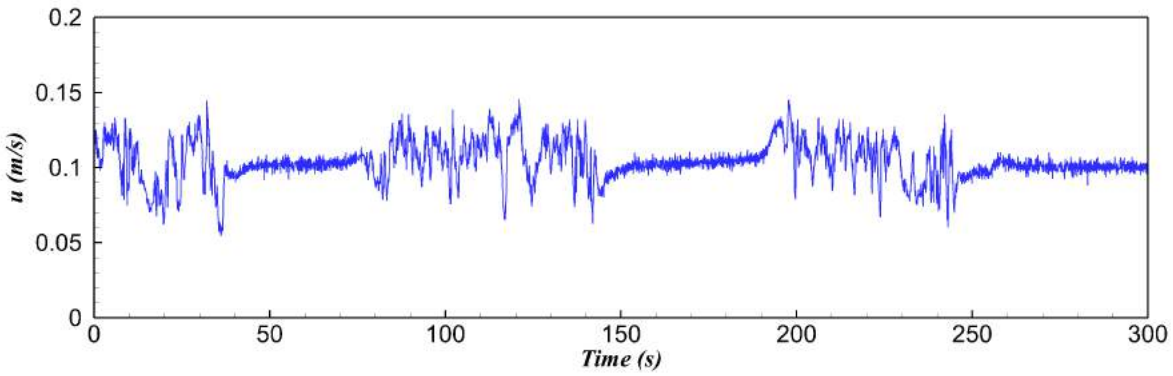

Figure 5.14: The LDV measurement of axial velocity near the wall region $r/R = 0.8$ at Re_w=7200 for 0.15% xanthan gum aqueous solution. Clear intermittency can be observed in the transitional regime.

some high frequency small amplitude fluctuation still exists, caused by the LDV noise. This low amplitude fluctuation is actually caused by external disturbances such as the noise of the pump etc.. This intermittency characterizes the transitional flow and is used as the indicator of transition, therefore, we can estimate the Reynolds number for transition using non-Newtonian fluids.

5.5 Evolution of the asymmetry with *Re*

The existing studies [51, 54, 64], although limited, reveal that above a certain Reynolds number, the asymmetry appears in pipe flow for shear-thinning fluids. However, particular attention of previous investigations was placed on the laminar turbulent transition regime using

single-point, single velocity component LDV. There is no virtually data elaborating how the asymmetry appears when Reynolds number exceeds the critical Reynolds number and how the asymmetry develops. Therefore an understanding of the mechanism underlying the onset of the asymmetry is quite poor. The following section presents novel SPIV experimental data covering a range of Reynolds numbers which span laminar, transitional and turbulent regimes to illuminate the development of the asymmetries with Reynolds number Re.

5.5.1 Time-averaged velocity profiles for a range of Reynolds numbers

We first investigated the flow asymmetry for various Reynolds numbers using a 0.15% xanthan gum solution. The Reynolds number based on the wall shear stress i.e. Re_w was utilized and the variation of Reynolds number was implemented by changing the mass flow rate of fluid flowing through the pipe. The normalized velocity profiles from purely laminar regime ($Re_w \approx$ 990) to transitional regime ($Re_w \approx 8000$) are presented in Figure 5.15. Before acquisition of the SPIV data for individual Re_w, the flow was pumped for a couple of minutes to reach steady state. The mean velocity profile was averaged over 200 seconds, corresponding to $t^* \approx 490$ (for $Re_w \approx 990$) and $t^* \approx 1720$ (for $Re_w \approx 8000$) due to different bulk velocities U_b. The large dimensionless time scale of experimental duration was required for an acceptable time convergence of the data at each Re_w. The flow regime was indicated by normalized pressure fluctuation level $p_{rms}/\overline{P}$, where $\overline{P}$ is the time-averaged pressure value.

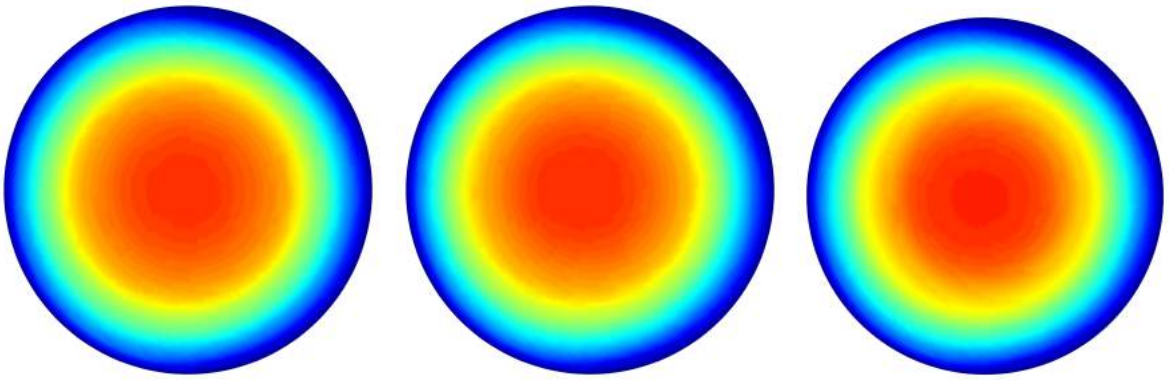

(a) $Re_w \approx 990$, $\overline{\alpha} \approx 0.023$, $p_{rms}/\overline{P} \approx 0.004$ (b) $Re_w \approx 1210$, $\overline{\alpha} \approx 0.025$, $p_{rms}/\overline{P} \approx 0.005$ (c) $Re_w \approx 1963$, $\overline{\alpha} \approx 0.028$, $p_{rms}/\overline{P} \approx 0.006$

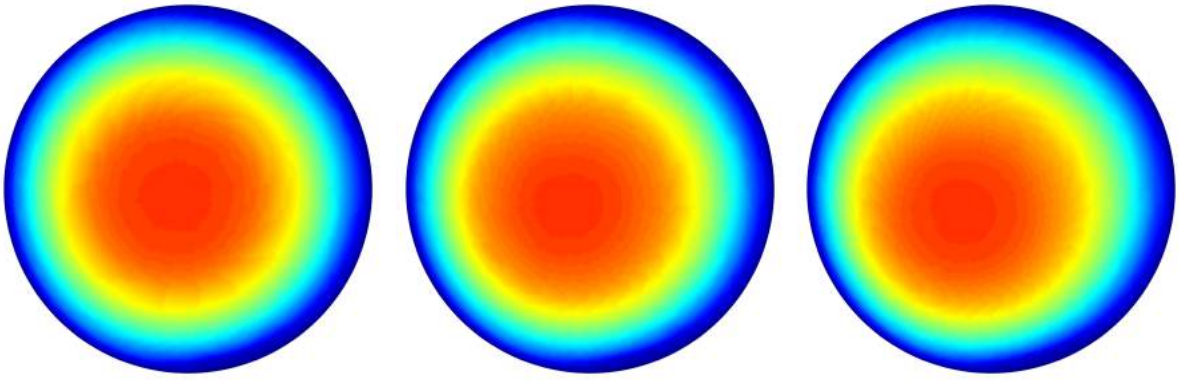

(d) $Re_w \approx 2390$, $\overline{\alpha} \approx 0.037$, $p_{rms}/\overline{P} \approx 0.007$ (e) $Re_w \approx 3019$, $\overline{\alpha} \approx 0.065$, $p_{rms}/\overline{P} \approx 0.007$ (f) $Re_w \approx 3596$, $\overline{\alpha} \approx 0.081$, $p_{rms}/\overline{P} \approx 0.008$

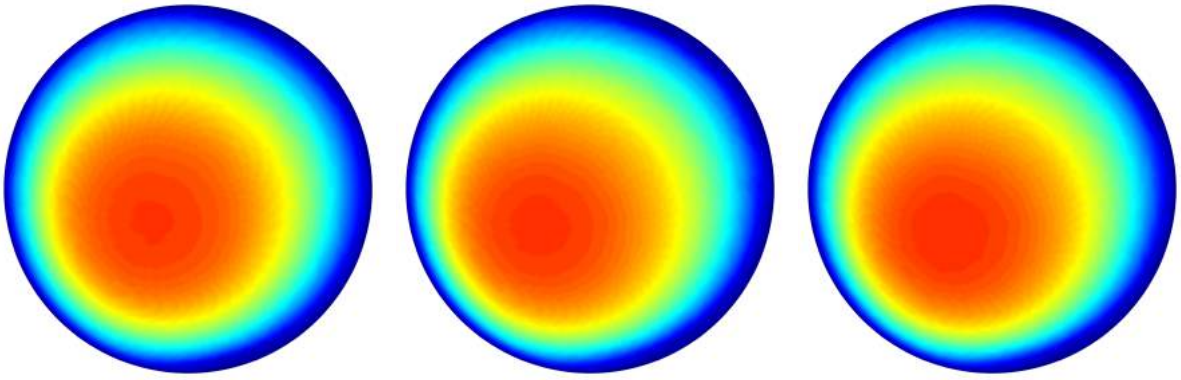

(g) $Re_w \approx 4054$, $\overline{\alpha} \approx 0.104$, $p_{rms}/\overline{P} \approx 0.010$ (h) $Re_w \approx 4996$, $\overline{\alpha} \approx 0.138$, $p_{rms}/\overline{P} \approx 0.011$ (i) $Re_w \approx 5742$, $\overline{\alpha} \approx 0.158$, $p_{rms}/\overline{P} \approx 0.012$

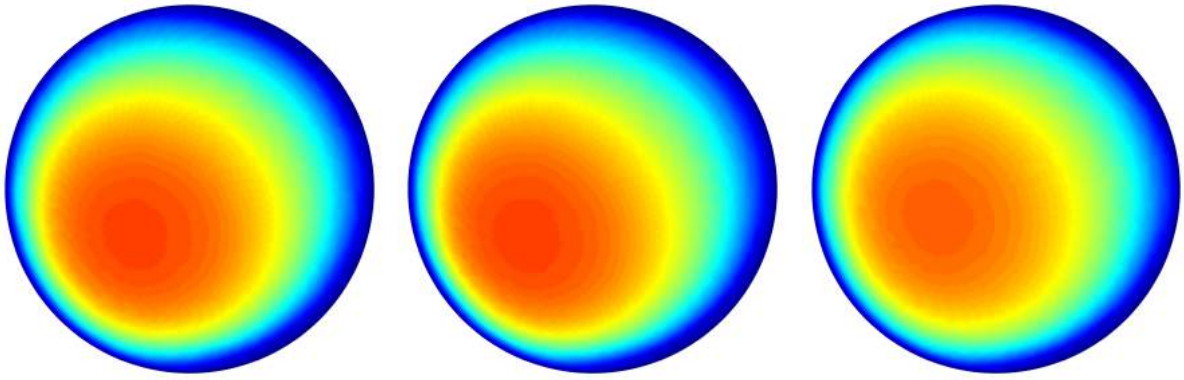

(j) Re_w≈6539, $\overline{\alpha}$≈0.163, $p_{rms}/\overline{P}$≈0.014 (k) Re_w≈7450, $\overline{\alpha}$≈0.188, $p_{rms}/\overline{P}$≈0.033 (l) Re_w≈7939, $\overline{\alpha}$≈0.151, $p_{rms}/\overline{P}$≈0.079

Figure 5.15: The normalized streamwise velocity profiles for various Re_w from laminar regime to transitional regime using identical contour level. The acquisition time is 200 seconds when flow is steady. The corresponding asymmetry factors are calculated based on the time-averaged velocity profiles, respectively.

It is worth noting that when Re_w was 7450, the pressure fluctuation increased dramatically, illustrating the onset of laminar turbulent transition. The appearance of a number of turbulent puffs at Re_w≈7450 led to a strong pressure fluctuation level, however the puff frequency at this Reynolds number was low compared with that when Re_w≈7939, indicating the flow was indeed at the initial stage of transition. The asymmetry factor reached the peak at Re_w≈7450 due to the higher Reynolds number in comparison with that at Re_w≈6539. At Re_w≈7939, more turbulent puffs appeared and contributed to the increase of pressure fluctuation. However, the degree of asymmetry decreased at Re_w≈7939 as the turbulent puffs restored the flow into axisymmetry.

When Reynolds number was at 6539 or below, no turbulent puff was observed and the pressure fluctuation level grew smoothly with respect to increasing Reynolds number in this range, suggesting the flow was in the laminar regime. Intriguingly, the flow manifested some degree of asymmetry in the span of Reynolds numbers *prior to* the turbulent puffs. This finding agrees to the previous LDV experimental data to some degree: in existing LDV data, despite the asymmetry reached to a very high degree in the transitional regime which is reasonably consistent with the SPIV data, however, at moderate Reynolds numbers in laminar regime, the asymmetry did appear in LDV data as well [51, 54], although not as conspicuous as that in higher Reynolds numbers. This phenomenon was observed in a number of LDV data but not

highlighted by the authors. This is probably due to the significant time effort that is required to obtain the mean velocity profile for each individual Reynolds number using the pointwise LDV experimental technique, therefore quite limited Reynolds numbers in the laminar regime were selected to implement LDV measurements, resulting in this behaviour being relatively unexplored. A complete description of the time-averaged velocity profiles in the laminar regime is given in Figure 5.15 (a)$\sim$(j). When the Reynolds numbers are below 1963 (Figure 5.15 (a)$\sim$(c)), the asymmetry is barely observable and the flow pattern could be deemed as axisymmetric. The slight value (approximately 2%) of the asymmetry factor that appears when $Re_w < 1963$ is due to the SPIV measurement noise. When the Reynolds number is above this critical value, the asymmetry starts to appear and becomes progressively more pronounced with increasing Reynolds number. It indicates the preferential asymmetry position is Reynolds number dependent and with the increasing Re_w, the asymmetry eventually evolves to the most asymmetric position i.e. the largest departure from axisymmetry as shown in Figure 5.15 (k). However, when the Re_w continues to grow, the turbulent puff will appear (indicated by the abrupt jump of pressure fluctuation) and the turbulent puffs return the asymmetry instantaneously to quasi-axisymmetric state and the time-averaged flow pattern had a lower asymmetry factor.

5.5.2 Time series of asymmetry factor α

The aforementioned content in subsection 5.5.1 provides the time-averaged velocity profiles for a large range of Reynolds numbers. A growing degree of asymmetry is observed with increasing Reynolds number. The following subsection provides the time history of the instantaneous asymmetry factor for extended Reynolds numbers, attempting to shed light on how the asymmetry arises and develops.

Figure 5.16 shows the time history of the asymmetry factor α when the flow develops from purely laminar to turbulent state. The data acquisition was only commenced when the mass flow rate was constant and the flow was in a steady state for each Reynolds number.

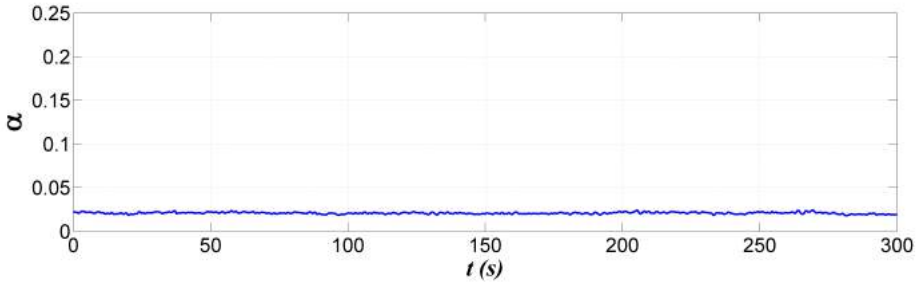

(a) $Re_w \approx 990$, $\overline{\alpha} \approx 0.023$

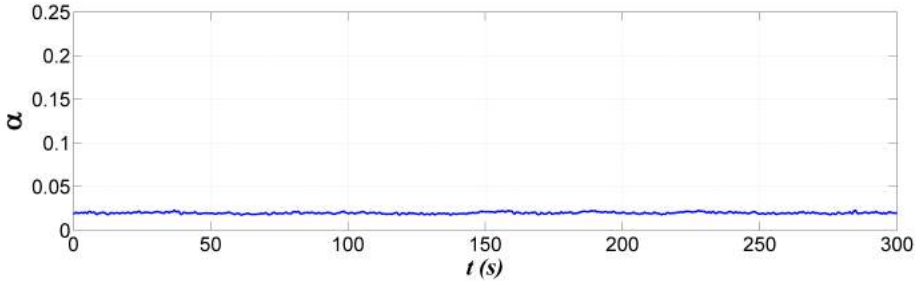

(b) $Re_w \approx 1210$, $\overline{\alpha} \approx 0.025$

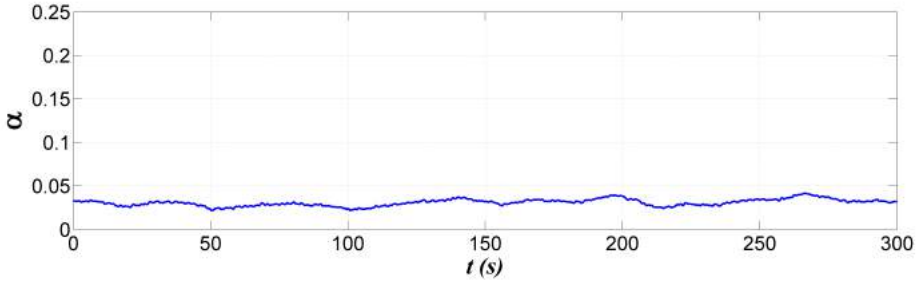

(c) $Re_w \approx 2390$, $\overline{\alpha} \approx 0.037$

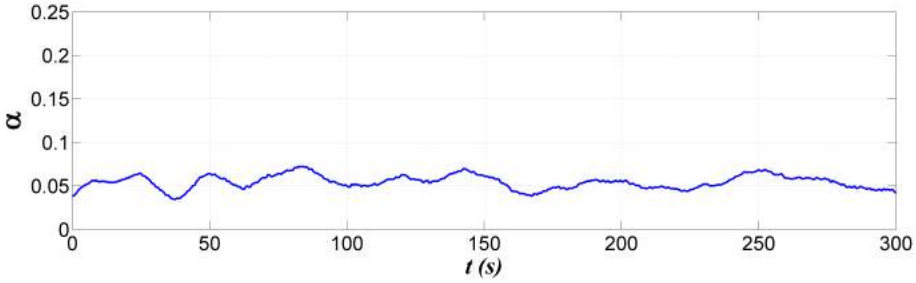

(d) $Re_w \approx 3019$, $\overline{\alpha} \approx 0.065$

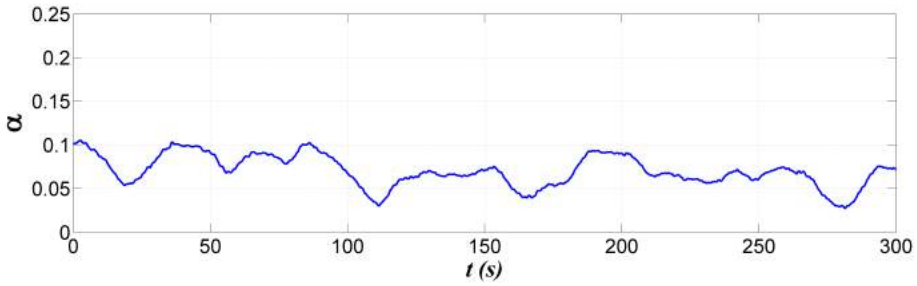

(e) $Re_w \approx 3596$, $\overline{\alpha} \approx 0.081$

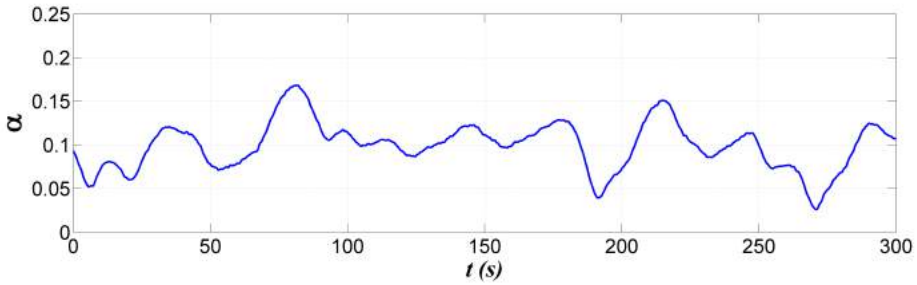

(f) $Re_w \approx 4054$, $\overline{\alpha} \approx 0.104$

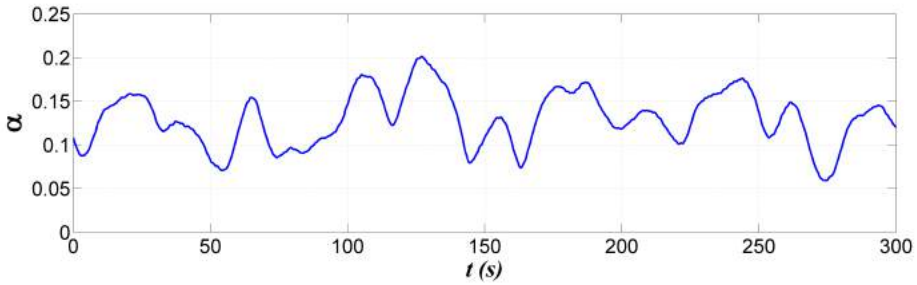

(g) $Re_w \approx 4996$, $\overline{\alpha} \approx 0.138$

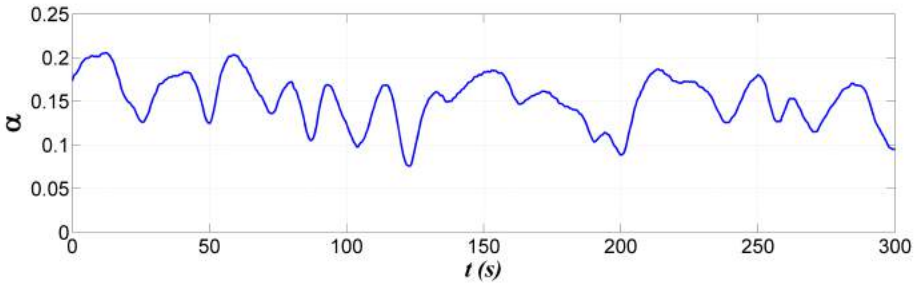

(h) $Re_w \approx 5742$, $\overline{\alpha} \approx 0.158$

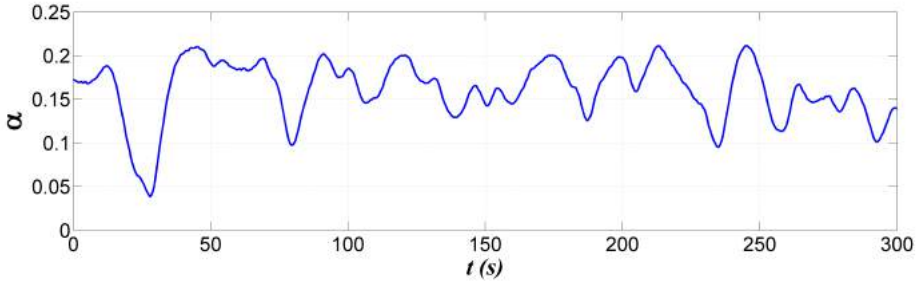

(i) $Re_w \approx 6539$, $\overline{\alpha} \approx 0.163$

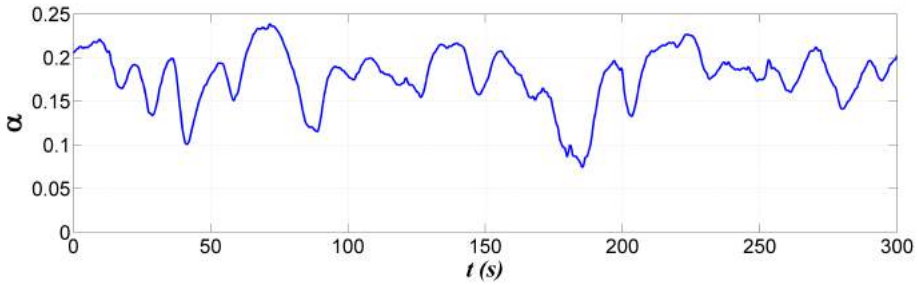

(j) $Re_w \approx 7450$, $\overline{\alpha} \approx 0.188$

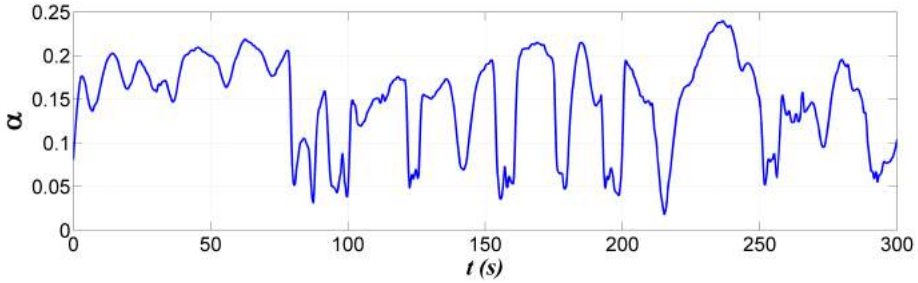

(k) $Re_w \approx 7939$, $\overline{\alpha} \approx 0.151$

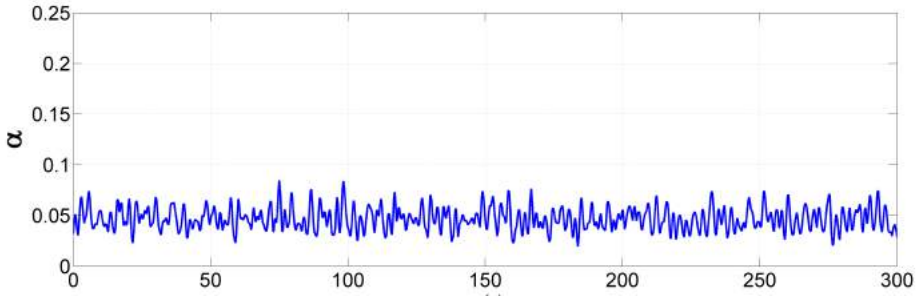

(l) $Re_w \approx 14720$, $\overline{\alpha} \approx 0.0492$

Figure 5.16: Time series of asymmetry factor α for Reynolds numbers $990 < Re_w < 14720$, covering laminar, transitional and fully turbulent regime. The asymmetry occurs when the Reynolds number is above a critical value and grows with increasing Reynolds numbers until the fully turbulent regime is reached, where the mean α reaches to a low value.

In the purely laminar flow i.e. in cases of (a) and (b) in Figure 5.16, the time series of the asymmetry factor is steady and no obvious fluctuations were observed in these Reynolds numbers. The mean asymmetry factor has a non-zero value solely as a result of SPIV measurement noise. In the purely laminar regime, the average asymmetry factor α was generally a constant ($\alpha \approx 0.023$) regardless of the variation of Re_w number and in this regime, the flow is essentially axisymmetric.

When Re_w grows above the critical Reynolds number, the asymmetry factor begins to fluctuate and the average asymmetry factor grows above the base value. With increasing Re_w, both the mean value and the magnitude of the fluctuation of asymmetry factor grow progressively, which reveals the characteristics of the evolution process from axisymmetry to asymmetry. The growing mean asymmetry factor physically represents a stronger departure from axisymmetry of the mean velocity profile and the variation in magnitude of the asymmetry factor indicates the asymmetric flow pattern is indeed non-stationary and moves around the favoured asymmetry position for each Re_w.

It is worth noting that the flow is in the laminar regime until $Re_w \approx 6539$, where the turbulent puff and abrupt jump of pressure fluctuation was observed revealing the asymmetry arises and develops prior to the turbulent puff, which is consistent with the observation of time-averaged velocity distribution. This result suggests that the occurrence of the asymmetry is actually independent of the laminar-turbulent transition process but is attributed to an instability of the laminar base flow. Once Re_w exceeds the laminar-turbulent transition critical Reynolds number, with progressively increasing Re_w, the turbulent puffs grow and eventually saturate the pipe as shown in Figure 5.16 (l) and the flow evolves into the fully turbulent state, the mean asymmetry factor returns to a low value and the variation in magnitude of the asymmetry is more frequent and random in the fully turbulent regime.

5.5.3 Streamwise velocity fluctuations

Figure 5.17 shows the contour plot of normalized velocity fluctuations in the streamwise direction and corresponding time-averaged axial velocity profile (U/U_b) for a range of Reynolds numbers from laminar to transitional, i.e. 1210< Re_w <7939. The data was obtained at 5 velocity profiles per second for a time duration of 200 seconds, which produces 1000 successive velocity vectors fields. The time-averaged axial velocity U contour was generated by calculating the algebraic mean of axial velocity component of the 1000 velocity vector maps. The normalized streamwise velocity fluctuation, i.e. u_{rms}/U_b colour map was obtained by calculating the square root of the arithmetic mean of $(u-U)^2$, as shown in equation 5.8, where m is the number of frames, i.e. 1000, u_i is the i^{th} instantaneous axial velocity of each individual SPIV frame, U is the time-averaged axial velocity of the 1000 successive velocity vectors and U_b is the bulk velocity:

$$u_{rms}/U_b = \frac{\sqrt{\sum_{i=1}^{m}(u_i-U)^2/m}}{U_b} \tag{5.8}$$

When the flow is in the purely laminar regime, the mean velocity profile is axisymmetric and the axial velocity fluctuations are very small. When the Reynolds number progressively increases, some velocity fluctuation appears in a curved region around the peak axial velocity location, i.e. near the preferred orientation of asymmetry. This indicates that when the asymmetry arises in the *Re*-dependent preferential location, the asymmetric flow pattern oscillates around the preferred asymmetric location and thus produces velocity fluctuation curved region in the vicinity of the peak velocity. With growing Re_w, the normalized axial velocity fluctuation u_{rms}/U_b has a higher amplitude illustrating the oscillation of the asymmetric flow pattern increases accordingly. It is noteworthy that this fluctuation is observed in the laminar regime and is essentially different from the turbulent fluctuations associated with laminar-turbulent transition. The conventional velocity fluctuations in turbulent flow are spatially random and the time scale of the turbulent fluctuations are much shorter than that of the velocity variation due to the moving asymmetry. Moreover, conventional velocity fluctuation appears in the manner of abrupt change, i.e. the magnitude of the velocity fluctuation will have a sudden jump once the

turbulent puff appears. The development of the

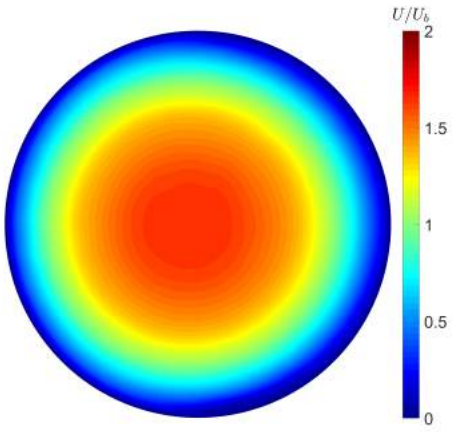

(a) U/U_b at Re_w≈1210, $\overline{\alpha}$≈0.025

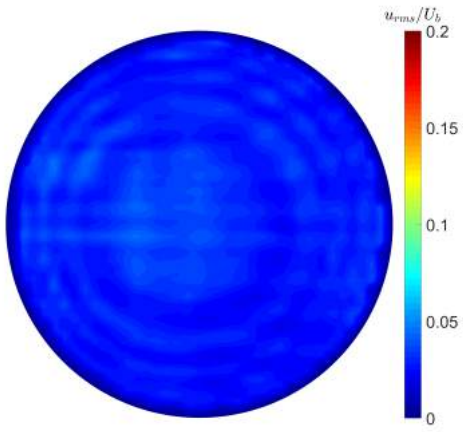

(b) u_{rms}/U_b at Re_w≈1210, $\overline{\alpha}$≈0.025

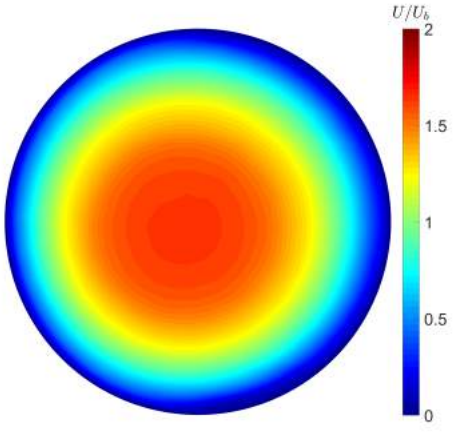

(c) U/U_b at Re_w≈1963, $\overline{\alpha}$≈0.028

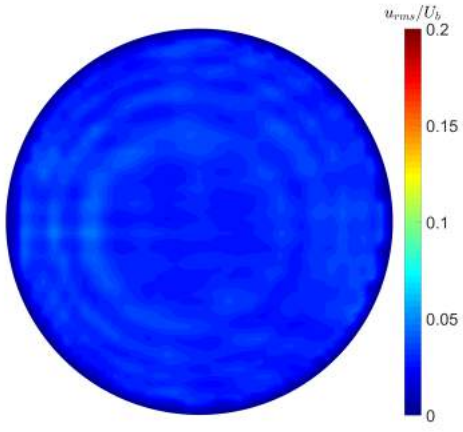

(d) u_{rms}/U_b at Re_w≈1963, $\overline{\alpha}$≈0.028

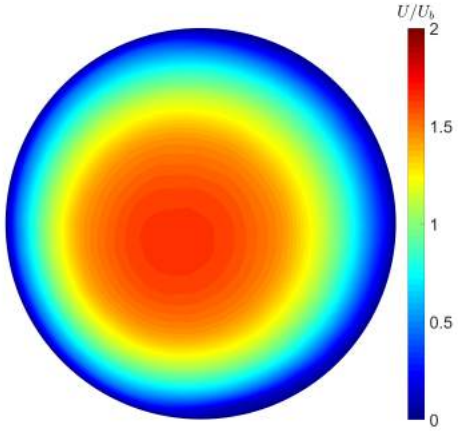

(e) U/U_b at Re_w≈2390, $\overline{\alpha}$≈0.037

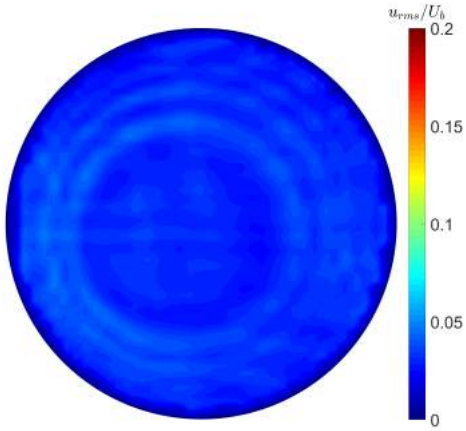

(f) u_{rms}/U_b at Re_w≈2390, $\overline{\alpha}$≈0.037

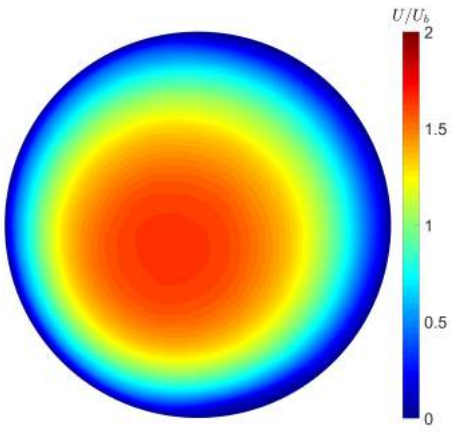

(g) U/U_b at Re_w≈3019, $\overline{\alpha}$≈0.065

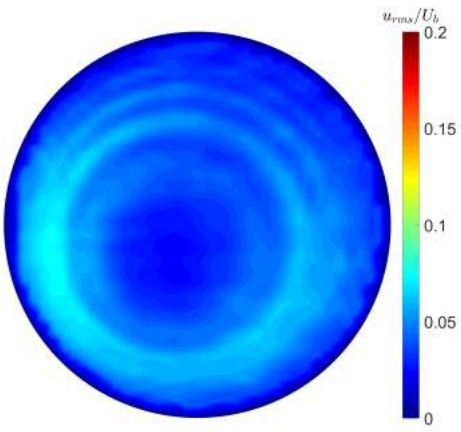

(h) u_{rms}/U_b at Re_w≈3019, $\overline{\alpha}$≈0.065

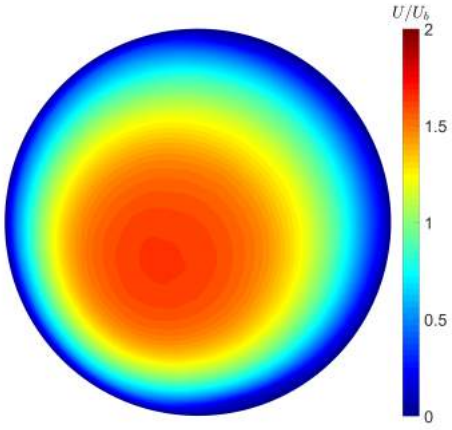

(i) U/U_b at Re_w≈3596, $\overline{\alpha}$≈0.081

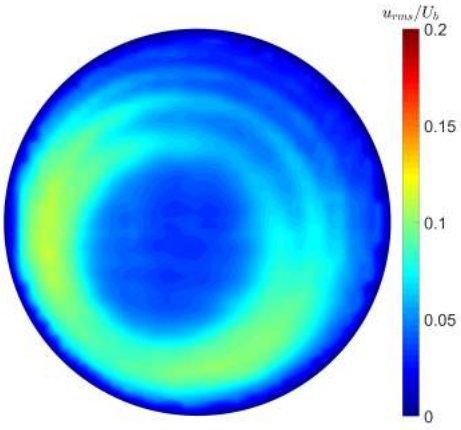

(j) u_{rms}/U_b at Re_w≈3596, $\overline{\alpha}$≈0.081

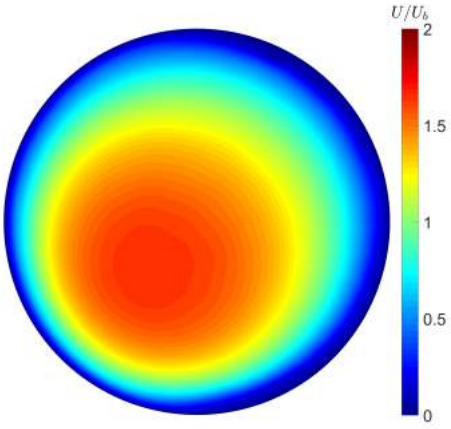

(k) U/U_b at Re_w≈4054, $\overline{\alpha}$≈0.104

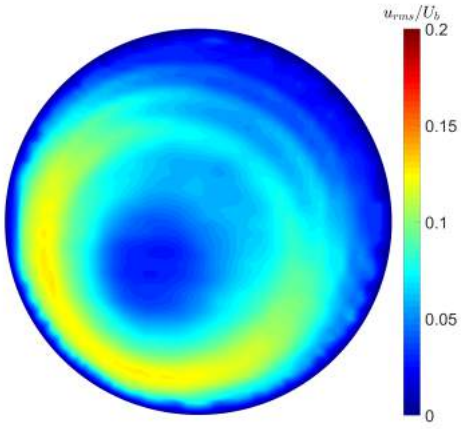

(l) u_{rms}/U_b at Re_w≈4054, $\overline{\alpha}$≈0.104

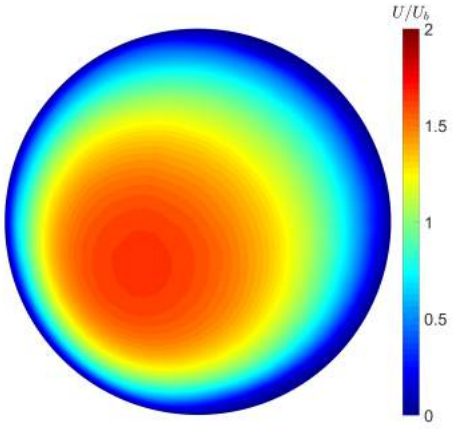

(m) U/U_b at Re_w≈4996, $\overline{\alpha}$≈0.138

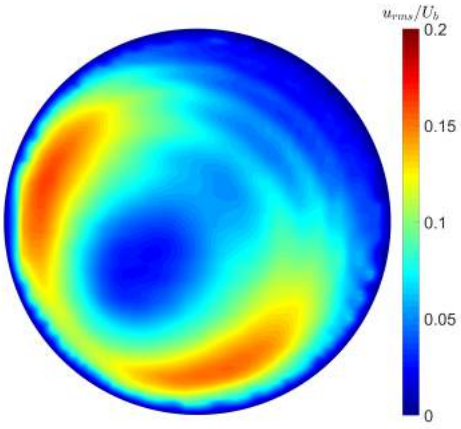

(n) u_{rms}/U_b at Re_w≈4996, $\overline{\alpha}$≈0.138

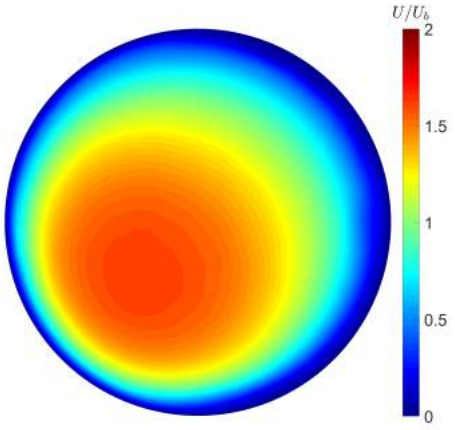

(o) U/U_b at Re_w≈6539, $\overline{\alpha}$≈0.163

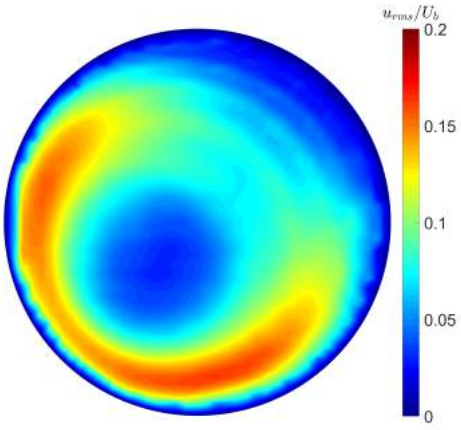

(p) u_{rms}/U_b at Re_w≈6539, $\overline{\alpha}$≈0.163

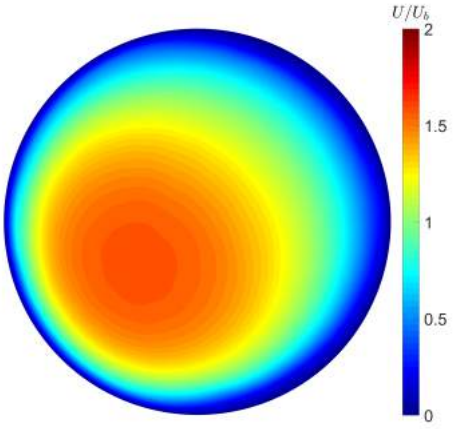

(q) U/U_b at Re_w≈7450, $\overline{\alpha}$≈0.188

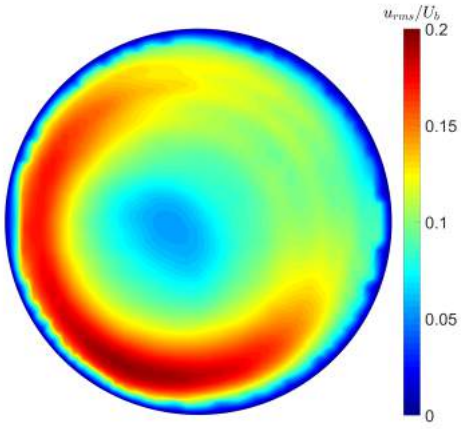

(r) u_{rms}/U_b at Re_w≈7450, $\overline{\alpha}$≈0.188

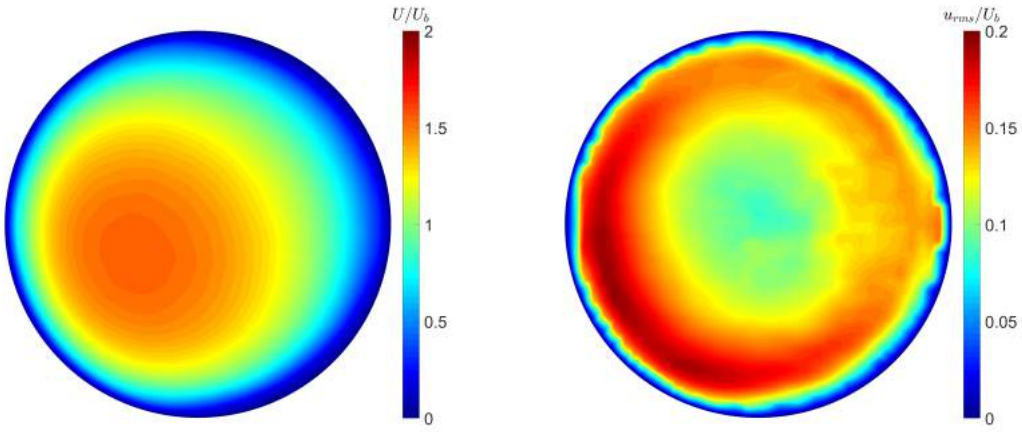

(s) U/U_b at Re_w≈7939, $\overline{\alpha}$≈0.151 (t) u_{rms}/U_b at $\overline{\alpha}$≈7939, $\overline{\alpha}$≈0.151

Figure 5.17: Contour of normalized axial velocity flucutaion u_{rms}/U_b and corresponding time-averaged axial velocity U/U_b at a range of Re_w from laminar to transitioanl regime.

fluctuation of asymmetric pattern grows in a smooth way, i.e. the u_{rms}/U_b evolves gradually with increasing Re_w instead of a sudden change. The following section will further study the velocity fluctuation in the $r-\theta$ plane, i.e. $v_{r\theta,rms}/U_b$ to characterize the flow in the cross-stream plane.

5.5.4 Cross-stream velocity fluctuations

Figure 5.18 shows the contour of normalized velocity fluctuation in cross-sectional plane and corresponding time-averaged axial velocity in the identical experiment conditions as mentioned in section 5.5.3. The normalized $v_{r\theta,rms}$ colour map was obtained by calculating the square root of the arithmetic mean of $(v-V)^2+(w-W)^2$, see equation below:

$$v_{r\theta,rms}/U_b = \frac{\sqrt{\sum_{i=1}^{m}\left\{(v_i-V)^2+(w_i-W)^2\right\}/m}}{U_b} \tag{5.9}$$

where v , w is instantaneous in-plane velocity components of each individual SPIV frame and V , W is the time-averaged in-plane velocity components of 1000 successive velocity vectors, U_b is the bulk velocity and m is number of frames, i.e. 1000 frames. The $v_{r\theta,rms}/U_b$ did not present a high fluctuation region in the vicinity of peak velocity location at high laminar Reynolds

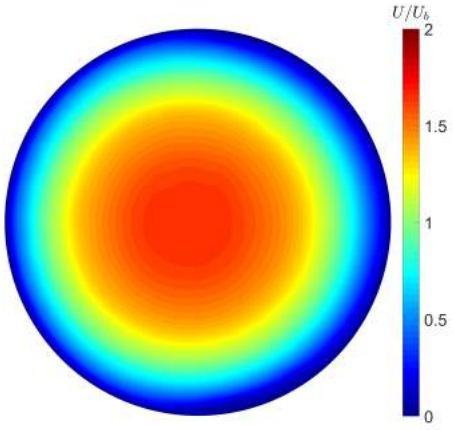

(a) U/U_b at Re_w≈1210, α≈0.025

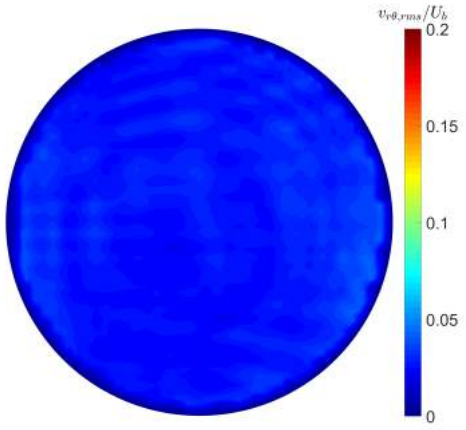

(b) $v_{r\theta,rms}/U_b$ at Re_w≈1210, α≈0.025

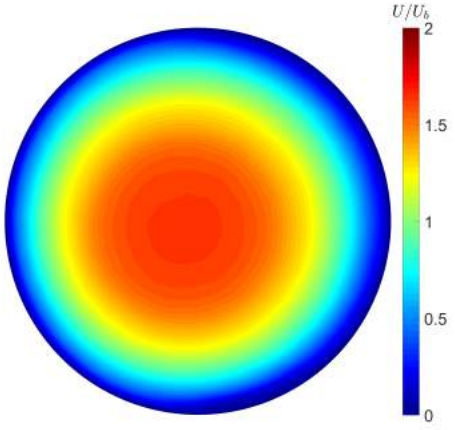

(c) U/U_b at Re_w≈1963, α≈0.028

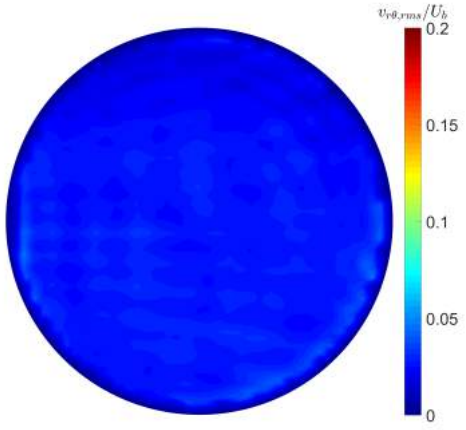

(d) $v_{r\theta,rms}/U_b$ at Re_w≈1963, α≈0.028

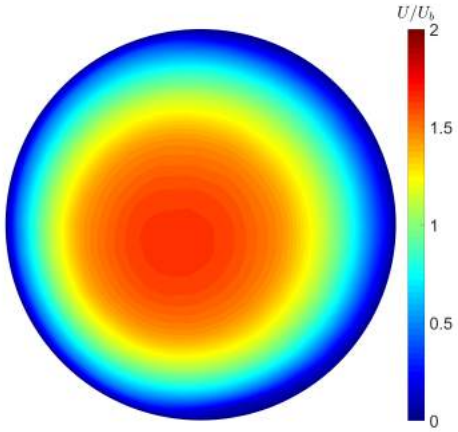

(e) U/U_b at Re_w≈2390, α≈0.037

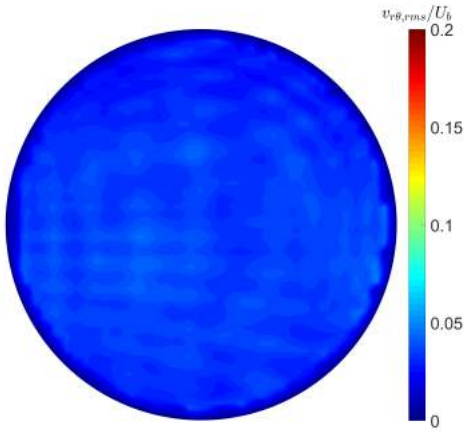

(f) $v_{r\theta,rms}/U_b$ at Re_w≈2390, α≈0.037

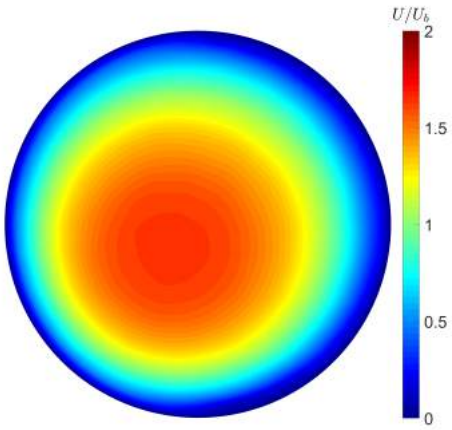

(g) U/U_b at Re_w≈3019, α≈0.065

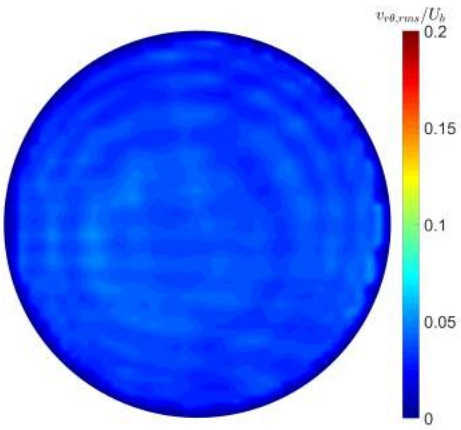

(h) $v_{r\theta,rms}/U_b$ at Re_w≈3019, α≈0.065

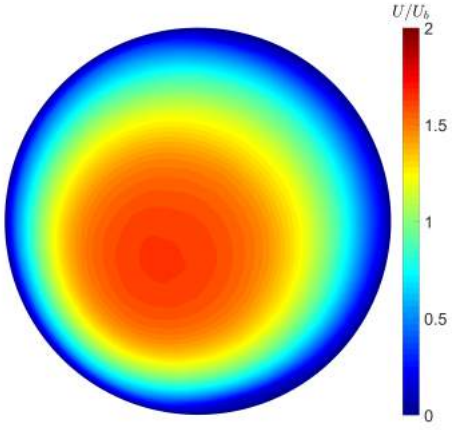

(i) U/U_b at Re_w≈3596, α≈0.081

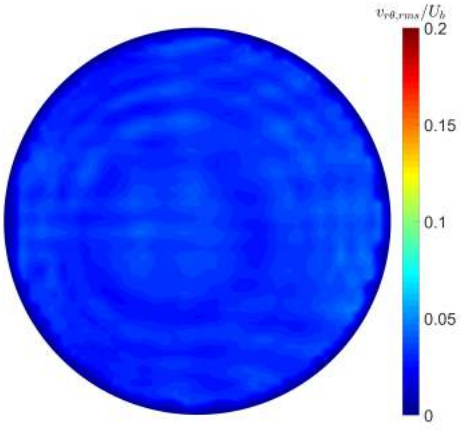

(j) $v_{r\theta,rms}/U_b$ at Re_w≈3596, α≈0.081

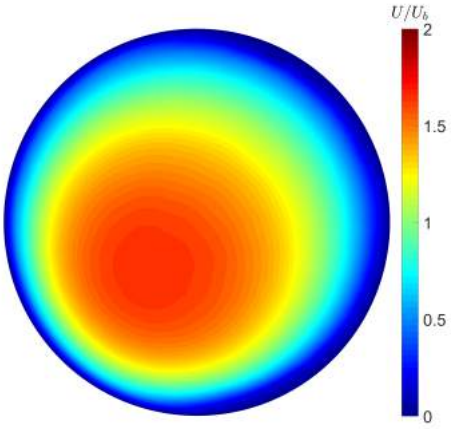

(k) U/U_b at Re_w≈4054, α≈0.104

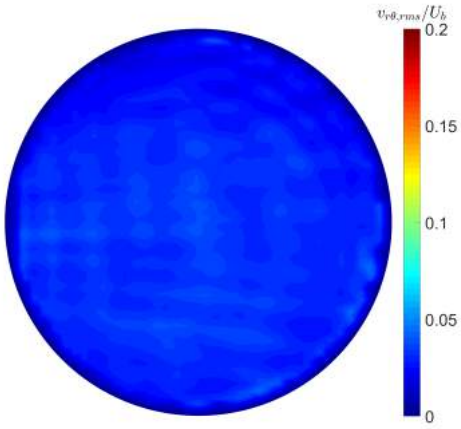

(l) $v_{r\theta,rms}/U_b$ at Re_w≈4054, α≈0.104

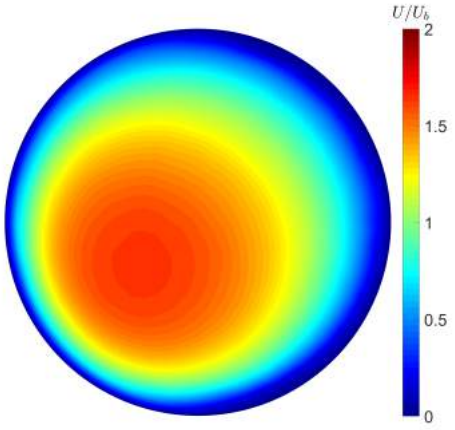

(m) U/U_b at Re_w≈4996, α≈0.138

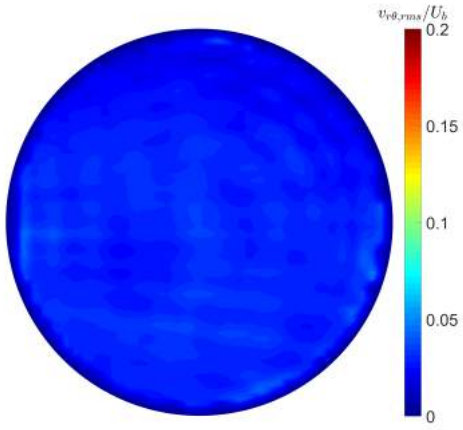

(n) $v_{r\theta,rms}/U_b$ at Re_w≈4996, α≈0.138

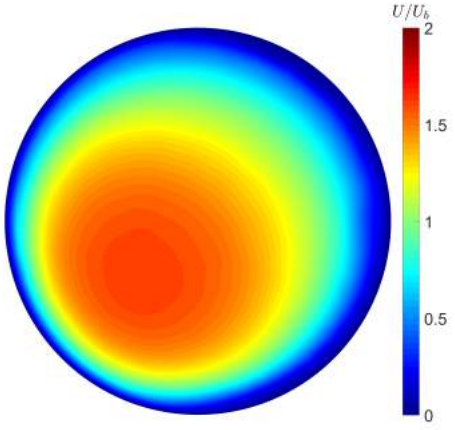

(o) U/U_b at Re_w≈6539, α≈0.163

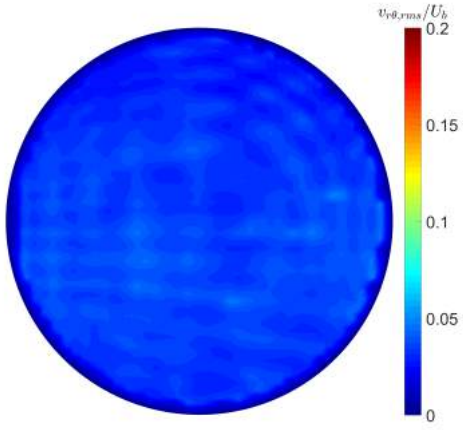

(p) $v_{r\theta,rms}/U_b$ at Re_w≈6539, α≈0.163

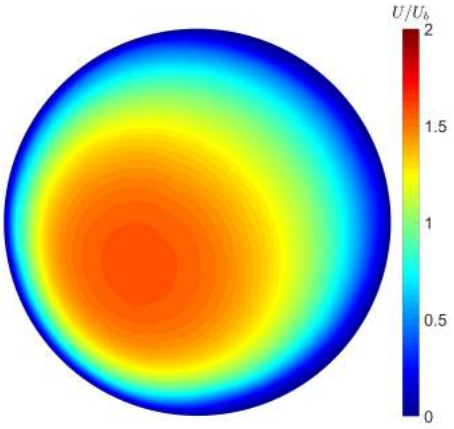

(q) U/U_b at Re_w≈7450, α≈0.188

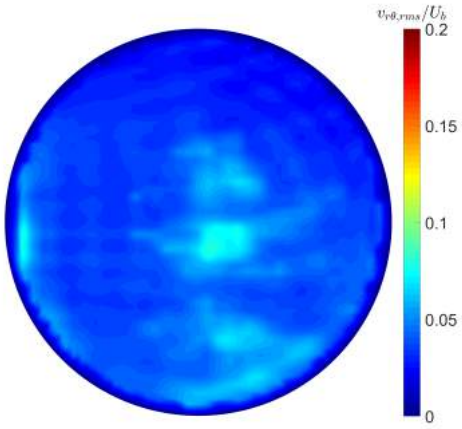

(r) $v_{r\theta,rms}/U_b$ at Re_w≈7450, α≈0.188

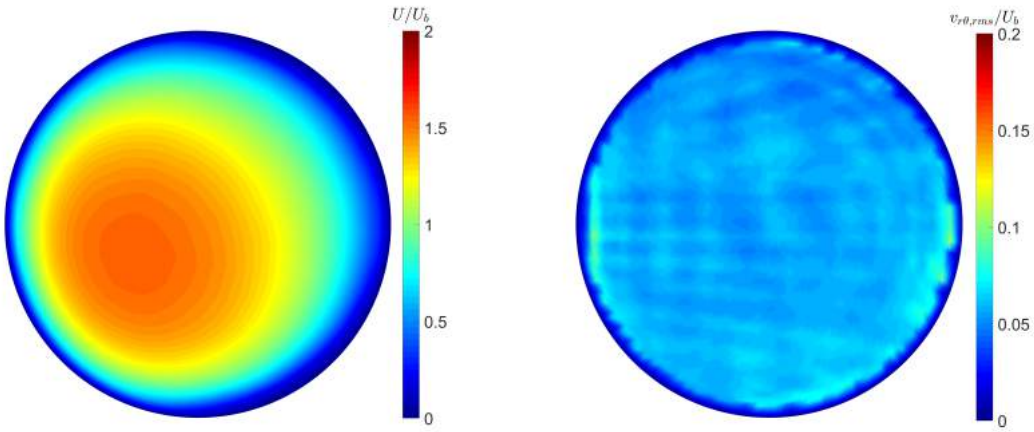

(s) U/U_b at Re_w≈7939, α≈0.151 (t) $v_{r\theta,rms}/U_b$ at Re_w≈7939, α≈0.151

Figure 5.18: Contour of cross-stream axial velocity fluctuation $u_{r\theta,rms}/U_b$ and corresponding time-averaged axial velocity U/U_b at a range of Re_w from laminar to transitional regime.

numbers or in the transitional regime. The color scale of $v_{r\theta,rms}/U_b$ is the same as that of u_{rms}/U_b in subsection 5.5.3 to make a direct comparison of the amplitude of velocity fluctuation between streamwise and cross-sectional direction. With increasing Reynolds number, the amplitude of $v_{r\theta,rms}/U_b$ did not increase steadily but had an abrupt change when a turbulent puff appears (as shown in Figure 5.18(r)), which indicates $v_{r\theta,rms}/U_b$ behaves significantly different to u_{rms}/U_b. When Reynolds number continues to increase, more and more turbulent puffs occur and merge, triggering a large amplitude of in-plane velocity fluctuation (as shown in Figure 5.18(t)). This results from the fact that the turbulent puff is featured by turbulent characteristics and thus inducing the high *rms* value of in-plane velocity fluctuation abruptly once the transition occurs. Therefore, the development of $v_{r\theta,rms}/U_b$ is essentially a laminar-turbulent transition indicator.

5.5.5 Evolution of the magnitude of the asymmetry

Heretofore, the evolution of the asymmetry factor, velocity fluctuation and pressure fluctuations for an extended range of Reynolds numbers from purely laminar to transitional have been investigated respectively. In this section, a comprehensive analysis of the current experimental

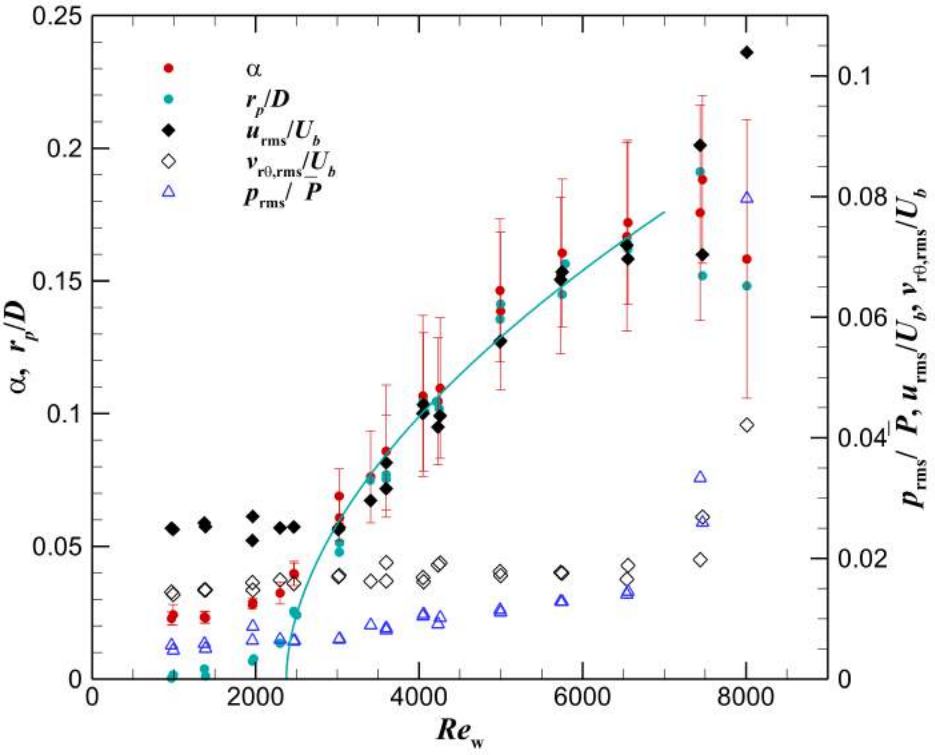

Figure 5.19: Transition from axisymmetry to asymmetry: the asymmetry indicated by α and r_p/D grows in form of a supercritical bifurcation with square-root dependence on Reynolds number Re_w before the appearance of turbulent puffs at $Re_w \sim 8000$

data will be given.

Figure 5.19 shows the symmetry-breaking evolution from axisymmetry to asymmetry. The degree of asymmetry is quantitatively described by either by the asymmetry factor α or the radius of peak velocity r_p/D. Comparing the two bifurcation indicators, the asymmetry factor globally measures the distortion of velocity field by integrating the velocity field over the entire cross-sectional plane of the pipe (see Equation 5.5) while r_p/D calculates the radius of the peak velocity by comparing the amplitude of velocity locally. When the flow is in the purely laminar regime, i.e. the velocity distribution is theoretically axisymmetric, the r_p/D value is close to zero while the asymmetry factor is approximate to 2%. This non-zero value is due to the fact that the integral over the entire velocity field in the α calculation accumulates experimental error and thus produces a larger misregistration than the r_p/D calculation, especially for the

low Reynolds numbers where the relative error is large. However, it is still useful to employ the α criteria to indicate the asymmetry as α quantifies the asymmetry from the perspective of the whole flow field with a reasonable PIV data error of approximately 2%. Moreover, applying α to quantify the degree of asymmetry is also consistent with previous LDV studies [54] because a similar calculation was used, albeit one-dimensionally, in LDV studies. The velocity fluctuation data u_{rms}/U_b and $v_{r\theta,rms}/U_b$ in Figure 5.19 are calculated by spatially averaging the fluctuation maps shown in Figure 5.17 and 5.18 for each individual Reynolds number. The pressure drop measurement was implemented in conjunction with the aforementioned SPIV measurements, thus the flow conditions were identical. The acquisition rate of pressure transducer was 100Hz during the experiment and the normalized *rms* of pressure fluctuation was calculated to indicate the flow regime.

In Figure 5.19, the α and r_p/D data reveal that, below a critical Reynolds number Re_{wc}, the flow was axisymmetric and no asymmetry was observed. When Re_w continues to grow above the critical Reynolds number, the α and r_p/D values both exceed their base values in purely laminar flow indicating the onset of an axisymmetry to asymmetry transition. With increasing Re_w, the deviation from the axisymmetric laminar base state is observed to develop gradually. It is essentially different from laminar-turbulent transition, which is usually associated with non-smooth variation.

The solid blue-green curve fits the r_p/D points in the functional form of $r_p/D = a \cdot (Re_w - Re_{wc})^b$ and the Re_w fitting range was selected in purely laminar flow ($2100 < Re_w < 6500$). There are three free parameters in the fitting, i.e. b the power law index of r_p/D growth curve, Re_{wc} the critical Reynolds number where the asymmetry first occurs and a the multiplication coefficient. The data fitting gives b=0.55 and Re_{wc}=2375 which illustrates the asymmetry develops in a form characteristic of a supercritical bifurcation with approximately square-root dependence on Reynolds number. The axial velocity fluctuation u_{rms}/U_b also evolves in the manner of a supercritical bifurcation, gradually increasing with growing Reynolds number. The previous bifurcation theories [81, 83] indicate the square root dependence of the measure (i.e. Reynolds

number in this case) is consistent with the presence of a pitchfork bifurcation and the mathematical investigation of the bifurcation indicates this pitchfork bifurcation is associated with the linear instability [70], which can not be observed in Newtonian fluids. The pitchfork bifurcation is suggestive of the asymmetry is not induced by laminar-turbulent transition process but appears to be a linear instability of the laminar base state. The onset of laminar-turbulent transition, indicated by the *rms* of pressure fluctuation and velocity fluctuation in the $r-\theta$ plane ($v_{r\theta,rms}/U_b$), shows a sharp increase at Re_w≈7000, demonstrating the laminar-turbulent transition process appearing in a subcritical form. The observation is of importance as it implies that the laminar flow of shear-thinning fluids may be linearly unstable to asymmetric disturbances, which is not something that has previously been considered.

5.5.6 Frequency power spectra of axial velocity fluctuations

Frequency power spectra of axial velocity fluctuations was investigated in the vicinity of the peak velocity location just above the Reynolds number at which the asymmetry appears. The peak velocity location was obtained based on the SPIV time-averaged asymmetric velocity profile, then a probe point was set to the location of the peak velocity to extract the instantaneous velocity of each frame. The frame rate of SPIV experiment was 5Hz and the total measurement time was 200s, i.e. 1000 measured axial velocity points were obtained to calculate the frequency power spectra. Particular attention was put on the Reynolds numbers near the critical numbers when asymmetry occurred. Figure 5.20 shows the time history of normalized axial velocity u/U_b in the location of the peak velocity and frequency power spectra $E(f)$ of the corresponding axial velocity fluctuation at Re_w≈1963, Re_w≈2390, Re_w≈3019. When Re_w≈1963, the asymmetry factor α is approximate 0.028 (the asymmetry factor in purely laminar flow is at this level ≈0.025 due to the SPIV noise), indicating the flow is essentially axisymmetric. The normalized axial velocity u/U_b is around 1.6 and there is no significant axial velocity fluctuation observed.

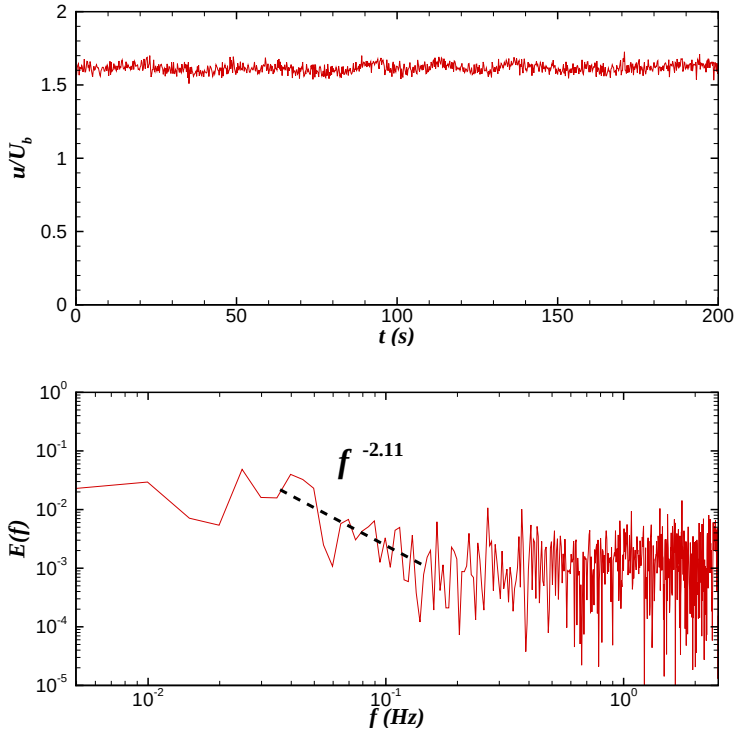

(a) $Re_w \approx 1963$, $\alpha \approx 0.028$

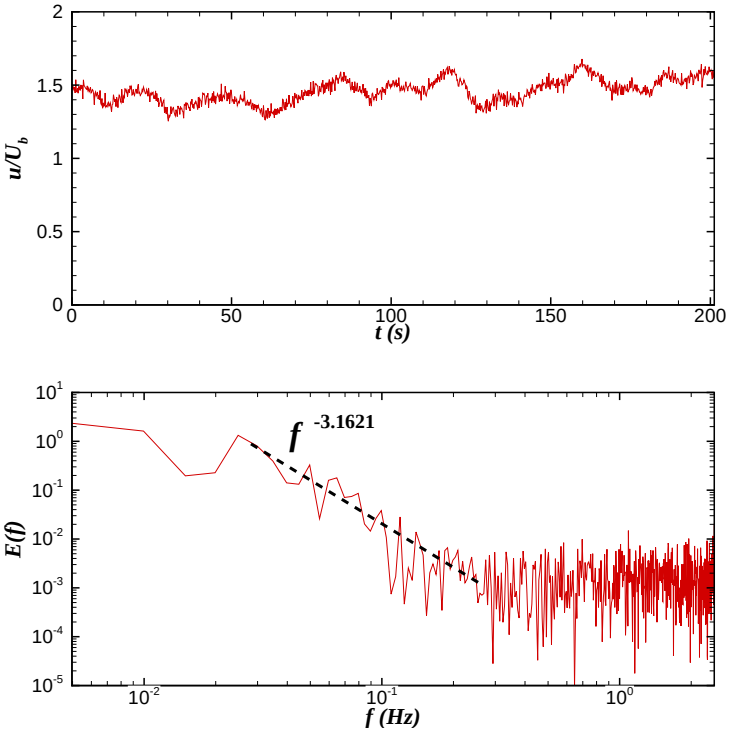

(b) $Re_w \approx 2390$, $\alpha \approx 0.037$

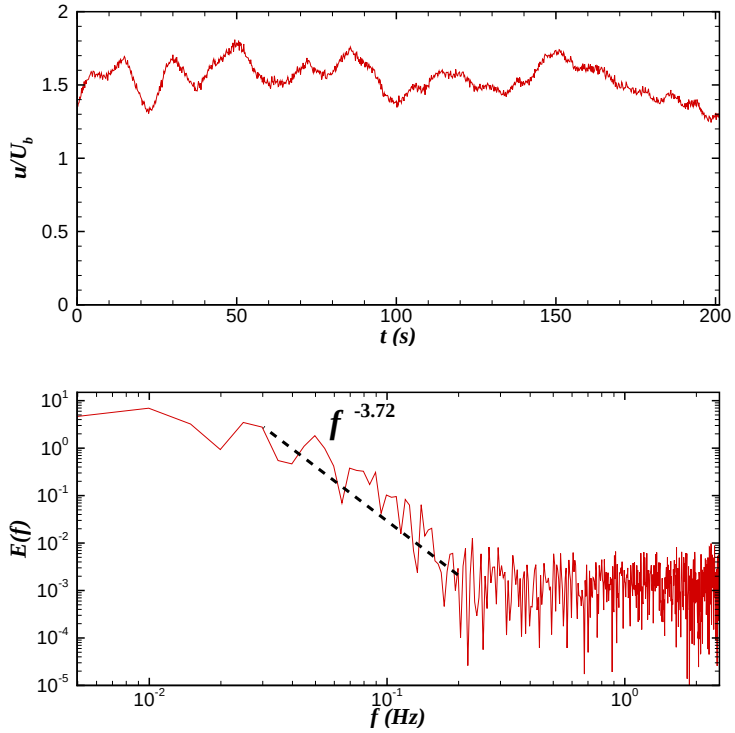

(c) Re_w≈3019, α≈0.065

Figure 5.20: The normalized axial velocity u/U_b and frequency power spectra $E(f)$ of corresponding axial velocity fluctuation near the peak velocity position below and little further above the critical Reynolds numbers when asymmetry occurs.

The magnitude of frequency power spectra of velocity fluctuation at Re_w≈1963 is about 10^{-2}, which is 2 order of magnitude lower than that of Re_w≈2390 ($E(f)$≈10^0). The asymmetry factor α at Re_w≈2390 is 0.037, which is significantly higher than the value of laminar base flow (α≈0.025), indicating the onset of asymmetry. The axial velocity also manifested significant fluctuation, which is due to the time-varying nature of the asymmetry. We observed oscillations across a range of low frequencies (f≈0.1Hz) where the fluctuation energy decays according to a power law $E(f)\sim f^{-\alpha}$ with α close to 3. This result is similar to the LDV experimental work of Esmael *et al.* (2010) [56]. Due to the limitations of their experiment (single-point measurements of one component of velocity), Esmael *et al.* were not able to identify a supercritical bifurcation and interpreted their results as indicating a weakly turbulent state, which was chaotic in time and regular in space, induced by the shear-thinning behaviour of the fluid. While our results are

entirely consistent with their data, our interpretation is quite different as we are able to associate these oscillations with the observed supercritical instability.

5.5.7 Evolution of the location of the asymmetry

In subsection 5.5.1, it is noteworthy that the favoured radial and azimuthal location of the asymmetry is Reynolds number dependent. However, it is intriguing to know whether the favoured location of asymmetry exhibits any hysteresis when the Reynolds number increases and decreases. Figure 5.21 shows the instantaneous location of the peak velocity when the Reynolds number varies. Each dot corresponds to the location of the peak velocity at an instant in time. Each colour corresponds to a nominal step change in Re_w, although it should be noted that throughout the whole duration of the experiment the flow is transiently changing as at no point does it reach a true steady state. The experiment was initially conducted when flow was steady in the purely laminar regime (Re_w=1960) and Reynolds number gradually increased until Re_w=6740, which is in the vicinity of the transitional regime, as shown in Figure 5.21 (a). The reversed experimental process is shown in Figure 5.21 (b), the data began to be acquired at the steady state when Re_w=6740 and gradually decreases to the purely laminar regime (Re_w=1960) with the identical Re_w interval as that when Re_w increases. The time spacing of SPIV data sampling for each individual Reynolds number was 30 seconds and the total experimental duration regardless of Re_w increases or decreases was identical. The trajectory of peak velocity was colour-coded based on nominal Re_w, i.e. the same Re_w has the same colouring. Apart from the Re-dependent favoured asymmetry location, a preferential axisymmetry-asymmetry transition path was observable. The trajectory of asymmetry when Re_w increases is shown in Figure 5.21 (a), the radius of the peak velocity initially grows until reaching a certain value ($r_p/D \approx 0.2$), then the azimuthal angle of asymmetry began to alter while the radius of the peak velocity remains approximately constant. The trajectory of asymmetry with decreasing Re_w was plotted in Figure 5.21 (b). The asymmetry returns to the axisymmetry following the similar preferential path but in reverse. The azimuthal angle of the asymmetry reduces firstly and then the

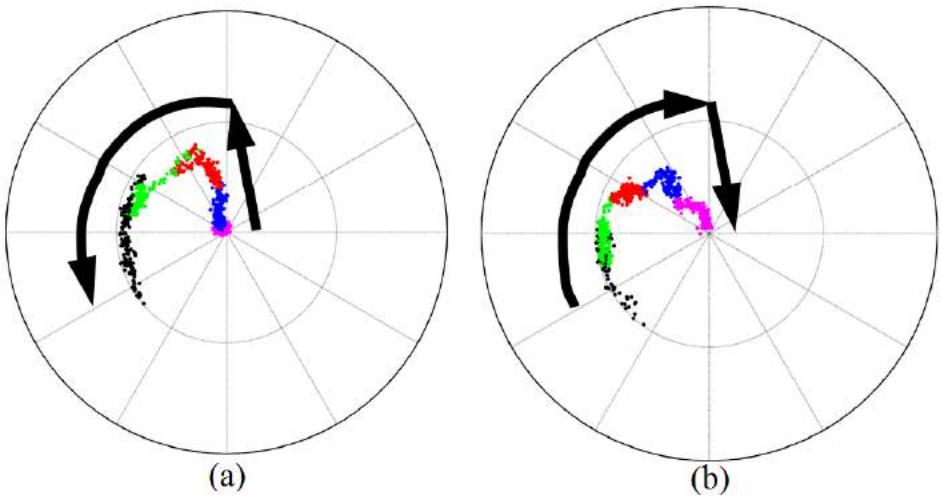

Figure 5.21: Traces of the peak velocity during the transient processes of axisymmetric-asymmetric transition (a) and asymmetric-axisymmetric relaminarisation (b). Each dot corresponds to an instant in time color-coded by its nominal Re_w according to Re_w=1960 (pink), Re_w=3400 (blue), Re_w=4230 (red), Re_w=5750 (green) and Re_w=6740 (black) with the time delay between each Re_w being 30 seconds. The arrows indicate the direction of movement with time.

radius of peak velocity decreases until reaching the axisymmetric state. Figure 5.21 shows that, remarkably, the asymmetry is non-hysteretic and reversible: it has a preferred route between axisymmetry and asymmetry, which it adheres to regardless of whether it is approaching transition to turbulence or relaminarising. The non-hysteretic characteristic can be explained that for the supercritical transition, the continuous evolution of states indicates the bifurcated state remains close to the bifurcating state therefore leading to no hysteretic behavior.

5.6 Non-helical mode of asymmetry

Most of the previous LDV studies [51, 54, 64] and the current SPIV study, of the flow asymmetry implemented the experiments in a single cross-sectional $(r-\theta)$ plane of the pipe at a fixed axial location x. An interesting aspect to the study is to investigate the asymmetry in all three spatial dimensions $(r-\theta-x)$, for example, to study whether the asymmetrical flow develops in a particular streamwise location.

The variation with streamwise position x, can show us the form of the asymmetry, for ex-

ample, it could have a helical structure. A simple test is to compare the time-averaged streamwise velocity at a fixed point in the $r-\theta$ plane while changing the axial location x along the pipe. If the asymmetry develops in a helical mode, the spiral structure will produce a streamwise velocity u variation with different x for the fixed point in the $r-\theta$ plane. Since the spatial periodic form characterizes the helix, uneven streamwise spacing was used when changing the axial position x to prevent the streamwise spacing coincidently equalling to the pitch of the spiral structure. The x position of the SPIV (x/D=220) was set as the reference location for the LDV measurement and all the LDV probing points were located upstream of the SPIV reference plane. The LDV probing point in the $r-\theta$ plane was in the vicinity of the favoured location of asymmetry at x/D=220 when the experiment performed at the $Re_w = 4200$ using 0.15% xanthan gum aqueous solution. The acquisition time of LDV measurements was 500 seconds and repeated twice for each axial location.

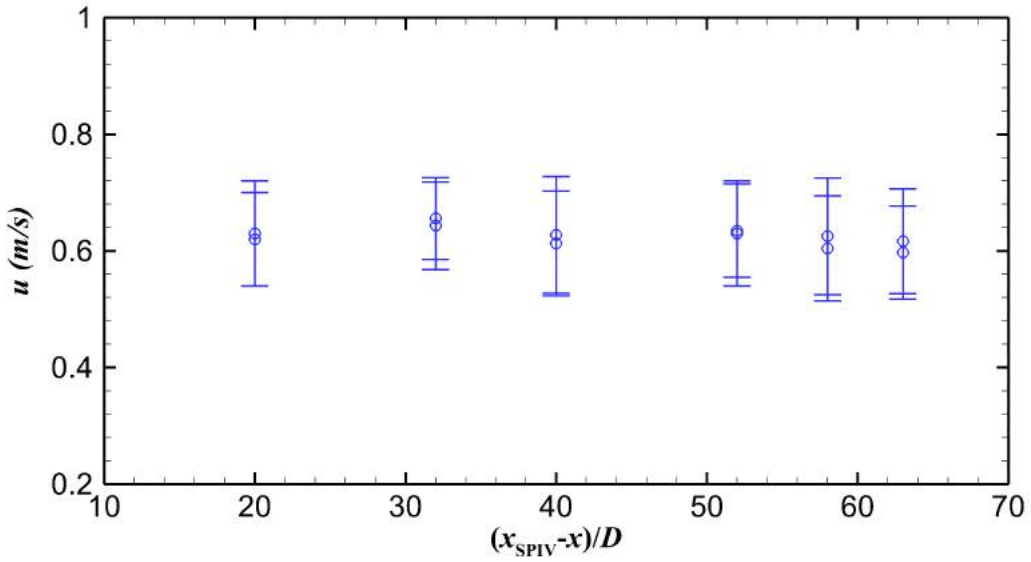

Figure 5.22: Time-averaged streamwise velocity at different axial locations at $Re_w = 4800$ for 0.15% xanthan gum aqueous solution. The blue circles represent the time-averaged value and the blue bars indicate the variation of streamwise velocity.

Figure 5.22 shows the time-averaged mean value and variation of u velocity component at x/D =20, 32, 40, 52, 58, 63, respectively. A slight random difference is observed for the time-averaged velocity for each axial location and this difference could be due to the slight

misalignment of the laser control volume in $r-\theta$ plane when changing the x position. The variation of the u component is linked with the time-varying nature of the asymmetry, as the flow asymmetry alters azimuthal angle around the favoured $r-\theta$ location which leads to the variation of the u velocity component at fixed point, see subsection 5.3.3. Although the pointwise LDV measurement could not provide the full picture of the velocity distribution at the different axial positions, the essentially unchanged mean velocities for fixed point in $r-\theta$ plane indicate the asymmetry does not have a helical structure.

5.7 Conclusions

In this section, the time-varying nature of asymmetry was first revealed and the preferred asymmetry location was observed to be *Re*-dependent. Then we discovered that after exceeding a critical Reynolds number, the asymmetry starts to grow in the form of a supercritical bifurcation with square-root dependence on Reynolds number before the onset of turbulent puffs, and the opposite to what was previously believed is that the laminar-turbulent transition process is responsible for restoring the flow into axisymmetry. From this experimental evidences we could get such a scenario of the asymmetry: for the shear-thinning fluids, the asymmetry is induced by the instability of the laminar base state and grows with increasing Reynolds number, however, when the flow is in the laminar-turbulent transition regime, the dynamics of turbulence dominate the flow and break these asymmetrical flow pattern and returns the flow into axisymmetry.

Chapter 6

Effect of shear-thinning characteristics on asymmetry

In this chapter, we study how the shear-thinning characteristics of working fluid affect the flow asymmetry. In order to do this, we use aqueous solution of xanthan gum in a range of concentrations, namely, 0.07%, 0.08%, 0.1%, 0.125%, 0.15% and 0.2%. The existing studies, regardless of previous LDV or current SPIV investigations, have already strongly implied that the asymmetry is triggered by the shear-thinning property of the fluid. This chapter elaborates on how the behaviour of the asymmetry varies when the shear-thinning characteristics of fluid alters. A number of questions can be naturally put forward when the concentration of the fluid changes:

- how the degree of asymmetry varies with different concentrations?
- how the critical Reynolds number for transition from axisymmetry to asymmetry varies?
- does the asymmetry develop in the similar form as that of 0.15% xanthan gum solution which is highlighted in *chapter 5* for other concentrations?

The following investigation answers these questions.

6.1 Test fluids

Due to the 'rod-like' molecular structure of the xanthan gum polymer, the fluid is essentially inelastic and viscoelasticity is neglected in the range of nominal concentrations from 0.07% to 0.2% in this study [95]. In the mixing process, the mixing (shearing) time varies to attain a homogenous fluid for different concentrations, therefore, the fluid preparation procedures are first introduced in subsection 6.1.1. The rheological properties were also measured to quantitatively describe the shear-thinning characteristics for comparison purposes in subsection 6.1.2. A generalized Reynolds number Re_{MR} is also introduced in subsection 6.1.3.

6.1.1 Preparation of test fluids

The selection of concentrations of the working fluid is subject to the need to acquire distinguishable non-Newtonian behaviours at viscosities adequately low for all Reynolds numbers to be achievable at the mass flow rates which the pump can obtain. All the xanthan gum polymer utilized in the project is the food grade KELTROL® xanthan gum from CP Kelco manufacturer in the form of a powder. The xanthan gum polymer is dissolved in approximately $750L$ volume of tap water (in addition of 75 ppm formaldehyde, the concentration value is recommended in [137]) and the weight of xanthan gum solute for different concentrations is calculated based on this water volume. Before the mixing, the facility was initially operated with water only to remove any bubbles or dissolved air. When there are no visible bubbles or dissolved air in pipe, the mixing-loop then closed off and the fluid mixed with the xanthan gum powder in the tank separately.

In the mixing process, the xanthan gum was gradually added into the mixing tank and mixed for several hours at a low pump speed until no xanthan gum was visible in the mixing tank. Then the mixing-loop was opened again and the fluid circulated around the entire pipe system until it was visibly homogeneous. The mixing time (shearing time) to attain homogeneity varied for different concentrations of xanthan gum solution but the shear strength was strictly

controlled during the mixing process. The pump speed was constantly set to 5Hz and the corresponding mixing shear rate near the pipe wall was approximate 20-40 s^{-1} calculated from the pressure drop measurement in conjunction with rheological data for different concentrations. In the mixing procedure, the higher concentration solution required a several hours longer mixing time to attain complete homogeneity. The mixing (shearing) time of the lowest concentration (0.07%) xanthan gum solution was roughly about 20 hours, i.e. 10 hours in mixing tank and 10 hours circulations in the whole pipe system and the mixing time of the highest concentration (0.2%) was up to 35 hours, i.e. 20 hours in mixing tank and 15 the hours in pipe. After the fluid was uniformly mixed (tested by the rheological data at different positions in the pipe), the fluid was left to rest for several hours to return to ambient temperature. The deviation of fluid temperature for all sets of experiments varied from 18.2^{o} C to 18.8^{o} C, with the measurement location located near the pipe inlet. The rheological data of different concentrations of fluid will be presented in the following section.

6.1.2 Discussion of rheological results

A comparative study of viscometric properties of different concentrations was conducted to characterize the shear-thinning ability of the xanthan gum aqueous solutions. To ensure the consistency of the rheological data, all the viscosity measurements were implemented using the TA instruments AR 1000N controlled shear stress rheometer with 6 *cm* and 2^{o} cone geometry. The measuring temperature was all set to 20 ^{o} C using the water bath. The shear viscosity curves of xanthan gum solution at different concentrations are depicted in Figure 6.1.

The shear-thinning feature of fluid was apparent for all concentrations of xanthan gum solutions with higher concentration having a higher zero-shear rate viscosity and a higher degree of shear thinning. The shear-thinning region extended to a lower shear rate with increasing fluid concentration. For all concentrations of fluid, the rheological data exhibited power-law characteristics over three decades of shear rate $\sim$ (1-1000 s^{-1}). At high shear rates ($>$1000 s^{-1}), the apparent viscosity increased slightly which is caused due to the onset of a secondary flow.

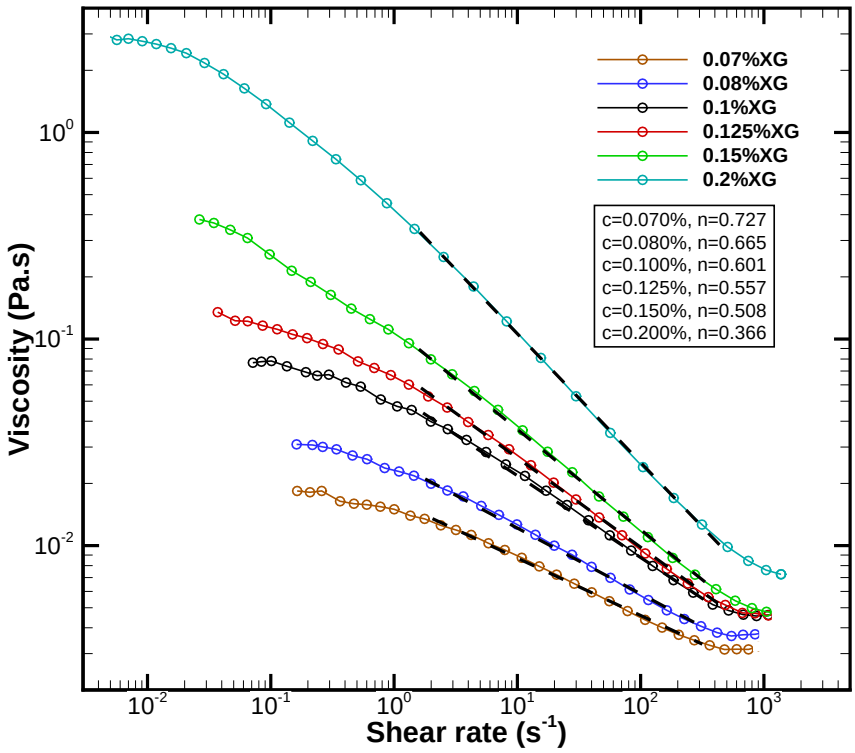

Figure 6.1: The effect of polymer concentration on viscosity curves of xanthan gum aqueous solutions. The dashed line illustrates the slope of the viscosity versus shear rate data indicating the shear-thinning characteristics of fluid.

The shear rate regions experienced by the fluid at the pipe wall from purely laminar to fully turbulent were all in the shear-thinning region of the flow curve. The viscosity data was locally fitted in the shear rate range corresponding to the shear rate at the wall of the flow in the pipe facility at approximately $1000 < Re_w < 13000$ by the power law model and the power law index is used to quantitatively indicate the extent of shear-thinning. The higher concentration of fluid possessed lower flow shear-thinning index (n) indicating increasing shear-thinning characteristics, see Table 6.1. The quantitative rheological characterization for different concentrations of fluid allows us to investigate the effect of the degree of shear-thinning on the asymmetry.

concentration (%)	0.07	0.08	0.1	0.125	0.15	0.2
flow behaviour index n	0.727	0.665	0.601	0.557	0.508	0.366
flow consistency index k (Pa·s^n)	0.016	0.027	0.056	0.074	0.1163	0.4604

Table 6.1: The flow behaviour index n and flow consistency index k of different concentrations of xanthan gum solution using power-law fitting.

6.1.3 Definition of Reynolds number

Due to the intrinsic complication of viscosity involved in non-Newtonian fluids, a variety of Reynolds number definitions (i.e. the ratio of inertia to viscous forces) have been proposed to analyze non-Newtonian flows [25]. The definition of Reynolds number adopted in *chapter 5* is based upon wall shear viscosity i.e. $Re_w = \rho U_b D/\mu_w$, where μ_w is derived from pressure-drop measurements in conjunction with rheological data. The Re_w definition is appropriate in many applications [124], e.g. in turbulent pipe flows or in pipe flows with sudden changes in cross-sectional area [123] and adopting the Re_w definition is also consistent with previous LDV studies on the pipe flow asymmetry. A disadvantage of the Re_w definition is that using Re_w does not provide a unique friction factor f-Reynolds number curve for shear-thinning fluids in the laminar region because the f-Re_w relationship is dependent on the flow behaviour index n in the power-law model. To obviate this difficulty, Metzner & Reed [105], and subsequently followed by numerous other workers [96, 109, 140], outlined a generalized definition of the Reynolds number Re_{MR}, which is widely used to characterize time-independent non-Newtonian fluids. The utility of the generalized definition Re_{MR} is to reconcile the friction factor regardless of the shear-thinning ability of fluids in laminar regime, therefore a unique $f \cdot Re_{MR}$=16 is acquired in laminar flow for shear-thinning and viscoelastic fluids [30, 106, 119]. Chhabra & Richardson's work [25] also suggests for the flow of highly shear-thinning inelastic and viscoelastic polymer solutions, Re_{MR} could give a good $f - Re$ collapse in the range $0.28 \leq n \leq 0.92$ (the fluids utilized in this project are in this region), where n is the flow behaviour index for power-law fluids. In their work, they also suggest the stable laminar flow prevails for inelastic fluids for Re_{MR} up to about 2000-2500.

Since the flow behaviour index n and flow consistency index k of xanthan gum solutions for all concentrations have been obtained from the rheological data fitting by power-law model, it provides an opportunity to apply the Re_{MR} definition (see Equation 6.1) to characterize the flow, particularly in the laminar regime.

$$Re_{MR} = \frac{\rho U_b^{2-n} D^n}{k} 8 \left(\frac{n}{6n+2} \right)^n \tag{6.1}$$

where U_b represents bulk velocity, n is flow behaviour index, k is flow consistency index and Table 6.1 gives corresponding n, k values for different concentrations of xanthan gum solutions. In subsequent investigations, the Re_{MR} definition will be adopted when the flow is in vicinity of laminar regime to reconcile the friction factor and collapse the data in some manner.

6.2 Shear-thinning effect on asymmetric flow pattern

With regard to 0.15% xanthan gum solution, a favoured asymmetric position has been revealed to exist [51, 54]. When the investigations are extended to various concentrations of xanthan gum solution, i.e. different shear-thinning abilities, one of the study objectives is to verify whether the asymmetry does exist in other concentrations and how the asymmetric flow pattern changes if the asymmetry still appears. The asymmetric flow pattern can be primarily characterized by two aspects: the azimuthal and radial positions of the favoured asymmetry location.

In the investigation of 0.15% xanthan gum solution, for a certain fixed Reynolds number, i.e. $Re_w \approx 7439$, which is in the laminar-transitional regime, the SPIV experiments were repeated 21 times with a dimensionless acquisition time t^*=1800 for each run, in order to achieve a good statistical convergence. In the test cases, the asymmetry appeared in the same flavoured azimuthal and radial position. The preferred asymmetry location is Reynolds number dependent: the radius of peak velocity is initially in the centre of pipe when the flow is in the purely laminar regime and when the Reynolds number progressively increases and exceeds the critical Reynolds number, the asymmetry occurs. The degree of asymmetry (indicated by asymmetry

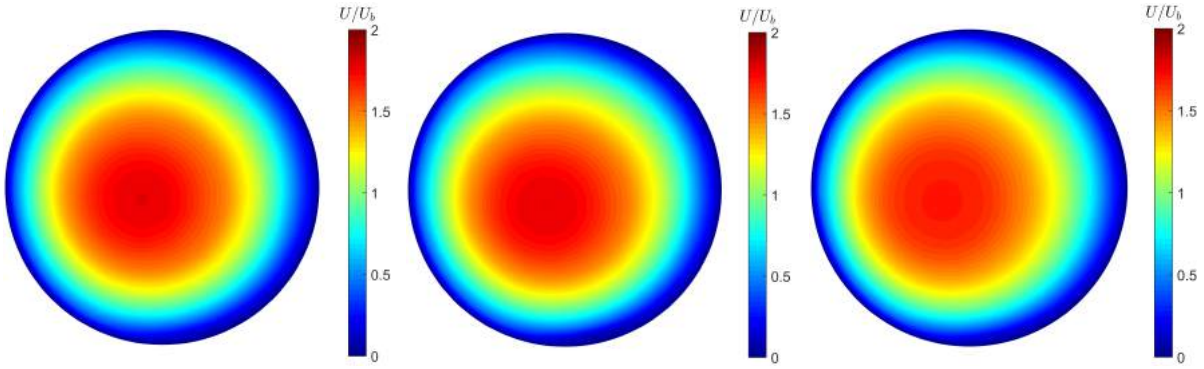

(a) c=0.07%, α≈0.049 (b) c=0.08%, α≈0.061 (c) c=0.10%, α≈0.079

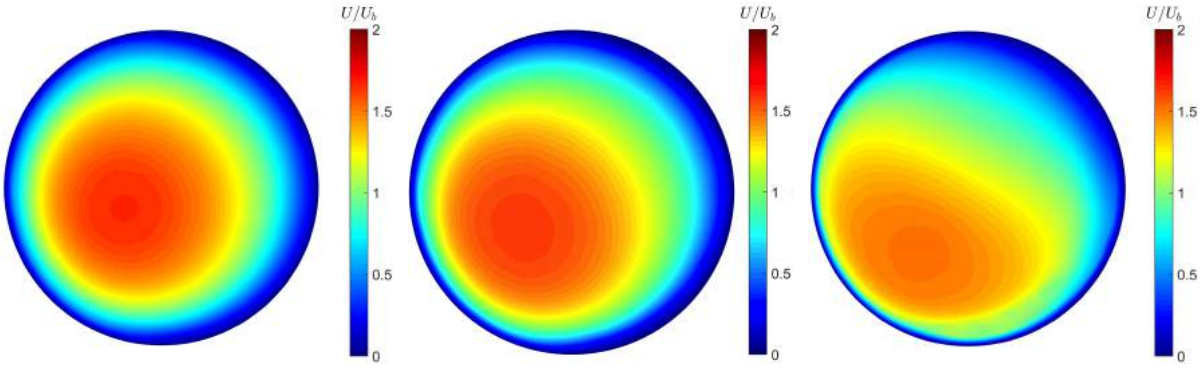

(d) c=0.125%, α≈0.110 (e) c=0.15%, α≈0.163 (f) c=0.20%, α≈0.239

Figure 6.2: The normalized streamwise velocity profiles for various concentrations (c) of xanthan gum solutions. The velocity profile was selected when the maximum degree of asymmetry occurs for corresponding concentrations just before the onset of transition.

factor α or radius of peak velocity r_p/D) grows with the Reynolds number until the emergence of turbulent puffs. The asymmetry actually reaches the maximum degree just prior to the onset of turbulent puffs since the role of turbulent puffs is to return the flow into axisymmetry, as has previously been demonstrated in Chapter 5.

Figure 6.2 compares the time-averaged velocity profiles just before the onset of turbulent puffs for different concentrations of xanthan gum. The favoured azimuthal position of the asymmetry does not demonstrate significant changes when the flow behaviour index of fluid alters from 0.07% to 0.2% as shown in Figure 6.2. However, with the increase of shear-thinning characteristics of fluid, the radius of peak velocity (i.e. a measure of the asymmetry) presents a significant growth. For the flow using 0.07% xanthan gum solution, the observable maximum degree of asymmetry merely shows a slight departure from axisymmetry just above the SPIV

noise. While the shear-thinning characteristics of the fluid grows, the asymmetry becomes more and more apparent. When the concentration is 0.2%, the velocity profile reveals a very distinct asymmetry and the peak velocity region deforms to a strongly elliptical shape.

concentration (%)	0.07	0.08	0.1	0.125	0.15	0.2
flow behaviour index n	0.727	0.665	0.601	0.557	0.508	0.366
flow consistency index k (Pa·s^n)	0.016	0.027	0.056	0.074	0.1163	0.4604
radius of peak velocity r_p/D	0.047	0.064	0.081	0.115	0.166	0.25
asymmetry factor α	0.049	0.061	0.079	0.110	0.163	0.239

Table 6.2: The observable maximum radius of peak velocity and asymmetry factor for different concentrations of xanthan gum solution. The flow behaviour index n and flow consistency index k are obtained using power-law fitting.

The relationship between the maximum degree of asymmetry and shear-thinning characteristics of fluid is given in Table 6.2. The power law model is used to fit the viscometric data due

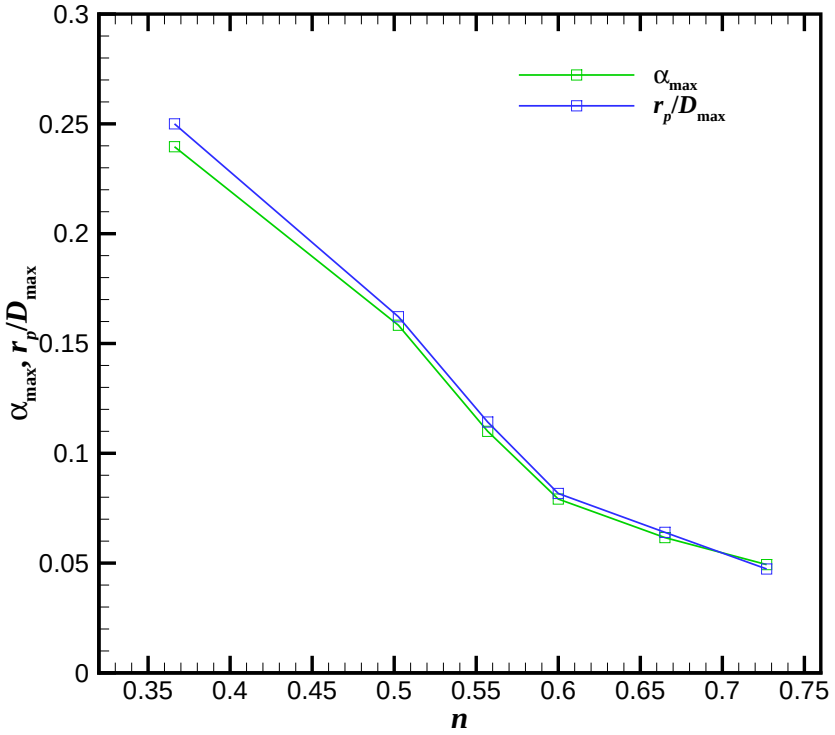

Figure 6.3: The shear-thinning effect on maximum degree of asymmetry indicated by $\alpha_{\max}$ and $r_p/D_{\max}$ using different concentrations of xanthan gum solutions.

to the applicability of the power law model over the shear rate range from 10^0 to 10^4 s^{-1}[132] to obtain the flow behaviour index n and flow consistency index k. Table 6.2 and Figure 6.3 clearly shows that the lower flow behaviour index n, i.e. stronger shear-thinning characteristics yields a higher maximum degree of asymmetry, indicated by both $\alpha_{\max}$ and $r_p/D_{\max}$, revealing the shear-thinning effect on maximum degree of asymmetry. This new experimental data provides a direct evidence to validate the previous common view i.e. the asymmetry is linked to the shear-thinning nature of the fluid and also it reveals the stronger shear-thinning ability of the fluid produces a more significant departure from axisymmetry as depicted in Figure 6.2 and Figure 6.3. In the subsequent content, how the bifurcation process, i.e. axisymmetry to asymmetry transition process, changes with different concentrations of xanthan gum will be studied.

6.3 Shear-thinning effect on bifurcation process

In chapter 5, several methods were implemented to characterize the axisymmetry to asymmetry transition process for 0.15 % xanthan gum solution. The data for the 0.15% xanthan gum solution data exhibits a supercritical bifurcation process in the axisymmetry to asymmetry transition prior to the onset of turbulent puffs at much higher Reynolds number. A similar approach will be applied to analyse the bifurcation process when the shear-thinning characteristics alter in this chapter.

Before discussing the results, the experimental procedures will be described briefly to make clear how the data was obtained. For the experimental datasets of all concentrations, the SPIV measurements were implemented at 5Hz camera frame rate for a time duration of 200 seconds which produces 1000 successive velocity vectors for each run. The dimensionless time t^* varies from a few hundred to a few thousand indicating a flow with a length of a few hundred to a few thousand pipe diameter passing through the laser sheet (measurement plane) for each run. The Reynolds number range for each concentration covers from the purely laminar to the fully turbulent regime and for each individual Reynolds number, each experiment was at

least repeated twice. The pressure-drop measurements were also conduced over a length of 8.2m for all concentrations. The pressure transducer used was always the Validyne® DP-15 transducer but different diaphragms (dash No.20 for 0.07%, 0.08%, 0.1% concentration data and dash No.22 for 0.125%, 0.15%, 0.2% concentration data) were employed to enable the pressure transducer to work in the optimized pressure range (in the range between 1/3 and 2/3 of full scale). The pressure transducers were all calibrated before use and the mean pressure drop and pressure-drop fluctuation could be obtained based on the instantaneous pressure. The Reynolds number was altered by changing the pump speed i.e. bulk velocity of fluid, initially starting from a low pump speed, i.e. a purely laminar state. For each Reynolds number, the SPIV data measurement was implemented once the flow was steady. The flow data in transitional and turbulent flow regimes were acquired towards the end of the experiment to minimize the mechanical degradation of the polymer solution.

In the axisymmetry to asymmetry transition process, the Reynolds number could be selected as Re_w or Re_{MR}. The advantages and disadvantages of using the definition of Re_w and Re_{MR} are discussed in subsection 6.1.3. To reiterate concisely here, the generalized Reynolds number Re_{MR} has the capacity to reconcile the friction data for a broad range of fluids in the laminar regime, such that the data collapses to a single value $f \cdot Re_{MR}$=16. The robustness of the generalized Reynolds number Re_{MR} is relevant to axisymmetry to asymmetry transition process as the onset of asymmetry is indeed in the laminar regime. For comparison purposes, the axisymmetry to asymmetry transition process, applied in both Re_w and Re_{MR} definition, is depicted in Figure 6.4 and Figure 6.5, respectively. Some shared features are observed in the axisymmetry to asymmetry bifurcation process for all concentrations of xanthan gum: the asymmetry appears when the Reynolds number exceeds a critical Re, then the asymmetry starts to grow and the degree of asymmetry depends on Reynolds number. Regardless of the concentration, the asymmetry develops gradually in an apparently supercritical form prior to the appearance of turbulent puffs. This chief distinguishing feature of the axisymmetry to asymmetry transition process arises throughout the different datasets of all concentrations of xanthan

gum and characterizes the flow before the laminar turbulent transition. When turbulent puffs emerge, which is indicated by an increased pressure fluctuation level and velocity fluctuation in $r-\theta$ plane, the intense shearing in the turbulent puff violently breaks the distinct asymmetric flow pattern and turns it into the flow pattern characterized by some chaotic turbulent velocity fluctuations, which will be statistically axisymmetric in a long time average and is instantaneously quasi-axisymmetric. These prevalent characteristics of flow asymmetry are observable in all xanthan gum solutions without exception.

However, besides this common ground, obvious discrepancies can be seen in the axisymmetry to asymmetry transition process when shear-thinning characteristic of the xanthan gum solution changes. The maximum degree of asymmetry (indicated by $\alpha_{\max}$ and $r_p/D_{\max}$) is clearly reduced when the shear-thinning ability decreases (indicated by higher flow behaviour index n). For the 0.2% xanthan gum solution, which is the largest concentration, the maximum dimensionless radius of the peak velocity is 0.25 pipe diameter (i.e. $r_p/D_{\max}$=0.25) and a pronounced asymmetry was visible. The maximum degree of asymmetry in 0.2% xanthan gum solution was approximately 5 times larger than that of 0.07% solution, which the maximum dimensionless radius of peak velocity was roughly 0.05 pipe diameter.

At fairly low Reynolds number, the flow is in the axisymmetric equilibrium state, which can be referred as *laminar base flow*. In laminar base flow, the asymmetry indicators, α and r_p both have a small value which is a consequence of SPIV measurement noise and the velocity profile is observed axisymmetric and stationary in time. With increasing *Re*, the flow starts to bifurcate from this axisymmetric purely laminar flow. The Reynolds number can be interpreted as the distance to equilibrium state in laminar base flow and due to the intrinsic complexity of defining the Reynolds number in non-Newtonian fluids, herein two different definitions of *Re* are introduced and employed for comparison shown in Figure 6.4 and 6.5.

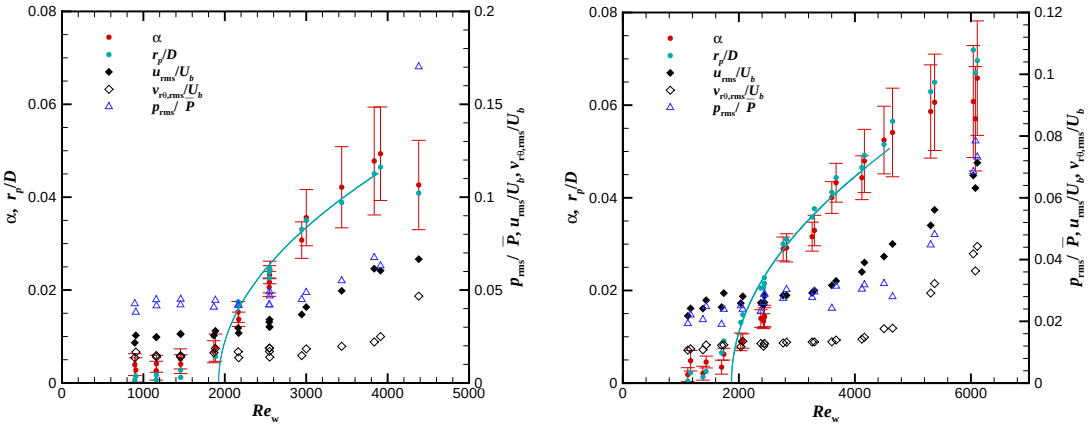

(a) c=0.07%, n≈0.727 (b) c=0.08%, n≈0.665

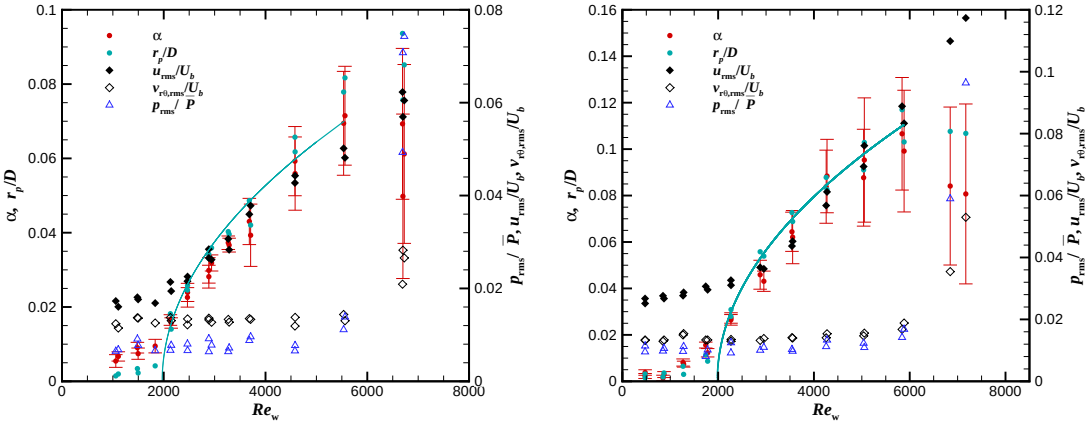

(c) c=0.10%, n≈0.601 (d) c=0.125%, n≈0.557

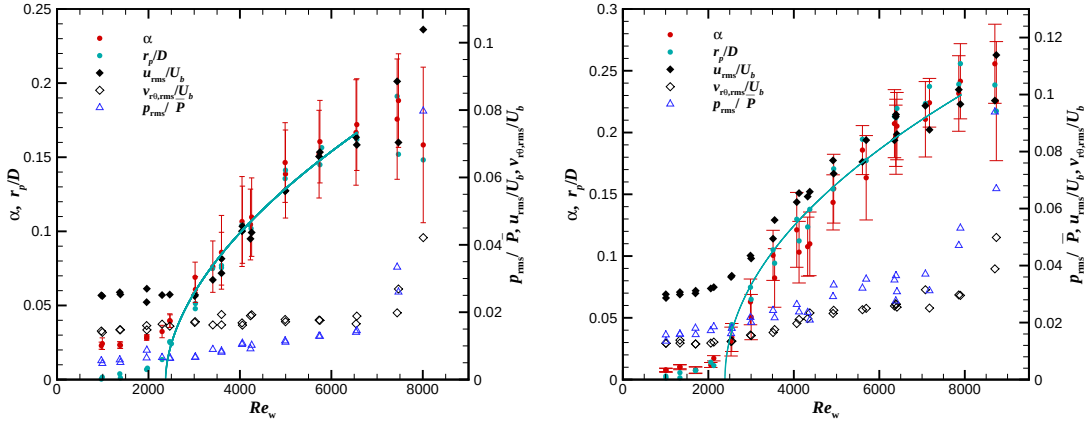

(e) c=0.15%, n≈0.508 (f) c=0.20%, n≈0.366

Figure 6.4: The axisymmetry to asymmetry transition process for various concentrations of xanthan gum solution. The Re_W is selected to measure the distance to equilibrium state in laminar base flow, c represents the polymer concentration and n is the flow behaviour index.

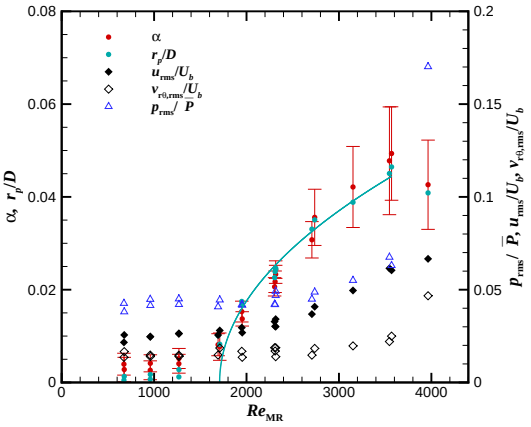

(a) c=0.07%, n≈0.727

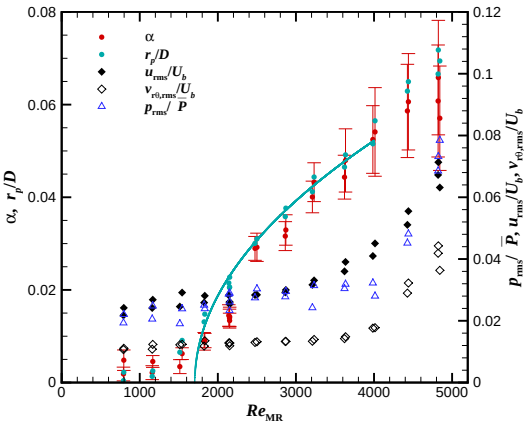

(b) c=0.08%, n≈0.665

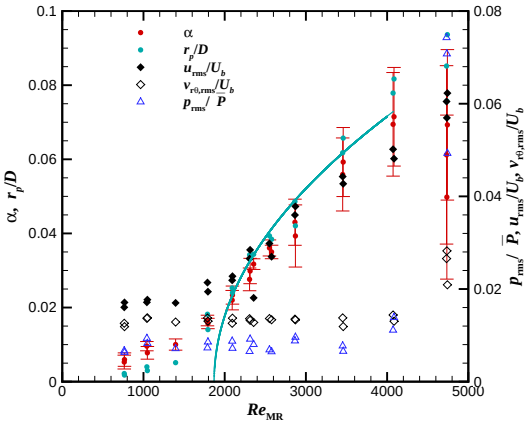

(c) c=0.10%, n≈0.601

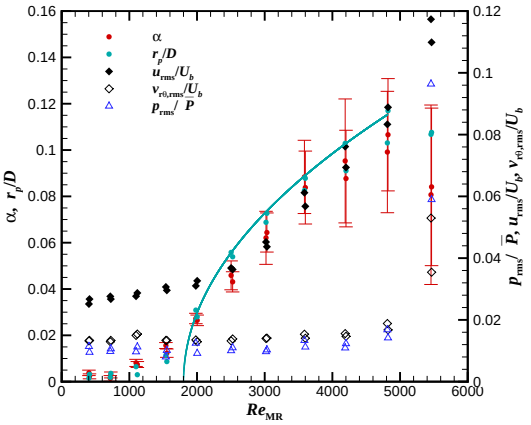

(d) c=0.125%, n≈0.557

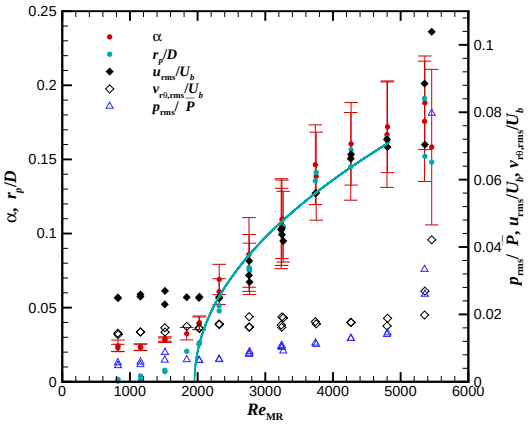

(e) c=0.15%, n≈0.508

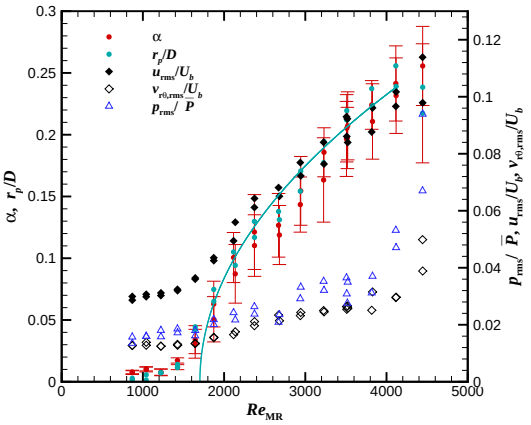

(f) c=0.20%, n≈0.366

Figure 6.5: The axisymmetry to asymmetry transition process for various concentrations of xanthan gum solution. The generalized Reynolds number Re_{MR} is selected to measure the distance to equilibrium state in laminar base flow, c represents the polymer concentration and n is the flow behaviour index.

A notable feature in all axisymmetry to asymmetry transition processes is that the asymmetry evolves continuously in the form of supercritical pitchfork bifurcation. The supercritical bifurcation results in the non-hysteretic behaviour due to the continuous evolution between the bifurcated states and the existing experimental evidence in chapter 5 already revealed the presence of the pitchfork bifurcation behaviour and non-hysteresis feature in 0.15% xanthan gum solution, which is suggestive of a linear instability leading to the asymmetry. When the control parameter (Re) exceeds the bifurcation threshold (i.e. the critical Reynolds number), the bifurcation state develops with an approximately square root dependence on Re. The square root relationship was obtained from the free parameter fitting as shown in Equation 6.2:

$$r_p/D = a \cdot (Re - Re_c)^b \tag{6.2}$$

where Re_c is the critical Reynolds number, b is the fit value in free parameter fitting and a is the coefficient. The identical free parameter curve fit method was applied to all concentrations of xanthan gum solution in axisymmetry asymmetry transition process. The asymmetry indicator r_p was selected for the curve fit as the r_p shows a smaller error (close to theoretical value of 0) in the laminar base flow. The fit is depicted using a solid cyan curve in Figure 6.4 and 6.5. This fit of the radius of peak velocity broadly describes the axisymmetry-asymmetry transition process and comparison of these transition processes provides an opportunity to investigate the effect of shear-thinning characteristics on the asymmetry. Since the square root dependence on Reynolds number in pitchfork supercritical bifurcation process was already revealed, the fit value b in Equation 6.2 was fixed to 0.5 thus the fit function is in the form of $r_p/D = a \cdot (Re - Re_c)^{0.5}$, where r_p/D is the dimensionless radius of peak velocity, Re is the Reynolds number based on the wall stress viscosity and Re_c is the critical Reynolds number which is the bifurcation threshold. The fitting data range was selected near the critical Reynolds number in which the Re is roughly between 2000 and 3000 as the square-root behaviour is excepted near the bifurcation point. The fitting curve matches with the experimental data well in the vicinity of the critical Reynolds number, which suggests the pitchfork supercritical bifurcation prevails in all concentration data as shown in Figure 6.4 and 6.5. The vertical red bar of r_p data was

not strictly the uncertainty of the experiment but is provided to demonstrate the variation of the asymmetry which results from the time-varying nature of asymmetry. The higher variation of r_p at higher Reynolds numbers physically indicates the asymmetry moves around the favoured asymmetry location more significantly.

To further examine the goodness of square root fit of r_p/D, the residual sum of squares (RSS) of the fitting curve using the Levenberg-Marquardt algorithm [113] are calculated using OriginLab®. This method is essentially a least squares estimation technique, demonstrated in Equation 6.3:

$$RSS = \sqrt{\sum_{i=1}^{n} (y_i - f(x_i))^2} \tag{6.3}$$

where y_i is the i^{th} value of the variable to be predicted, x_i is the i^{th} value of the explanatory variable, and $f(x_i)$ is the predicted value of y_i in curve fitting.

The residual sum of squares measures the discrepancy between the data and an estimated fitting curve, therefore the RSS is capable of indicating the goodness of the fit and a small RSS value demonstrates a tight fit of the model to the data. The RSS of free parameter curve fitting, i.e. using $r_p/D = a \cdot (Re - Re_c)^b$, where b is free to vary, is listed in Table 6.3. The objective of comparing the RSS between the square root fit and free parameter fit is to evaluate the goodness of fixed square-root fitting for all concentrations of solution. When the free parameter fit was applied to low concentration data, i.e. 0.07% and 0.08% data, the power law index was slightly higher than 0.5, being 0.65 and 0.62, respectively as shown in Table 6.3. This is because the degree of asymmetry in low concentration is much less pronounced than that of high concentration solution thus the relative error of r_p is comparatively high, particularly in the vicinity of the critical Reynolds number, introducing some curve fit error. This uncertainty is pertinent to the moderate resolution of SPIV technique as the pipe diameter is 10 *cm* therefore a large field of view is a prerequisite but there is a limitation in the fixed number of camera pixels (1280×800 pixels). The analysis of 0.15% xanthan gum solution data, which the asymmetry is very pronounced i.e. low relative error, reveals that the pitchfork supercritical bifurcation characterizes the flow with square-root dependence with Reynolds number, therefore, the fixed

square root fitting was applied to all concentration of data. The residual sum of squareness for free parameter fitting and square root fitting are listed in Table 6.3 below:

concentration (%)	RSS of square root fit	RSS of free fit	Relative deviation	b
0.07% XG	1.7632E-5	1.2412E-5	29.5 %	0.65
0.08% XG	1.7276E-4	1.3084E-4	24.2 %	0.62
0.10% XG	5.9577E-4	4.8744E-4	18.1 %	0.58
0.125% XG	7.5440E-4	7.3178E-4	3.1 %	0.49
0.15% XG	1.3100E-3	1.1034E-3	16.0 %	0.55
0.2% XG	5.5900E-3	4.8020E-3	14.1 %	0.53

Table 6.3: Comparison of residual sum of squares (RSS) in square fit and free parameter fit using Levenberg-Marquardt algorithm, where b is the fit value in Equation $r_p/D = a \cdot (Re - Re_c)^b$.

The free parameter fit in Table 6.3 indicates that for low concentration data (0.07% and 0.08%), the power indexes slightly deviate from square root dependence and for higher concentration data (greater than 0.10% xanthan gum solution), the power law index was approximately to 0.5. The residual sum of squares (RSS) in free curve fitting and fixed parameter fitting are both calculated to indicate the goodness of fitting. The discrepancy between the two different fitting methods is illustrated by relative deviation, which is determined by subtraction of RSS of square root fit and free fit and then normalized by RSS of free fit, shown in Equation 6.4:

$$\text{relative deviation} = \frac{\text{RSS of square root fit} - \text{RSS of free fit}}{\text{RSS of square root fit}} \tag{6.4}$$

Relatively large deviation values are found in the low concentration cases. This can be explained that in low concentration, i.e. low shear-thinning characteristics, the degree of asymmetry is not as pronounced as that in high concentration, therefore yields a larger relative error. However, in general, the power index reasonably agrees with the square root dependence for all concentration data as the maximum power index is 0.65 in 0.07% case and for higher concentration cases, the power law index is approaching 0.5 which is suggestive of the pitchfork supercritical bifurcation dominates the axisymmetry asymmetry transition process.

In all concentration data, the asymmetry is characterized by a time-varying nature and the asymmetric flow pattern sways around the *Re*-dependent preferential asymmetric position, which gives high axial velocity fluctuations u_{rms}/U_b. The asymmetry gradually grows

to the maximum degree of asymmetry in the form of supercritical pitchfork bifurcation and the achievable maximum degree of asymmetry, prior to the onset of turbulence, is linked with shear-thinning characteristics of fluid.

6.4 Effect of shear-thinning on critical Reynolds number

Figure 6.6 illustrates the effect of shear-thinning on the critical Reynolds numbers from the axisymmetry to asymmetry transition, laminar to turbulent transition and the maximum degree of asymmetry achievable. The critical Reynolds number for the axisymmetry to asymmetry transition is represented by Re_{c1} and the critical Reynolds number for laminar to turbulent transition is represented by Re_{c2}. Once again, different definitions of Reynolds number are introduced: the generalized Reynolds number Re_{MR} and Re_w which is based on the wall viscosity. To recap each of the approaches to define the Reynolds number have their own advantages and disadvantages. In laminar regime, the Metzner-Reed Reynolds number Re_{MR} reconciles the friction factor data for all shear-thinning characteristics, therefore a unique $f \cdot Re_{MR}$=16 curve collapses the data [124]. When the flow is dominated by turbulent characteristics, the Re_w definition is more widely used [123] as the near-wall flow events are more active, thus the wall shear stress viscosity is a good parameter to characterize the flow. Understanding the advantages and disadvantages of the different definitions of Reynolds number is helpful to select which Re definition is more applicable in certain flow regime. With regards to critical Reynolds number Re_{c1}, the Re_{MR} is more appropriate to non-dimensionalize the flow as the onset of the axisymmetry to asymmetry transition occurs in the laminar regime. For the critical Reynolds number Re_{c2}, since the turbulent puff emerges, the Re_w definition is perhaps more appropriate to employ considering the active turbulent flow dynamics near the wall.

The effect of shear-thinning on critical Reynolds number Re_{c1} and Re_{c2} is revealed in Figure 6.6. The critical number Re_{c1} is determined by the intersection point of r_p fitting curve and x-axis i.e. Re-axis in Figure 6.4 and 6.5. The error bar of Re_{c1} is set to a value which is

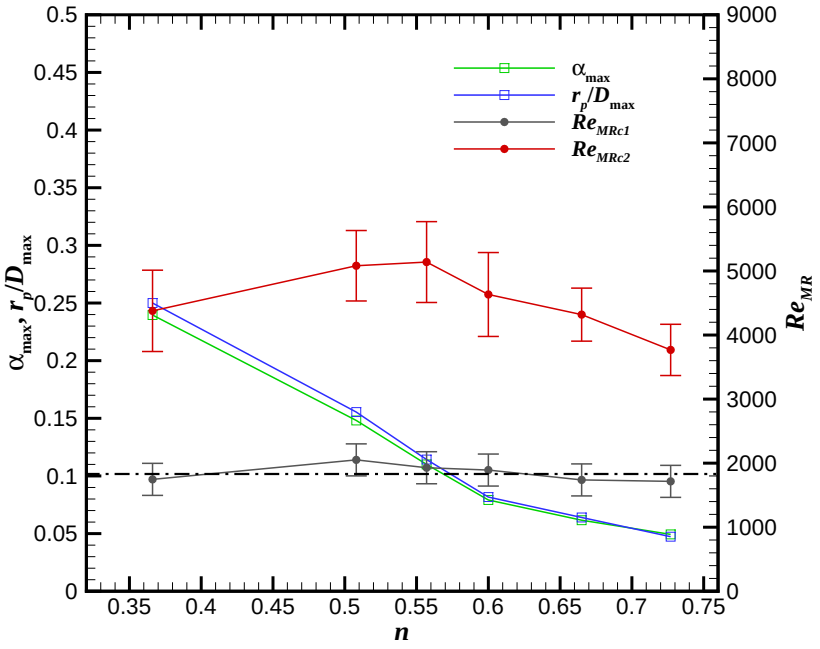

(a) based on Re_{MR}

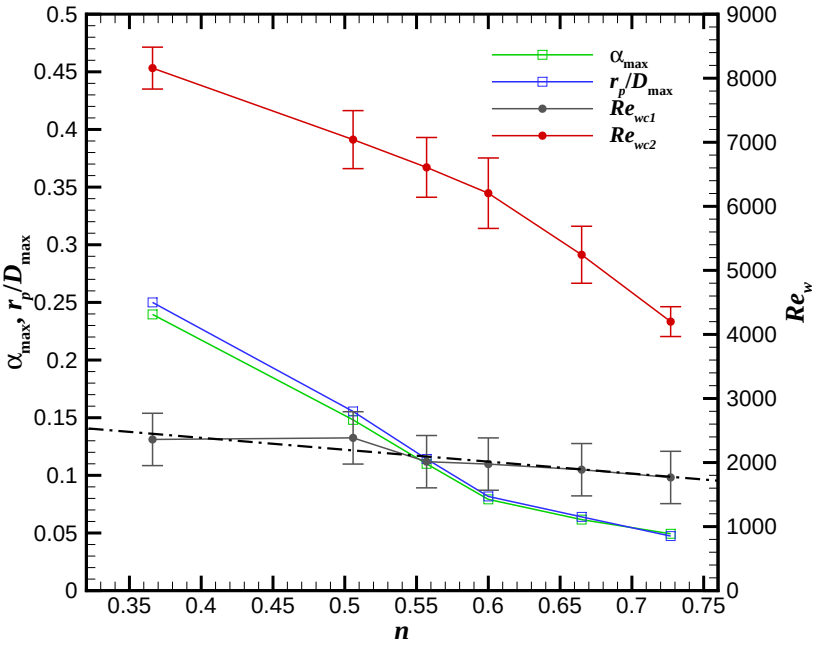

(b) based on Re_w

Figure 6.6: The shear-thinning effect on the critical Reynolds number for transition from axisymmetry to asymmetry (Re_{wc1}, Re_{MRc1}) and transition from laminar to turbulent (Re_{wc2}, Re_{MRc2}) together with maximum degree of asymmetry ($\alpha_{\max}$, $r_p/D_{\max}$). The dashed line indicates the variation trend of critical Reynolds number.

determined by subtracting the maximum Re_{c1} and minimum Re_{c1} throughout all concentration data. The dashed line represents a linear fit of the critical Reynolds number Re_{c1}. If the Metzner-Reed Reynolds number Re_{MR} is used to identify transition from axisymmetry to asymmetry, the value of Re_{MRc1} is generally unchanged, which is indicated by the dot dash line at value of Re_{MRc1}=1820. This suggests that the point at which the flow bifurcates does not depend on the shear-thinning characteristics of the fluid and is perhaps universal. In terms of the critical Reynolds number Re_{c2} for the laminar to turbulent transition process, Re_{wc} is selected to analyse the flow. The Re_{wc} is approximated as the mean value between the measurement Reynolds number at which a turbulent puff is first observed and the measurement Reynolds number just prior to this in laminar regime. The error bar of Re_{wc} is calculated by the difference between the two measurement Reynolds numbers either side of transition. The Re_{wc2} in 0.07% xanthan gum is approximately 4000, which is at the end of the range higher for Newtonian fluids (roughly $2000 < Re_{wc2} < 4000$). With increasing shear-thinning characteristics of fluid, the onset of turbulence is further delayed, indicating that shear-thinning delays the onset of laminar-turbulent transition. This conclusion is consistent with previous work reported in earlier work [18, 54, 64].

The stronger shear-thinning characteristics were also observed to enhance the degree of asymmetry. The maximum degree of asymmetry, demonstrated by $r_p/D_{\max}$ and $\alpha_{\max}$, increased along the growing shear-thinning characteristics of xanthan gum solutions. The maximum radius of peak velocity $r_p/D_{\max}\approx$ when $n \approx$0.37 is 0.25, which is five times greater than that ($r_p/D_{\max}\approx$0.05) when n is about 0.73. For the Newtonian fluids, where the flow behaviour index n is 1, no asymmetry was observed. The r_p and α curves illustrate a trend that the degree of asymmetry asymptotically approaches to zero when the flow behaviour index tends to 1.

The axisymmetry to asymmetry transition processes for all concentrations of fluids are depicted in Figure 6.7. The transition processes are illustrated by the fit curves of radius of peak velocity r_p, indicating the evolution of asymmetry along with the increasing Reynolds number. The data fit range was in vicinity of critical Reynolds number for transition from axisymmetry

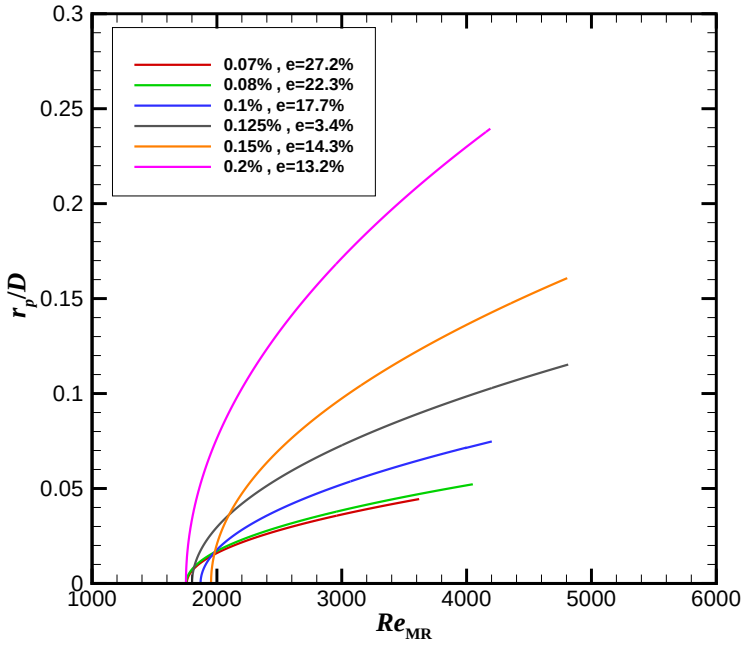

(a) Re_{MR} is selected

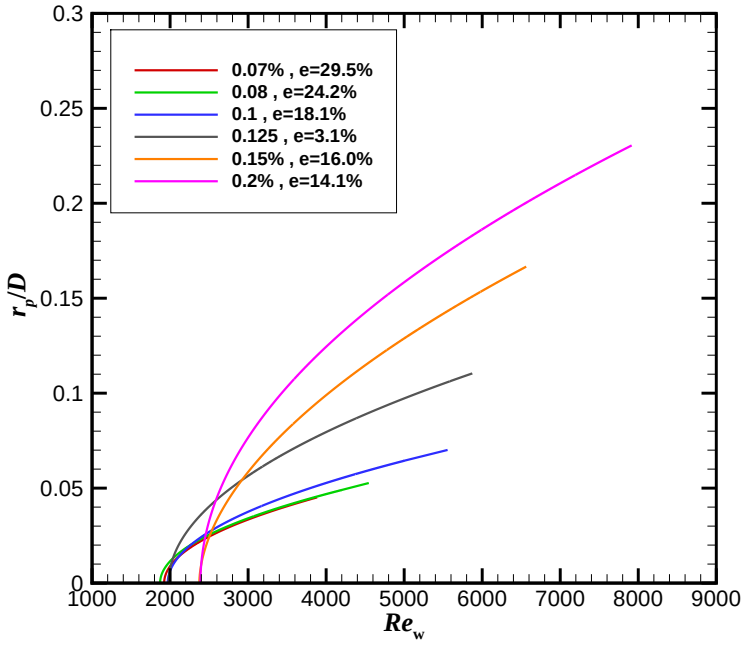

(b) Re_w is selected

Figure 6.7: The axisymmetry asymmetry transition process for different concentrations of fluids. The uncertainties of fit curves (e) are evaluated based on the calculation of residual sum of squares (RSS) of each curve. The supercritical pitchfork bifurcation characterizes the transition process suggesting the appearance of the linear instability of the laminar base flow.

to asymmetry after the asymmetry was observed to appear. This results from the fact that when the Reynolds number continues to grow, the turbulent puff will appear and dominate the flow thus the bifurcation mechanics will alter, therefore the curve fitting ceases prior to the turbulent puffs. By contrast, the generalized Reynolds number Re_{MR} and wall shear viscosity Reynolds number Re_w were both employed as the bifurcation parameters. For all transition processes, despite the different shear-thinning characteristics of the fluids, the supercritical pitchfork bifurcation characterizes the axisymmetry to asymmetry transition process. This supercritical bifurcation and square root dependence on Reynolds number also suggests the asymmetry is not induced by laminar-turbulent transition process but appears to be a linear instability of the laminar base state.

6.5 Conclusions

In this chapter, the effect of different levels of shear-thinning on flow asymmetry was investigated using xanthan gum solutions with concentrations of 0.07%, 0.08%, 0.1%, 0.125%, 0.15% and 0.2%, respectively. Throughout the data of all tested concentrations, some ubiquitous features of the flow asymmetry are discovered. The experimental observations throughout all solution concentrations demonstrate the asymmetry is prevalent in shear-thinning fluids. Concerning the evolution of the asymmetry, the axisymmetry to asymmetry transition processes are universally observed to conform with supercritical bifurcation behaviour prior to the appearance of turbulent puffs. Once the flow is in the laminar-turbulent transition regime, the turbulent puffs prevail and restore the flow into axisymmetry. In terms of the dataset in a certain concentration, the favoured asymmetry position exists and alters along with Reynolds number when the Reynolds number is beyond the critical Reynolds number. The asymmetry is not stationary and oscillates around the preferential asymmetry position resulting in a variation of asymmetry factor. These are the common features observed in xanthan gum solution despite different shear-thinning characteristics of fluid.

With regards to the shear-thinning effect on the asymmetry, we reveal the higher shear-thinning characteristics enhance the degree of asymmetry. The maximum radius of peak velocity r_p/D significantly increases from approximately 0.05 to 0.25 when fluid concentration rises from 0.07% to 0.2%. The laminar-turbulent transition is studied by monitoring the pressure fluctuations and velocity fluctuations in the $r-\theta$ plane. The onset of turbulent puffs is observed to be delayed in comparison with Newtonian fluids and higher concentration of fluid, i.e. higher shear-thinning characteristics of fluid can further delay the onset of laminar turbulent transition, indicating the shear-thinning nature could possibly stabilize the flow and postpone the critical Reynolds number for transition from laminar to turbulent. The critical Reynolds number Re_{MR} for transition from axisymmetry to asymmetry remains unchanged when the shear-thinning characteristics of the fluid are varied. The asymmetry all emerged at a $Re_{MR} \approx 2000$ despite the different flow behaviour indexes, suggesting a possible unchanged bifurcation threshold. The deviation from the axisymmetric laminar state is observed to develop in the form of a super-critical bifurcation with square-root dependence on Reynolds number prior to the turbulent puff and the greater the shear-thinning characteristics, the stronger the fluid asymmetry appears.

Chapter 7

The effect of viscoelasticity on asymmetry

The previous LDV studies [51, 54] reported that the asymmetry, to varying degrees, had been observed not only in largely inelastic shear-thinning fluids (e.g. xanthan gum solution), but also in some viscoelastic fluids such as polyacrylamide (PAA) solution and yield stress fluids (e.g. carbopol solution). In this chapter, we investigate polyacrylamide solutions at different concentrations as well as polyacrylamide/xanthan gum mixtures by means of the SPIV technique. We also deliberately imposed shear-induced degradation on purely polyacrylamide solution to significantly reduce the viscoelastic characteristics while the shear-thinning characteristics of fluid are largely conserved, therefore allowing us to study the effect of strong viscoelasticity on the asymmetry.

7.1 Flow of polyacrylamide solutions

Polyacrylamide (hereafter referred to as PAA) is extensively used in fundamental research and industrial applications [33, 41, 161]. At moderate concentrations, PAA is shear-thinning with a highly flexible molecular structure which provides a strong viscoelasticity. The PAA used in the project is FLOPAM^{TM} AN934SH supplied by Floerger SNF with a very high molecular weight (20 million g/mol, indicated by manufacturer). At low shear rates, the PAA is in a

randomly coiled molecular structure and with increasing shear stress, the molecular configuration is elongated and eventually becomes a fully extended structure [98]. At high shear rates, the molecular chain suffers some mechanical scissions and thus deteriorates the overall performance of the polymer, particularly the viscoelastic characteristics. The concentrations tested in the project include 0.09%, 0.125% and 0.2% PAA solutions. At these concentrations, all solutions are reported to have a significant drag-reducing property, producing a drag-reduction degree close to the maximum drag reduction asymptote [53].

7.1.1 Rheological characterization

The rheological characterizations of PAA solutions, namely concentrations of 0.09%, 0.125% and 0.2% together with that of 0.15% xanthan gum solution are depicted in Figure 7.1. In the mixing procedure, the lowest attainable pump speed was used to minimize the mechanical degradation. The mixing time of the PAA solution was generally longer than that of xanthan gum solution to obtain a homogeneous state and a suitable amount (at a concentration of 75 ppm) of formaldehyde solution (35% w/w solution) was added to inhibit bacteriological degradation. The distinct shear-thinning characteristics were observed for all concentrations of PAA and the fluids were working in the shear-thinning region when the SPIV experiments were implemented. The reason to select 0.125% PAA solution was that previous work [137] reported that the flow curve of 0.125% of PAA was similar to that of 0.15% xanthan gum indicating a rough matching of the shear-thinning characteristics. The PAA polymer used in [137] was Separan AP273E from SNF UK limited, in a molecular weight of 1.9×10^6 g/mol. However, in current project, the polyacrylamide polymer is FLOPAM^{TM} AN934SH Floerger SNF, which the molecular weight is 20 million g/mol provided by the manufacturer. Due to different polymers used and differences in mixing procedure (e.g. different mixing time, different wall shear stress, different dissolving method of PAA), present rheological measurement indicates the 0.09% concentration of PAA gives the most similar shear-thinning characteristics to that of 0.15% xanthan gum solution, which bas been intensively studied in chapter 5. Due to these

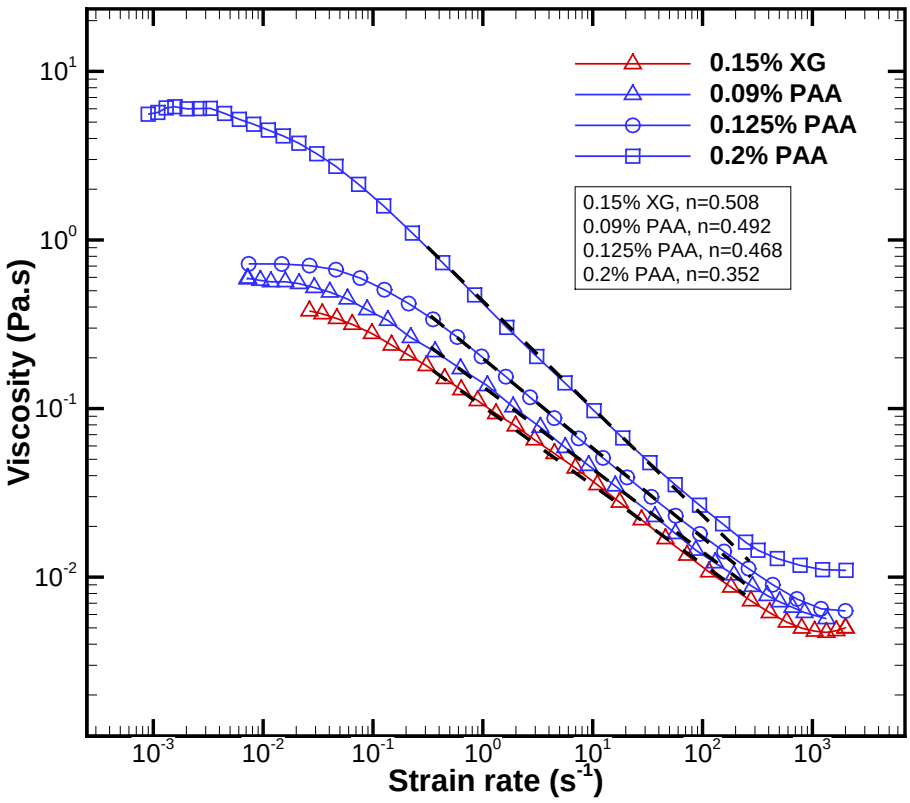

Figure 7.1: Viscometric data for various concentrations of polyacrylamide solutions. The red symbol represents the viscosity data of 0.15% xanthan gum solution for comparison. The black dashed line demonstrates the power law decay of viscosity, indicating different shear-thinning characteristics of fluids, which is described by the flow behaviour index n.

distinctive approaches, the SPIV and LDV technique require different testing time (shearing time) in the experimental process, which leads to a discrepancy in rheology characteristics of fluids. This is because the SPIV provides whole flow field information simultaneously while LDV gives a single point-wise flow information, therefore demanding a much longer measurement time in order to traverse the flow field. This leads to a more severe degradation of polymer solution than that of SPIV. It could also be that in the current case the 0.09% PAA solution match the 0.15% xanthan gum solution because the PAA solution in the current study is much less degraded than that in the previous LDV study.

A higher concentration i.e. 0.2% of PAA solution was also measured as it possesses stronger shear-thinning and viscoelastic properties (shown in Figure 7.1) that will potentially affect the

asymmetry. The shear-thinning characteristics manifested in the flow curves in Figure 7.1 imply the asymmetry may emerge in the flow of the polyacrylamide solution, just as the in inelastic shear-thinning liquid xanthan gum solution. Existing experimental evidence has already illustrated that the shear-thinning nature of the fluid triggers the asymmetry and a stronger shear-thinning characteristics leads to a more pronounced asymmetric flow behaviour. However, this speculation is based on less elastic fluids i.e. xanthan gum solution, and the precise effect of viscoelasticity on the asymmetry onset is yet unknown, although it has been studied previously with LDV, further investigation is still required.

7.1.2 Time-averaged velocity profiles for a range of Reynolds numbers

In this section, the time-averaged velocity profiles of pure PAA solution for Reynolds numbers 2210-7012 were studied to examine the flow asymmetry. Previous LDV studies [51, 54, 69] illustrated that the asymmetry was observable in the PAA solution, thus in the current SPIV investigation the asymmetry was expected to be seen. The SPIV experimental data was collected when the flow was in a steady-state since prior to the implementation of SPIV measurements, the fluid was pumped for a couple of minutes at a constant mass flow rate until a steady state was reached. The camera frame rate was set to 5Hz, and the corresponding acquisition time was 200 seconds. During SPIV observation time of 200 seconds, equivalent to a few hundred to a few thousand pipe diameters of fluid convected through the laser plane (measurement plane), depending on the different bulk velocity, thus the time-averaged velocity profiles were statistically converged.

Figure 7.2 shows the normalized time-averaged streamwise velocity profiles for the range of Reynolds numbers when the concentration of PAA solution is 0.09%. The exponent of the power law variation of viscosity in 0.09% PAA solution is close to that of 0.15% xanthan gum solution, suggesting the similar shear-thinning characteristics. Surprisingly, the flow patterns, even at the highest Reynolds numbers tested, all exhibit an axisymmetric velocity profile and the asymmetry factors are approximately about 0.02, which is due to the SPIV noise (estimated

from the measurement of purely laminar flow using xanthan gum). This results contradictory to previous LDV results, in which a significant asymmetry was observed using the PAA solutions.

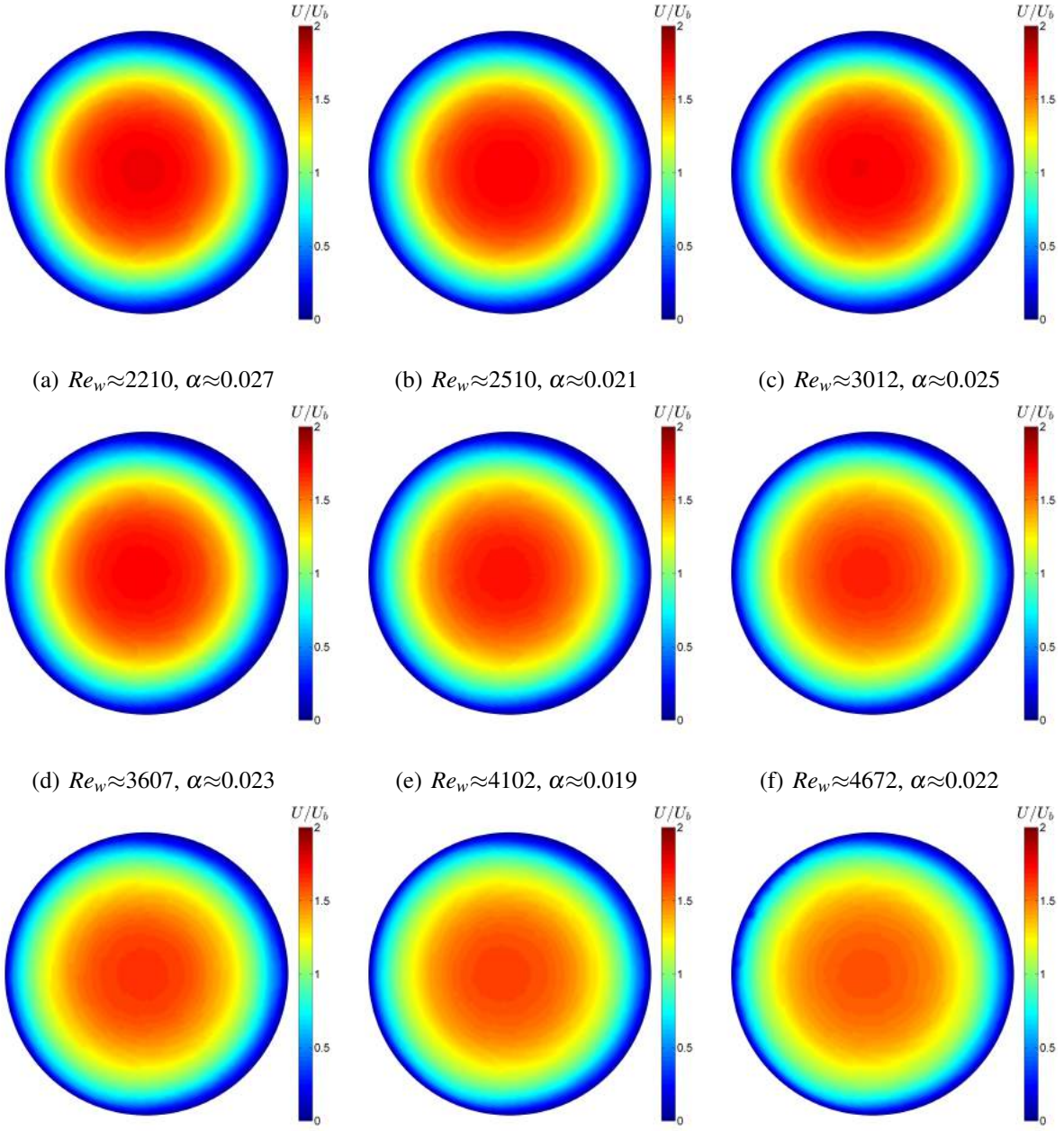

(a) Re_w≈2210, α≈0.027 (b) Re_w≈2510, α≈0.021 (c) Re_w≈3012, α≈0.025

(d) Re_w≈3607, α≈0.023 (e) Re_w≈4102, α≈0.019 (f) Re_w≈4672, α≈0.022

(g) Re_w≈5340, α≈0.025 (h) Re_w≈6240, α≈0.029 (i) Re_w≈7012, α≈0.027

Figure 7.2: The normalized time-averaged streamwise velocity profiles of 0.09% polyacrylamide solution for extended Reynolds numbers. The low asymmetry factors (α) indicate the flow is essentially axisymmetric for all Reynolds numbers tested. Note that the noise level of the SPIV is approximately α≈0.02, which is estimated from the measurements of laminar velocity profiles using xanthan gum solution.

Initially, the speculation is that the absence of the asymmetry results from the fact that the PAA solution was degraded even at low mixing speed, since the PAA solution is known to be much less resistant to mechanical degradation than the xanthan gum solution. However, we compared the pressure drop data before and after experiments at Reynolds numbers of Re_w ≈3607, Re_w≈4672 and Re_w≈6240 and the pressure drop was only increased by 3.9%, 5.5% and 4.6% respectively. This suggests the mechanical degradation indeed existed and weakened the drag-reducing ability of PAA solution, however, the degradation was reasonably low and was not intense enough to indicate the shear-thinning and viscoelastic ability of fluid have been completely destroyed. We also compared with the viscosity curve before and after the SPIV experiment, the shear-thinning characteristics still dominated the fluid after the SPIV experiment, therefore, some as yet unknown mechanics, lead to the suppression of asymmetry despite the shear-thinning characteristics of 0.09% PAA being similar to that of 0.15% xanthan gum solution, where the asymmetry was found.

As no asymmetry was found in the current SPIV investigation, we redid the SPIV experiments using an entirely new mix of 0.09% PAA solution, in which the viscosity curve matched well with the 0.15% xanthan gum solution and still the asymmetry was absent for a wide range of Reynolds numbers in the SPIV observation.

The other concentrations of PAA solutions were also examined since they possessed different shear-thinning and viscoelastic characteristics to affect the asymmetry. The 0.2% PAA was selected as the shear-thinning characteristic of 0.2% PAA was higher than that of 0.15% xanthan gum solution (see flow curve in Figure 7.1), which was supposed to boost the asymmetry to a more pronounced level, at least for xanthan gum solutions as shown in chapter 6. However, still no asymmetry was found for 0.2% PAA. Figure 7.3 shows the radius of peak velocity r_p/D of time-averaged velocity profiles for a range of Reynolds numbers when the concentrations of PAA solution are 0.09% and 0.2%. The mean r_p/D was roughly 0.01, demonstrating the flow was essentially axisymmetric. The fluctuation of r_p/D is due to the SPIV experimental uncertainty and r_p/D did not rise with increasing Reynolds numbers. This is fundamentally

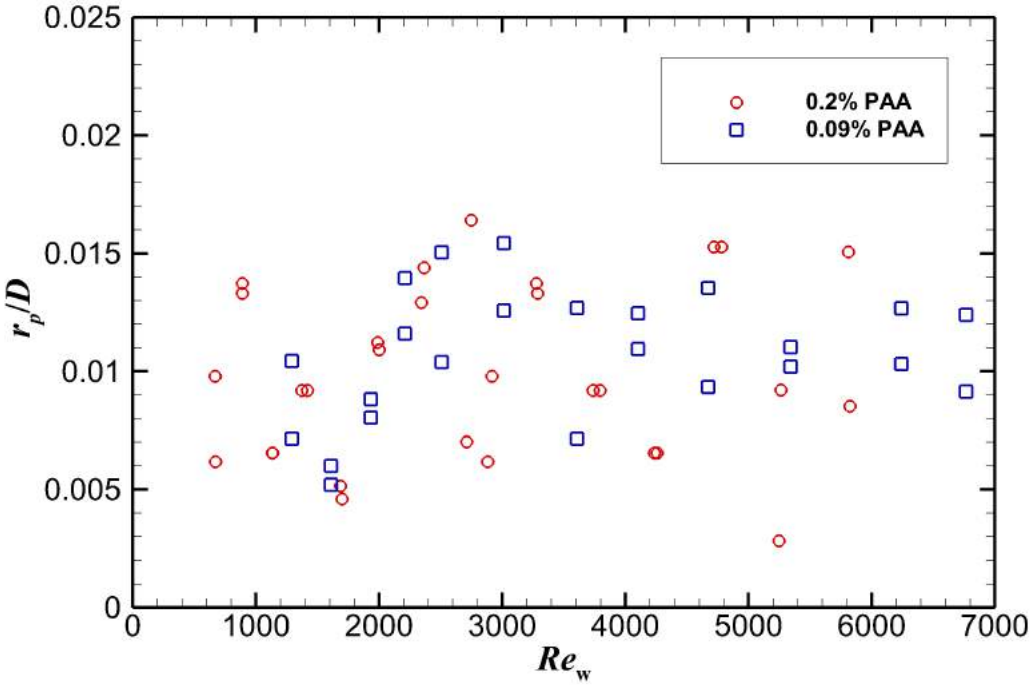

Figure 7.3: The normalized radius of peak velocity r_p/D for a range of Reynolds numbers using 0.09% and 0.2% polyacrylamide solution. The mean r_p/D was approximately 0.01, indicating the absence of asymmetry.

different from the flow scenarios observed in xanthan gum solutions. In the test cases of xanthan gum solutions at different concentrations, the significant asymmetry was observed when the Reynolds number was above approximately 2000 (see Figure 6.7) and the degree of asymmetry increased with Reynolds numbers until the onset of turbulent puffs. The turbulent puffs were observed at different Reynolds numbers for different concentrations of xanthan gum solutions, approximately in the Re_w range of 4000 (0.07% xanthan gun solution) to 8000 (0.2% xanthan gun solution). With regards to PAA solutions, in both of the concentrations tested i.e. 0.09% and 0.2% PAA solution, no asymmetry was observed when Re_w <7000, where the pronounced asymmetry was observed for xanthan gum solutions. For the 0.2% PAA solution, since the fluids is very viscous (see the viscous curves in Figure 7.1), the pressure fluctuation is damped in the tubing which connects the pressure transducer and pressure tapping on the pipe wall, therefore we cannot detect the onset of transition by observing the *rms* of pressure

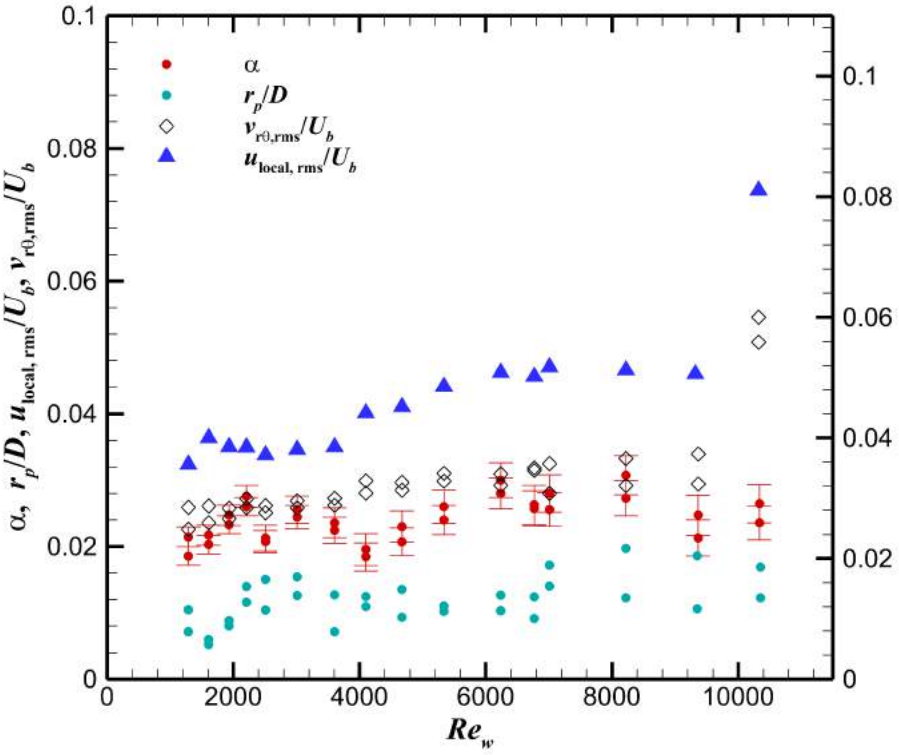

Figure 7.4: The variation of asymmetry factor α and radius of peak velocity r_p/D for different Reynolds numbers when fluid is 0.09% PAA solution. The flow is axisymmetric when the Re_w is up to approximately 10000. The cross-stream velocity fluctuation $v_{r\theta,rms}$ and local streamwise velocity $u_{\text{local,rms}}$ measured by LDV indicate the flow is in transitional regime when Re_w is above 10000.

fluctuation. The velocity fluctuations were calculated in cross-stream plane, i.e. $v_{r\theta,rms}$ to indicate laminar turbulent transition, however, no significant growth of $v_{r\theta,rms}$ was observed even at the maximum pump speed achievable in our rig and the Reynolds numbers Re_w for 0.2% PAA solution at the highest pump speed is 5824 due to the high viscosity of the fluid. Therefore, there is no evidence for 0.2% PAA solution to show the flow is in the transitional regime or not even at maximum pump speed implemented. However, For the 0.09% PAA solution, we set up the LDV device, approximately 20 pipe diameters upstream of the SPIV, in a horizontal plane at $r/R = 0.8$ close to the pipe wall. Figure 7.4 shows the variation of asymmetry factor α and radius of peak velocity r_p/D for different Reynolds numbers for 0.09% PAA solution. No symmetry-breaking bifurcation is observed in purely 0.09% PAA solution as both the asymme-

try factor α and radius of peak velocity r_p/D did not manifest a significant growth even when the flow is transitional at $Re_w \approx 10000$, which is indicated by a jump of cross-stream velocity fluctuation $v_{r\theta,rms}$ and local streamwise velocity $u_{\text{local,rms}}$ measured by LDV. This experimental evidence indicates that for significantly viscoealstic fluid, the asymmetry is suppressed even when the Reynolds numbers are in the vicinity of laminar-turbulent transitional regime.

7.1.3 Instantaneous velocity profiles for a range of Reynolds numbers

The previous subsection discussed the time-averaged velocity profiles of PAA solution in a wide range of Reynolds numbers. No pronounced asymmetry was observed in any of the flow cases (at concentrations of 0.09%, 0.125% and 0.2%) in terms of the time-averaged velocity profiles. In this subsection, the instantaneous velocity profile will be examined to investigate the flow characteristic of PAA solution at different Reynolds numbers.

Figure 7.5 illustrates the instantaneous peak velocity locations of 1000 velocity vector maps for a variety of Reynolds numbers using the 0.09% PAA solution. The peak velocity location was determined as the flow-weighted (weighted by the local streamwise velocity) mean position of the fastest 20% of the flow, a more robust measure than simply the instantaneous maximum velocity of each frame. The peak velocity points were coloured in red initially and in blue ultimately based on time sequence. The velocity profiles were examined in the Reynolds number range from 1290 to 7012. Figure 7.5 clearly demonstrates that, with increasing Reynolds numbers, the flow fluctuation became progressively obvious. At low Reynolds numbers (below 2000), the peak velocity position was generally restricted to one point, indicating the flow was in purely laminar flow. When the Reynolds numbers increased, the distribution of peak velocity position enlarged which is a result of a stronger fluctuation of the flow. However, in general, the peak velocity positions were statistically located in the pipe centre, revealing a time-averaged velocity was still essentially axisymmetric. This instantaneous track of the peak velocity position sheds more light on the flow characteristics of the PAA solution. Some flow instabilities, which are indicated by the stronger velocity fluctuation, were exhibited at high Reynolds num-

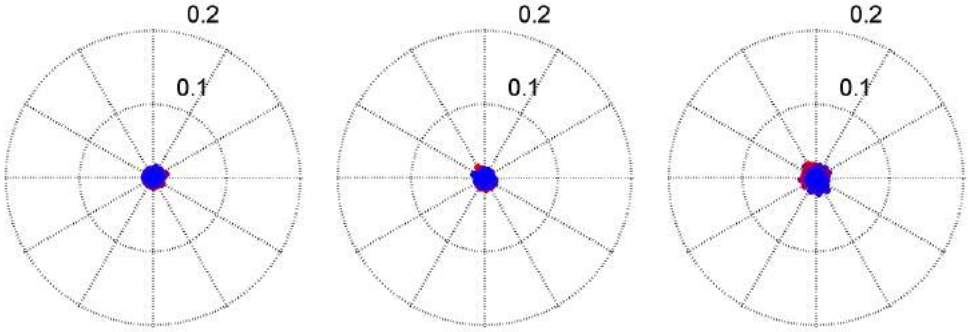

(a) Re_w≈1290, α≈0.020 (b) Re_w≈1610, α≈0.021 (c) Re_w≈1932, α≈0.024

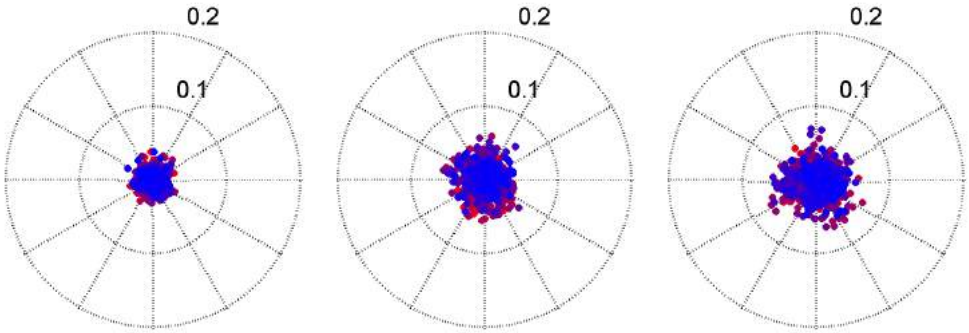

(d) Re_w≈2210, α≈0.027 (e) Re_w≈2510, α≈0.021 (f) Re_w≈3012, α≈0.025

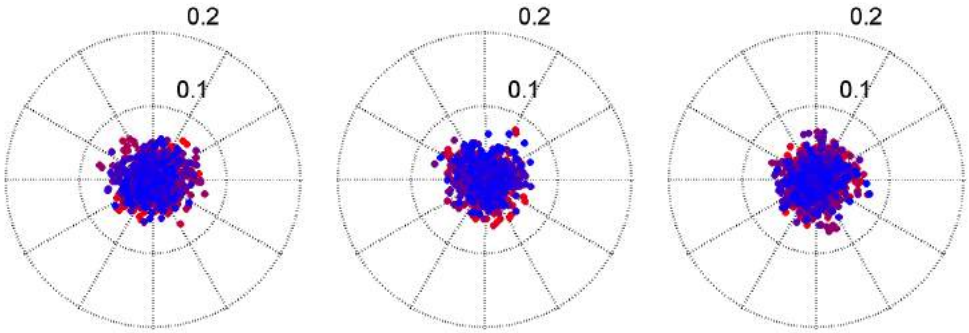

(g) Re_w≈3607, α≈0.023 (h) Re_w≈4102, α≈0.019 (i) Re_w≈4672, α≈0.022

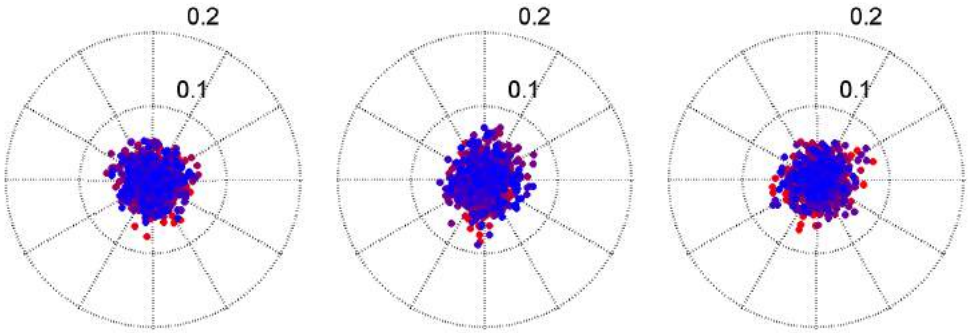

(j) Re_w≈5340, α≈0.025 (k) Re_w≈6240, α≈0.029 (l) Re_w≈7012, α≈0.027

Figure 7.5: The instantaneous peak velocity locations of each individual frames are presented in coloured points, initially with red colour and ultimately with blue colour in time sequence. The Reynolds numbers Re_w and asymmetry factor α are also calculated for 0.09% PAA solution. The radial length is normalized by pipe inner radius R.

ber and become progressively more obvious with increasing Reynolds number. However, no symmetry-breaking bifurcation was observed with increasing Reynolds numbers for viscoelastic fluids and the greater Reynolds number only yields a larger velocity fluctuation, while the time-averaged velocity profile is still axisymmetic.

7.2 Addition of polyacrylamide to xanthan gum

Since the asymmetry was absent in various concentrations of purely PAA solution, in this section, polyacrylamide polymer was added to xanthan gum polymer (where pronounced asymmetry was observed) to examine the effect of viscoelastic characteristics on asymmetry. The tested solution includes 0.15% xanthan gum solution with 100, 200 and 500 ppm polyacrylamide.

7.2.1 Rheological characterization

The preparation procedures of PAA and xanthan gum blended solutions are as follows: a certain amount of polyacrylamide polymer (calculated based on the concentration of PAA, i.e. 100, 200, 500ppm) was weighed and uniformly mixed with a fixed amount of xanthan gum polymer (calculated based on 0.15%), and then dissolved into tap water in the volume of 750L. To inhibit biological degradation, 75 ppm formaldehyde was also added to the solvent. The solution was circulated in the pipe at a low pump speed until the solution was homogeneously mixed. The viscosity data is presented in Figure 7.6. The viscosity data of 0.15% xanthan gum solution and 0.125% PAA solution are also displayed as benchmark comparison data. The mixture viscosity with addition of PAA polymer was overall higher than pure 0.15% xanthan gum solution and clear shear-thinning characteristics of the mixed solutions were manifest. The shear-thinning characteristics are quantitatively described by the flow behaviour index n via power-law fitting over a shear rate range $3 < \dot{\gamma} < 321\ s^{-1}$.

The flow behaviour index n of all solutions are listed in Table 7.1. With increasing PAA

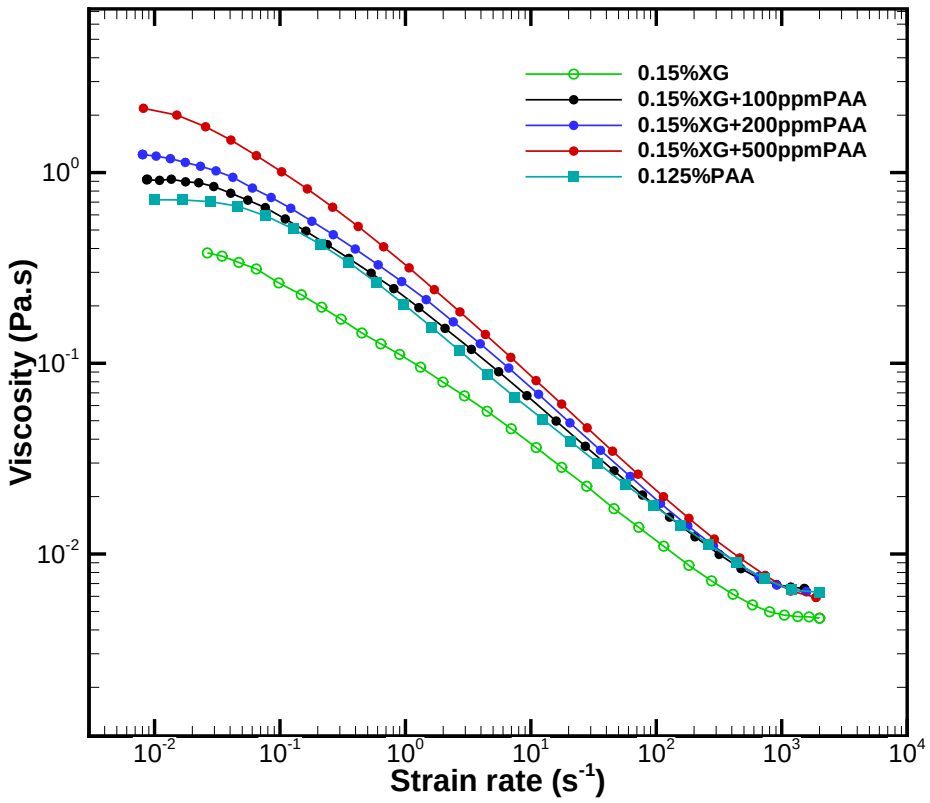

Figure 7.6: Viscometric data for various concentrations of polyacrylamide/xanthan gum mixed solutions. The green empty circle represents the viscosity data of 0.15% xanthan gum solution for comparison purpose.

concentration (%)	0.15% XG pure	0.15% XG + 100ppm PAA	0.15% XG + 200ppm PAA	0.15% XG + 500ppm PAA
flow behaviour index n	0.508	0.444	0.428	0.389

Table 7.1: The flow behaviour index n of pure 0.15% xanthan gum solution and blended solution in addition of 100, 200 500ppm PAA using power-law fitting.

concentration, the flow behaviour index decreases, indicating stronger shear-thinning characteristics. In the pure xanthan gum solution, which is essentially inelastic, in chapter 6 it was observed that the greater the shear-thinning ability, the stronger the fluid asymmetry will appear. The addition of PAA polymer, where the fluid possesses strong viscoelasticity, allows the study of the asymmetry by investigating the maximum degree of asymmetry together with the critical Reynolds number.

7.2.2 Suppression of maximum asymmetry

The SPIV experiments were conducted in order to examine the flow when the PAA concentration was 100ppm, 200ppm and 500ppm, respectively. For each PAA concentration, the experimental data was collected for a wide range of Reynolds numbers when the flow was in a steady state. The SPIV data acquisition rate was still 5Hz to obtain a long time-averaged result.

Figure 7.7 illustrates the variation of degree of asymmetry when adding different concentrations of PAA (i.e. 100ppm, 200ppm and 500ppm) to 0.15% xanthan gum solution. The pure 0.15% xanthan gum solution data is also presented for comparison. The higher concentration of PAA solution indicates a stronger shear-thinning characteristics (as indicated in Table 7.1) and stronger viscoelastic characteristics. For inelastic shear-thinning fluid, stronger shear-thinning characteristics are supposed to enhance the asymmetry, however, once the PAA polymer (viscoelastic) was added, the higher PAA concentration (possessing higher shear-thinning characteristics) presents a lower degree of asymmetry, suggesting that viscoelasticity might inhibit the asymmetry as shown in Figure 7.7. The maximum degree of asymmetry (indicated by the radius of peak velocity r_p/D) achievable when adding 100ppm, 200ppm and 500ppm PAA is approximately 0.12, 0.11 and 0.08, respectively, which are all lower than that of pure 0.15% xanthan gum solution. The degree of asymmetry in addition of different PAA solutions, all grow gradually along with the increasing Reynolds number in the form of supercritical bifurcation when exceeding the critical Reynolds number. This behaviour is consistent with the observation of pure xanthan gum solution, nevertheless, the degree of asymmetry was reduced by viscoelasticity. The critical Reynolds number for transition from axisymmetry to asymmetry appears to be slightly delayed with increasing concentration of PAA in comparison with that of the pure 0.15 xanthan gum solution. It is particularly significant for the 500ppm solution, which is the highest concentration of PAA addition. The pressure fluctuation, p_{rms}/P, streamwise velocity fluctuations, u_{rms}/U_b and cross-stream velocity fluctuations, $v_{r\theta,rms}/U_b$, are also calculated. The transition from laminar to turbulent flow is indicated by the variation of pressure fluctuation, p_{rms}/P and cross-stream velocity fluctuations, $v_{r\theta,rms}/U_b$. When the PAA concen-

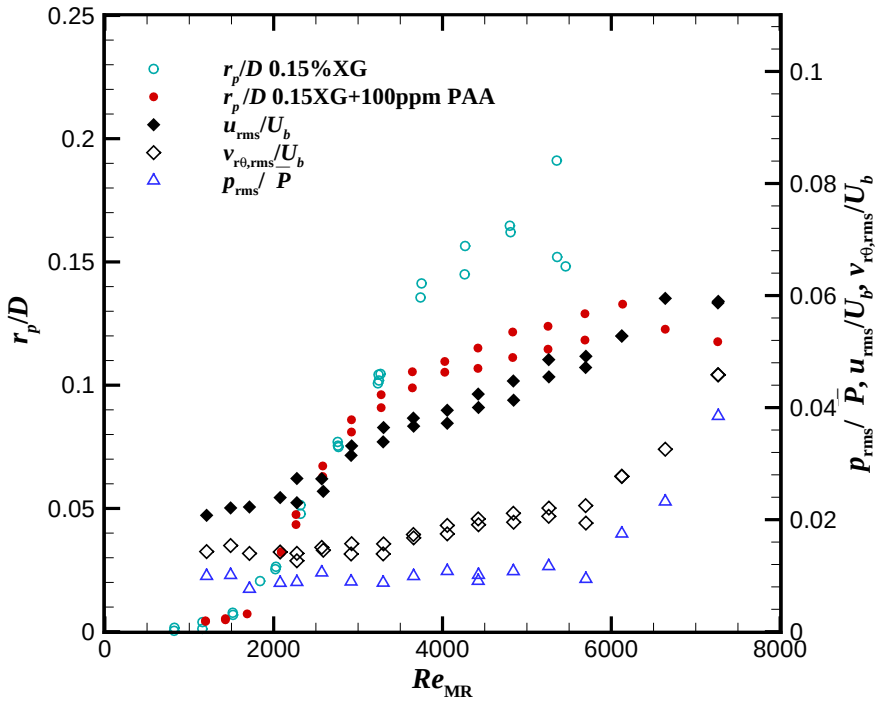

(a) 0.15% xanthan gum with 100ppm PAA

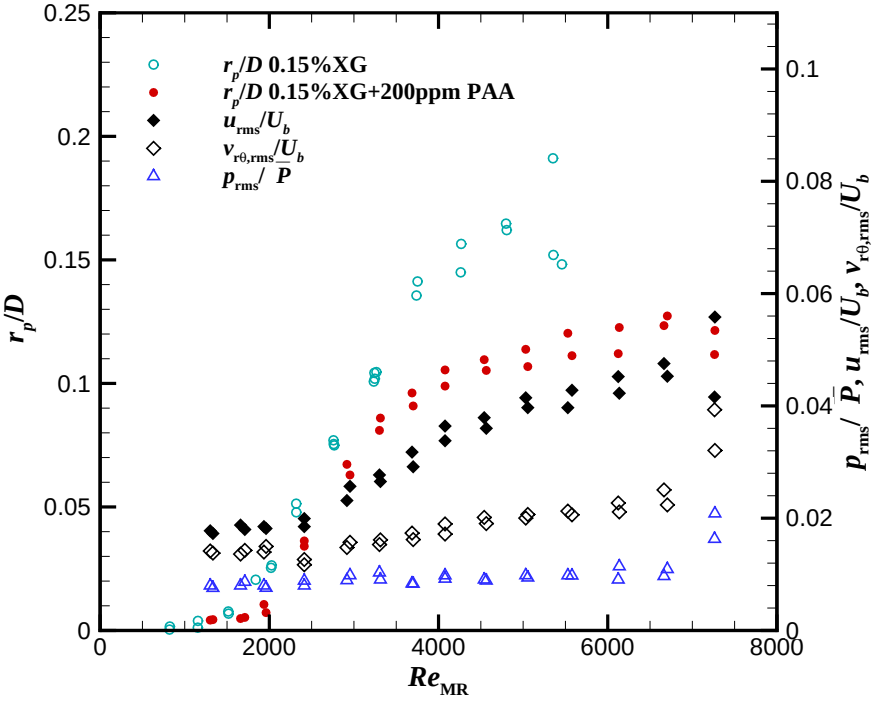

(b) 0.15% xanthan gum with 200ppm PAA

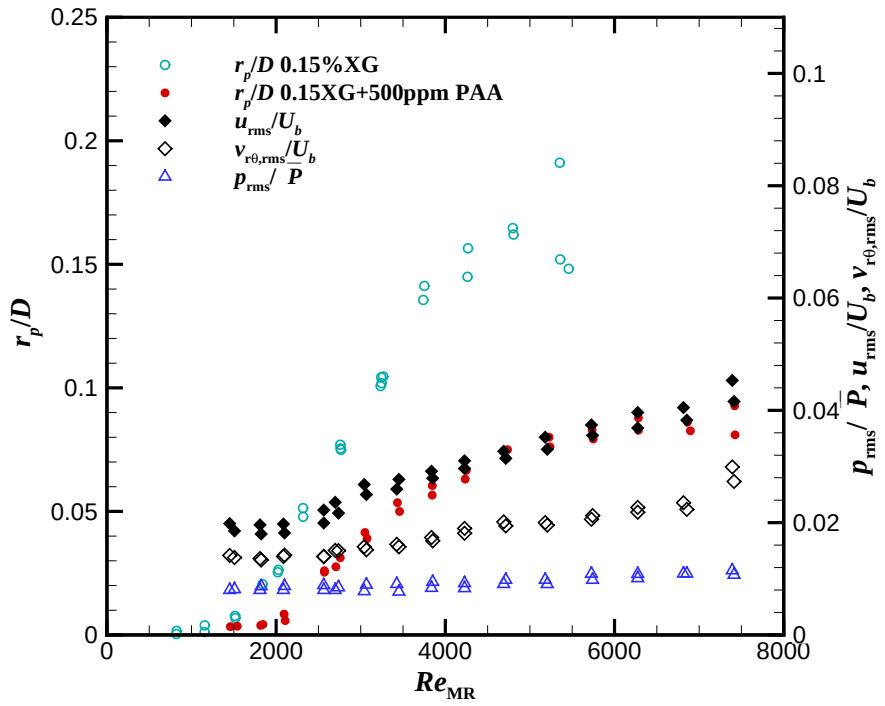

(c) 0.15% xanthan gum with 500ppm PAA

Figure 7.7: The variation of degree of asymmetry when adding different concentrations of PAA solution into 0.15% xanthan gum solution. The pure 0.15% xanthan gum solution data was presented in empty dots for comparison. The velocity and pressure fluctuations were calculated using 0.15% xanthan gum and 500 ppm PAA mixed solution.

tration is 100ppm and 200ppm, a sudden increase of pressure fluctuation was observed when Reynolds number was above 6000. This is consistent with the jump of cross-stream velocity fluctuations as the passing turbulent puff in transitional regime leads to these fluctuations. However, for 500ppm PAA solution, because of high viscosity, the pressure fluctuation was damped in the connecting tubing between the pressure transducer and pressure tappings, therefore the sudden increase of pressure fluctuation was absent. The increase of cross-stream velocity fluctuation was observed when Reynolds number was close to 8000, which showed the onset of transition when PAA concentration was 500ppm.

Figure 7.8 plots the viscoelastic effect on the maximum degree of asymmetry and critical Reynolds number for transition from axisymmetry to asymmetry together with critical Reynolds

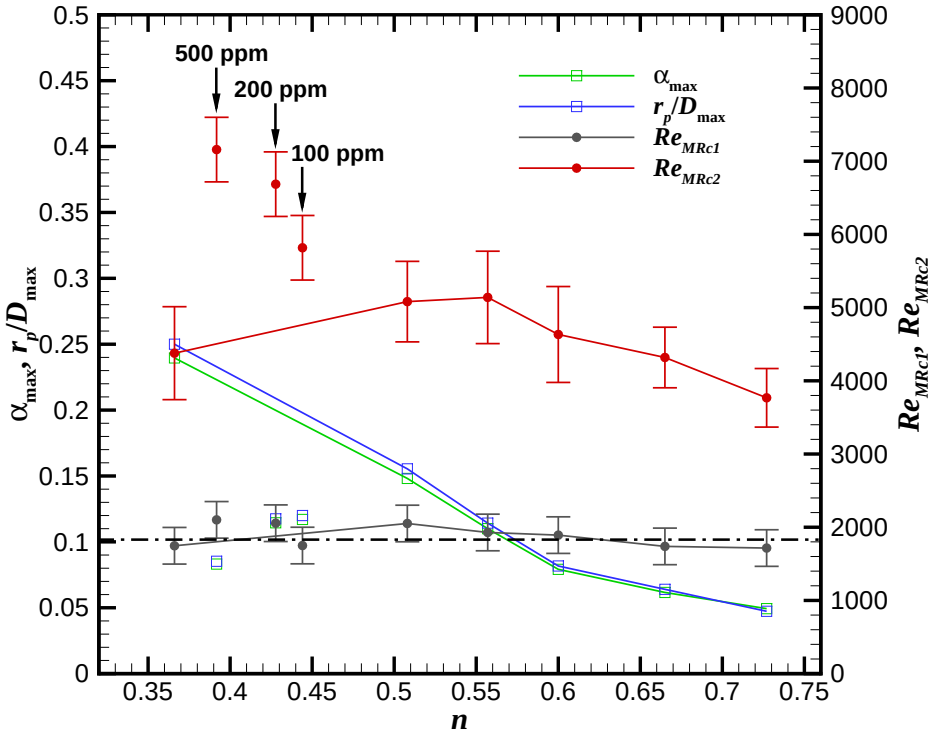

Figure 7.8: The viscoelastic effect on the critical Reynolds number for transition from axisymmetry to asymmetry (Re_{MRc1}) and transition from laminar to turbulent (Re_{MRc2}) together with maximum degree of asymmetry ($\alpha_{\max}$,$r_p/D_{\max}$).

number for transition from laminar to turbulent flow. The solid lines connecting data points present the pure xanthan gum solution with different concentrations (i.e. different shear-thinning characteristics) and the individual data points (without connection of solid line and highlighted by solid black arrows) demonstrate the xanthan gum/PAA blended solutions. The dashed line indicates the trend of critical Reynolds number Re_{MRc1}. The $\alpha_{\max}$ and $r_p/D_{\max}$ in xanthan gum/PAA mixed solutions are significantly lower than the interpolation value (indicated by the connecting solid line) of inelastic xanthan gum solutions, revealing the maximum degree of asymmetry was clearly reduced in the presence of viscoelasticity. The critical Reynolds number for transition from laminar to turbulent (Re_{MRc2}) was obviously delayed, indicating that viscoelasticity stabilizes the flow and delays the transition to turbulence [41, 48]. The critical Reynolds number for transition from axisymmetry to asymmetry (Re_{MR12}) was also slightly

delayed, particularly at the 500 ppm PAA solution, suggesting the viscoelasticity might also inhibit the onset of asymmetry.

7.3 Deliberate degradation of viscoelasticity

In this section, the shear-induced degradation was purposely imposed on a 0.125% PAA solution to further investigate the effect of the viscoelasticity on asymmetry. For this purpose, 0.125% PAA was selected as the significant asymmetry was observed previously using LDV [54]. The shear-induced degradation was designed to significantly reduced the viscoelasticity while preserving the shear-thinning characteristics. It could provide us more experimental evidence to examine the effect of viscoelastic on the asymmetry.

7.3.1 Rheological characterization

The intended shear-induced degradation was conducted by imposing intense mechanical shearing on the fluid i.e. circulating the fluid in turbulent flow regime for a few days. The fluid was sampled at various time points when the fluid was newly mixed, i.e. 'fresh' and after 24 hours, 48 hours and 72 hours of degradation. The viscometric data of 0.125% PAA solution before and after degradation is presented in Figure 7.9. All sampled fluids exhibit shear-thinning characteristics and the mechanical degradation decreases the zero-shear viscosity plateau. The infinite shear viscosity generally remains unchanged. This is because the zero shear viscosity η_0 is sensitive to polymer molecular weight and zero-shear viscosity of a polymer is reported [136] to follow a power law dependence on molecular mass described by $\eta_0 \sim M_w^{\beta}$, where M_w is molecular weight and β is 3.4. It indicates the mechanical shearing fragments polymer molecules and leads to the loss of viscoelasticity, however the fractured molecular chain is still large enough to retain the shear-thinning characteristics of the fluid.

To examine the viscoelastic characteristics of 0.125% PAA solution before and after degradation, the dynamic modulus of each solution was studied. The fluid's linear viscoelastic region

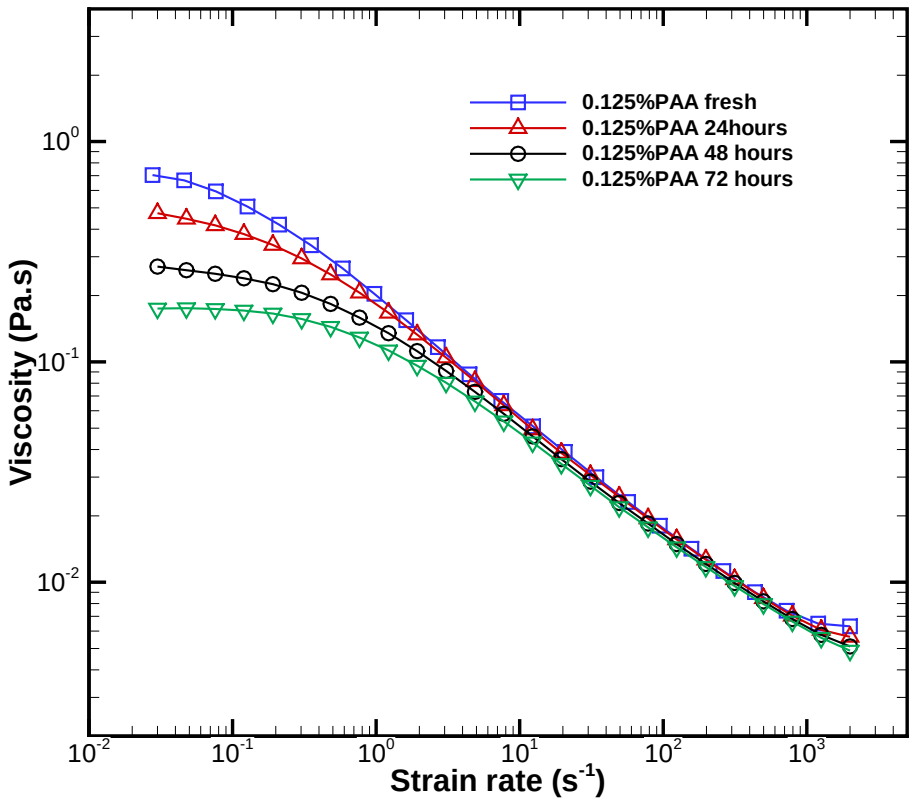

Figure 7.9: Viscometric data for 0.125% PAA solution in 'fresh' state and after 24 hours, 48 hours, 72 hours shear-induced degradation.

was first determined by a strain sweep in the rheometer, and then the storage modulus G' and loss modulus G'' were measured in the linear viscoelastic region. This is because the viscoelastic behaviour exhibited by polymer is directly linked with molecular structure. To precisely evaluate the relationship between molecular structure and viscoelasticity, a rheological measurement is required to implement in region where the viscoelasticity measured is independent of imposed stress or strain, i.e. in the linear viscoelastic region. The storage G' and loss G'' modulus in viscoelastic materials measure the stored energy, representing the elastic portion, and the energy dissipated as heat, representing the viscous portion, respectively. Figure 7.10 illustrates in low sweep frequency range, the storage modulus G' is higher than loss modulus G'' for all fluids suggesting the polymer is more solid-like. The more severe degradation leads to the decrease of the G' modulus and G'' modulus particularly in low sweep frequency region. With the increasing sweep frequency, the polymer becomes progressively more fluid-like, and

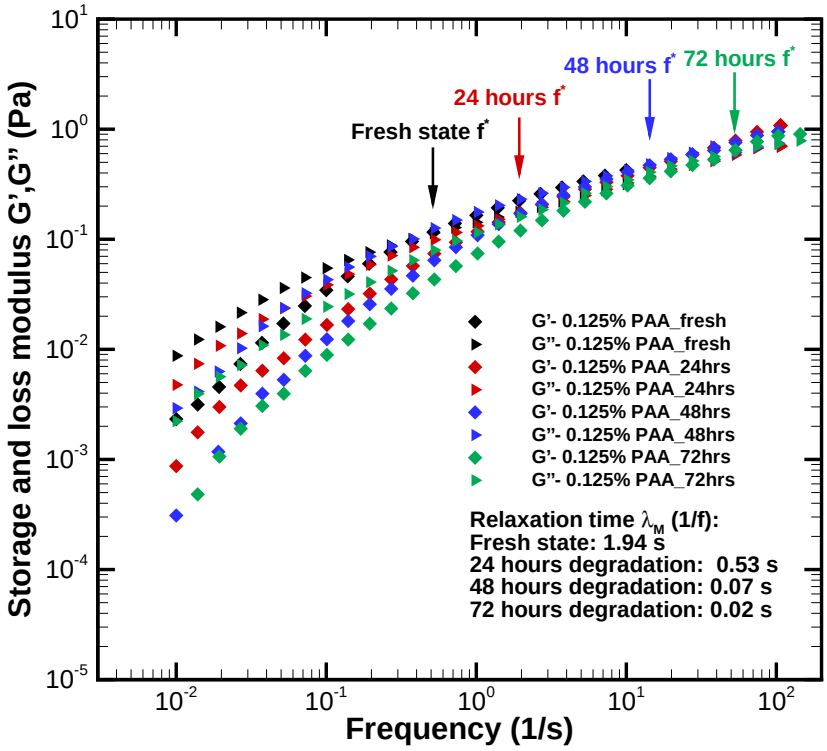

Figure 7.10: Small amplitude oscillatory shear (SAOS) measurement of 0.125% PAA solution before and after shear-induced degradation. The storage modulus G' and loss modulus G'' were measured in linear viscoelastic region. The relaxation time λ_M was determined by the reciprocal of critical frequency f^*, which was intersection point of G' and G'' curves.

the G''modulus exceeds G' modulus eventually.

The viscoelasticity of fluid can be indicated by the relaxation time, which is characteristic time required for the polymer coil to relax from a deformed state to its equilibrium configuration [87]. An engineering approximation of the relaxation time is to take the value of the critical frequency f^* at which the G' and G'' curves cross and apply $\lambda_M = 1/f^*$ as the approximation of the relaxation time [171]. This approximation is based on a single mode Maxwell model where the viscoelasticity is modelled as a spring and dashpot in series [9] and the subscript $_M$ in τ_M stands for the Maxwell model. The relaxation time of PAA solution in fresh state and after degradation of 24, 48 and 72 hours is measured to be 1.94s, 0.53s, 0.07s and 0.02s respectively, at a temperature of 20 °C. The decrease of the relaxation time reveals the shear-induced

degradation causes a significant loss of viscoelasticity while the shear-thinning characteristics remain, which is indicated by the power law variation of the viscosity along with the shear rate as shown in Figure 7.9.

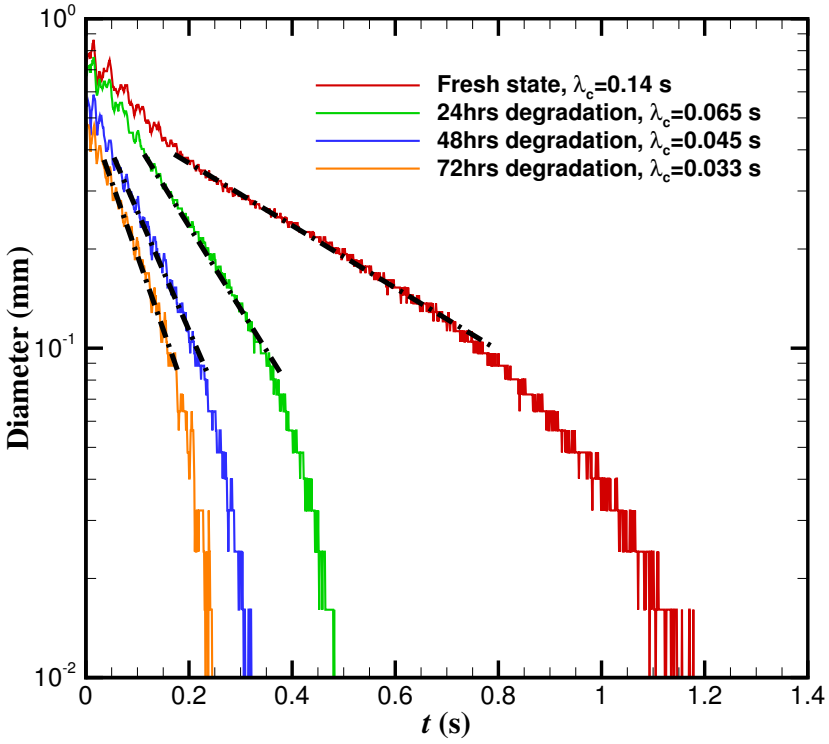

Figure 7.11: Transient midpoint diameter in capillary breakup extensional rheometer (CaBER) measurement for 0.125% PAA solution. The black dashed line illustrates the exponential decay of the filament diameter in elongational stretching process.

A real polymer may have several different relaxation times associated with different molecular motions. The relaxation time τ_M in Maxwell model is essentially obtained from a response of imposed small amplitude oscillatory shear on fluid. The capillary breakup extensional rheometer (CaBER) is also used to determine the relaxation time, which is a transient extensional flow measurement in nature [5, 151]. The experiment was implemented in ambient temperature 22.6 °C and a nearly cylindrical PAA solution sample was placed between the two end plates of the filament stretching rheometer. The diameter of the sample fluid started to shrink when two end plates began to separate. Instead of breakup, a cylindrical filament was

formed due to the high viscoelastic stresses. Figure 7.11 presents the transient midpoint diameter of shrinking filament in elongational stretching process. More severely degraded solution underwent a more rapid tensile fracture process. An exponential decay of the filament diameter in time was discerned. The filament thinned exponentially with time which could be described by the relationship: $D(t) = D_0 \cdot e^{-t/\lambda_c}$, where $D(t)$ is transient diameter of filament, D_0 is the diameter where the exponential decay began and λ_c is the characteristic time of thinning to feature the relaxation process. By exponential fitting of $D(t)$ data, which is illustrated by black dashed line in Figure 7.11, the relaxation time λ_c measured by CaBER was 0.14s, 0.065s, 0.045s and 0.033s for fresh state, 24 hours, 48 hours and 72 hours degraded PAA solution, respectively. It is consistent with the result of relaxation time λ_M obtained from the storage and loss modulus data that the shear-induced degradation weakens the viscoelasticity of PAA solution while the λ_c measurement is from a perspective of elongational flow.

7.3.2 Time-averaged velocity profiles after degradation

Figure 7.12 illustrates the time-averaged velocity profiles for 0.125% PAA solution before and after the fluid was degraded. The SPIV data was collected when the flow was in a steady state and the mean streamwise velocity was normalized by the bulk velocity. The measurement time was 200s and the Reynolds numbers were selected in the intermediate range, namely Re_w = 2860, 3950 and 5152. These Reynolds numbers were supposed to be sufficiently away from the laminar base state and the pronounced symmetry-breaking bifurcated state was observed in this selected Reynolds number range when using xanthan gum solution with various concentrations.

When the PAA solution was in a fresh state, i.e. the fluid was very viscoelastic, no perceptible asymmetry was observed. It agrees with the results obtained from other concentrations (0.09% and 0.2%) of PAA solutions that no asymmetry was observed in pure PAA solution. However, when the PAA solution underwent a 24 hours shear-induced degradation, significant asymmetry arised in all selected Reynolds numbers. With the increasing degradation time, the

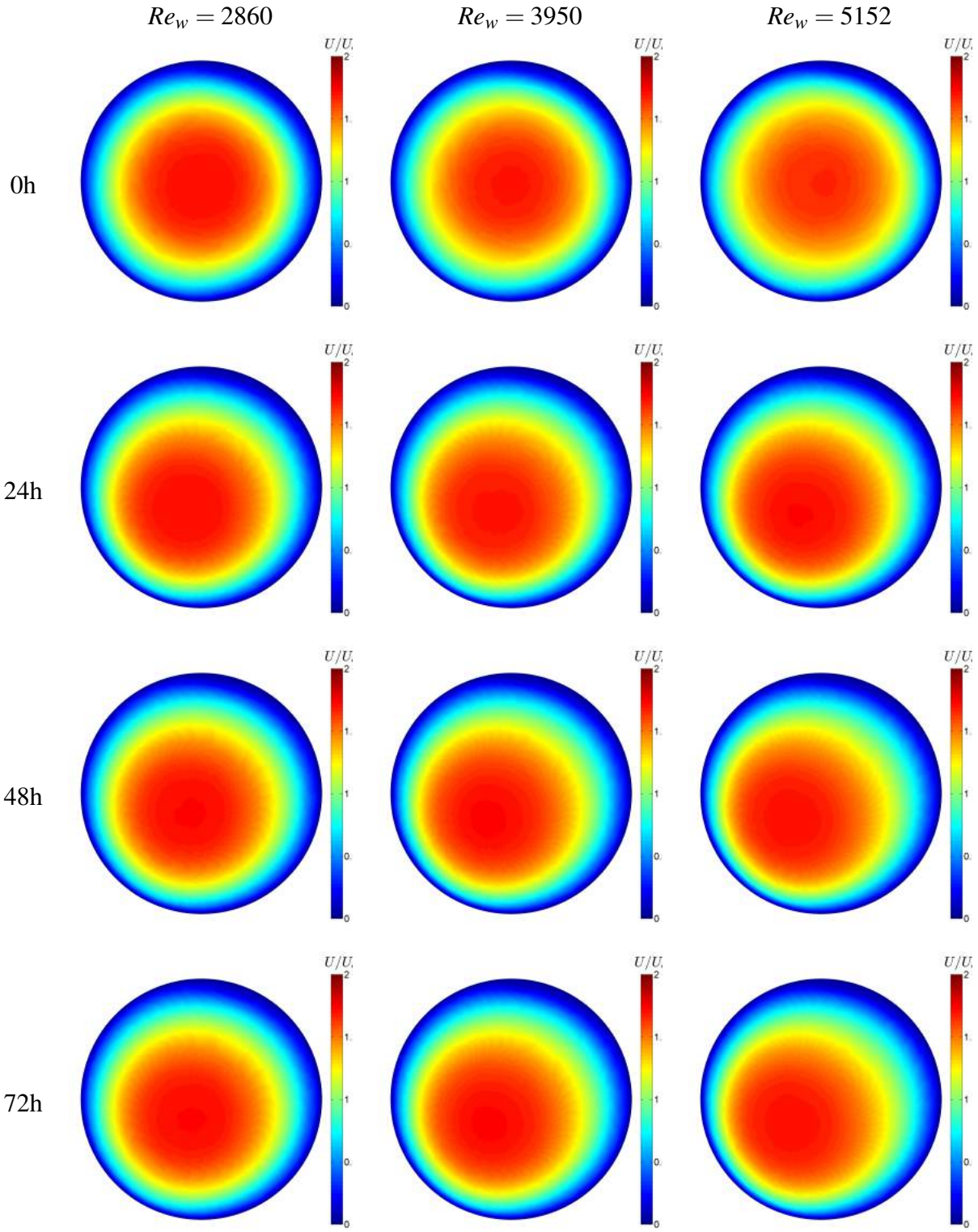

Figure 7.12: The time-averaged velocity profiles for 0.125% PAA solution when the fluid was in fresh state (marked as 0h) and degraded after 24, 48 and 72 hours. The flow was examined at Re_w = 2860, 3950 and 5152, respectively.

asymmetry remained and the degree of asymmetry generally increased with the increasing Reynolds number in the selected Reynolds range. Note that the shear-thinning characteristics of PAA solution had no obvious change before and after deliberate mechanical degradation, which is illustrated by the viscometric data in Figure 7.1. This feature results from that the shear-induced scission fractures a very long molecular chain (loss of viscoelasticity) into a relatively smaller piece while these smaller molecular chain still exhibits the shear-thinning characteristics. This observation is of importance as it reveals the effect of viscoelastic characteristics on the asymmetry: viscoelasticity plays the role of suppressing the asymmetry.

The observation in Figure 7.12 also explains why in the previous LDV data the asymmetry was observed while in the current SPIV data the asymmetry was absent in the pure PAA solutions. Since LDV is a single point technique for velocity measurements, to generate the velocity profile in a certain plane, generally dozens of probing points are required, which needs several experimental hours (a velocity profile consisting of 50 points took between 3 and 4 hours in LDV measurement [54]). However, SPIV is a whole-flow-field technique which could acquire three-component velocity vectors in measurement plane simultaneously. The experimental duration in SPIV is broadly one order magnitude lower than that of LDV, e.g. in current project, to acquire the time-averaged velocity profile in a certain Reynolds number, the SPIV technique consumes 200 seconds to collect 1000 individual frames to take averaging velocity profile while using LDV technique, generally 3 or 4 hours is in demand merely for one certain Reynolds number. Therefore, the long test time i.e. long shearing time in LDV results in the heavy loss of viscoelasticity in PAA solution, thus the asymmetry was observed using LDV due to absence of viscoelasticity. It is actually consistent with current SPIV data as in the flow scenario when the shear-induced degradation was imposed on the PAA solution, the asymmetry was also observed in the SPIV data, although initially no asymmetry was found in SPIV when the fluids was in a fresh state, indicating the viscoelasticity actually suppresses the asymmetry.

7.3.3 Effect of viscoelasticity on maximum degree of asymmetry

With regards to the 0.125% PAA solution, on which the shear-induced degradation was imposed, the maximum asymmetry factor of the time-averaged velocity profile was calculated while the corresponding relaxation time λ_c and λ_M of the fluid were presented simultaneously in Figure 7.13. When the PAA solution was fresh (labelled as t=0), the maximum asymmetry factor was about 0.025, which is due to the SPIV experimental noise, illustrating the flow was essentially axisymmetric. The relaxation time of PAA solution, regardless of λ_c or λ_M, both had a relatively large value, describing the pronounced viscoelasticity of the fluid in fresh state. The relaxation time λ_M is roughly one order of magnitude higher than the relaxation time λ_c. This

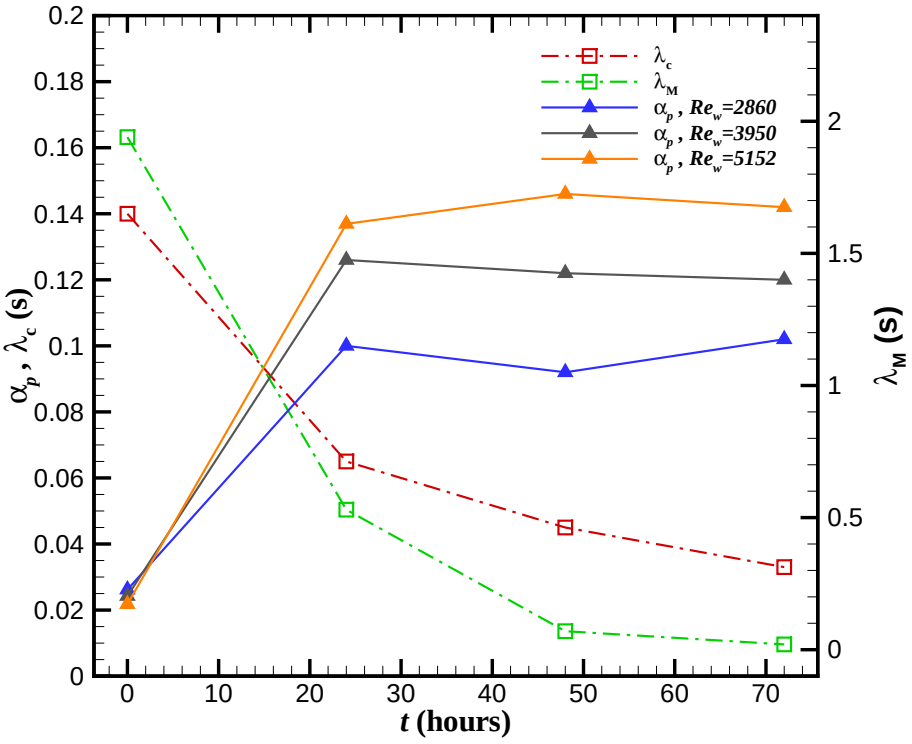

Figure 7.13: The achievable maximum degree of asymmetry (indicated by α_p) versus the viscoelasticity (indicated by the relaxation times λ_c and λ_M) for a various Reynolds numbers at Re_w=2860, Re_w=3950 and Re_w=5152.

is because these two different relaxation times were obtained from different flow scenarios, λ_M

was measured in the cone-plate-geometry of rheometer as shear flow while λ_c was measured in capillary breakup extensional rheometer from an elongational flow. The molecular structure and formulation in these two flow scenarios were totally different in essence, yielding a distinctive viscoelastic behaviour of the fluid. Although, the relaxation time λ_c and λ_M have different magnitude, they agree reasonably to describe the viscoelasticity of the fluids, i.e. they exhibit similar decreasing tendency of viscoelasticity along with increasing degradation time.

When the fluid underwent 24 hours of shear-induced degradation, the maximum asymmetry factors achievable in all flow scenarios (Re_w=2860, Re_w=3950, Re_w=5152) had a dramatic increase to a level, which the significant symmetry-breaking bifurcation was exhibited. The corresponding relaxation time, both λ_M and λ_c of the PAA solution decreased dramatically, indicating the significant loss of viscoelasticity after the deliberate degradation. When degradation time increased to 48 and 72 hours, the relaxation time approached asymptotically to zero while the asymmetry factor plateau was observed, showing the maximum degree of asymmetry approximately remained unchanged.

For each individual Reynolds numbers tested, i.e. Re_w=2860, Re_w=3950 and Re_w=5152, the maximum degree of asymmetry is approximately a constant after 24 hours degradation. However, after 24 hours degradation, we observed the maximum degree of asymmetry also increased with Reynolds numbers, from $\alpha_p \approx 0.1$ at Re_w=2860, $\alpha_p \approx 0.12$ at Re_w=3950, to $\alpha_p \approx 0.14$ at Re_w=5152. These results are consistent with the observation for inelastic 0.15% xanthan gum solutions that with increasing Reynolds number, the asymmetry develops when the shear-thinning characteristics dominates the degraded PAA solution, as indicated in the flow curve in Figure 7.9.

7.3.4 Evolution of asymmetry after deliberate degradation

In subsection 7.3.3, the effect of viscoelasticity on the maximum degree of asymmetry α_p has been revealed. The maximum degree of asymmetry is suppressed by the viscoelastic characteristics of fluids and the asymmetry reappears when the fluid is deliberately degraded.

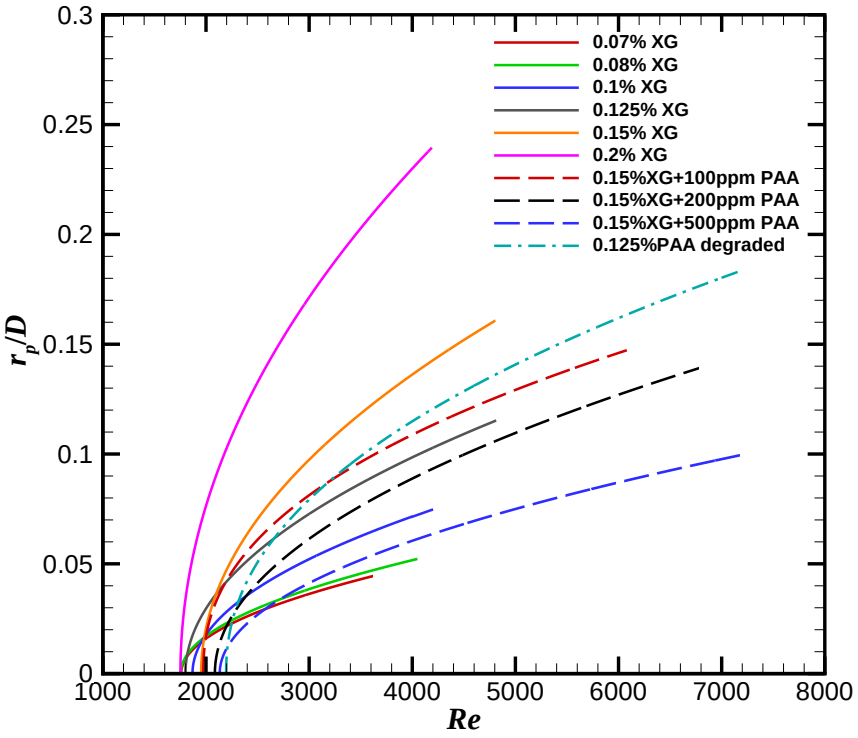

Figure 7.14: The comparison of supercritical symmetry-breaking bifurcation processes for different concentrations of xanthan gum solutions and PAA solutions. The solid curves indicate the xanthan gum solution, the dashed curves are xanthan gum/PAA mixed solution and the dash dot curves represent the degraded 0.125% PAA solution.

One interesting question may be brought up: will the asymmetry in degraded PAA solution still evolve in the form of supercritical bifurcation as it does in inelastic XG solution? To answer this question, we first purposely pumped the 0.125% PAA solution at high pump speed to degrade the fluid. Then we implemented SPIV experiment across a range of Reynolds numbers. The similar symmetry-breaking supercritical bifurcation was observed when the Reynolds number was above a critical value for degraded 0.125% PAA solution, shown in Figure 7.14. To note, if the 0.125% PAA solution is not degraded, the flow is essentially axisymmetric and no symmetry-breaking bifurcation was found. However, once the viscoelasticity of fluid was largely diminished, the pipe flow exhibits supercritical bifurcation again. The critical Reynolds number for transition from axisymmetry to asymmetry is generally unchanged, approximately

at $Re_w \approx 2000$. The supercritical instability is also observed to be ubiquitous for fluids which possess the shear-thinning characteristics with low or no elasticity.

7.4 Conclusions

The effect of viscoelastic characteristics on asymmetry was investigated in this chapter using polyacrylamide aqueous solutions. Different concentrations, namely 0.09%, 0.125% and 0.2% pure polyacrylamide solution were first examined and no asymmetry was observed in all concentrations of fluids, although significant shear-thinning characteristics were exhibited. This observation was initially deemed in conflict with previous LDV data, in which the asymmetry was observed in pure 0.125% polyacrylamide solution. Then 100, 200 and 500ppm PAA solutions mixed with 0.15% xanthan gum solution were investigated. The maximum degree of asymmetry appears to be reduced with the increasing viscoelasticity, suggesting the viscoelasticity inhibits asymmetry. The critical Reynolds number for transition from laminar to turbulent flow was delayed, and the viscoelasticity was also deemed as to delay the critical Reynolds number for transition from axisymmetry to asymmetry. The asymmetry reappeared when the shear-induced degradation was deliberately imposed on pure 0.125% PAA solution to inhibit the viscoelasticity while preserving the shear-thinning characteristics of fluid. These additional experimental results give direct experimental evidence revealing that viscoelasticity suppresses the symmetry-breaking bifurcation and constrains the shear-thinning induced instability as once the viscoelasticity was diminished, the symmetry-breaking bifurcation was observed to reappear.

Chapter 8

Conclusions and future works

This chapter summaries the contributions of this thesis to the knowledge of flow asymmetry observed in circular pipe flow near the laminar-turbulent transitional regime using shear-thinning fluids. First, in section 8.1, we will review the rheological characteristics of working fluids, in which the flow asymmetry was seen. In section 8.2 to 8.4, 0.15% xanthan gum solution was selected to study the flow behaviour and characteristics of asymmetry. The various concentrations of xanthan gum soluitons, namely 0.07%, 0.08%, 0.1%, 0.125%, 0.15% and 0.2%, were investigated to reveal the effect of shear-thinning on flow asymmetry in section 8.5. The effect of viscoelasticity on asymmetry was also investigated using pure PAA solution (without and with deliberately shear-induced degradation) and PAA/XG mixed solution, explained in section 8.6. Some suggestions of future work will be given as well to propose what should be addressed in next step.

8.1 Working fluids

All working liquids investigated displayed time-independent shear-thinning characteristics, which can be represented by the power-law or Carreau-Yasuda models. In the early stage of this project, a 0.15% xanthan gum solution was utilized, which possesses significant shear-

thinning characteristics without large elasticity. The selection of 0.15% xanthan gum is suggested by the results of previous LDV studies (see Table 4.1 in chapter 3) and these previous studies strongly imply the asymmetry is caused by the shear-thinning characteristics of fluids, as the common ground of various non-Newtonian liquids in which the asymmetry was observed, is shear-thinning. Although previous investigations suggest the asymmetry is induced by the shear-thinning, there is no solid experimental evidence to reveal how different shear-thinning characteristics affect the flow asymmetry. Therefore, in the second stage of the project, we also utilized different concentrations of xanthan gum solutions, namely 0.07%, 0.08%, 0.1%, 0.125%, 0.15%, 0.2%. The viscometric data for different concentrations of xanthan gum solutions were measured by a rheometer. They all manifest significant shear-thinning nature and the viscosity data was fitted by the power-law model (see Equation 2.6). The obtained power-law exponent quantitatively indicates the shear-thinning characteristics of fluids and the higher concentration of the fluid, the stronger shear-thinning property the fluid has. Then different polymeric solutions were also tested, i.e. PAA solution, which is also shear-thinning but with a pronounced elasticity. Initially, we examined the pure PAA solution with different concentrations. Contrary to previous results, no observe apparent asymmetry was observed in pure PAA solution using SPIV, although it possesses the similar shear-thinning characteristics to xanthan gum solution. This unexpected absence of asymmetry in pure PAA solution conflicts with previous LDV investigation of pure PAA solution [51, 54, 64], in which the asymmetry was present. Therefore we speculate that viscoelasity may inhibit the asymmetry, which has not been revealed before. To verify this speculation, two approaches were implemented: one is to mix some PAA polymer into 0.15% xanthan gum, the other is to degrade the viscoelasity while preserving the shear-thinning characteristics of PAA solution. In the first approach, 100ppm, 200ppm and 500ppm PAA were added into 0.15% xanthan gum solution, then the flow regime across a range of Reynolds numbers was investigated to compare the variation of degree of flow asymmetry. In the second approach, to quantify the degradation of viscoelasity, the relaxation time of fluids was measured via small amplitude oscillatory shear (SAOS) measurement

and Capillary Breakup Extensional Rheometer (CaBER). The degradation of viscoelasity was conducted by introducing the intense shearing to the fluids. Then the velocity profiles were compared before and after the degradation of PAA solution, which revealed the reappearance of asymmetry, but also investigated how the asymmetry develops once the PAA solution was degraded.

8.2 Time-varying nature of asymmetry

In this work new experimental results have been obtained that simultaneously capture the three-component velocity field across the entire pipe cross-section, a significant advancement on the exclusively point-wise single-component measurements of previous works. This leads to a much clearer picture of the behaviour of the asymmetric velocity profile and reveals that the asymmetry is produced by a pathway that has not previously been proposed. One of the major insights provided by our SPIV measurements in comparison to all other previous work is the time-varying behaviour of the asymmetric flow pattern, which was hitherto considered stationary. The general consensus about the asymmetry before the project is that the asymmetric location of the peak velocity remained at a fixed point in space. This is due to the limitation of previous investigations as previous studies [51, 52, 54, 64] largely concentrated on the description of the asymmetric distortion of the time-averaged streamwise velocity profile using single-point, single velocity component Laser Doppler Velocimetry in a long-time average (a few hours), therefore the long-time averaged result leads to the time-varying nature of asymmetry unnoticed.

In this project, we first implemented our SPIV experimental work in laminar-turbulent transition regime ($Re_w \approx 8000$) using 0.15% xanthan gum solution. The transitional regime was selected as previous studies [51, 52, 54, 64] of shear-thinning fluids in pipe flow discovered the time-averaged velocity profile was asymmetric in the laminar-turbulent transition regime while it was axisymmetric when the flow was in purely laminar or fully turbulent region. Our results

confirm the significant departures from axisymmetry in transitional flows of shear-thinning fluids (see Figure 5.8), in addition to the observation that the asymmetric flow pattern is not stationary, the peak velocity is seen to preferentially arise at certain azimuthal locations. The time-varying nature of the asymmetric flow pattern is presented by the time history of asymmetry factor and the instantaneous cross-stream snapshots of the streamwise velocity, which is displayed in Figure 5.9. The characteristics of time-varying nature of asymmetry are manifested in the following aspects:

(a) although the asymmetric velocity profile is time-varying, the asymmetric flow indeed has a preferred orientation, in which the flow spends most of its time and therefore has a profound influence on the asymmetric time-averaged velocity profile. We have confirmed that this favoured location is largely invariant with axial location by taking LDV measurements at many locations (over several metres) upstream of the SPIV measurement plane and finding little change in the orientation of the asymmetry. The invariance of the orientation with axial location indicates that the asymmetry is not due to a helical instability spiralling down the pipe.

(b) frequent dramatic drops in time series of the asymmetry factor signal that the flow is briefly returning to a quasi-axisymmetric state. The instantaneous flow pattern temporarily exhibits axisymmetry even through the long-time averaged flow pattern is asymmetric in the transitional regime.

(c) the asymmetric flow pattern does not permanently stay in the preferred orientation, a brief visit to asymmetric flow with an alternative orientation is also observed in the experiment. The asymmetry appears in a different orientation and then slowly rotates to its preferred location, following a preferred path. However, this distinct phenomenon appeared in a much shorter time scale after the puff, this brief visit to the alternative orientation is very quick (dimensionless time t^* is in the order of 10) compared with the time scale when the flow is in the preferred orientation.

To note, this time-varying nature is not only exhibited in the laminar-turbulent transition regime, it is also observed when flow is at high Reynolds numbers in laminar regime (i.e. no turbulent puff occurs in the pipe). However, the time-varying nature is fundamentally different for the laminar flow and transitional flow. In laminar regime, when Reynolds numbers are high, the flow pattern also moves around the preferred asymmetric orientation, leading to the fluctuation of asymmetry factor, but we did not observe the quasi-axisymmetric state as we observed in the transitional case. This time-varying nature, which is indicated by the fluctuation of asymmetry factor, becomes more and more obvious with increasing Reynolds numbers. This observation of time-varying nature of asymmetry provide new insight in this poorly understood phenomenon.

8.3 Elimination of asymmetry by turbulent puffs

Since we observed some quasi-axisymmetric states in transitional regime, we did some further experimental investigations using high-speed SPIV (The SPIV acquisition rate is 200Hz). At high acquisition rate, the turbulent puff is pseudo-spatially reconstructed using Taylor's approximation. We experimentally observed the temporary elimination of the asymmetry is associated with a turbulent puff passing through the measurement plane, see Figure 5.10. This is in contradiction with what previously speculated: the laminar-turbulent transition leads to this asymmetry, given that the velocity profile in both the laminar and turbulent flow regimes is axisymmetric while in transitional regime, it is found to be asymmetric.

We observed that when the puff passing through the measurement laser plane, the swirling strength (determined by imaginary part of the complex eigenvalue of the 3D velocity gradient tensor averaged across the pipe cross-section) has a dramatic increase, indicating the onset of turbulent puff. The instantaneous velocity profile and corresponding asymmetry factor are examined in the presence of turbulent puff, both exhibiting the temporary elimination of asymmetry. After the passing of the puff, the flow profile returns to the asymmetric state. This return

to asymmetry is much slower than the asymmetry elimination process and occurs over a time period significantly longer than that of the characteristic time-scale of the turbulent puff itself. This effect of turbulent puff on asymmetry observed in the SPIV experiments is an advancement of understanding of the transitional pipe flow using shear-thinning fluids.

The turbulent puff intermittently appears at arbitrary location in the pipe. With the increasing Reynolds numbers, the turbulent puff grows in size and merges with neighbouring puffs into large region. Eventually the puffed are fully saturated into the pipe and the flow reaches the fully turbulent regime. This explains the reason why in the fully turbulent flow no asymmetry was observed as the fully turbulent flow can be interpreted as the flow which is saturated with turbulent puffs and the asymmetry was eliminated by puffs.

8.4 Evolution of asymmetry with *Re*

We also investigated how the asymmetry first forms and how the asymmetry develops. These questions are answered by taking SPIV measurements across a range of Reynolds numbers from laminar through to transitional *Re*. We observed that beyond a critical Reynolds number (Re_c) the magnitude of the asymmetry factor (α) increases steadily with *Re*. This is essentially different from classical transition to turbulence in many parallel shear flows, including pipe flow, when the working fluid is Newtonian. The transition to turbulence in Newtonian fluids is subcritical, i.e. some flow parameters, e.g. pressure fluctuation, have an abrupt change when turbulent puff occurs. However, the transition from axisymmetry to asymmetry is in the supercritical form as it approximately grows with the square root of *Re*. The square-root behaviour of the asymmetry indicates that the asymmetry is not due to the laminar-turbulent transition process and the evolution of asymmetry in fact appears prior to the onset of laminar-turbulent transition (the *Re* at which transition to turbulence is occurring is determined by examining cross-steam velocity fluctuation and pressure fluctuation).

The streamwise velocity fluctuations follow the trend of the asymmetry measures with

a square-root dependence on *Re* whereas the velocity fluctuations in the cross-stream plane, i.e. radial-azimuthal (r-θ) plane follow a trend similar to that of the pressure fluctuations. The square-root behaviour is not observed in pressure and cross-steam velocity fluctuations and instead we see a sudden increase in pressure and cross-steam velocity fluctuations (i.e. subcritical transition). The reason that the streamwise component follows the trend of the asymmetry measures is due to the fact that the asymmetry is not stationary in time, it therefore creates a fluctuation in axial velocity due to this movement, which is not seen in the in-plane velocity components (because the asymmetry is not seen in those components in our experiment).

Besides the investigations of evolution of the magnitude of asymmetry, we also studied the path that the asymmetry takes to reach its favoured orientation as the Reynolds number is varied as shown in subsection 5.5.7. We observed the asymmetry is non-hysteretic and reversible: it has a preferred route between axisymmetry and asymmetry, which it adheres to regardless of whether it is approaching transition to turbulence or relaminarising.

This experimental evidence reveals that the asymmetry in pipe flow of shear-thinning fluids is not caused by the laminar-turbulent transition process (as previously believed [51, 52, 54, 64]) but is a distinct supercritical instability of the laminar base flow, which is in fact eliminated by the turbulent structures that are formed during classical subcritical, laminar-turbulent transition. We have therefore identified a new flow instability that is unique to strongly shear-thinning fluids. This implies that the laminar flow of shear-thinning fluids may be linearly unstable to asymmetric disturbances, which is not something that has previously been considered and presents many new questions for all researchers interested in the stability of fluid flows.

8.5 Effect of shear-thinning characteristics on asymmetry

The conclusion draw in section 8.4 is based on the experimental work using 0.15% xnathan gum solution. We also studied the shear-thinning effect on flow asymmetry using the xanthan gum solution in the concentration of 0.07%, 0.08%, 0.1%, 0.125%, 0.15%, 0.2%, respectively.

The higher concentration of xanthan gum solution possesses stronger shear-thinning characteristics and throughout the data of all tested concentrations, some ubiquitous features of flow asymmetry are discovered which are ascribed to the nature of shear-thinning property.

First, the asymmetry is prevalent throughout all xanthan gum solutions with different shear-thinning characteristics. It suggests the asymmetry is actually universal in pipe flow of shear-thinning fluids. For all xanthan gum solutions, the asymmetry is not stationary and the preferred asymmetric orientation is *Re*-dependent once Reynolds number is beyond the critical value. Concerning the evolution of asymmetry, the axisymmetry asymmetry transition processes are universally observed to conform with supercritical bifurcation behaviour prior to the appearance of a turbulent puff for all concentrations of xanthan gum soluitions.

Second, we reveal that the higher shear-thinning characteristics enhance the degree of asymmetry, i.e. the greater the shear-thinning characteristics, the stronger the fluid asymmetry will appear, see Figure 6.6. However, the critical Reynolds number Re_{MR} for transition from axisymmetry to asymmetry remains unchanged when the shear-thinning characteristics of fluid varied. The asymmetry all emerged at the $Re_{MR} \approx 2000$ despite the different shear-thinning behaviour index, suggesting the unchanged bifurcation threshold.

Third, the onset of turbulent puff was observed to be delayed comparing with Newtonian fluids and higher concentration of fluid, i.e. higher shear-thinning characteristics of fluid could further delay the onset of laminar turbulent transition, indicating the shear-thinning nature possibly stabilizes the flow and postpone the critical Reynolds number for transition from laminar to turbulent.

8.6 Effect of viscoelastic characteristics on asymmetry

For pure PAA solution (in concentration of 0.09%, 0.125% and 0.2%), there is no pronounced asymmetry observed in the vicinity of laminar-turbulent transition, although the fluid possess significant shear-thinning characteristics. Then 100, 200 and 500ppm PAA solution

mixed with 0.15% xanthan gum solution were investigated for comparison with pure 0.15% xanthan gum.

The maximum degree of asymmetry appears to be reduced after the PAA was added into the 0.15% xanthan gum solution. With the increasing concentration of PAA, the maximum degree of asymmetry was decreased, also suggesting the viscoelasticity inhibits asymmetry. Shear-induced degradation was deliberately imposed on the 0.125% PAA solution to destruct the viscoelasticity of fluid while the shear-thinning characteristics was still preserved. For the degraded PAA solution, i.e. in absence of large viscoelasticity, we observed the asymmetry reappeared and the asymmetry was seen to evolve in a supercritical form.

It gives direct experimental evidence revealing that viscoelasticity suppresses the symmetry-breaking bifurcation and constrains the shear-thinning induced instability as once the viscoelasticity is reduced (the relaxation time λ_c decreased from 0.14s to 0.033s, see Figure 7.13), the symmetry-breaking bifurcation was observed to reappear.

8.7 Future works

Many advancements have been made in this project, giving a much clearer picture of the behaviour of the asymmetric velocity profile of shear-thinning fluids. However, there are still open questions and information in some areas is lacking. Here, we propose some suggestions on which future research would be beneficial.

Experimentally, there is a lack of studies to observe how the preferred asymmetric orientation changes if some fluids are asymmetrically or symmetrically injected (i.e. disturbances) into the main flow in the direction perpendicular to the wall near pipe inlet. In current experiments, when the asymmetry was observed, the natural disturbance existed in the experimental facility, such as the vibration of pump, noise of SPIV system etc.. Once the injection is imposed, some interesting questions are raised, for example: will the asymmetry stay in the same favoured orientation with same magnitude of asymmetry after injection? if not, how will the magnitude and

preferred orientation of asymmetry alter with different injection speed and injection direction? How the injection affects the critical Reynolds number for the axisymmetry asymmetry transition? Solving these questions is helpful to understand the flow characteristics of asymmetry and could be a direction of future work.

More experimental works can be focused on the flow regime, which is in vicinity of critical Reynolds number for axisymmetry asymmetry transition. In current SPIV experiments, the field of view of CMOS cameras is quiet large (10 cm diameter pipe), which fully covers the cross-section of pipe and give a complete view of velocity vector field in cross-sectional plane. To achieve this complete observation in pipe, some high accuracies of SPIV observation are sacrificed. When the flow asymmetry just occurs or the flow is in the regime in which the Reynolds number is slightly beyond the critical Reynolds number for axisymmetry asymmetry transition, it is natural to speculate that there may be some secondary flows in cross-sectional plane and this secondary flow (or some flow structures) may lead to the position of peak velocity located off the central axis of the pipe. However, this magnitude of this secondary flow is very small and we can not observe this secondary flow in our very large scale pipe facility using current CMOS cameres (full resolution is 1290×800 pixels and pixel depths are 12 bits/px). For some small diameter pipe facilities (i.e. the field of view is smaller), this secondary flow may be possibly observed therefore can be a direction of future study. Alternatively, for some large diameter pipes, we can also confine the field of view of cameras to a certain part of pipe (e.g. partly concentrates on the flow region near the peak velocity) instead of entire pipe cross-sectional plane to improve observation accuracy. In general, if we could observe some flow structures or distinct secondary flow in the early onset of asymmetry, it will be beneficial to understand some other flow features of asymmetry.

Further investigation using a more wide range of non-Newtonian fluids is also helpful to understand the asymmetry. The current experimental work studied the flow scenario using shear-thinning and viscoelastic fluids. Future experimental works can be implemented using some fluids with yield stress, e.g. carbopol solution using SPIV investigation. Recently, the

asymmetry is also observed in the surfactant and bio-fluid, like human blood. The future experiments can examine the asymmetry in these types of fluids and compare the flow characteristics of asymmetry with xanthan gum and PAA solutions.

Our experimental evidence reveals that the asymmetry is caused by a newly-identified supercritical instability linked with the shear-thinning nature of fluids. This indicates the pipe flow is linearly unstable for shear-thinning fluids, which is fundamentally different from that of Newtonian fluids. In pipe flow of Newtonian fluids, the flow was theoretically and numerically proved to be linear stable, i.e. any finite-amplitude disturbances will eventually decay. Simulations have been performed using an extension of the openpipeflow.org Navier-Stokes solver for the experimental parameters from the work of Ashley P. Willis. However, in this numerical work, the subcritical turbulence was found for $Re_w \gtrsim 6500$ as observed in experiments. Below this Re_w, the perturbations return to the axisymmetric state in simulations. However, the experimental evidence firmly shows that there is a growing asymmetric state prior to the laminar turbulent transition, therefore, identifying this symmetry-breaking supercritical instability before the turbulent puff could be a motivation for future numerical efforts.

For Newtonian fluids there is recent work on travelling waves at Reynolds numbers in these ranges, e.g. Kerswell & Tutty (2007) [77] (a families of unstable travelling wave solutions in pipe flow at Reynolds numbers lower than the transitional range), Pringle *et al.* (2007) [128] (asymmetric travelling wave in pipe flow). Our data may correspond to a non-Newtonian version of such structures, we have no strong evidence and prefer to leave the interpretation open to the reader. Therefore, for the mathematical perspective, this observation of asymmetry using shear-thinning fluids in pipe flow could excite the research interest of mathematicians, as there is virtually no analytical investigation on this phenomenon to date. Also, our new experimental data implies that the laminar flow of shear-thinning fluids may be linearly unstable to asymmetric disturbances, which is not something that has previously been considered and presents many new questions for all researchers interested in the stability of fluid flows.

Appendices

I. Taylor's hypothesis

Taylor's hypothesis states that "*if the velocity of the air stream which carries the eddies is very much greater than the turbulent velocity, one may assume that the sequence of changes in U at the fixed point are simply due to the passage of an unchanging pattern of turbulent motion over the point* ". It indicates if the relative turbulence intensity u' is assumed to be small enough compared to the mean advection speed U:

$$\frac{u'}{U} \ll 1 \tag{.1}$$

the time-history of the flow signal from a stationary probe can be regarded as that due to convection of a frozen spatial pattern of turbulence past the probe with the mean convection speed U, i.e.

$$u(x,t) = u(x - U\Delta t, t + \Delta t) \tag{.2}$$

where Δt is the time delay and should not be too large. Taylors hypothesis is effectively a method to transfer the time dependent measurement results to a spatial domain. The Taylor's "frozen turbulence "assumption is the theoretical basis to transfer temporal experimental measurements (eg. a time series of SPIV measurement) into a spatial domain that enables to extract flow structure.

References

[1] Adrian R.J. Hairpin vortex organization in wall turbulence. *Physics of Fluids*, 19:041301, 2007.

[2] Adrian R.J., Meinhart C.D., and Tomkins C.D. Vortex organization in the outer region of the turbulent boundary layer. *Journal of Fluid Mechanics*, 422(1):1–54, 2000.

[3] Adrian R.J. and Westerweel J. *Particle image velocimetry*, volume 30. Cambridge University Press, 2010.

[4] Albrecht H.E., Damaschke N., Borys M., and Tropea C. *Laser Doppler and phase Doppler measurement techniques*. Springer Science & Business Media, 2013.

[5] Arnolds O.and Buggisch H., Sachsenheimer D., and Willenbacher N. Capillary breakup extensional rheometry (CaBER) on semi-dilute and concentrated polyethyleneoxide (PEO) solutions. *Rheologica Acta*, 49(11-12):1207–1217, 2010.

[6] Bahrani S.A. and Nouar C. Intermittency in the transition to turbulence for a shear-thinning fluid in Hagen-Poiseuille flow. *Journal of Applied Fluid Mechanics*, 7(1):1–6, 2014.

[7] Bandyopadhyay P.R. Aspects of the equilibrium puff in transitional pipe flow. *Journal of Fluid Mechanics*, 163:439–458, 1986. cited By (since 1996)25.

[8] Barnes H.A. A review of the rheology of viscoelastic systems. *Rheology Reviews*, pages 1–36, 2003.

[9] Barnes H.A., Hutton J.F., and Walters K. *An introduction to rheology*, volume 3. Elsevier, 1989.

[10] Bastiaans R.J.M. *Cross-correlation PIV; theory, implementation and accuracy*. Eindhoven University of Technology, Faculty of Mechanical Engineering, 2000.

[11] Ben-Dov G. and Cohen J. Critical reynolds number for a natural transition to turbulence in pipe flows. *Physical Review Letters*, 98(6), 2007.

[12] Benslimane A., Bekkour K., François P., and Bechir H. Laminar and turbulent pipe flow of bentonite suspensions. *Journal of Petroleum Science and Engineering*, 139:85–93, 2016.

[13] Berkooz G., Holmes P., and Lumley J. L. The proper orthogonal decomposition in the analysis of turbulent flows. *Fluid Mechanics*, 25(25):539–575, 1993.

[14] Berman N.S. Drag reduction by polymers. *Annual Review of Fluid Mechanics*, 10(1):47–64, 1978.

[15] Bertola V. and Cafaro E. Intermediate asymptotic behaviour of fluid flows by scale-size analysis. *Proceedings of the Royal Society A*, 461(2055):755–760, 2005.

[16] Bird R.B. Useful non-Newtonian models. *Annual Review of Fluid Mechanics*, 8(1):13–34, 1976.

[17] Birkhoff G. *Hydrodynamics*. Princeton University Press, 2015.

[18] Biswas D., Casey D.M., Crowder D.C., Steinman D.A., Yun Y.H., and Loth F. Characterization of transition to turbulence for blood in a straight pipe under steady flow conditions. *Journal of Biomechanical Engineering*, 138(7):071001, 2016.

[19] Bonnet J.P., Cole D.R., Delville J., Glauser M.N., and Ukeiley L.S. Stochastic estimation and proper orthogonal decomposition: Complementary techniques for identifying structure. *Experiments in Fluids*, 17(5):307–314, 1994.

[20] Brossard C., Monnier J.C., Barricau P., and Vandernoot F.X. Principles and applications of particle image velocimetry. *Optical Diagnostics of Flows*, 2005.

[21] Caruso M.M., Davis D.A., Shen Q., Odom S.A., Sottos N.R., White S.R., and Moore J.S. Mechanically-induced chemical changes in polymeric materials. *Chemical Reviews*, 109(11):5755–5798, 2009.

[22] Chakraborty P., Balachandar S., and Adrian R.J. On the relationships between local vortex identification schemes. *Journal of Fluid Mechanics*, 535:189–214, 2005.

[23] Chantry M., Willis A.P., and Kerswell R.R. Genesis of streamwise-localized solutions from globally periodic traveling waves in pipe flow. *Physical Review Letters*, 112(16):164501, 2014.

[24] Chhabra R.P. Non-Newtonian fluids: an introduction. In *Rheology of Complex Fluids*, pages 3–34. Springer, 2010.

[25] Chhabra R.P. and Richardson J.F. *non-Newtonian flow in the process industries: fundamentals and engineering applications*. Butterworth-Heinemann, 1999.

[26] Chhabra R.P. and Richardson J.F. *Non-Newtonian flow and applied rheology: engineering applications*. Butterworth-Heinemann, 2011.

[27] Christensen K.T. and Adrian R.J. Statistical evidence of hairpin vortex packets in wall turbulence. *Journal of Fluid Mechanics*, 431:433–443, 2001.

[28] Chung J.S. and Graebel W.P. Laser anemometer measurements of turbulence in non-Newtonian pipe flows. *Physics of Fluids*, 15:546, 1972.

[29] Clasen C. Capillary breakup extensional rheometry of semi-dilute polymer solutions. *Korea-Australia Rheology Journal*, 22(4):331–338, 2010.

[30] Coleman B.D. *Viscometric flows of non-Newtonian fluids: theory and experiment*, volume 5. Cambridge Univ Press, 1966.

[31] Darbyshire A.G. and Mullin T. Transition to turbulence in constant-mass-flux pipe flow. *Journal of Fluid Mechanics*, 289:83–114, 1995.

[32] de Lozar A., Mellibovsky F., Avila M., and Hof B. Edge state in pipe flow experiments. *Physical Review Letters*, 108(21):214502, 2012.

[33] den Toonder J.M.J., Hulsen M.A., Kuiken G.D.C., and Nieuwstadt F.T.M. Drag reduction by polymer additives in a turbulent pipe flow: numerical and laboratory experiments. *Journal of Fluid Mechanics*, 337(1):193–231, 1997.

[34] Denn M.M. Issues in viscoelastic fluid mechanics. *Annual Review of Fluid Mechanics*, 22(1):13–32, 1990.

[35] Denn M.M. Fifty years of non-Newtonian fluid dynamics. *AIChE Journal*, 50(10):2335–2345, 2004.

[36] Dennis D.J.C. and Nickels T.B. On the limitations of taylor's hypothesis in constructing long structures in a turbulent boundary layer. *Journal of Fluid Mechanics*, 614:197–206, 2008.

[37] Dennis D.J.C. and Nickels T.B. Experimental measurement of large-scale three-dimensional structures in a turbulent boundary layer. Part 1. Vortex packets. *Journal of Fluid Mechanics*, 673:180–217, 4 2011.

[38] Dennis D.J.C. and Nickels T.B. Experimental measurement of large-scale three-dimensional structures in a turbulent boundary layer. Part 2. Long structures. *Journal of Fluid Mechanics*, 673:218–244, 4 2011.

[39] Dennis D.J.C. and Sogaro F.M. Distinct organizational states of fully developed turbulent pipe flow. *Physical Review Letters*, 113(23):234501, 2014.

[40] Doi Y., Gray F.M., Buchholz F.L., Graham A.T., Striegel A., Yau W.W., Kirkland J.J., and Bly D.D. *Rheology: principles, measurements, and applications*. Wiley-VCH Verlag GmbH, 1994.

[41] Draad A.A., Kuiken G.D.C., and Nieuwstadt F.T.M. Laminar-turbulent transition in pipe flow for Newtonian and non-Newtonian fluids. *Journal of Fluid Mechanics*, 377:267–312, 1998.

[42] Drazin P.G. and Reid W.H. *Hydrodynamic stability*. Cambridge university press, 2004.

[43] Dubief Y. and Delcayre F. On coherent vortex identification in turbulence. *Journal of Turbulence*, 1(1):011–011, 2000.

[44] Duguet Y., Willis A.P., and Kerswell R.R. Slug genesis in cylindrical pipe flow. *Journal of Fluid Mechanics*, 663:180–208, 2010.

[45] Durst F. and Unsal B. Forced laminar to turbulent transition of pipe flows. *Journal of Fluid Mechanics*, 560(560):449–464, 2006.

[46] Eckhardt B. Turbulence transition in pipe flow: 125th anniversary of the publication of reynolds' paper. *Philosophical Transactions of the Royal Society A: Mathematical, Physical and Engineering Sciences*, 367(1888):449–455, 2009.

[47] Eckhardt B., Schneider T.M., Hof B., and Westerweel J. Turbulence transition in pipe flow. *Annual Review of Fluid Mechanics*, 39:447–468, 2007.

[48] Escudier M.P., Gouldson I.W., and Jones D.M. Flow of shear-thinning fluids in a concentric annulus. *Experiments in Fluids*, 18(4):225–238, 1995.

[49] Escudier M.P., Gouldson I.W., Pereira A.S., Pinho F.T., and Poole R.J. On the reproducibility of the rheology of shear-thinning liquids. *Journal of non-Newtonian Fluid Mechanics*, 97(2):99–124, 2001.

[50] Escudier M.P., Nickson A.K., and Poole R.J. Turbulent flow of viscoelastic shear-thinning liquids through a rectangular duct: Quantification of turbulence anisotropy. *Journal of non-Newtonian Fluid Mechanics*, 160(1):2–10, 2009.

[51] Escudier M.P., Poole R.J., Presti F., Dales C., Nouar C., Desaubry C., Graham L., and Pullum L. Observations of asymmetrical flow behaviour in transitional pipe flow of yield-stress and other shear-thinning liquids. *Journal of non-Newtonian Fluid Mechanics*, 127(2):143–155, 2005.

[52] Escudier M.P. and Presti F. Pipe flow of a thixotropic liquid. *Journal of non-Newtonian Fluid Mechanics*, 62:291–306, 1996.

[53] Escudier M.P., Presti F., and Smith S. Drag reduction in the turbulent pipe flow of polymers. *Journal of non-Newtonian Fluid Mechanics*, 81(3):197–213, 1999.

[54] Escudier M.P., Rosa S., and Poole R.J. Asymmetry in transitional pipe flow of drag-reducing polymer solutions. *Journal of non-Newtonian Fluid Mechanics*, 161(1):19–29, 2009.

[55] Esmael A. and Nouar C. Transitional flow of a yield-stress fluid in a pipe: Evidence of a robust coherent structure. *Physical Review E*, 77:1–4, 2008.

[56] Esmael A., Nouar C., Lefévre A., and Kabouya N. Transitional flow of a non-Newtonian fluid in a pipe: Experimental evidence of weak turbulence induced by shear-thinning behavior. *Physics of Fluids*, 22:1–4, 2010.

[57] Reid L. B. Evans R. C. and Drake E. M. Non-newtonian flow and heat transfer. a.h.p.skelland. wiley, new york, 1967. *Journal of Polymer Science Part A-2: Polymer Physics*, 5(6):1327–1328, 1967.

[58] Faisst H. and Eckhardt B. Traveling waves in pipe flow. *Physical Review Letters*, 91(22):224502, 2003.

[59] Ferry J.D. *Viscoelastic properties of polymers*. John Wiley & Sons, 1980.

[60] Ganapathisubramani B., Longmire E.K., and Marusic I. Characteristics of vortex packets in turbulent boundary layers. *Journal of Fluid Mechanics*, 478(35-46):35–46, 2003.

[61] Gennes P. G. De . Coil-stretch transition of dilute flexible polymers under ultrahigh velocity gradients. *Journal of Chemical Physics*, 60:12(12):5030–5042, 1974.

[62] Ghaem-Maghami E. and Johari H. Velocity field of isolated turbulent puffs. *Physics of Fluids (1994-present)*, 22(11):115105, 2010.

[63] Gustavsson L. H. Energy growth of three-dimensional disturbances in plane Poiseuille flow. *Journal of Fluid Mechanics*, 224:241–260, 1991.

[64] Güzel B., Burghelea T., Frigaard I.A., and Martinez D.M. Observation of laminar-turbulent transition of a yield stress fluid in Hagen-Poiseuille flow. *Journal of Fluid Mechanics*, 627:97, 2009.

[65] Hamilton J.M., Kim J., and Waleffe F. Regeneration mechanisms of near-wall turbulence structures. *Journal of Fluid Mechanics*, 287:317–348, 1995.

[66] Higgins C.W., Froidevaux M., Simeonov V., Vercauteren N., Barry C., and Parlange M.B. The effect of scale on the applicability of taylors frozen turbulence hypothesis in the atmospheric boundary layer. *Boundary-layer Meteorology*, 143(2):379–391, 2012.

[67] Hof B., van Doorne C.W.H., Westerweel J., Nieuwstadt F.T.M., Faisst H., Eckhardt B., Wedin H., Kerswell R.R., and Waleffe F. Experimental observation of nonlinear traveling waves in turbulent pipe flow. *Science*, 305(5690):1594–1598, 2004.

[68] Hyun K., Wilhelm M., Klein C.O., Cho K.S., Nam J.G., Ahn K.H., Lee S.J., Ewoldt R.H., and McKinley G.H. A review of nonlinear oscillatory shear tests: Analysis and application of large amplitude oscillatory shear (LAOS). *Progress in Polymer Science*, 36(12):1697–1753, 2011.

[69] Jaafar A., Escudier M.P., and Poole R.J. Laminar, transitional and turbulent annular flow of drag-reducing polymer solutions. *Journal of non-Newtonian Fluid Mechanics*, 165(19):1357–1372, 2010.

[70] Joseph D.D. Hydrodynamic stability and bifurcation. In *Hydrodynamic Instabilities and the Transition to Turbulence*, pages 27–76. Springer, 1981.

[71] Joseph D.D. *Fluid dynamics of viscoelastic liquids*, volume 84. Springer Science & Business Media, 2013.

[72] Kachanov Y.S. Physical mechanisms of laminar boundary layer transition. *Annual Review of Fluid Mechanics*, 26(1):411–482, 1994.

[73] Katzbauer B. Properties and applications of xanthan gum. *Polymer degradation and stability*, 59(1):81–84, 1998.

[74] Kawahara G., Uhlmann M., and van Veen L. The significance of simple invariant solutions in turbulent flows. *Annual Review of Fluid Mechanics*, 44:203–225, 2012.

[75] Keane R.D. and Adrian R.J. Theory of cross-correlation analysis of PIV images. *Applied Scientific Research*, 49(3):191–215, 1992.

[76] Kerswell R.R. Recent progress in understanding the transition to turbulence in a pipe. *Nonlinearity*, 18(6):R17, 2005.

[77] Kerswell R.R. and Tutty O.R. Recurrence of travelling waves in transitional pipe flow. *Journal of Fluid Mechanics*, 584:69–102, 2007.

[78] Kiijarvi J. Darcy friction factor formulae in turbulent pipe flow. *Lunowa Fluid Mechanics Paper*, 110727, 2011.

[79] Kim K., Adrian R.J., Balachandar S., and Sureshkumar R. Dynamics of hairpin vortices and polymer-induced turbulent drag reduction. *Physical Review Letters*, 100(13):134504, 2008.

[80] Kulicke W.M., Kötter M., and Gräger H. Drag reduction phenomenon with special emphasis on homogeneous polymer solutions. In *Polymer Characterization/Polymer Solutions*, pages 1–68. Springer, 1989.

[81] Kuznetsov Y.A. *Elements of applied bifurcation theory*. Springer-Verlag,, 2013.

[82] Landahl M.T. and Mollo-Christensen E. *Turbulence and random processes in fluid mechanics*. Cambridge University Press, 1992.

[83] Lashgari I., Pralits J.O., Giannetti F., and Brandt L. First instability of the flow of shear-thinning and shear-thickening fluids past a circular cylinder. *Journal of Fluid Mechanics*, 701(6):201–227, 2012.

[84] Leite R.J. An experimental investigation of the stability of Poiseuille flow. *Journal of Fluid Mechanics*, 5(01):81–96, 1959.

[85] Lessen M., Sadler S.G., and Liu T. Stability of pipe Poiseuille flow. *Physics of Fluids (1958-1988)*, 11(7):1404–1409, 1968.

[86] Levenspiel O. *Engineering flow and heat exchange*. Springer, 2014.

[87] Li D. *Encyclopedia of Microfluidics and Nanofluidics*, chapter Relaxation Time of the Viscoelastic Fluid, pages 1781–1781. Springer US, Boston, MA, 2008.

[88] Lindgren E.R. Propagation velocity of turbulent slugs and streaks in transition pipe flow. *Physics of Fluids*, 12:418, 1969.

[89] Lindgren E.R. The transition process and other phenomena in viscous flows. *Journal of Physics and Mathematics*, 2012.

[90] López-Carranza S. N., Jenny M., and Nouar C. Instability of streaks in pipe flow of shear-thinning fluids. *Physical Review E Statistical Nonlinear & Soft Matter Physics*, 88(2):023005–023005, 2013.

[91] López-Carranza S.N., Jenny M., and Nouar C. Pipe flow of shear-thinning fluids. *Comptes Rendus Mécanique*, 340(8):602–618, 2012.

[92] Luchik T.S. and Tiederman W.G. Turbulent structure in low-concentration drag-reducing channel flows. *Journal of Fluid Mechanics*, 190(5):241–263, 1988.

[93] Lumley J.L. Drag reduction by additives. *Annual Review of Fluid Mechanics*, 1(1):367–384, 1969.

[94] L'vov V.S., Pomyalov A., Procaccia I., and Tiberkevich V.l . Drag reduction by polymers in wall bounded turbulence. *Physical Review Letters*, 92(24):244503, 2004.

[95] Ma L. and Barbosa-Canovas G.V. Rheological characterization of mayonnaise. part ii: Flow and viscoelastic properties at different oil and xanthan gum concentrations. *Journal of Food Engineering*, 25(3):409 – 425, 1995.

[96] Madlener K., Frey B., and Ciezki H.K. Generalized reynolds number for non-Newtonian fluids. In *Progress in Propulsion Physics*, volume 1, pages 237–250. EDP Sciences, 2009.

[97] Manneville P. and Pomeau Y. Transition to turbulence. *Scholarpedia*, 4(3):2072, 2009.

[98] Manson J.A. *Polymer blends and composites*. Springer Science & Business Media, 2012.

[99] Mathieu J. and Scott J. *An introduction to turbulent flow*. Cambridge University Press, 2000.

[100] McDonough J.M. Lectures on turbulence. *University of Kentucky*, 2007.

[101] McKeon B.J., Swanson C.J., Zagarola M.V., Donnelly R.J., and Smits A.J. Friction factors for smooth pipe flow. *Journal of Fluid Mechanics*, 511:41–44, 2004.

[102] McKinley G.H. and Sridhar T. Filament-stretching rheometry of complex fluids. *Annual Review of Fluid Mechanics*, 34(1):375–415, 2002.

[103] Mellibovsky F., Meseguer A., Schneider T.M., and Eckhardt B. Transition in localized pipe flow turbulence. *Physical Review Letters*, 103(5):054502, 2009.

[104] Meseguer A. and Trefethen L.N. Linearized pipe flow to Reynolds number 10^7. *Journal of Computational Physics*, 186(1):178–197, 2003.

[105] Metzner A.B. and Reed J.C. Flow of non-Newtonian fluids: correlation of the laminar, transition and turbulent-flow regions. *AIChE Journal*, 1(4):434–440, 1955.

[106] Meyer W.A. A correlation of the frictional characteristics for turbulent flow of dilute viscoelastic non-Newtonian fluids in pipes. *AIChE Journal*, 12(3):522–525, 1966.

[107] Mezger T.G. *The rheology handbook: for users of rotational and oscillatory rheometers*. Vincentz Network GmbH & Co KG, 2006.

[108] Miller E., Clasen C., and Rothstein J.P. The effect of step-stretch parameters on capillary breakup extensional rheology (CaBER) measurements. *Rheologica Acta*, 48(6):625–639, 2009.

[109] Mishra P. and Tripathi G. Transition from laminar to turbulent flow of purely viscous non-Newtonian fluids in tubes. *Chemical Engineering Science*, 26(6):915–921, 1971.

[110] Moffatt H. K. *The Topology of Turbulence*. Springer Berlin Heidelberg, 2000.

[111] Moin P. Revisiting taylor's hypothesis. *Journal of Fluid Mechanics*, 640:1–4, 2009.

[112] Monin M.A.S., Yaglom A.M., and Lumley J.L. Statistical fluid mechanics. *Physics and Astronomy*, 1971.

[113] Moré J.J. The Levenberg-Marquardt algorithm: implementation and theory. In *Numerical Analysis*, pages 105–116. Springer, 1978.

[114] Rott N. Note on the history of the reynolds number. *Annual Review of Fluid Mechanics*, 22(1):1–12, 1990.

[115] Nishi M., Ünsal B., Durst F., and Biswas G. Laminar to turbulent transition of pipe flows through puffs and slugs. *Journal of Fluid Mechanics*, 614:425, 2008.

[116] Okamoto K.L., Nishi S., Saga T., and Kobayashi T. Standard images for particle-image velocimetry. *Measurement Science and Technology*, 11(6):685, 2000.

[117] Pak K.S. and Nasser M.T. Experimental study on the rheological properties of polymer solutions and solid suspensions. *International Journal of Current Engineering and Technology*, 5(2):1170–1177, 2015.

[118] Paterson R.W. and Abernathy F.H. Transition to turbulence in pipe flow for water and dilute solutions of polyethylene oxide. *Journal of Fluid Mechanics*, 51(01):177–185, 1972.

[119] Patterson G.K., Zakin J.L., and Rodriguez J.M. Drag reduction-polymer solutions, soap solutions, and solid particle suspensions in pipe flow. *Industrial & Engineering Chemistry*, 61(1):22–30, 1969.

[120] Peixinho J. and Mullin T. Finite-amplitude thresholds for transition in pipe flow. *Journal of Fluid Mechanics*, 582:169–178, 2007.

[121] Peixinho J., Nouar C., Desaubry C., and Théron B. Laminar transitional and turbulent flow of yield stress fluid in a pipe. *Journal of non-Newtonian Fluid Mechanics*, 128(23):172 – 184, 2005.

[122] Pinho F.T. and Whitelaw J.H. Flow of non-Newtonian fluids in a pipe. *Journal of non-Newtonian Fluid Mechanics*, 34(2):129–144, 1990.

[123] Poole R.J. and Escudier M.P. Turbulent flow of viscoelastic liquids through an axisymmetric sudden expansion. *Journal of non-Newtonian Fluid Mechanics*, 117(1):25–46, 2004.

[124] Poole R.J. and Ridley B.S. Development-length requirements for fully developed laminar pipe flow of inelastic non-Newtonian liquids. *Journal of Fluids Engineering*, 129(10):1281–1287, 2007.

[125] Pope S.B. *Turbulent flows*. Cambridge University Press, 2000.

[126] Prasad A.K. Stereoscopic particle image velocimetry. *Experiments in Fluids*, 29(2):103–116, 2000.

[127] Prasad A.K. and Jensen K. Scheimpflug stereocamera for particle image velocimetry in liquid flows. *Applied Optics*, 34(30):7092–7099, 1995.

[128] Pringle C.T. and Kerswell R.R. Asymmetric, helical, and mirror-symmetric traveling waves in pipe flow. *Physical Review Letters*, 99(7):074502, 2007.

[129] Ptasinski P.K., Nieuwstadt F.T.M., van den Brule B.H.A.A., and Hulsen M.A. Experiments in turbulent pipe flow with polymer additives at maximum drag reduction. *Flow, Turbulence and Combustion*, 66(2):159–182, 2001.

[130] Raffel M., Willert C.E., Werely S.T., and Kompenhans J. *Particle Image Velocimetry-A Pratical Guide*. Springer, 2nd edition edition, 2007.

[131] Rallison J.M. and Hinch E.J. Do we understand the physics in the constitutive equation? *Journal of non-Newtonian Fluid Mechanics*, 29:37–55, 1988.

[132] Rao M.A. Flow and functional models for rheological properties of fluid foods. In *Rheology of Fluid, Semisolid, and Solid Foods*, pages 27–61. Springer, 2014.

[133] Robinson S.K. Coherent motions in the turbulent boundary layer. *Annual Review of Fluid Mechanics*, 23(1):601–639, 1991.

[134] Rochefort W.E. and Middleman S. Rheology of xanthan gum: salt, temperature, and strain effects in oscillatory and steady shear experiments. *Journal of Rheology (1978-present)*, 31(4):337–369, 1987.

[135] Rodd L.E., Scott T.P., Cooper-White J.J., and McKinley G.H. Capillary break-up rheometry of low-viscosity elastic fluids. *Applied Rheology*, 15(1), 2004.

[136] Rodriguez F., Cohen C., Ober C.K., and Archer L. *Principles of polymer systems*. CRC Press, 2014.

[137] Rosa S. *Laminar-turbulent transition for pipe flow of yield-stress and other shear-thinning liquids*. PhD thesis, School of Engineering, University of Liverpool, 2008.

[138] Rubin Y., Wygnanski I., and Haritonidis J.H. Further observations on transition in a pipe. *Interim Report, Mar. 1978-Mar. 1979 Tel-Aviv Univ.(Israel). School of Engineering.*, 1, 1979.

[139] Rudman M., Blackburn H.M., Graham L.J.W., and Pullum L. Turbulent pipe flow of shear-thinning fluids. *Journal of non-Newtonian Fluid Mechanics*, 118(1):33–48, 2004.

[140] Ryan N.W. and Johnson M.M. Transistion from laminar to turbulent flow in pipes. *AIChE Journal*, 5(4):433–435, 1959.

[141] Ryskin G. Turbulent drag reduction by polymers: a quantitative theory. *Physical Review Letters*, 59(18):2059, 1987.

[142] Sá Pereira A. and Pinho F.T. Turbulent pipe flow characteristics of low molecular weight polymer solutions. *Journal of non-Newtonian Fluid Mechanics*, 55(3):321–344, 1994.

[143] Salwen H., Cotton F.W., and Grosch C.E. Linear stability of Poiseuille flow in a circular pipe. *Journal of Fluid Mechanics*, 98(02):273–284, 1980.

[144] Scarano F., David L., Bsibsi M., and Calluaud D. SPIV comparative assessment: image dewarping plus misalignment correction and pinhole plus geometric back projection. *Experiments in Fluids*, 39(2):257–266, 2005.

[145] Schlichting H. and Gersten K. *Boundary layer theory*. Springer Science & Business Media, 2003.

[146] Schmid P.J. Nonmodal stability theory. *Annual Review of Fluid Mechanics*, 39:129–162, 2007.

[147] Schmid P.J. and Henningson D.S. *Stability and transition in shear flows*, volume 142. Springer Science & Business Media, 2012.

[148] Schramm G. *A practical approach to rheology and rheometry*. Haake Karlsruhe, 1994.

[149] Shan H., Ma B., Zhang Z., and Nieuwstadt F.T.M. Direct numerical simulation of a puff and a slug in transitional cylindrical pipe flow. *Journal of Fluid Mechanics*, 387:39–60, 1999.

[150] Sreenivasan K.R. and White C.M. The onset of drag reduction by dilute polymer additives, and the maximum drag reduction asymptote. *Journal of Fluid Mechanics*, 409:149–164, 2000.

[151] Stelter M., Brenn G., Yarin A.L., Singh R.P., and Durst F. Investigation of the elongational behavior of polymer solutions by means of an elongational rheometer. *Journal of Rheology (1978-present)*, 46(2):507–527, 2002.

[152] Tabor M. and de Gennes P.G. A cascade theory of drag reduction. *EPL (Europhysics Letters)*, 2(7):519, 1986.

[153] Taylor G.I. The spectrum of turbulence. In *Proceedings of the Royal Society of London A: Mathematical, Physical and Engineering Sciences*, volume 164, pages 476–490. The Royal Society, 1938.

[154] Theunissen R., Scarano F., and Riethmuller M.L. An adaptive sampling and windowing interrogation method in PIV. *Measurement Science and Technology*, 18(1):275, 2006.

[155] Toms B.A. Some observation on the flow of linear polymer solutions through straight tubes at large reynolds numbers. In *Proceedings 1st International Congress on Rheology*, 1949.

[156] Trefethen L.N., Trefethen A.E., Reddy S.C., and Driscoll T.A. Hydrodynamic stability without eigenvalues. *Science*, 261(5121):578–584, 1993.

[157] van Doorne C.W.H. Stereoscopic PIV on transition in pipe flow. *TU Delft University*, 2004.

[158] van Doorne C.W.H., Hof B., and Lindken R.H. Time resolved stereoscopic PIV in pipe flow, visualizing 3D flow structures. In *5th International Symposium on Particle Image Velocimetry*, September 2003.

[159] van Doorne C.W.H. and Westerweel J. Measurement of laminar, transitional and turbulent pipe flow using stereoscopic-PIV. *Experiments in Fluids*, 42(2):259–279, 2007.

[160] van Doorne C.W.H. and Westerweel J. The flow structure of a puff. *Philosophical Transactions of the Royal Society A: Mathematical, Physical and Engineering Sciences*, 367(1888):489–507, 2009.

[161] Virk P.S. Drag reduction fundamentals. *AIChE Journal*, 21(4):625–656, 1975.

[162] Waleffe F. Hydrodynamic stability and turbulence: beyond transients to a self-sustaining process. *Studies in applied mathematics*, 95(3):319–343, 1995.

[163] Waleffe F. On a self-sustaining process in shear flows. *Physics of Fluids (1994-present)*, 9(4):883–900, 1997.

[164] Wedin H. and Kerswell R.R. Exact coherent structures in pipe flow: travelling wave solutions. *Journal of Fluid Mechanics*, 508(333-371):2–5, 2004.

[165] Westerweel J. Fundamentals of digital particle image velocimetry. *Measurement Science and Technology*, 8(12):1379, 1997.

[166] White C.M. and Mungal M.G. Mechanics and prediction of turbulent drag reduction with polymer additives. *Annual Review of Fluid Mechanics*, 40:235–256, 2008.

[167] White W.D. and McEligot D.M. Transition of mixtures of polymers in a dilute aqueous solution. *Journal of Basic Engineering*, 92:411, 1970.

[168] Willis A.P. and Kerswell R.R. Critical behavior in the relaminarization of localized turbulence in pipe flow. *Physical Review Letters*, 98(1):014501, 2007.

[169] Willis A.P. and Kerswell R.R. Coherent structures in localized and global pipe turbulence. *Physical Review Letters*, 100(12):124501, 2008.

[170] Willis A.P., Peixinho J., Kerswell R.R., and Mullin T. Experimental and theoretical progress in pipe flow transition. *Philosophical Transactions of the Royal Society A: Mathematical, Physical and Engineering Sciences*, 366(1876):2671–2684, 2008.

[171] Winter H. and Chambon F. Analysis of linear viscoelasticity of a crosslinking polymer at the gel point. *Journal of Rheology (1978-present)*, 30(2):367–382, 1986.

[172] Wygnanski I.J. and Champagne F.H. On transition in a pipe. Part 1. The origin of puffs and slugs and the flow in a turbulent slug. *Journal of Fluid Mechanics*, 59:281–335, 6 1973.

[173] Wygnanski I.J., Sokolov M., and Friedman D. On transition in a pipe. Part 2. The equilibrium puff. *Journal of Fluid Mechanics*, 69(02):283–304, 1975.

[174] Yasuda K.Y., Armstrong R.C., and Cohen R.E. Shear flow properties of concentrated solutions of linear and star branched polystyrenes. *Rheologica Acta*, 20(2):163–178, 1981.

[175] Zakin J.L., Myska J., and Chara Z. New limiting drag reduction and velocity profile asymptotes for nonpolymeric additives systems. *AIChE Journal*, 42(12):3544–3546, 1996.

[176] Zakin J.L., Ni C.C., Hansen R.J., and Reischman M.M. Laser Doppler velocimetry studies of early turbulence. *Physics of Fluids (1958-1988)*, 20(10):S85–S88, 2008.

[177] Zhou J., Adrian. R.J., Balachandar S., and Kendall T.M. Mechanisms for generating coherent packets of hairpin vortices in channel flow. *Journal of Fluid Mechanics*, 387:353–396, 1999.